

VISUALISING AND MODELLING FLOW
PROCESSES IN FRACTURED CARBONATE
ROCKS WITH X-RAY COMPUTED
TOMOGRAPHY

CLAUDIA FRICKE

PhD Thesis
Heriot-Watt University
School of Energy, Geoscience, Infrastructure and Society (EGIS)
August 2020

The copyright in this thesis is owned by the author. Any quotation from the thesis or use of any of the information contained in it must acknowledge this thesis as the source of the quotation or information.

ABSTRACT

Naturally Fractured Reservoirs (NFR) have typically very complex geometries from the pore scale to the field scale – discontinuities can be found at each scale. This makes NFRs hard to accurately be modelled for flow simulations. Fractures are especially difficult to incorporate in the simulations. The topology of a single fracture is usually simplified to a plane or disk, and apertures are usually averaged to be implemented in the simulation models. The fracture aperture distribution of a single fracture is already very heterogeneous though. Contact areas in fractures can detain flow, whereas connected fracture regions with larger apertures can result in preferred flow paths and lead to early breakthrough.

To help understanding how well current Discrete Fracture and Matrix (DFM) models are suitable to retain fracture influences on flow in carbonates, this research project combines the simulation of miscible single-phase flow through fractures in carbonates with precise fracture measurements (comprising fracture aperture distributions and 3D topologies) and the visualization of real single and two-phase flow experiments in fractured carbonate cores. The simulation approach employs a DFM model with a hybrid finite element/ finite volume (FEFV) method. The fractured core samples and the flow experiments are imaged with high-resolution X-ray computer tomography (CT), or X-ray radiography respectively.

The main goals are to develop and optimize an image processing workflow from the X-ray CT fracture measurement to an according mesh generation as input for simulations, and to be able to compare simulations and flow experiment studies qualitatively to analyse how well the DFM approach is able to capture the true nature of fluid flow in fractures with real aperture distributions. To obtain most relevant comparisons, we conduct numerical simulations and flow experiments on the same fracture geometries, which have been measured before non-destructively.

*The fishermen know that the sea is dangerous and the storm terrible,
but they have never found these dangers sufficient reason for remaining ashore.*

— Vincent Van Gogh

ACKNOWLEDGMENTS

This work was supported by the ExxonMobil research alliance "Fundamental Controls of Flow in Carbonates" (FC)², a UK's Engineering and Physical Sciences Research Council (EPSRC) Case Award, and the Edinburgh Collaborative of Subsurface Science and Engineering (ECOSSE). The project started in May 2008 at the Institute of Petroleum Engineering, Heriot Watt University Edinburgh, supervised by Prof. Dr. Sebastian Geiger and, in collaboration with the University of Edinburgh, co-supervised by Dr. Ian Butler and Dr. Stephen Elphick.

Research Thesis Submission

Please note this form should be bound into the submitted thesis.

Name:	Claudia Fricke		
School:	Energy, Geoscience, Infrastructure and Society		
Version: <small>(i.e. First, Resubmission, Final)</small>	Final	Degree Sought:	PhD

Declaration

In accordance with the appropriate regulations I hereby submit my thesis and I declare that:


1. The thesis embodies the results of my own work and has been composed by myself
2. Where appropriate, I have made acknowledgement of the work of others
3. The thesis is the correct version for submission and is the same version as any electronic versions submitted*.
4. My thesis for the award referred to, deposited in the Heriot-Watt University Library, should be made available for loan or photocopying and be available via the Institutional Repository, subject to such conditions as the Librarian may require
5. I understand that as a student of the University I am required to abide by the Regulations of the University and to conform to its discipline.
6. I confirm that the thesis has been verified against plagiarism via an approved plagiarism detection application e.g. Turnitin.

ONLY for submissions including published works


Please note you are only required to complete the Inclusion of Published Works Form (page 2) if your thesis contains published works)

7. Where the thesis contains published outputs under Regulation 6 (9.1.2) or Regulation 43 (9) these are accompanied by a critical review which accurately describes my contribution to the research and, for multi-author outputs, a signed declaration indicating the contribution of each author (complete)
8. Inclusion of published outputs under Regulation 6 (9.1.2) or Regulation 43 (9) shall not constitute plagiarism.

* Please note that it is the responsibility of the candidate to ensure that the correct version of the thesis is submitted.

Signature of Candidate:		Date:	16.08.2020
-------------------------	---	-------	------------

Submission

Submitted By <small>(name in capitals)</small> :	CLAUDIA FRICKE
Signature of Individual Submitting:	
Date Submitted:	16.08.2020

For Completion in the Student Service Centre (SSC)

Limited Access	Requested	Yes	No	Approved	Yes	No
<i>E-thesis Submitted (mandatory for final theses)</i>						
Received in the SSC by <small>(name in capitals)</small> :				Date:		

CONTENTS

1	INTRODUCTION	1
1.1	Carbonates	3
1.2	Naturally fractured reservoirs	5
1.3	Characteristics of Porous Media and Fractures	6
1.3.1	Porous Media	6
1.3.2	Fractures	9
1.4	Dual Porosity and Dual Permeability Models	16
1.5	DFM flow modelling	20
1.6	CSMP++	24
1.7	X-ray CT of geomaterials	25
1.8	Image processing and analysis	28
1.9	Flow experiments visualized with CT	35
1.10	Review summary	41
1.11	Objectives and structure of the thesis	43
2	METHODOLOGY	46
2.1	Introduction	46
2.2	Carbonate Samples	46
2.3	Imaging Equipment	48
2.3.1	Background of μ -CT	48
2.3.2	CT scanner development	53
2.3.3	CT Control Software Development	54
2.3.4	Optimization of Data Collection	58
2.4	Image Artefact Correction	63
2.5	Fracture Aperture Measurement	67
2.6	Numerical Flow Modelling	71
2.7	Simulations	74
2.7.1	Governing Equations for Single-Phase Flow	75
2.7.2	Numerical Formulation	75
2.7.3	Example simulation of 2D tracer transport	79
2.7.4	Example 3D simulation of tracer transport in a fracture	83

2.7.5	2D simulation of tracer transport in fractures in Baker Dolomite and San Andreas Carbonate	84
2.8	Single and Two Phase Flow Experiments	87
2.8.1	Experimental Setup	87
2.8.2	Flow Experiments	89
2.9	Summary of methodology	91
3	PHOTOGRAPHIC IMAGE CORRECTION FOR CMOS PANEL DETECTORS	94
3.1	Introduction	94
3.2	New Image Correction Method	97
3.2.1	Linear gain correction	99
3.2.2	Fit to piecewise quadratic polynomial	100
3.2.3	Gain Correction	101
3.2.4	Error calculation	102
3.3	Conclusions	104
4	CORE FRACTURE ANALYSIS	106
4.1	Introduction	106
4.2	Fracture Aperture Measurements with combined PH and FWHM method	108
4.2.1	Calibration measurements	108
4.2.2	Aperture measurements	116
4.3	Statistical Analysis of Fracture Aperture	119
4.4	Discussion	121
5	FLOW EXPERIMENTS	123
5.1	Experimental Set-Up	123
5.2	Single-Phase Flow Experiments	126
5.3	Two-Phase Flow Experiments	139
5.4	Discussion	149
6	USING X-RAY CT DERIVED FRACTURE APERTURES FOR SIMULATING MISCIBLE FLUID FLOW IN FRACTURED CARBONATES	150
6.1	Mesh generation	150
6.1.1	Upscaling of fracture aperture information	150
6.2	Influence of fracture apertures on flow rates	151
6.3	Single-Phase Flow Simulations	155
6.4	Discussion	156

7	CONCLUSIONS AND DISCUSSION	164
A	APPENDIX	190
A.1	Governing equations for two-phase flow	190
A.2	Developed Matlab Program for Image Correction of CMOS Panel Detectors	193
A.3	CT Scanner – Table and Camera Control	197

LIST OF FIGURES

Figure 1	Sketch illustrating the transformation of sediment into limestone via diagenesis (from James et al., 2015 [94]).	4
Figure 2	Geologic complexity of an outcrop of Liassic limestone on the southern Bristol Channel. (A) Photograph of small-scale fold structure intersected by carbonate veins crosscut by later Alpine joints. Camera lid has 5 cm diameter, for scale. (B) Free-form NURBS CAD model of the same structure. Similar CAD model constructions can be used in the DFM simulations in CSMP++ (from Paluszny et al., 2007 [158]).	7
Figure 3	Definition of an REV for a porous medium (after Helmig, 1997 [81]).	9
Figure 4	Schematic of a fracture confined by two rough surfaces, which are separated by an aperture a . The two surfaces touch in one position (red arrow). Two reference planes are drawn, separated by a distance d , which can be used to define the roughness of the surfaces as a perpendicular distance to the corresponding reference plane, and also help to calculate the fracture aperture as the distance between the opposing rock surfaces perpendicular to a nominal fracture plane, which can usually be defined locally (from Zimmermann and Main, 2004 [213]).	11

Figure 5	<p>A Barton Comb, here being used in a field measurement, is a profile gauge commonly used for the classification of roughness profiles of rock surfaces. Joint roughness coefficients (JRC) for the surface can be determined by comparing the fracture surface geometry with Barton’s standard profiles — cf. Barton and Choubey, 1977 [14]. (Image from Hubbard Brook Ecosystem Study [87]). 12</p>
Figure 6	<p>Idealisation of a fractured system as two conceptual domains (from Warren and Root, 1963 [203]). 16</p>
Figure 7	<p>Schematic illustration of different recovery processes in fractured reservoirs: (a) fluid expansion, (b) imbibition, (c) gravity drainage, and (d) diffusion. (from Lu et al., 2008 [123]). 17</p>
Figure 8	<p>Fracture maps of a joint system in Devonian sandstones in western Norway at two different scales from aerial photographs. The right image shows a section of the left image with a higher resolution. Left: The smallest resolved fracture is ca. 10m long, the largest fracture ca. 300m. Right: The smallest resolved fracture is ca. 1m long, the largest fracture ca. 30m. Longer fractures (here blue) cannot be observed on the smaller scale because of the size of the domain considered. Further it is notable that only a small amount of the fractures are connected and the connectivity changes with scale (see Odling, 1997 [152]). 19</p>
Figure 9	<p>Fracture length distribution for the joint system in Devonian sandstones in western Norway. The dashed line indicates a power law correlation between the fracture length and the number of fractures (from Odling, 1997 [152]). 19</p>
Figure 10	<p>Construction of the node-centered finite volumes at nodes i and j with triangular finite elements $e_{i1} - e_{in}$ ($e_{j1} - e_{jn}$, respectively) and segments $s_{i1} - s_{in}$ ($s_{j1} - s_{jn}$, respectively) (from Geiger et al., 2004 [77]). 21</p>

Figure 11	Complementary mesh for the combined FE-FV method. Left: Triangular 2D finite element mesh. Right: Corresponding node-centred finite volume mesh. The red 1D elements/volumes represent a sub-horizontal 1D fracture. (from Geiger et al., 2009 [74])	22
Figure 12	Different finite element types commonly used for domain discretisation in the so called hybrid-element method in mixed-dimensional systems. In DFM, the fractures are represented by elements with one dimension less than the surrounding elements, representing the rock matrix. The different element types are used simultaneously for a hybrid-element discretisation to reduce the number of unknowns significantly (from Geiger et al., 2009 [74]).	22
Figure 13	Difficult fracture intersections for automatic mesh generation, since it is complicated to differentiate between intersecting fractures (1, 4) and disconnected fractures (2, 3) (from Reichenberger et al., 2006 [172]).	24
Figure 14	Example for a CSMP++ application: Model BED ₄ – Reservoir during primary drainage. This simulation illustrates the influence of well-connected fractures on the saturation distribution. The white iso-contours on the model boundaries indicate the fluid pressure distribution. (a) Reservoir at water-breakthrough after 5.4 hours, average oil saturation ca. 20%. The oil first enters the connected fractures (dark green). (b) The reservoir towards the end of the primary drainage after 234 days, average oil saturation ca. 80%. The oil is diffusing into the surrounding matrix (from Matthäi et al., 2007 [130]).	26

Figure 15	<p>(a) Two-dimensional cross-section of three-dimensional micro-CT images of Ketton limestone, an oolitic quarry limestone of Jurassic age. The pore space is shown dark. Diameter of sample is 5mm. The grains are smooth spheres with large pore spaces. The grains themselves contain micro-pores that are not resolved.</p> <p>(b) Pore-space image of (a) has been binarized into pore and grain. A central 1000^3 section has been extracted. The images show only the pore space.</p> <p>(c) Pore network extracted from (b). The pore space is represented as a lattice of wide pores (shown as spheres) connected by narrower throats (shown as cylinders). The size of the pore or throat indicates the inscribed radius (from Blunt et al., 2013 [23]). 28</p>
Figure 16	<p>Left: Highlighted cross-section of San Andreas carbonate. Blue: rock matrix, white: fracture. The yellow line denotes the location the line profile. Right: Corresponding graph (line profile) of the sample's apparent grey values perpendicular to the fracture. This profile indicates an existing region of lower density in the sample, which is assigned to the fracture. 31</p>
Figure 17	<p>(a) An attenuation profile of a fracture perpendicular to the fracture plane in a homogeneous medium would deliver a rectangular signal. (b) If noise and heterogeneities in the rock matrix (e.g. pores below the voxel resolution) superimpose, the signal becomes slightly blurred. (c) The dip in the profile is due to the partial volume effect and the superimposed point-spread function (PSF), which cause the fracture boundaries to be less "steep". 33</p>

Figure 18	CT images of granite samples with aperture sizes ranging from 0.076mm to 3.937mm. Spatial image resolution 1.4mm by 1.4mm by 5mm. Narrow fractures show a signal peak of the profile that is significantly higher than air, and for very narrow fractures hardly distinguishable from the surrounding pores or noise signal (from Johns et al., 1993 [97]).	34
Figure 19	CT images for "filling-fracture" system for different times. This regime shows a plane source that grows with time due to relatively slow water flow through fractures. Fracture initially air-filled. Dark shading indicates zero water saturation while white indicates fully water saturated. Water injection at 1cc/min in a fracture 0.1mm thick. Injection is from lower left corner and production from lower right corner (from Rangel-German, 2002 [168]).	36
Figure 20	Two-dimensional oil distribution development during waterflooding of a moderately oil-wet core. NMRI images at orthogonal directions. Each time step has a longitudinal image showing the stacked cores (inlet core, fracture, outlet core) and a transverse image of the fracture. Oil appears bright and lack of color equals reduced oil saturation. Oil was produced from the inlet core in the form of droplets growing on the fracture surface (from [66]).	38
Figure 21	Green: Oil residence relative to local fracture aperture (dark and light grey represent small and large apertures, respectively) generated by x-ray microtomography at the end of different experimental stages (from Piri and Karpyn, 2007 [161]).	41
Figure 22	Carbonate Samples: (a) San Andreas Carbonate (SAC), (b) Baker Dolomite (BD) cores with a single artificial fracture. Diameter 3.81cm.	48

Figure 23	Modified Brazilian test. The cylindrical rock cores are clamped between two wedges. The vertical pressure is slowly increased until a fracture forms along the length of the core sample.	49
Figure 24	Initial configuration of a CT Scanner; (a) X-ray source, (b) rotary table for sample, (c) X-ray camera/detector (by Ian Butler).	49
Figure 25	Typical radiograph and stack of cross sections (a) Indiana limestone sample containing an artificial fracture (diagonal to the core length) filled with lead oxide loaded epoxy particles (diameter 1.27cm). (b) Single 2D X-ray projection of the same sample (in the x - z -plane), (c) example images out of 900 of the stack of reconstructed tomographic cross-sections (in the x - y -plane) acquired from 50 projections from different angles.	50
Figure 26	Reconstruction of an example object consisting of an Indiana limestone sample containing an artificial fracture (diagonal to the core length) filled with lead oxide loaded epoxy (fig. 25) acquired from 50 projections. Dark streaks are caused by beam hardening, which can also cause the outer areas to be brighter. Further streak (or star) artefacts can be caused by too little projections. The cause for ring artefacts lies usually in defect pixels at the detector which are then "reconstructed" over the whole cross-section (Kak, 1999 [101]).	53
Figure 27	X-Ray CT scanner components: (a) X-ray source (Fe-infocus dual head transmission/directional nano/microfocus tube), (b) Air-bearing rotary table (Micos UPR-160F SMC Pegasus with Taurus motion controller), (c) 4 MP Gadox X-ray camera (Rad-icon Shad-o-Box) with vertical adjustable mounting.	55

Figure 28	Graphical User Interface (GUI): The developed Test-point front end provides a user friendly interface for the operation of the CT. It operates the camera and the rotating table in the background by calling the developed external C++ routine to control the camera, and piloting the hardware controller of the table via the parallel port. 57
Figure 29	(a) Indiana limestone sample containing an artificial fracture (brown line in the centre of the core, diagonally to the core length), diameter 1.27cm. (b) Single 2D X-ray projection of the same sample. Dark areas mark a higher cumulative density as the X-rays are attenuated relating to the material density and the path length the X-rays travel through the sample object. The rectangular pattern across the image is caused by the camera consisting of an array of eight image sensors. Note that the example of a fractured Indiana Limestone is for illustration only - the location of the fracture is not suitable for flow experiments. A linear fracture through the center of a core plug had to be manufactured for the subsequent studies. 59
Figure 30	18 example images out of 900 of the stack of reconstructed tomographic cross-sections acquired from 50 projections from different angles around the sample object in fig. 29. Each image corresponds to a slice of the object and to one pixel row on the detector. Realization with Octopus. 59

Figure 31	<p>Rendered 3D computer model of the sample object in fig. 29 built from the stack of cross-sections from fig. 30. (a) Complete 3D model of the limestone core. The fracture is clearly recognizable diagonal to the core length. The scattered voxels around the object refer to "bad pixels" on the camera. (b) Visualization of only the lead-epoxy filled fracture by excision of brighter voxels referring to less dense material. (c) Cross-section in the x-plane through the 3D model. Dark blue color refers to less dense areas in the object, white areas mark high density. Any possible slicing and any data extraction depending on the gray value of the voxels can be realized. Rendering and visualization software: Octopus 3D Viewer.</p>	60
Figure 32	<p>Schematic of CT scanner components to influence magnification.</p>	61
Figure 33	<p>Reconstruction: Reconstructed tomographic cross-sections of the samples in fig. 22 (a) SAC acquired from 360 projections, (b) BD acquired from 700 projections. Due to beam hardening, the samples appear to be brighter towards the rim. Software: Octopus.</p>	61
Figure 34	<p>Rendered 3D computer model: Comparison of SAC (left, blue) and BD (right, red). Top: 3D visualisation of a slice of the reconstructed core. Bottom: Straight cut through the sample with the cutting plane along the fracture. Note that the finer grained material in the SAC is part of the matrix. The fracture is slightly curved (see fig. 33) and hence the straight cut-plane intersects fracture and matrix. Rendering and visualization software: ImageVis3D.</p>	62
Figure 35	<p>Reconstruction of a scanned BD sample which shows a significant spot artefact in the middle.</p>	64

Figure 36	Flat-Field image of the camera showing 2-by-4 panel pattern. The camera consists of a 2-by-4 array of CMOS photodiode panels. A standard image normalization method cannot cancel this evolving pattern.	65
Figure 37	X-ray phantom image of the cylindric carbonate core with a vertical fracture visible in the centre of the sample. (a) Carbonate sample \varnothing 3.81 cm with a single fracture; (b) Original radiographic image including the artefact that shows the 2-by-4 sensor panels clearly; (c) Standard linear corrected image that does not remove the artefact completely; (Images b and c are gamma corrected by 4.0 for the purpose of clarity. Camera: Shad-o-Box TM 4K from Rad-Icon Imaging Corp (now Teledyne Dalsa).	65
Figure 38	Top: Projection images (left) before and (right) after correction using the piecewise polynomial approach. Bottom: Reconstructed CT images for the (left) uncorrected and (right) corrected projections.	66
Figure 39	Sketch depicting the different methods to quantify fracture apertures; green: full width at half maximum (FWHM), red: peak height (PH), yellow: missing attenuation area (MA)	68

Figure 40	<p>Image Processing Sequence. For a quantitative analysis of the fracture geometry and volume extraction an accurate image segmentation algorithm is crucial. To simplify matters, the two core halves of the BD sample (fig. 33(b)) were gapped out by about 1-2 mm to increase the image contrast. 700 projections were recorded, reconstructed, and segmented to obtain a 3D fracture volume (see fig. 41). (a) Original reconstructed slice, (b) cropped area of (a), (c) histogram based contrast enhancement, (d) application of Median filter (3×3 neighborhood, 10 iterations), (e) binarization with a global threshold, (f) concluding automated cavity removal. A slice-wise treatment of the measured volume was possible due to its clear-cut feature geometry. The sequence works well with this data set as it preserves the fracture roughness well enough while pore and noise information is discarded. For finer fractures and multi-phase images advanced volumetric image processing algorithms are necessary. Realization with Matlab Image Processing Toolbox.</p>	69
Figure 41	<p>Stereographic 3D Representation of Fracture Volume. Segmented fracture volume of the BD sample (fig. 33(b)) from front and back view, which was implemented in the conceptual flow simulation study (see section 2.7). (Please use red-cyan 3D glasses.) Realization with ImageVis3D.</p>	69
Figure 42	<p>Visual representation of the fracture aperture distributions [mm] (left) and topology (right). Top: Baker Dolomite, Bottom: San Andreas Carbonate (see fig. 22). Voxel resolution $23.6\mu\text{m}$. Dimension of the fractures is 3.8 by ~ 10 cm.</p>	71
Figure 43	<p>Geometric representation of a 2D fracture embedded in a 3D cylindric rock core with Rhinoceros 4.0.</p>	72

Figure 44	Generated example mesh with about 10000 finite elements, where the fracture contains about 4000 2D finite elements. Software Ansys ICEM.	73
Figure 45	Sketch depicting the test for a measurement point being inside a finite element. Left: Point with aperture measurement (red) outside finite element (blue). The area of the triangles 1-2-a, 2-3-a, 1-3-a sums up to a larger area than the area of the finite element 1-2-3. Right: Point with aperture (red) inside finite element (blue). The area of the triangles 1-2-a, 2-3-a, 1-3-a sums up to the same area as of the finite element 1-2-3. . . .	74
Figure 46	(a) Real fracture aperture measured with High Resolution Computer Tomography (from Karpyn et al., 2007 [106]), min. aperture 0mm, max. aperture 1.6mm, mean aperture 0.58mm, standard deviation 0.25mm. (b) Fracture aperture field with the same statistical properties.	81
Figure 47	Flow simulation showing the tracer concentration in the statistically generated fracture aperture distribution (Fig. 46 (b)) at different time steps. Flow is from left to right. Red: Concentration $c = 1$, Blue: Concentration $c = 0$. Initially, the concentration in the fracture is zero. Fluid with high concentration enters at the left boundary. Note the stagnant areas where the local aperture is small. We simulated advection and dispersion, assuming that the fracture permeability scales locally with the cube of the fracture aperture.	82

Figure 48	<p>(a) Breakthrough curves showing the concentration at the right boundary for different permeability models: (1) statistically generated fracture with an overlying permeability distribution, (2) fit with uniform mean permeability computed for the flow field by Darcy's Law, (3) fit with uniform upscaled permeability using the cubic law and a mean aperture. (b) Improved fits for the upscaled breakthrough curves: (1) statistically generated fracture, (2) uniform upscaled permeability using the cubic law and a mean aperture, (3) and (4) fit with uniform upscaled permeability and adjusting the longitudinal (α_L) and the transversal (α_T) dispersivity coefficients (1) and (2) $\alpha_L = 3 \cdot 10^{-5}$ m, $\alpha_T = 3 \cdot 10^{-6}$ m, (3) $\alpha_L = 1 \cdot 10^{-2}$ m, $\alpha_T = 2.5 \cdot 10^{-4}$ m, (4) $\alpha_L = 1 \cdot 10^{-3}$ m, $\alpha_T = 1 \cdot 10^{-5}$ m.</p>	83
Figure 49	<p>Top: Non-uniform fracture aperture distribution generated with a random field generator algorithm (right: histogram); bottom: Corresponding permeability calculated via cubic law. The fracture is 10 by 15 cm.</p>	84
Figure 50	<p>Simulation of a single phase tracer transport in a 3D core geometry with the non-uniform aperture data from fig. 49 mapped onto the 2D fracture embedded along the core length (horizontal and vertical cut through a core at different time steps), as schematically shown in the small inlet box (bottom right). Core diameter 0.1 m, core length 0.15 m, matrix permeability 0.05 D, pressure gradient 5 Pa. Flow is from left to right. Initial tracer concentration in core and fracture is zero.</p>	85
Figure 51	<p>Simulation of a single phase tracer transport in a 2D fracture, frontal view . Top: Baker Dolomite. Bottom: San Andreas Carbonate. Flow is from left to right. The inflow rate is 10ml s^{-1}. Initial concentration in the fracture is zero.</p>	86

Figure 52	Flow cell suitable for X-Ray CT experiments with minimal beam attenuation and smooth fluid pressure distribution on the inlet and outlet area. The flow cell mainly consists of two epoxy platens simply extending the core, with a thin latex jacket surrounding the core. This creates minimal and uniform X-ray beam attenuation which can minimize artefacts and enhance data collection times.	88
Figure 53	Measured grey values (high values indicate low beam attenuation) from normalized images depending on the beam intensity for potassium iodide (KI), potassium chloride (KCl) solutions, water, oil, and Baker Dolomite.	89
Figure 54	Radiography time series of single-phase tracer transport in a Baker Dolomite core (\varnothing 3.81 cm, length 10 cm) with a single artificial fracture. Top row: side view (looking along the fracture surface), bottom row: front view (looking at the fracture surface). Flow is vertically upwards. Approximately 450 images were acquired in the experiments and each image acquisition process took about 3 seconds.	90
Figure 55	Workflow overview outlining the various steps of the applied methodology to realize a comparison of flow experiments in fractured carbonates with simulations accounting for the non-uniformity of the fracture. . . .	93
Figure 56	Flat-Field image of camera shows 2-by-4 panel pattern. The camera consists of a 2-by-4 array of CMOS photodiode panels. The image normalization method applied cannot cancel the evolving pattern. (Image shown already in chapter 2 (fig. 36).)	96

Figure 57	X-ray phantom image of the cylindric carbonate core with a vertical fracture visible in the centre of the sample. (a) Carbonate sample \varnothing 3.81 cm with a single fracture; (b) Original radiographic image including the artefact that shows the 2-by-4 sensor panels clearly; (c) Standard linear corrected image that does not remove the artefact completely; (Images b and c are gamma corrected by 4.0 for the purpose of clarity. Camera: Shad-o-Box™ 4K from Rad-Icon Imaging Corp (now Teledyne Dalsa). (Image shown already in chapter 2 (fig. 37).)	97
Figure 58	Reconstruction of fig. 2(c) which shows a spot artefact in the middle, and several ring artefacts as a result of the non-linearity of the sensors. (Image shown already in chapter 2 (fig. 35).)	98
Figure 59	Left: X-ray phantom image of the cylindric carbonate core after correction with a quadratic fit polynomial. Right: Reconstruction of the quadratic linearisation, which still shows a spot artefact in the middle.	98
Figure 60	Measured detector response as set of flat field images at different beam intensities. The value at 25% for the exposure time was 0.625 sec, with the 0.005 sec increment not been resolved from the frame grabber.	99
Figure 61	Piecewise polynomial fits for two different sets of input parameters (see legend). Blue 20%-60%, green 25%-50%. The blue curve represents the measured camera response more accurately, especially at lower intensities, which is important for the high density materials we are considering in our CT scans.	102
Figure 62	Top: Projection images (left) before and (right) after correction using the piecewise polynomial approach. Bottom: Reconstructed CT images for the (left) uncorrected and (right) corrected projections. (Image shown already in chapter 2 (fig. 38).)	103

Figure 63	Left: CT image of a limestone sample with variable aperture fracture. Center: Line profile across the fracture. Right: Sketch depicting the different measurement methods (from Vandersteen et al., 2003 [193]). 107
Figure 64	Scans of calibration pieces gapped out with plastic shims of different thicknesses. Top row: Baker Dolomite, bottom row: San Andreas Carbonate. 109
Figure 65	Measured values and fitting curves for the BD calibration sample. Top: PH method. Bottom: FWHM method. 112
Figure 66	Measured values and fitting curves for the SAC calibration sample. Top: PH method. Bottom: FWHM method. 113
Figure 67	Fracture aperture distributions [mm] (left) and topology (right). Top: BD, Bottom: SAC (see fig. 22). Voxel resolution 23.6 μm . Dimension of the fractures is 3.8 by ~ 10 cm. 118
Figure 68	Top: Histogram of apertures measured for BD. Bottom: Histogram of apertures measured for SAC. For clarity, apertures larger than 1 mm are not shown. 120
Figure 69	Sketch depicting the flow cell construction. The flow cell mainly consists of two epoxy platens that extend the core. A thin latex jacket surrounds the core. 124
Figure 70	Flow cell with BD sample. The bottom tube connects to the inlet slit, whereas the top tubes comprise the fluid outlet for the fracture and the drainage outlets for the rock matrix. 125
Figure 71	Experimental set-up. A syringe pump ensures a constant inflow rate. The flow direction of the brine or oil is from bottom to top. The porous medium header and fracture header were set up at the same height to ensure a constant pressure differential between fracture and matrix. Copper (II) sulfate (CuSO_4) was used to check for iodine (I^-) at the fracture and porous medium outlets. 126

Figure 72	Single-phase flow experiments in BD. Top row: BD ₁ . Middle row: BD ₂ . Bottom row: BD ₃ (cf. table 10). Each column presents the flow patterns in frontal view of the fracture (i.e. the fracture is located perpendicular to the view plane). The images have been recorded at 75, 300, 1200, 2000 seconds after injection commenced. Darker colours indicate higher concentrations of the KI tracer. Note the different air bubbles present in the inlet slit of the flow cell. The bubbles did not change size or position during the runs. 129
Figure 73	Juxtaposition of experiments BD ₃ and BD ₄ (cf. table 10). Each column presents the flow patterns in frontal and side view of the fracture (i.e. the fracture is located perpendicular, or along to the view plane, respectively). The images have been recorded at 75, 300, 1200 seconds after injection commenced. Darker colours indicate higher concentrations of the KI tracer. 130
Figure 74	Breakthrough curves (BTC) for experiments BD ₁ (top) and BD ₂ and BD ₃ (bottom) (cf. table 10). 131
Figure 75	Single-phase flow experiment in BD ₈ (cf. table 10). Each column presents the flow patterns in frontal and side view of the fracture (i.e. the fracture is located perpendicular, or along to the view plane, respectively). The images have been recorded at 600, 1200, 1800, 3600, 7200, 10100 seconds after injection commenced. Darker colours indicate higher concentrations of the KI tracer. Heterogeneous flow patterns are emerging in matrix and fracture. 132

Figure 76	Contour plot of single-phase flow experiment BD8 (cf. table 10). Each column presents the flow patterns in frontal and side view of the fracture (i.e. the fracture is located perpendicular, or along to the view plane, respectively). The images have been recorded at 600, 1200, 1800, 3600, 7200, 10100 seconds after injection commenced. Darker colours indicate higher concentrations of the KI tracer. Colored according to grey values (0 - 255) in images. Heterogeneous flow patterns are emerging in matrix and fracture. 133
Figure 77	Breakthrough curves (BTC) from experiments BD8 and BD9 (cf. table 10). 134
Figure 78	Comparison of tracer distribution after 168 minutes in experiment BD8 (table 10) in frontal view of the fracture and the fracture aperture distribution of the BD sample. 135
Figure 79	Single-phase flow experiment in SAC ₁ (cf. table 11). Each column presents the flow patterns in frontal and side view of the fracture (i.e. the fracture is located perpendicular, or along to the view plane, respectively). The images have been recorded at 600, 1200, 1800, 3600, 7200, 8650 seconds after injection commenced. Darker colours indicate higher concentrations of the KI tracer. Heterogeneous flow patterns are emerging in matrix and fracture. Note how the matrix is invaded preferentially in the top part of the matrix. 137

Figure 80	<p>Contour plot of single-phase flow experiment in SAC₁. Each column presents the flow patterns in frontal and side view of the fracture (i.e. the fracture is located perpendicular, or along to the view plane, respectively). The images have been recorded at 600, 1200, 1800, 3600, 7200, 8650 seconds after injection commenced. Colored according to grey values (0 - 255) in images. Heterogeneous flow patterns are emerging in matrix and fracture. Note how the matrix is invaded preferentially in the top part of the matrix. 138</p>
Figure 81	<p>Breakthrough curves (BTC) from experiments SAC₁ and SAC₂. The outlier in experiment SAC₂ is due to the X-ray source losing power for taking a couple of images. 139</p>
Figure 82	<p>Comparison of tracer distribution after 144 minutes in experiment SAC₁ (table 10) in frontal view of the fracture and the fracture aperture distribution of the SAC sample. 140</p>
Figure 83	<p>BD flood with dodecane-iododecane with a flow rate of 1 mL hr⁻¹ at 28 min, 68 min, 128 min after injection commenced. Each column presents the flow patterns in frontal and side view of the fracture (i.e. the fracture is located perpendicular, or along to the view plane, respectively). Darker colours indicate higher concentrations of dodecane-iododecane. Right column: Contour plot at time 128 min. (colored according to grey values (0 - 255) in images). The fracture is filled slowly. No flow occurs in the BD matrix. The bright area at the left side in the images in the bottom row is due to some misalignment of the core sample. . 142</p>

Figure 84 Continued experiment. BD flood with dodecane-iododecane with a flow rate of 10 mL hr^{-1} at 278 min, 318 min, 358 min after injection commenced. Each column presents the flow patterns in frontal and side view of the fracture (i.e. the fracture is located perpendicular, or along to the view plane, respectively). Darker colours indicate higher concentrations of dodecane-iododecane. Right column: Contour plot at time 358 min. (colored according to grey values (0 - 255) in images). The fracture is filled completely. First flow occurs in the BD matrix. The bright area at the left side in the images in the bottom row is due to some misalignment of the core sample. 143

Figure 85 Continued experiment. BD flood with dodecane-iododecane with a flow rate of 50 mL hr^{-1} at 0 min, 15 min, 31 min after leaving the sample to rest for 17.5 hrs. Each column presents the flow patterns in frontal and side view of the fracture (i.e. the fracture is located perpendicular, or along to the view plane, respectively). Darker colours indicate higher concentrations of dodecane-iododecane. Right column: Contour plot at time 31 min. (colored according to grey values (0 - 255) in images). Flow occurs in the matrix and in the fracture. In the bottom of the sample the matrix flow is piston-like, whereas in the top part two patches of dodecane-iododecane form. The bright area at the right side in the images in the bottom row is due to some misalignment of the core sample. 144

Figure 86 Continued experiment. BD flood with deionized water with a flow rate of 1 mL hr^{-1} at 51 min, 111 min, 251 min after water injection commenced. Each column presents the flow patterns in frontal and side view of the fracture (i.e. the fracture is located perpendicular, or along to the view plane, respectively). Darker colours indicate higher concentrations of dodecaneiododecane. Right column: Contour plot at time 251 min. (colored according to grey values (0 - 255) in images). Fracture and matrix oil is replaced simultaneously by water. The bright area at the right side in the images in the bottom row is due to some misalignment of the core sample. 146

Figure 87 Continued experiment. BD flood with deionized water with a flow rate of 10 mL hr^{-1} at 286 min, 326 min, 376 min after water injection commenced. Each column presents the flow patterns in frontal and side view of the fracture (i.e. the fracture is located perpendicular, or along to the view plane, respectively). Darker colours indicate higher concentrations of dodecaneiododecane. Right column: Contour plot at time 376 min. (colored according to grey values (0 - 255) in images). Further drainage of matrix and fracture can be observed. The oil patches in the top of the sample are reduced. Oil is pushed from the fracture further into the matrix. The bright area at the right side in the images in the bottom row is due to some misalignment of the core sample. 147

Figure 88	Continued experiment. BD flood with deionized water with a flow rate of 50 mL hr^{-1} at 44 min, 84 min, 124 min after leaving the sample at rest for 16 hrs. Each column presents the flow patterns in frontal and side view of the fracture (i.e. the fracture is located perpendicular, or along to the view plane, respectively). Darker colours indicate higher concentrations of dodecane-iododecane. Right column: Contour plot at time 124 min. (colored according to grey values (0 - 255) in images). Oil remains in the matrix and is still distributed heterogeneously. The bright area at the right side in the images in the bottom row is due to some misalignment of the core sample. 148
Figure 89	Upscaled fracture apertures measured for the BD sample and mapped to the coarse (Mesh13, top), medium (Mesh10, middle), and fine (Mesh12, bottom) finite element meshes (table 12). The aperture distributions show good agreement with the measured apertures (bottom, cf. fig. 67). 152
Figure 90	Upscaled fracture apertures measured for the BD sample and mapped to the coarse (Mesh14, top), medium (Mesh11, middle), and fine (Mesh15, bottom) finite element meshes (table 12). The aperture distributions show good agreement with the measured apertures (bottom, cf. fig. 67). 153
Figure 91	Histograms of the fracture apertures of the BD and SAC meshes in table 12. In comparison to the measured aperture distributions (cf. fig. 68), the extreme values in the long tail of the aperture distribution have decreased. This is an averaging effect. Note that the finer meshes exhibit more finite elements with aperture = 0, which is due to averaging as well. . . . 154
Figure 92	Pressure distributions of BD and SAC. Top: BD Mesh13, Bottom: SAC Mesh14. Flow is from left to right. . . . 156

Figure 93	Magnitude of the Darcy velocity of BD and SAC. Top: BD Mesh ₁₃ , Bottom: SAC Mesh ₁₄ . Flow is from left to right.	157
Figure 94	Concentration at different timesteps in the BD sample (BD Mesh ₁₃).	158
Figure 95	Concentration at different timesteps in the SAC sample (SAC Mesh ₁₄).	159
Figure 96	Breakthrough curves for BD and SAC.	160
Figure 97	Experimental breakthrough curves for the BD sample (cf. 77).The early process, in which mainly the fracture is filled with tracer fluid, occurs much faster than the diffusion into the porous matrix. It is plausible that the fast slope of the BTC on the left corresponds to this early stage of the flow experiment. Once the fracture is entirely saturated with tracer fluid only diffusion into the matrix remains. The corresponding transition point from steep to linear concentration growth in the BTC has been denoted in the image as 100% fracture saturation. The full saturation of the entire core sample is not reached within the measured time period.	162

LIST OF TABLES

Table 1	Relative Error	104
Table 2	Shim Thicknesses	108
Table 3	Average grey value of rock types	110
Table 4	Calibration measurement BD PH	114
Table 5	Calibration measurement BD FWHM	114
Table 6	Calibration measurement SAC PH	115
Table 7	Calibration measurement SAC FWHM	115
Table 8	Mean absolute errors	116
Table 9	Comparison of BD and SAC	121
Table 10	BD single-phase Experiments	128
Table 11	SAC single-phase Experiments	136
Table 12	SAC BD Meshes	151

INTRODUCTION

This chapter provides a brief literature review of flow simulations in fractured porous media, computer tomography for geomaterials and flow experiments in carbonate studies.

The accurate simulation of single- and multi-phase flow models through realistic fracture networks in porous media and predictions about the quality of the simulation is an on-going research field. Fractures can provide the main flow domain in a reservoir, or can act as barriers to fluid flow, whereas the rock matrix usually comprises the main storage capacity (Berkowitz, 2002 [20]; Nelson, 2001 [146]). Traditionally, the simulation of fluid flow and transport through fractured hydrocarbon reservoirs was undertaken via Dual Porosity and Dual Permeability models (Warren and Root, 1963 [203]). They generalize the geometric model of fractures and rock matrix to resemble a "sugar cube geometry", where fractures cross the rock matrix in a perpendicular network. Transfer functions model the fluid exchange between matrix and fractures. More recently, Discrete Fracture and Matrix (DFM) models have been used for simulating flow and transport in fractured geological formations (Karimi-Fard et al., 2004 [102]; Moinfair et al., 2011 [137]). They account for the natural geometry of the fractures and matrix and do not require a transfer function to model the exchange of fluids between both domains. DFM models are hence an excellent tool to validate and improve classical Dual Porosity and Dual Permeability methods and perhaps even model fluid flow in field-scale fractures. Many simulators are able to realize DFM as modelling approach (Sandve et al., 2012 [178]; Karimi Fard et al., 2004 [102]). In this thesis we use CSMP++ (Complex System Modelling Platform) (Matthäi et al., 2007 [129]), which is a finite element and finite volume based code library, designed to simulate complex multi-

INTRODUCTION

physics problems of geologic processes, especially those involving fluid flow. CSMP++ has been co-developed by Heriot-Watt University, Montan University of Leoben (Austria), ETH Zurich (Switzerland), and at the University of Melbourne (Australia). We will have a closer look at the importance of single fractures and their apertures for the flow behaviour, which is debated in the literature (e.g. Zimmermann et al., 1992 and 2004 [216, 215]; Karpyn et al., 2009 [105]; Karpyn and Piri, 2007 [104]; Landry et al., 2014 [118]; Lee and Karpyn, 2010 [119]; Madadi and Sahimi, 2003 [126]; Ferno et al., 2011 [66]; Auradou, 2009 [8]).

In recent years, X-ray computer tomography (CT) systems were developed which allow to scan geomaterials with high resolution. It is now possible to scan core samples containing fractures with tens of microns resolution (e.g. Ketcham et. al, 2010 [113]), making fracture apertures measurable, and at the same time allow insight into rocks during various flow scenarios e.g. diffusion, drainage, and imbibition. This can help to understand the exact influence of fracture aperture distributions on flow in fractures and matrix, although these workflows are not established yet, and viable sample sizes may limit possible predictions to be made.

We combine CT and DFM flow simulations to compare the simulation of miscible single-phase flow through fractured carbonates with real flow experiments in fractured carbonate cores of 3.81 cm diameter and 10 cm length. Our special focus is herein to investigate how the aperture distribution of a fracture influences the flow and transport processes, and to investigate how DFM simulations can reproduce the results of experiments . CT allows us to measure the fracture apertures, which are implemented in the simulations with high accuracy. We also employ CT to visualize the flow experiments.

In the following a short introduction is given and the current state of research considering carbonates, naturally fractured reservoirs, the characteristics of porous media and fractures, Dual Porosity and Dual Permeability models, DFM flow modelling, CSMP++, X-ray CT of geomaterials, image processing and image analysis of CT data is highlighted, and explained how flow experiments are visualized with X-ray CT. In the end of this chapter the objectives and the structure of the thesis are summarized again.

1.1 CARBONATES

1.1 CARBONATES

Over 50% of the world's remaining conventional hydrocarbon reserves are held in carbonate reservoirs (Burchette, 2012 [30]; Garland et al., 2012 [70]). They are generally more heterogeneous than siliciclastic reservoirs and therefore more difficult to produce. This challenge is mainly related to the complex distribution of porosity and permeability fields caused by an often complex combination of deposition and diagenesis processes.

Carbonate sedimentary rocks are limestones and dolostones composed of the minerals calcite (CaCO_3) and dolomite ($\text{CaMg}(\text{CO}_3)_2$), respectively. They form mainly in shallow marine environments where many CaO-secreting animals, plants and bacteria live. The secretions, shells and skeletons of these biota accumulate over time. The build-up of these carbonate sediments is called deposition (e.g. Tiab et al. 2012 [190]). During and after deposition (i.e. burial history), the deposits will be affected by diagenesis. Diagenesis is defined for the most part as all processes of lithification and alteration (e.g. James et al., 2015 [94]). This includes but is not limited to cementation, mechanical and chemical compaction (see fig. 1). Depositional and diagenetical processes are the main controls on heterogeneities in carbonates that reflect different porosity and permeability formations (e.g. Lucia, 1995 and 2004 [124, 125]).

One of the most important diagenetic processes is dolomitization, which transforms carbonate sediments or limestones into dolomites. During dolomitization several thermodynamic and chemical conditions cause Ca^{2+} in the carbonate sediments/rocks to be replaced by Mg^{2+} . The results of dolomitization range from complete preservation to total obliteration of rock texture and fabric, which in turn may impact the petrophysical properties of the precursor limestone (Lucia, 2004 [125]). Dolomitization is hence considered to be a significant control on reservoir quality (Braithwaite et al., 2004 [29]).

In conclusion, porosity and permeability in limestones and dolostones are typically heterogeneous (as opposed to siliciclastic rocks) at all scales because they evolve through different diagenetic realms. They can be created and destroyed at spatially and temporally variable patterns. As a result, porosity and permeability in carbonates are difficult to predict and upscaling them can be very challenging.

1.1 CARBONATES

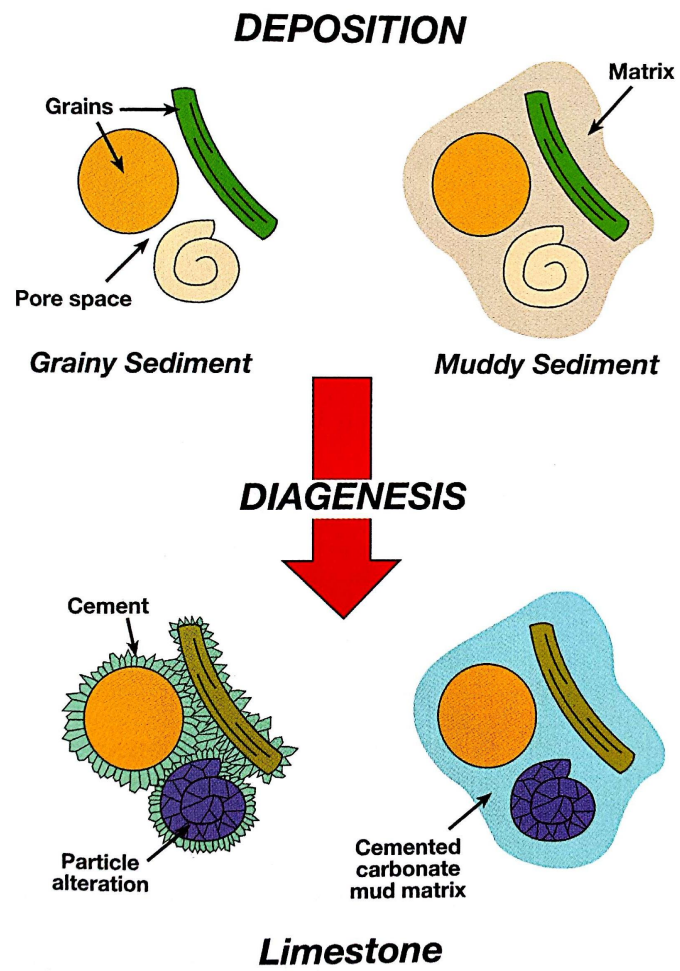


Figure 1: Sketch illustrating the transformation of sediment into limestone via diagenesis (from James et al., 2015 [94]).

1.2 NATURALLY FRACTURED RESERVOIRS

1.2 NATURALLY FRACTURED RESERVOIRS

Naturally fractured reservoirs (NFR), which amount to about 50% of the current hydrocarbon reservoirs worldwide, are difficult to produce. Globally, the recovery rates are 35% or even less (Montaron, 2008 [138]).

In general, naturally fractured reservoirs (NFR) are considered to be reservoirs, where fractures occur due to geologic events. NFRs can be classified on the basis of the geologic causative forces that lead to their formation, which are tectonic events, regional events (developed over large areas, cross-cutting local structures), contractional events (bulk volume reduction in the rock), or surface-related events, like weathering, unloading, release of stored strain, etc. (Nelson, 2001 [146]).

Reservoirs can also be classified on the basis of the effects the fracture system provides to the overall reservoir quality (Nelson, 2001 [146]):

- Type 1: Fractures provide the essential reservoir porosity and permeability.
- Type 2: Fractures provide only the essential reservoir permeability.
- Type 3: Fractures assist permeability in an already producible reservoir.
- Type 4: Fractures provide no additional porosity or permeability but create significant reservoir anisotropy (barriers).

Rock-fracture systems can also be classified in terms of physical morphology, distribution of fractures, and the estimation of reservoir properties (porosity, permeability, fluid saturation within the fractures and rock, recovery factor expected from the fracture system, etc.). The fracture morphology hereby is very important, as it determines the fracture's permeability. We distinguish between open fractures (no material filling, potential open conduits to fluid flow), deformed fractures (deformation bands with gouge-filled fractures, or slickensided (polished) fractures), mineral-filled fractures due to secondary or diagenetic mineralization, and vuggy fractures (e.g. caused by dissolution) (Nelson, 2001 [146]). Combinations are possible. The focus in our research on carbonate rocks is on open fractures only.

The understanding of flow physics (e.g. imbibition, drainage, diffusion) in fractured reservoirs is interesting not only for petroleum engineering, but

1.3 CHARACTERISTICS OF POROUS MEDIA AND FRACTURES

also for example for carbon capture storage (CCS), groundwater contamination, and high-enthalpy geothermal systems. The geological characterisation and static modelling of fractured reservoirs is challenging but also impacts the way how flow behaviours in the reservoir are predicted. Several modelling approaches are currently debated in the literature. A good overview can be found in Nelson, 2001 [146]; Narr et al., 2006 [145]; Agar and Geiger, 2015 [2].

Fig. 2 shows an example of a complexly, fractured carbonate (limestone) reservoir analogue, exposed at Kilve beach in the UK. In oil reservoirs, these complexly connected fracture networks can have a strong influence on the recovery factor. They affect the flow by creating high permeability pathways or barriers to flow and transport. Multiphase flow displacement patterns hence often result in fracture-assisted fingering or channelized flow where the pure piston-like flow front¹ disappears (Helmig, 1997[81]). The governing equations describing the flow physics in fractures and rock matrix during an incompressible two-phase flow can be found in section A.1.

1.3 CHARACTERISTICS OF POROUS MEDIA AND FRACTURES

1.3.1 Porous Media

The porosity ϕ of a medium is defined as the ratio of pore volume to total volume,

$$\phi = \frac{V_{porespace}}{V_{total}}, \quad (1)$$

where the total volume is the sum of the volume of the solid rock matrix and the volume of the voids. Permeability k denotes the degree of allowing fluids to pass through the porous medium, is defined after Darcy's law (eq. (2)) as proportionality constant, and is a property of the porous medium only. The hydraulic conductivity is defined as $K = \frac{k g}{\mu}$ (g constant of gravitational

¹ In a uniform system during a fully miscible displacement, the average water saturation over time should be a linear curve, with breakthrough after one pore volume is injected. This is called a piston-like displacement (Skjæveland and Kleppe, 1992 [184]).

1.3 CHARACTERISTICS OF POROUS MEDIA AND FRACTURES

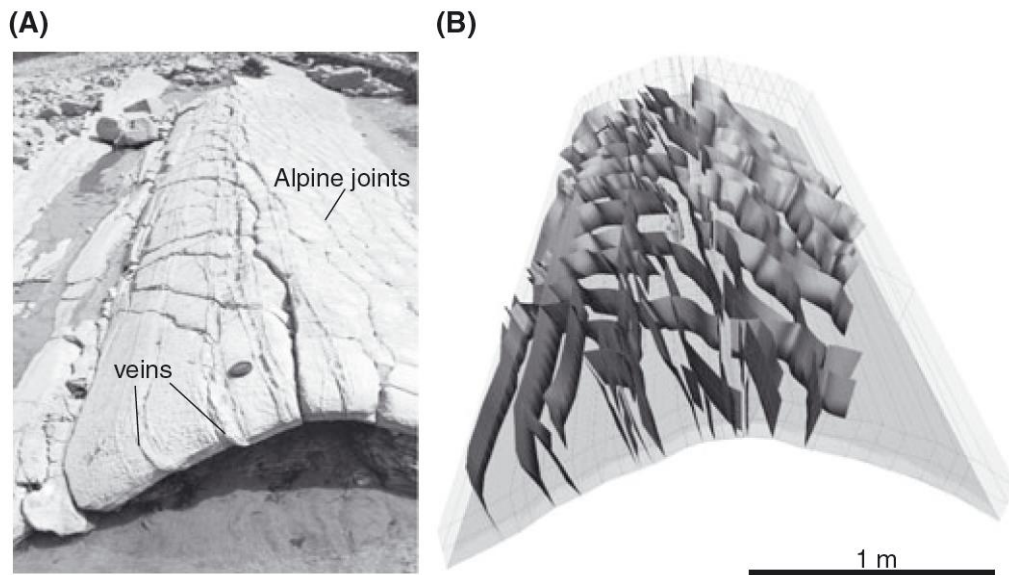


Figure 2: Geologic complexity of an outcrop of Liassic limestone on the southern Bristol Channel. (A) Photograph of small-scale fold structure intersected by carbonate veins crosscut by later Alpine joints. Camera lid has 5 cm diameter, for scale. (B) Free-form NURBS CAD model of the same structure. Similar CAD model constructions can be used in the DFM simulations in CSMP++ (from Paluszny et al., 2007 [158]).

1.3 CHARACTERISTICS OF POROUS MEDIA AND FRACTURES

acceleration, μ dynamic fluid viscosity) and is a combined property of the porous medium and the fluid flow through it (Bear, 1972 [18]).

Different classes of rocks have different typical porosity-permeability relationships. Typical porosities can range from less than 1% in very tight rocks to about 35% for sandstones (Bear, 1972 [18]). A high porosity does not always lead to a high permeability though. The pores can be disconnected, in carbonates for example, and therefore ϕ can be > 0 with $k = 0$, hence the importance of fractures.

In a porous medium all properties are scale dependent, which is important for the discussion of coupled flow and transport processes (Bear, 1972 [18]; Helmig, 1997 [81]). On the molecular scale, we consider the movement of single molecules. A description of flow and transport with regard to each molecule is not feasible at the reservoir scale. Instead we consider a fluid or rock as a continuous substance, which can be described by a set of continuous variables, that are functions of space and time (Helmig, 1997 [81]). The next larger scale is the micro scale, or pore scale, where solid and void spaces are distinguishable. Small discontinuities (e.g. micro cracks) can still be clearly recognized. The pore or grain diameter or the fracture aperture are large features relative to single molecules. Here, fluid flow is described by the Navier-Stokes equations, as the complex heterogeneous geometry of the connected pore-space has to be taken into account. If we average properties on the pore scale (e.g. porosity), the value is dependent of the volume considered, and continuous variables may fluctuate (Bear, 1972 [18]). By enlarging the considered volume, the fluctuations of the averaged variables become less. A macroscopic scale is reached, when discontinuities, which could be recognized, at the micro scale cannot be identified anymore (Helmig, 1997 [81]). The heterogeneities leading to the fluctuations of the variables at the smaller scale are counterbalanced, and averaging properties is independent of the considered volume. A volume where local discontinuities are no longer identifiable is called representative elementary volume (REV) (fig. 3). Rocks have multiple REVs (Corbett, 2009 [48]). The REV concept introduces effective parameters, e.g. permeability, or saturation, as well as *Darcy's Law*, which can be obtained by upscaling of the Navier-Stokes equation via homogenization (Bear, 1972 [18]).

1.3 CHARACTERISTICS OF POROUS MEDIA AND FRACTURES

Darcy's law states that flow through a porous medium is proportional to the pressure drop over a given distance. For horizontal flow it is

$$Q = -\frac{k \cdot A}{\mu} \left(\frac{\Delta P}{L} \right), \quad (2)$$

where A is the cross-sectional area of the porous medium and L is the length of the considered volume, ΔP is the pressure drop over the length of the volume, and k is the absolute permeability of the porous medium.

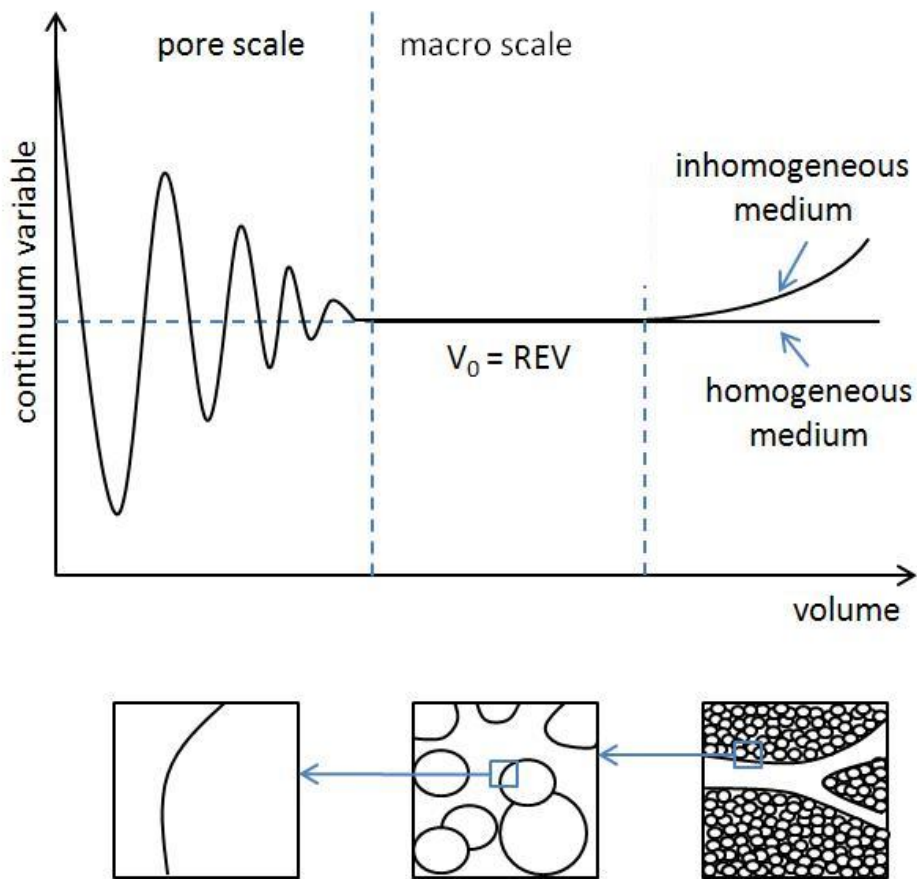


Figure 3: Definition of an REV for a porous medium (after Helmig, 1997 [81]).

1.3.2 Fractures

Looking at fractures closely is important, as the geometry of the fracture void space has in most cases a big influence on the hydromechanical behavior of

1.3 CHARACTERISTICS OF POROUS MEDIA AND FRACTURES

rocks with single fractures and fracture networks. Fractures in natural rocks or in laboratory settings form when the strength of the rock is exceeded under deviatoric load. Deviatoric stress, or differential stress, occurs when the stress components at a point in a body are not the same in every direction. Fractures can vary significantly in length, width and aperture (Berkowitz, 2002 [20]; Bonnet et al., 2001 [26]). The aperture of fractures in rock vary from less than $1\mu\text{m}$ of micro-cracks in grains to a couple of cm, whereas a fracture, or fault can expand in length over several kilometers (Berkowitz, 2002 [20]; Bonnet et al., 2001 [26]), but in fact the exact width, or distribution of widths, at reservoir conditions is unknown and may change during production (see Sanderson and Zhang, 1999 [177]).

1.3.2.1 *Geometry of fractures*

A fracture is considered to be a local discontinuity in a rock, concrete, or other material, defined as the void space between a pair of irregularly rough, nearly parallel planar surfaces. These two surfaces are usually in contact with each other in some positions, but do not touch in others, depending on shear and stress having been, or being applied to the fracture.

The aperture of a fracture is defined as the distance of the two fracture surfaces, and is usually measured perpendicular to the nominal fracture plane. The surface profile itself though can have a wide range in shape which is commonly denoted by surface roughness. Two main approaches exist to quantify the gap of the fracture. Either the surface profiles can be measured directly, or a local aperture can be calculated in each position of the fracture as the distance between the two confining rough surfaces (fig. 4).

The surface roughness can be determined by the use of contact or noncontact devices, so called profilometers, which are all types of callipers in one form or another. Hereby the surface is scanned along a certain path and the changes in surface height are recorded at discrete positions. The distance of these positions determines the scanning resolution of the profilometer. Various instruments exist for roughness measurements (cf. Bushan, 1996 [10]). They are either employing a mechanical approach by using a contact stylus tracing method — from very simple devices as the so called Barton comb, see fig. 5 to scanning probe microscopy (SPM) — or the surface rough-

1.3 CHARACTERISTICS OF POROUS MEDIA AND FRACTURES

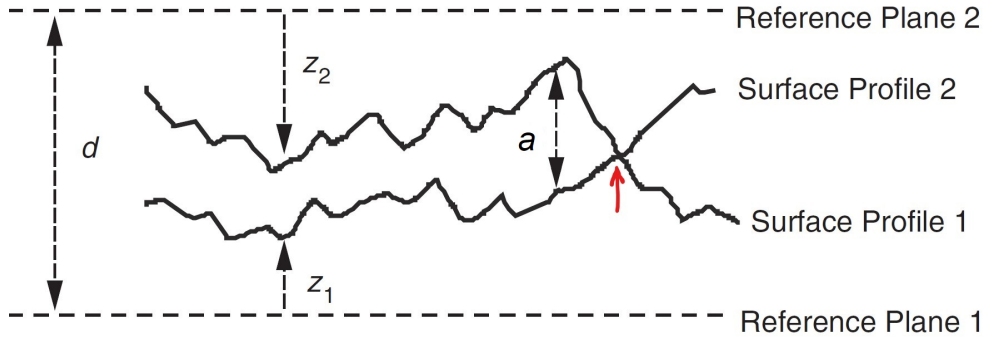


Figure 4: Schematic of a fracture confined by two rough surfaces, which are separated by an aperture a . The two surfaces touch in one position (red arrow). Two reference planes are drawn, separated by a distance d , which can be used to define the roughness of the surfaces as a perpendicular distance to the corresponding reference plane, and also help to calculate the fracture aperture as the distance between the opposing rock surfaces perpendicular to a nominal fracture plane, which can usually be defined locally (from Zimmermann and Main, 2004 [213]).

ness is scanned optically with noncontact devices such as e.g. low-energy electron diffraction, molecular-beam methods, field-emission microscopy for fine-scale details of surfaces, to portable 3D laser scanners combining light pulses with positional data of the system, so called Lidar (Light Detection and Ranging), being applied in field studies of fracture systems (e.g. Renard et al., 2008 [174]; Candela et al., 2012 [31]).

According to fig. 4, the local fracture aperture $a(x, y)$ is defined as

$$a(x, y) = d - z_1(x, y) - z_2(x, y) \quad (3)$$

where $z_1(x, y)$ and $z_2(x, y)$ be functions describing the parallel upper and lower reference planes separated by distance d . For the scope of this thesis, only the actual local fracture aperture is relevant, and its measurement is described in detail in the methodology section 2.5. For a more elaborated description of mathematical concepts to characterize surface roughness and fracture apertures see Zimmermann and Main, 2004 [213].

Additionally to the void space denoting the fracture porosity, fractures may be described by their local apertures, roughness, tortuosity, length, mean aperture, correlation lengths, or their aperture distribution, in the case of fracture networks by their density (the number of fractures per meter

1.3 CHARACTERISTICS OF POROUS MEDIA AND FRACTURES



Figure 5: A Barton Comb, here being used in a field measurement, is a profile gauge commonly used for the classification of roughness profiles of rock surfaces. Joint roughness coefficients (JRC) for the surface can be determined by comparing the fracture surface geometry with Barton's standard profiles — cf. Barton and Choubey, 1977 [14]. (Image from Hubbard Brook Ecosystem Study [87]).

1.3 CHARACTERISTICS OF POROUS MEDIA AND FRACTURES

e.g. along a borehole), connectivity (product of fracture permeability times fracture width), and orientation (dip-angle/dip-azimuth of the fracture planes) (Nelson, 2001 [146]).

If the topology of the two fracture surfaces could be measured exactly, equation 1.3.2.1 would determine the fracture aperture at each position, but the geometric information is usually not known in sufficient detail to derive all hydromechanical properties from this representation. Therefore, the fracture is characterized often by statistical parameters, such as calculating a hydraulic aperture from the actual mechanical aperture and the *joint roughness coefficient (JRC)* as proposed by Barton, 1982 [15].

1.3.2.2 Porosity and permeability of fractures

Fractures can have a distinct porosity-permeability relationship. Fracture porosity, like matrix porosity, is the percentage of void volume to total volume. Completely open fractures have a porosity of $\phi = 1$. Fracture and matrix porosity are different though in their effect on permeability. Fracture porosity is usually highly interconnected and therefore has a more dramatic effect on permeability (Nelson, 2001 [146]) – small increases in the fracture porosity can cause immense changes in reservoir permeability parallel to the fracture, as the volumetric flow rate is proportional to the fracture width, or cubed fracture aperture (see *cubic law (CL)* 4).

When simulating flow in an NFR, it is necessary to define the effective permeability for a fracture or fracture network. The idea is that a reservoir in which fractures play a significant role should be treated as a dual-porosity/dual-permeability system. A common assumption then is to treat the fractures and rock matrix as an effective porous medium for which an effective permeability for the fractured reservoir must be defined.

If a fracture consisted of two parallel smooth plates, fluid flow could be characterized fully by the distance of the fracture plates, using the so called *cubic law (CL)* (Witherspoon et al., 1980 [209]).

The cubic law represents flow in a fracture (Poiseuille flow between two smooth planes, solution of the Navier-Stokes equation). It states that the volumetric flow rate Q over a specific length L in the fracture is proportional

1.3 CHARACTERISTICS OF POROUS MEDIA AND FRACTURES

to the applied pressure gradient ΔP and the cube of the mean fracture aperture \bar{a} .

$$Q = \frac{\bar{a}^3}{12\mu} \Delta P \quad (4)$$

Together with Darcy's Law for fluid flow in porous media (eq. (2)), the effective permeability $k(\bar{a})$ can then be calculated depending on the fracture aperture

$$k(\bar{a}) = \bar{a}^2 / 12 \quad (5)$$

The cubic law can be assumed to be valid locally, so that the effective permeability can be calculated locally depending on the local fracture aperture a , and irregular shaped fractures can be modelled (e.g. Witherspoon et al., 1980 [209]; Crandall et al., 2010 [49]; Vilarrasa et al., 2011 [195]). However, this relation may not be uniformly valid, particularly for very narrow fractures (Dijk et al., 1999 [59]). Witherspoon et al., 1980 [209] investigated the validity of the cubic law and found several key issues:

- (a) The roughness of the fracture has an effect on the flow rate,
- (b) the flow rate is proportional to the cube of the mean aperture, but
- (c) for higher Reynolds numbers, the flow rate is no longer proportional to the pressure gradient.

Many researchers therefore investigated the influence of fracture roughness and tortuosity on the fracture transmissivity (e.g. Ge, 1997 [71]; Nicholl et al., 1999 [147]; Wang et al., 2015 [202]).

The transmissivity is defined as horizontal hydraulic conductivity K times thickness a . Instead of using the complete Navier-Stokes equations though, which in steady-state can be written as

$$\rho(\mathbf{u} \cdot \nabla)\mathbf{u} = -\nabla P + \mu \nabla^2 \mathbf{u} \quad (6)$$

(ρ fluid density, \mathbf{u} velocity vector), many analytical and numerical approaches use the simpler Reynolds lubrication equation

$$\nabla \cdot (a^3 \nabla P) = 0 \quad (7)$$

(a local aperture), which is often denoted as the *local cubic law (LCL)*. Zimmermann and Yeo, 2000 [214] derive the Reynolds equation from the Navier-Stokes equations by an order-of-magnitude analysis. They discuss the validity of the LCL and find that it should be valid for Reynolds numbers $Re < 10$, although other researchers found that even for low $Re < 1$ the LCL can overestimate the flow rate by up to two times (Nicholl et al., 1999 [147]; Wang et al., 2015 [202]). The effect of contact areas on the transmissivity or permeability of fractures is also discussed (Zimmermann et al., 1992 [216]). They show that as the fractional contact area increases the transmissivity decreases.

The validity of the Reynolds equation is also debated in Mourzenko et al., 1995 and 2001 [142, 143]. Many researchers therefore tried to define alternative mean apertures, other than the arithmetic mean (e.g. Tsang and Tsang, 1987 [191]), to fit the local cubic law (Ge, 1997 [71]). However, the roughness of fracture surfaces is usually too significant to be averaged. Channelized flow and stagnant zones can occur in the fracture (Zimmermann et al., 1997 [216]). Further discussion of the surface roughness influencing the hydraulic transmissivity is elaborated in Zimmermann and Main, 2004 [213].

In multi-phase flow, interfacial tension between the fluid phases plays a significant role in determining fluid configurations. The resulting capillarity cannot be neglected when the fracture surface has a preferential wettability (e.g. the fracture is water-wet). In this case, flow of two immiscible fluids in rough-walled fractures is not well represented by the parallel plate model (Prodanovic et al., 2010 [165]). Due to the scale of apertures there are similarities between capillarity in rough-walled fractures and capillarity in porous media (Piri and Karpyn, 2007 [161]). Therefore a more detailed description is necessary (e.g. Nuske et al., 2010 [150]). A complete Navier-Stokes simulation of whole fractures is difficult (Zimmermann et al., 2004 [215]; Cardenas et al., 2007 [33]) as the rough fracture planes lead to complex boundary conditions, and the simulation grid needs to resolve with a high resolution. Therefore, numerical simulations often assume laminar flow and apply the Reynolds equation, from which the cubic law (CL) can be derived (e.g. Oron and Berkowitz, 1998 [154]).

1.4 DUAL POROSITY AND DUAL PERMEABILITY MODELS

1.4 DUAL POROSITY AND DUAL PERMEABILITY MODELS

At the reservoir scale, production from NFR is typically simulated via Dual Porosity and Dual Permeability models (Warren and Root, 1963 [203]; Johns and Roberts, 1991 [96]; Hill and Thomas, 1985 [82]; Bai et al., [11]). The concept is based on the assumption of two distinct domains: a network of connected fractures and the domain of the porous rock matrix (fig. 6). In Dual Porosity models, the matrix blocks are assumed to be completely

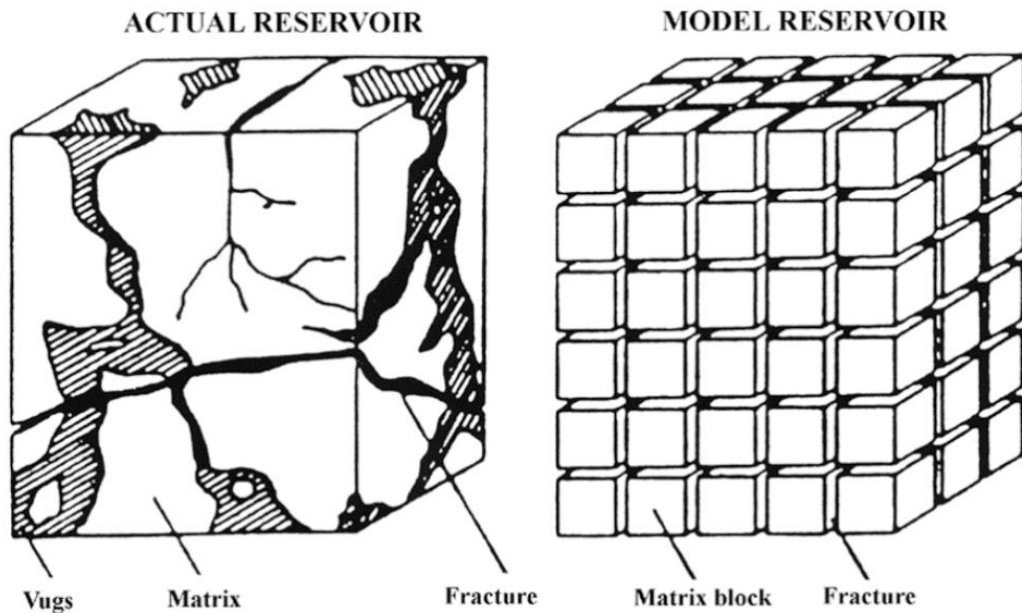


Figure 6: Idealisation of a fractured system as two conceptual domains (from Warren and Root, 1963 [203]).

separated and direct flow between the blocks is not possible. However, in Dual Permeability models advective transport can also occur inbetween matrix blocks (Hill and Thomas, 1985 [82]).

A key requirement in any Dual Porosity and Dual Permeability approach is to formulate an appropriate model that quantifies the fluid exchange between the rock matrix and the fractures. It is modelled by a transfer function $T = f(\sigma, \Delta p)$, which depends on the pressure gradient Δp between fracture and matrix, (relative) permeabilities, fluid viscosity, phase concentration, and a shape factor σ (Lu et al., 2008 [123]).

Four transfer processes between matrix and fracture can occur (fig. 7). These are fluid expansion, imbibition, gravity drainage, and diffusion. The

1.4 DUAL POROSITY AND DUAL PERMEABILITY MODELS

matrix-fracture transfer is considered to be a sum of the contributions from these different effects and can be expressed by adequate transfer functions (Lu et al., 2008 [123]).

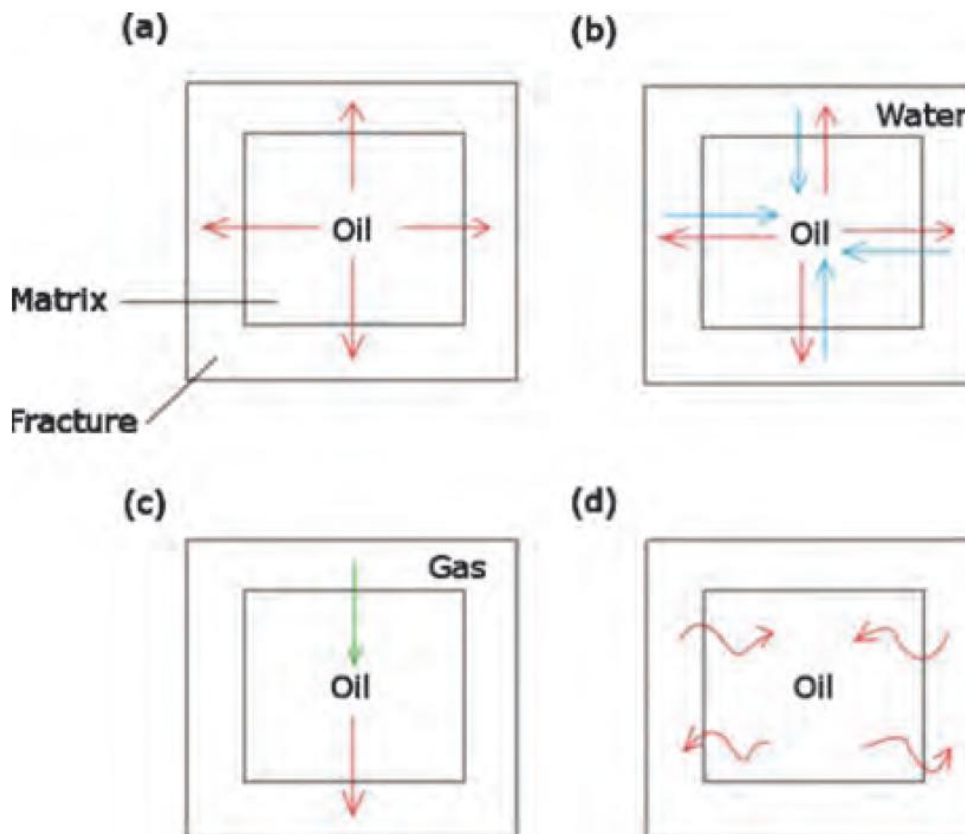


Figure 7: Schematic illustration of different recovery processes in fractured reservoirs: (a) fluid expansion, (b) imbibition, (c) gravity drainage, and (d) diffusion. (from Lu et al., 2008 [123]).

The shape factor, σ , is an empirically determined factor that represents the geometry of the rock matrix. However, which approach is the most accurate to generate a suitable shape factor for a complex geometry of nested and hierarchical fracture patterns is currently still debated (e.g. Sarma and Aziz, 2006 [179]; Lu et al., 2008 [123]; Rangel-German and Kovscek, 2002 [169]). The key advantage of Dual Permeability models lies in the direct applicability with standard simulation techniques such as Finite Difference (FD) methods or Finite Volume Methods (FV) for simulating fluid flow at the reservoir scale with conventional simulators. For a more detailed

1.4 DUAL POROSITY AND DUAL PERMEABILITY MODELS

description see Barenblatt et al., 1960 [13]; Warren and Root, 1963 [203]; Kazemi et al., 1976 [107].

Several key assumptions underpin the Dual Porosity model: The fractures are assumed to be well-connected. They have a normal length distribution with uniform and constant apertures. Therefore, a well-defined representative elementary volume (REV) can be assumed.

For real NFR some of the fundamental assumptions of Dual Porosity models do not match the physical reality (Berkowitz, 2002 [20]). The assumptions to be criticised are:

- The fractures in an NFR are complexly connected and connectivity controls permeability. There is also great uncertainty about the connectivity of the fractures since little data is available. Additionally, the scale considered influences the fracture size that can be resolved (fig. 8).
- The fracture length distribution is not normally distributed and can follow a power law (fig. 9).
- The fracture aperture distribution in one single fracture is neither constant nor unique. Instead the fracture has an inner roughness which influences both, flow in the fracture and the matrix-fracture transfer, via strongly varying capillary and imbibition/ drainage effects (e.g. Ersland et al., 2010 [64]). Moreover the fracture aperture can change during production (e.g. Sanderson and Zhang, 1999 [177]).
- The rock matrix does not only provide fluid storage. Significant fluid transport can also occur in the matrix domain (Nelson, 2001 [146]). In carbonates this is mainly the case.

In fact, it is usually not possible to define an adequate REV for the effective properties which is scale-independent (Berkowitz, 2002 [20]). In other words, the effective properties which are used in Dual Porosity models are influenced by the observation scale as an REV can only be defined for the scale of interest. Hence multi-scale modelling workflows (e.g. Bourbiaux et al., 2002 [27]) have been suggested where fracture networks are modelled differently in different regions of the reservoir, in order to better represent the local fracture network properties and their impact on flow.

1.4 DUAL POROSITY AND DUAL PERMEABILITY MODELS

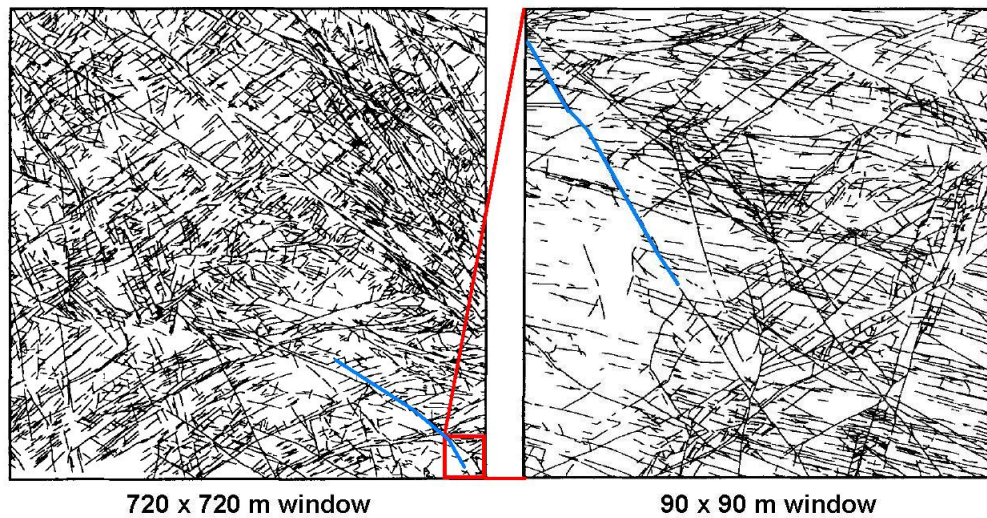


Figure 8: Fracture maps of a joint system in Devonian sandstones in western Norway at two different scales from aerial photographs. The right image shows a section of the left image with a higher resolution. Left: The smallest resolved fracture is ca. 10m long, the largest fracture ca. 300m. Right: The smallest resolved fracture is ca. 1m long, the largest fracture ca. 30m. Longer fractures (here blue) cannot be observed on the smaller scale because of the size of the domain considered. Further it is notable that only a small amount of the fractures are connected and the connectivity changes with scale (see Odling, 1997 [152]).

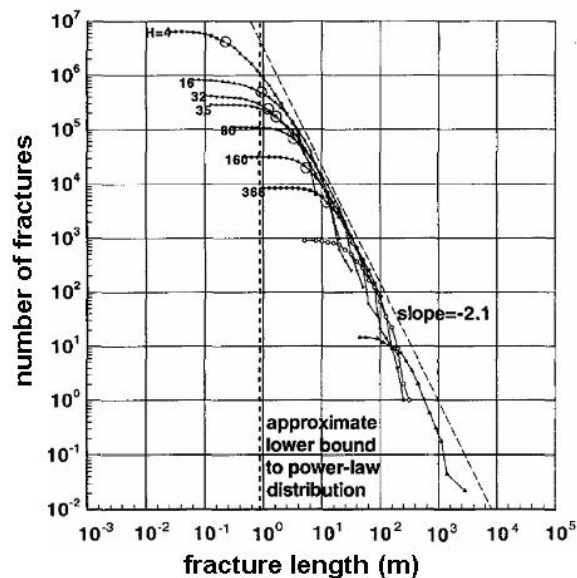


Figure 9: Fracture length distribution for the joint system in Devonian sandstones in western Norway. The dashed line indicates a power law correlation between the fracture length and the number of fractures (from Odling, 1997 [152]).

1.5 DFM FLOW MODELLING

1.5 DFM FLOW MODELLING

Since Dual Porosity models may not capture the flow physics and transport in NFR adequately, new techniques that can account for the natural geometry of the fractures and matrix flow have been developed. These so called Discrete Fracture and Matrix modelling (DFM) may lead to an improved prediction of fluid flow in fractured porous rock (e.g. Moinfair et al., 2011 [137]). The key idea of the DFM method is to study fluid flow while accounting explicitly for the fracture geometry. The governing equations (see section 2.7.1) can be discretised by different methods. As flow variables are assigned to the grid vertices in FV schemes and rock properties are associated with the control volumes, flux-based FV methods employ multipoint flux approximations (MPFA), which average the flux across control-volume boundaries. By this they yield flux continuity within a FV (e.g. Aavatsmark, 2002 [1]; Lie et al., 2011 [120]). Combined FV-transmissibility tensor methods on the other hand relate the pressure difference between neighbouring cells to the flow between these cells by introducing transmissibilities, which also ensure a flux-continuous pressure equation approximation (Edwards, 2002 [62]; Edwards and Zheng, 2010 [63]). Sandve et al., 2012 [178] use a control-volume discretization with MPFA to model a DFM system for anisotropic and fractured porous media for single-phase flow. In this hybrid approach, based on Karimi-Fard et al., 2004 [102], fractures are represented as lower-dimensional objects. Fluxes at the intersection between matrix and fracture are then treated separately, taking fracture apertures into account. The application of MPFA methods to multi-phase simulations in fractured porous media, especially when capillary pressure is taken into account, is not yet developed though (Schmid et al., 2013 [180]).

In this PhD thesis we focus on a grid-based method using a hybrid finite element finite volume (FEFV) method. The FE method is used for the diffusion terms and the FV method for the advection part in the governing partial differential equations (Geiger et al., 2009 [74]; Schmid et al., 2013 [180]). In such an approach, the domain is divided into finite elements (e.g. triangles or tetrahedra) to obtain a grid for the FE method. Then polygonal control volumes are constructed by joining the centroids of each FE with

the side-midpoints of the e.g. triangles. This yields in a complementary node-centred subgrid for the FV method around the corner nodes of each FE (fig. 10).

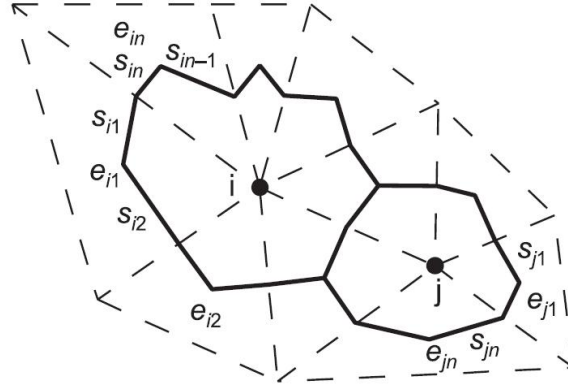


Figure 10: Construction of the node-centered finite volumes at nodes i and j with triangular finite elements $e_{i1} - e_{in}$ ($e_{j1} - e_{jn}$, respectively) and segments $s_{i1} - s_{in}$ ($s_{j1} - s_{jn}$, respectively) (from Geiger et al., 2004 [77]).

To avoid a huge amount of unknown variables by discretizing millimetre wide fractures in large models with volume or planar elements, the dimensionality of the fractures is reduced. That is, in 2D applications, fractures are represented by 1D lines, and in 3D applications by 2D surfaces (Karimi-Fard et al., 2004 [102]). A specific width, or aperture, is assigned to the fracture surfaces or lines from which a corresponding effective permeability can be computed using the cubic law (CL) (eq. (5)). The red horizontal line elements (left) and 1D finite volumes (right) in fig. 11 define a 1D fracture with a given width in a 2D matrix.

To reduce the number of unknowns and, therefore, reduce the CPU time further, the spacial domain can be discretised with a hybrid finite element mesh, composed of triangles, quadrilaterals, tetrahedra, hexahedra, prisms and pyramids (fig. 12) (Paluszny et al., 2007 [158]). Mathematically, mass conservation cannot be proven though for hybrid finite element meshes.

A detailed description of the hybrid FEFV discretisation can be found in Geiger et al., 2004, 2006, 2007 [77, 73, 75]; Paluszny et al., 2007 [158]; Matĕĕj et al., 2007 [129]. It should be noted that DFM methods are typically not used for field-scale simulations of NFR because, as discussed below, they are computationally too intensive. Instead, it is more common to use DFM methods to validate and improve constitutive models such as

1.5 DFM FLOW MODELLING

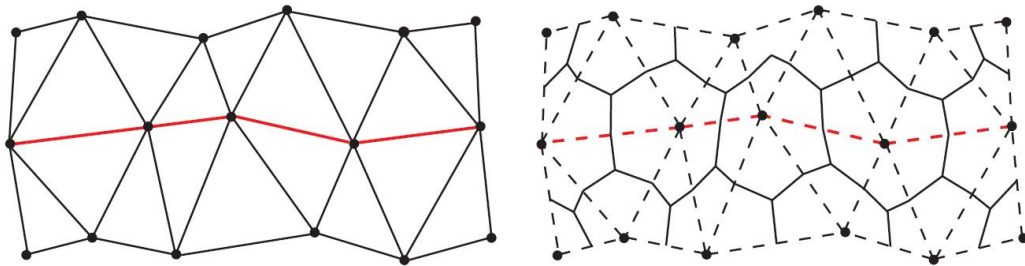


Figure 11: Complementary mesh for the combined FE-FV method. Left: Triangular 2D finite element mesh. Right: Corresponding node-centred finite volume mesh. The red 1D elements/volumes represent a sub-horizontal 1D fracture. (from Geiger et al., 2009 [74])

the Dual Porosity approach (see Geiger and Matthäi, 2014 [76]). However, some first attempts have recently been reported to incorporate aspects of the DFM approach into commercial reservoir simulators (e.g. Milliotte and Matthäi, 2014 [135]).

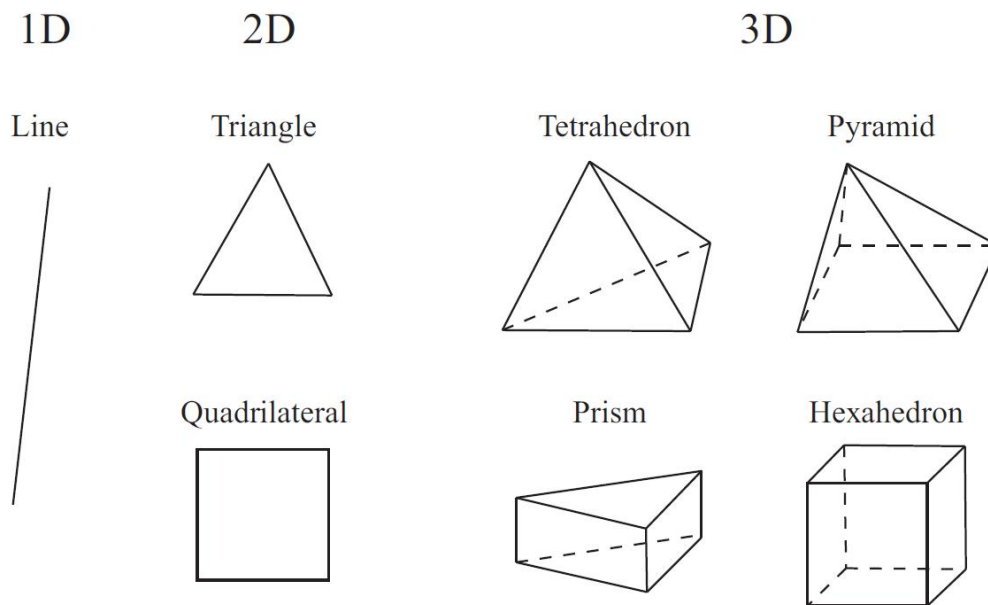


Figure 12: Different finite element types commonly used for domain discretisation in the so called hybrid-element method in mixed-dimensional systems. In DFM, the fractures are represented by elements with one dimension less than the surrounding elements, representing the rock matrix. The different element types are used simultaneously for a hybrid-element discretisation to reduce the number of unknowns significantly (from Geiger et al., 2009 [74]).

1.5 DFM FLOW MODELLING

A key idea of the FEFV method is to decouple the solution approach in one FE and one FV step (Geiger et al., 2004 [77]). Hence, the two governing equations for multiphase fluid flow, the pressure and the mass balance equations, can be solved separately. First, the FE method approximates the parabolic, or elliptic, pressure-diffusion equation. Based on the obtained pressure field, the velocity field is then computed by solving Darcy's Law for each FE. Subsequently, the resulting velocity field is used in the FV solution for the hyperbolic mass balance equation (see section 2.7.2).

In practise, the computational efficiency of DFM simulations is increased by using the state-of-the-art algebraic multigrid solver SAMG (Stüben, 2001 [186]). A parallel implementation of the FEFV method for unstructured hybrid-element grids was also developed (Geiger et al., 2009 [74]).

The advantages of the DFM method are that it has great geometric flexibility and that fluid flow in fracture and matrix can be accounted for simultaneously. Because of the FE method, irregularly shaped and multiple connected fracture domains can be handled. Hence, no transfer functions, shape factors or upscaling of the fracture geometry are necessary. The FV method allows a straight-forward physical interpretation for triangular and tetrahedral grids and is mass conserving.

However, DFM simulations also have some difficulties. Very complex geometries, for example with fractures intersecting at acute angles or fractures that are just disconnected (fig. 13), require a very fine mesh which becomes impracticable to generate or to use in numerical simulations. If the grid resolution is too low, an error in the pressure gradient between fracture and matrix can occur. The numerical discretisation of the capillary pressure at the fracture-matrix interface has a significant influence on the fluid flow and determines how well counter-current imbibition, i.e. one of the main processes for two-phase fluid exchange between fracture and matrix, can be modelled (see Reichenberger et al., 2006 [172]). Generally, the meshing of complex structures is slow and is significantly more challenging compared to Dual Porosity models, which rely on structured or corner point grids. Nevertheless, several applications of DFM simulations have been published with the aim to develop better upscaling approaches for flow and transport processes in fractured porous media, including the simulation of incompressible two-phase flow with gravity and capillary

1.6 CSMP++

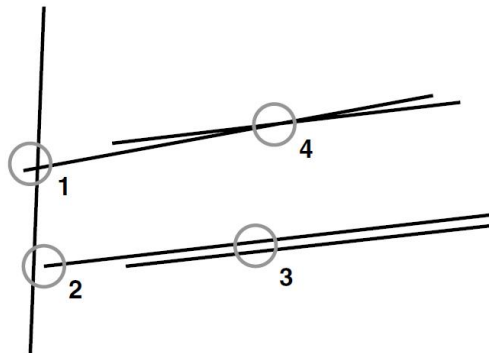


Figure 13: Difficult fracture intersections for automatic mesh generation, since it is complicated to differentiate between intersecting fractures (1, 4) and disconnected fractures (2, 3) (from Reichenberger et al., 2006 [172]).

effects (Karimi-Fard and Firoozabadi, 2003 [103]; Geiger et al., 2004 [77]; Reichenberger et al., 2006 [172]; Matthäi et al., 2007 [129]; Monteagudo and Firoozabadi, 2007 [139, 140]; Paluszny et al., 2007 [158]; Nick and Matthäi, 2011 [148]), compressible two-phase flow (Hoteit and Firoozabadi, 2005 [84]), and three-phase flow (Fu et al., 2005 [68]; Geiger et al., 2007 [75]), two-phase flow and simultaneous transport and adsorption of viscosifying species (Schmid et al., 2013 [180]), capillary trapping of CO₂ in fractured reservoirs (Annewandter et al., 2013 [5]), infiltration of Non-Aqueous Phase Liquids (NAPL) and remediation of groundwater systems (Monteagudo and Firoozabadi, 2004 [141]; Hoteit and Firoozabadi, 2008 [85]).

1.6 CSMP++

In this thesis, we are using CSMP++, the *Complex System Modelling Platform*, an object-oriented C++ simulation software for studying non-linear fluid-flow processes in geometrically complex geological formations such as naturally fractured rocks is used. An FEFV based DFM technique is implemented in CSMP++. CSMP++ can be run in parallel and has an interface to the SAMG and SAMGp multigrid solver (Stüben, 2001 [186]). CSMP++ has been used for a variety of applications, not only with respect to NFR (Geiger et al., 2006, 2007 [73, 75]; Matthäi et al., 2007 [129, 130], a combination of Dual Permeability Models with DFM (Maier et al., 2014 [128]), transport

1.7 X-RAY CT OF GEOMATERIALS

and two-phase flow with variable viscosities (Schmid et al., 2013 [180]), flow and transport in 3D pore geometries (Zaretskiy et al., 2010 [212]), capillary trapping of CO₂ in fractured formations (Annewandter et al., 2013 [5]), or the numerical propagation of fractures (Paluszny and Zimmermann, 2010 [159]), just to name a few.

Fig. 14 shows an example application of CSMP++ where primary drainage in a highly idealised NFR is modelled in 3D (Matthäi et al., 2007 [130]). It illustrates the influence of well-interconnected fractures on the saturation distribution.

In general, the workflow with CSMP++ consists of five steps:

1. Geological data is collected and analysed.
2. A CAD model of the geological structure of interest is built. This is done with Rhinoceros 3D, a commercial non-uniform regular B-splines (NURBS) based modelling software.
3. The CAD model is translated into an unstructured FE grid using the commercial software ANSYS.
4. The mesh is used in CSMP++ for various fluid flow simulations.
5. Finally, visualization and analysis of the results is done with Matlab or VTK.

1.7 X-RAY CT OF GEOMATERIALS

X-ray CT today is widely used in many different medical, industrial, and scientific applications. High-resolution CT is well-developed in material sciences, and has been used in geosciences for static and dynamic data acquirement. For an introduction in geoscience applications see Ketcham and Carlson, 2001 [111]; Kaestner et al., 2008 [100]; Wildenschild et al., 2002 [207]; Cnudde and Boone, 2013 [45], and with special respect to pore-scale applications cf. Wildenschild and Sheppard, 2012 [208]; Blunt et al., 2013 [23]. Recent developments can be found e.g. in the ICTMS conference proceedings [89, 90].

1.7 X-RAY CT OF GEOMATERIALS

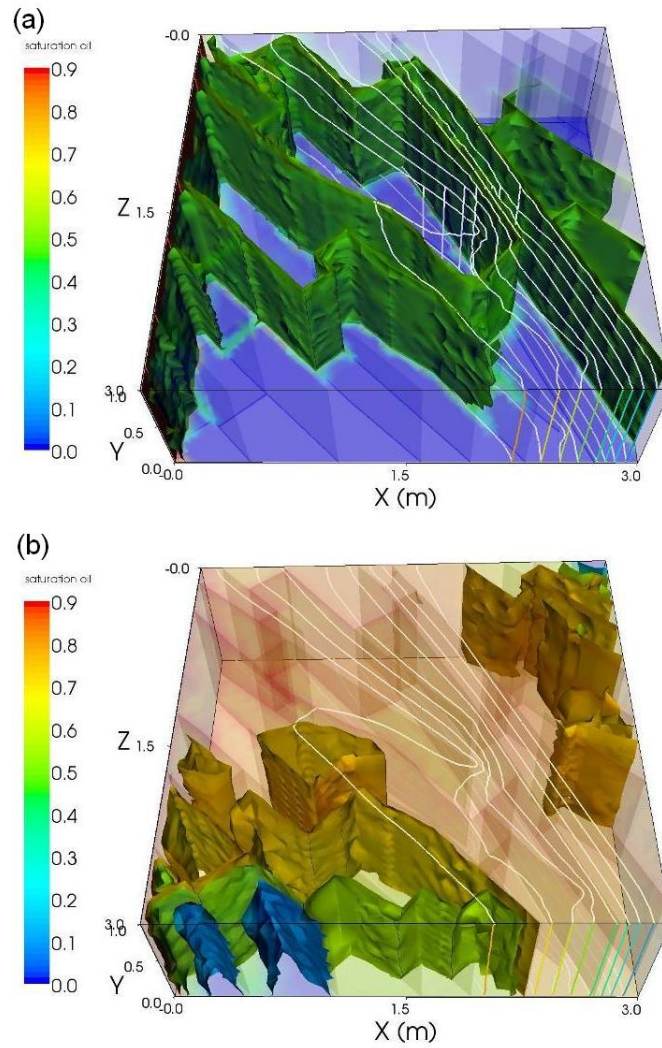


Figure 14: Example for a CSMP++ application: Model BED₄ – Reservoir during primary drainage. This simulation illustrates the influence of well-connected fractures on the saturation distribution. The white isocontours on the model boundaries indicate the fluid pressure distribution. (a) Reservoir at water-breakthrough after 5.4 hours, average oil saturation ca. 20%. The oil first enters the connected fractures (dark green). (b) The reservoir towards the end of the primary drainage after 234 days, average oil saturation ca. 80%. The oil is diffusing into the surrounding matrix (from Matthäi et al., 2007 [130]).

1.7 X-RAY CT OF GEOMATERIALS

A major application of μ -CT (where μ stands for micro, i.e. high-resolution X-ray CT) is to generate 3D pore scale images to analyse for example the pore-network structure of small rock samples for subsequent calculations of single- and multi-phase flow properties (Bhattad et al., 2011 [22]; Al-Raoush and Willson, 2005 [3]; Thompson et al., 2006, 2008 [189, 188]; Blunt et al., 2002, 2013 [24, 23]; Bertels et al., 2001 [21]; Arns et al., 2004 [6]; Turner et al., 2004 [192]), or to use μ -CT to visualize fluid occupancy in the porous medium (e.g. Prodanovic et al., 2007 [166]; Porter and Wildenschild, 2010 [163]; Menke et al., 2015 [134]; Iglauer et al., 2012, 2013 [91, 92]; Pak et al., 2015 [156]). However, pore-scale imaging using μ -CT occurs at a much smaller scale (at the micro scale) and higher resolution than practicable for the fracture-flow experiments in our work.

Other applications of μ -CT in geosciences comprise soil structure analyses (e.g. Vogel, 2001 [198]; Carminati et al., 2008 [36]; Houston et al., 2013 [86]), or to image and characterize compaction band formation in sand columns (Viggiani et al., 2004 [194]; Hall et al., 2010 [80]; Ando et al., 2013 [4]; Charalampidou et al., 2011 [39]).

Although our main focus is on the application for visualization and quantification of heterogeneous and porous geomaterials, especially fractured carbonates and fluid flow through them, similar challenges are encountered in applications such as civil engineering or ceramics fabrication, where e.g. fluid invasion in cracks or micro-fracture formation is visualized by X-ray CT (Carmeliet et al., 2004 [34]; Krause et al., 2010 [115]), applications for well stimulation where acid injection or hydraulic fracturing forms heterogeneous structures in geomaterials with similar properties in terms of CT imaging and image processing (Izgec et al., 2010 [93]; McDuff et al., 2010 [133]; Renard et al., 2009 [173]), or airport scanners for material detection by advanced radiography techniques, e.g. dual energy imaging (Rebuffel and Dinten, 2007 [171]). Learnings from such applications can be translated to our specific problems, for example optimizing data collection, or image processing.

Recently, synchrotron X-ray CT has been increasingly used for a variety of applications (Lindquist et al., 2000 [121]; Baruchel et al., 2006 [16]; Fousseis et al., 2014 [69]; Berg et al., 2013 [19]; Wildenschild and Sheppard, 2012 [208]; Blunt et al., 2013 [23]). Synchrotron X-ray CT has the advantage of

1.8 IMAGE PROCESSING AND ANALYSIS

emitting powerful X-ray beams which, depending on the applied source current, can result in shorter image acquisition times, higher resolution, or extreme material penetration.

For completeness, we note that flow in fractures can also be visualized by other means, for example Dijk et al., 1999 [59] have used nuclear magnetic resonance imaging (NMRI) to visualize single-phase flow in a rough-walled fracture. Neutron imaging is also relevant due to the ability to depict hydrogenous materials in porous media with high phase-contrast (Jasti and Fogler, 1992 [95]; Vontobel et al., 2005 [199]; Carminati et al., 2007 [35]). Neutron imaging therefore allows to visualize fluids in high density materials (e.g. rocks) (e.g. Ferno et al., 2015 [65]).

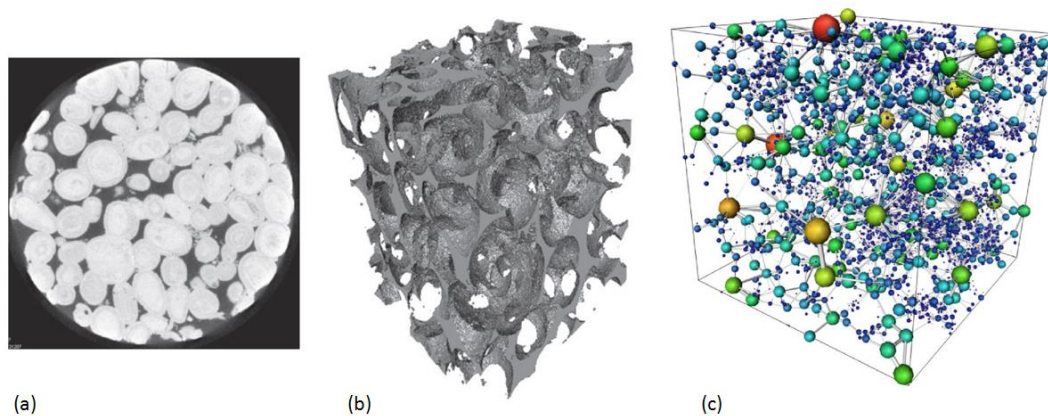


Figure 15: (a) Two-dimensional cross-section of three-dimensional micro-CT images of Ketton limestone, an oolitic quarry limestone of Jurassic age. The pore space is shown dark. Diameter of sample is 5mm. The grains are smooth spheres with large pore spaces. The grains themselves contain micro-pores that are not resolved. (b) Pore-space image of (a) has been binarized into pore and grain. A central 1000^3 section has been extracted. The images show only the pore space. (c) Pore network extracted from (b). The pore space is represented as a lattice of wide pores (shown as spheres) connected by narrower throats (shown as cylinders). The size of the pore or throat indicates the inscribed radius (from Blunt et al., 2013 [23]).

1.8 IMAGE PROCESSING AND ANALYSIS

Fractures have been imaged with conventional (medical/industrial) CT scanners since the early 90s. Johns et al., 1993 [97] explored the measurements of

fractures by employing a calibration method of scanning core samples with known gap sizes, and transferring the results to measurements of aperture distributions in real fractures.

Assuming that most imaging artefacts have been resolved adequately, a typical 3D image analysis consists of a segmentation step (the volume of greyscale voxels is converted into a set of objects with a similar greyscale/density), the possible separation of connected but different objects, and a parametrisation step, where the sample is characterised by the application of shape, size, or other post-processing parameters, for further quantitative data analysis, or to be used as input for simulations. The segmentation algorithm (or set of algorithms) hereby is most crucial to obtain high quantification accuracy [100] and therefore needs to be chosen carefully.

A possible image processing workflow can be described as follows:

- First, all distracting information from the acquired images needs to be removed. To characterize the solid and void phase in the 3D images best, several image enhancement methods, e.g. the application of a non-linear diffusion filter for noise reduction (Kaestner et al., 2008 [100]; Perona and Malik, 1990 [160]; Catte et al., 1992 [38]; Sheppard et al., 2004 [183]; Rudin et al., 1992 [175]), have been suggested, which can also erase interfering information from present pores, with minimal loss of information at phase boundaries; this is advantageous compared to standard methods (Gonzales and Woods, 2008 [78]). Other image enhancement methods include contrast improvement and artefact removal algorithms, inter alia.
- Second, in order to obtain a binary representation of the geometry, a subsequent segmentation algorithm is needed, which defines which voxels are part of the matrix region and which belong to the fracture. An overview of algorithms can be found in Chapter 10 of Gonzales and Woods, 2008 [78] and Pal and Pal, 1993 [157]. It has been discussed that contour tracking, region growing, or edge detection based algorithms deliver better results (good overview in Kaestner et al., 2008 [100], see also Oh and Lindquist, 1999 [153]; Ketcham, 2005 [110]) than global threshold methods (e.g. Otsu, 1979 [155]), as they apply a local

threshold depending on a neighbourhood region around the respective pixel. Voorn et al., 2013 [200] developed a fracture segmentation by multiscale methods to extract very narrow fractures from μ -CT data, as global thresholding techniques are usually not successful enough, but no aperture analysis was presented. Clustering methods, as e.g. watershed segmentation (see chapter 10. in Gonzales and Woods, 2008 [78]), are in this case not explicitly beneficial, as we consider the fracture as single entity; a watershed algorithm is able of separating individual image regions like grains, or pores, remaining cavities in the fracture and rock domain will be removed (filled). Many of these algorithms are already implemented in commercial and open source software (see below).

- Finally, from the binary voxel representation of the void and solid phase, a measurement of geometrical features is possible. As fractures are very narrow, though, the typical approach of segmenting the area of interest, gives usually too coarse results (apertures of just a few voxels) for a detailed aperture analysis.

A classical method to investigate aperture distributions of natural fractures with X-ray CT imaging was developed by Johns et al., 1993 [97]; it is now widely used (e.g. Keller 1997 [109]; Madadi et al., 2003 [127]; Oda et al., 2004 [151]; Auradou, 2009 [8]) and can be considered as the standard method for correct fracture aperture mapping. Johns et al., 1993 [97] considered the grey scale profile along a line perpendicular to a visible fracture in a reconstructed slice. The graphs indicate a region where the grey value (density) drops significantly to the value of the surrounding air, which can be associated with the void fracture aperture. The width of this "gap" in the line profile is called the *gap size*. The grey values for the rock material oscillate around the average attenuation response from the CT (cf. fig. 16). The aperture of wide open fractures can be obtained by measuring the distance between the left and right slope of the gap, after choosing a suitable threshold, and determining the direction normal to the fracture boundary. For narrower fracture apertures though, the values inside the gap have a higher level than air, mainly due to the voxels close to the fracture containing information of both, rock and air, so the corresponding voxels

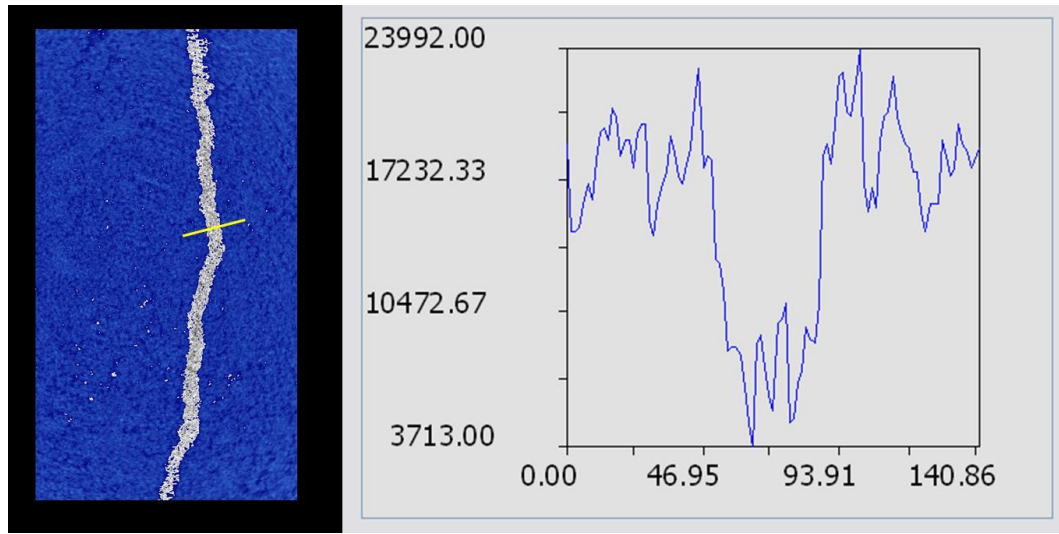


Figure 16: Left: Highlighted cross-section of San Andreas carbonate. Blue: rock matrix, white: fracture. The yellow line denotes the location the line profile. Right: Corresponding graph (line profile) of the sample's apparent grey values perpendicular to the fracture. This profile indicates an existing region of lower density in the sample, which is assigned to the fracture.

cover a *partial volume* of each material. Therefore, the distance across the gap cannot be matched to a fracture aperture of given size (e.g. by spreading a sample with a feeler gauge); instead it is oversampled (Johns et al., 1993 [97]). This effect is introduced as *partial volume effect* at the fracture-matrix interface. It is the reason why a quantitative analysis by segmentation often is not possible for small features in a CT image. Johns et al., 1993 [97] show that the attenuation response of a voxel which contains more than one material can be related linearly to the volume fractions and the attenuation coefficients of the pure materials (i.e. the composed attenuation coefficients, cf. Vinegar and Wellington, 1987 [196]).

$$\mu_{mix} = \mu_a S_a + \mu_b S_b + \mu_c S_c + \dots \quad (8)$$

where μ is the attenuation coefficient, and S the saturation of the material in the according voxel, the subscripts a, b, \dots refer to the pure material's properties, and mix to mixture properties, respectively. Based on this relation, they develop a quantitative calibration method to account for the partial volume effect. As the voxels surrounding the actual fracture are influenced, the integration over the gap area below the rock base line in the CT image

profile provides the cumulative response and is used to quantify the *missing rock mass* in the fracture. A series of aperture measurements of a core sample, consisting of two halves with flat polished (or ground) surfaces (to avoid roughness as much as possible), is carried out for different given apertures. The integration values of the missing mass in the gap area, m_g , can then be correlated linearly with the given gap sizes, a_g (compare section 2.5). The correlation curve is obtained by linear regression, and its slope, p , reflects the different attenuation coefficients of air and rock. Each rock type has therefore its own distinctly different calibration slope.

$$m_g = p a_g + q \quad (9)$$

The obtained best fit straight line can then be used to map the CT measured grey value distribution to the actual aperture distribution of a rough-walled fracture. It is important to note that this estimation procedure is mass conservative, because the actual material mass is used to determine the appropriate threshold for the aperture measurement. Note that this method can be extended as well to estimate the tracer concentration within a core of a known, i.e. previously measured, fracture aperture distribution by taking the brine attenuation coefficients into account and normalizing the concentration in the core against the inflowing concentration (Johns et al., 1993 [97]).

A different approach is described by Vandersteen et al., 2003 [193] and Ketcham et al., 2010 [113]. They observe that a point signal is spread out by X-ray CT by the various non-idealities of the scanning procedure (e.g. movements of the sample, X-ray focal spot size etc.). All these effects can be combined in the so called *point-spread function (PSF)*, which describes how a single point in the sample is spread out by the scanning and reconstruction process over its neighbourhood (fig. 17). Another observation is that fractures, which are more narrow than the PSF, due to these superpositioned effects do not show the attenuation signal of air in the centre but higher values (fig. 18). Vandersteen et al., 2003 [193] suggest to fit a Gaussian curve to the fracture dip to simulate a PSF, and correct for it inversely. Ketcham et al., 2010 [113] refined this method to the *Inverse PSF method (IPSF)*, where fracture position, fracture aperture, PSF, and average rock value are found it-

eratively. This method proved to be also suitable for heterogeneous samples consisting of multiple materials.

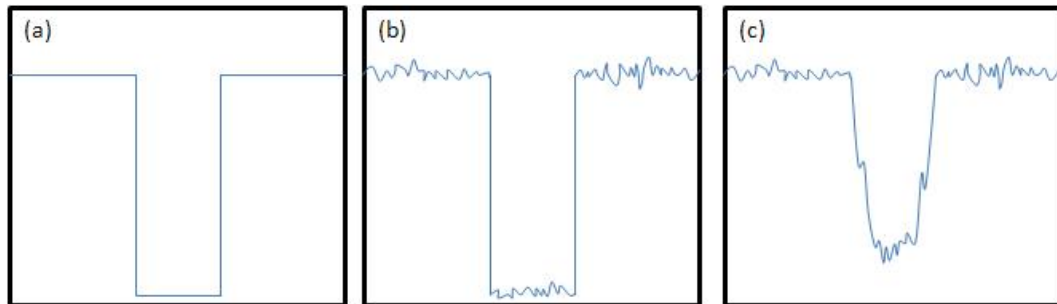


Figure 17: (a) An attenuation profile of a fracture perpendicular to the fracture plane in a homogeneous medium would deliver a rectangular signal. (b) If noise and heterogeneities in the rock matrix (e.g. pores below the voxel resolution) superimpose, the signal becomes slightly blurred. (c) The dip in the profile is due to the partial volume effect and the superimposed point-spread function (PSF), which cause the fracture boundaries to be less "steep".

Different approaches to measure fracture apertures are also possible. For example Detweiler et al., 1999 [56] used transparent fracture replicas to measure aperture distributions with transmissive light. Other three-dimensional measurements of aperture distributions in artificial and real fractures can be found in e.g. Power and Durham, 1997 [164]; Bertels et al., 2001 [21]; Nakashima et al., 2010 [144].

Several softwares exist for CT reconstruction and image analysis. One of the leading groups in the general development of X-ray CT systems and image processing software for the visualization of geomaterials is the Centre of X-Ray Tomography at University of Ghent, UGCT (Brabant et al., 2011 [28]; Cnudde et al., 2006, 2010 [46, 47]; Vlassenbroeck et al., 2007 [197]; Dierick et al., 2004 [58]; <http://www.ugct.ugent.be/>). Morpho+ is now available as Octopus Analysis by the UGCT spin-off company Inside Matters². Commercial packages are usually very convenient to use. Avizo by FEI (<http://www.fei.com/>), VGStudioMax by Volume Graphics (<http://www.volumegraphics.com/>), and ScanIP by Simpleware (<https://www.synopsys.com/simpleware.html>) are the leading prod-

² Meanwhile, Inside Matters is a joint venture with X-ray Engineering, another spin-off company from UGCT, operating as XRE <http://im-landing-page.s3-website-eu-west-1.amazonaws.com/>.

1.8 IMAGE PROCESSING AND ANALYSIS

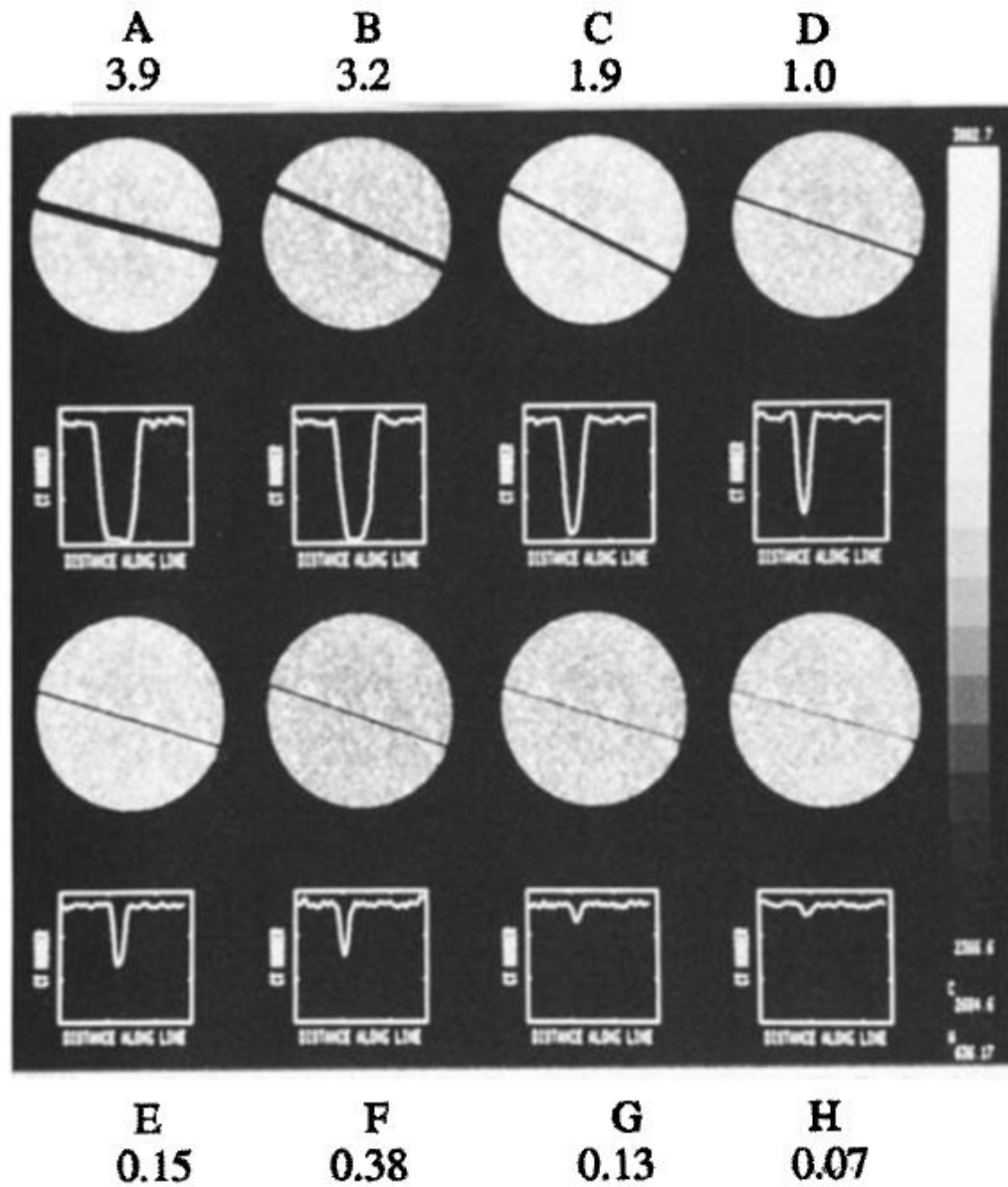


Figure 18: CT images of granite samples with aperture sizes ranging from 0.076mm to 3.937mm. Spatial image resolution 1.4mm by 1.4mm by 5mm. Narrow fractures show a signal peak of the profile that is significantly higher than air, and for very narrow fractures hardly distinguishable from the surrounding pores or noise signal (from Johns et al., 1993 [97]).

1.9 FLOW EXPERIMENTS VISUALIZED WITH CT

ucts on the market, whereas ImageJ (<http://imagej.nih.gov/ij/>), ImageVis3D and Seg3D (<http://www.sci.utah.edu/software/>), or Blob3D (<http://www.ctlab.geo.utexas.edu/software/>) provide good freeware alternatives. For an overview of open source software packages see Fuisseis et al., 2014 [69]. Also worth of mentioning is the Image Processing Toolbox in Matlab, which can analyse CT data slicewise.

1.9 FLOW EXPERIMENTS VISUALIZED WITH CT

Vinegar and Wellington, 1987 [196] were amongst the first to employ a medical CT to track fluid invasion into core samples. They used dopants in CO₂ displacement experiments to increase the phase contrast and were able to produce one of the first images of miscible fingering in Berea sandstone. An introduction to the early research can be found in Castanier, 1989 [37] and this changed petroleum research unimaginably. Petroleum research cannot be imagined without X-ray CT since. It is used for core descriptions, or to see saturation fronts in multi-phase flow experiments (e.g. Barbu et al., 1999 [12]; Sahni et al., 1998 [176]; Withjack et al., 2003 [210]).

As one of the first applications of μ -CT in fractured porous media, Rangel-German and Kavscek, 2002 [168, 169] from Stanford University studied multi-phase flow in sandstone with a special focus on matrix-fracture interaction and imbibition processes (see fig. 19). They investigated imbibition performances for various injection rates and fracture apertures on a core-scale model. They also designed an artificial micromodel to visualize fluid movement and matrix-fracture interaction at a pore-scale level. The results agreed well with a numerical simulation from which they proposed a new analytical model based on time-dependent matrix-shape factors for filling fractures (Rangel-German and Kavscek, 2005 [170]). However, Rangel-German and Kavscek were using a medical dual-energy CT scanner (Rangel-German, 2002 [168]), which usually have a low cross-sectional resolution (about 1mm) due to a low energy level. They hence did not resolve the flow processes in the fracture itself.

Several other studies of visualizing flow experiments in rock cores exist:

- Ferno et al., 2011 [66] employ nuclear magnetic resonance imaging (NMRI) to investigate wettability effects in fractures during oil-water

1.9 FLOW EXPERIMENTS VISUALIZED WITH CT

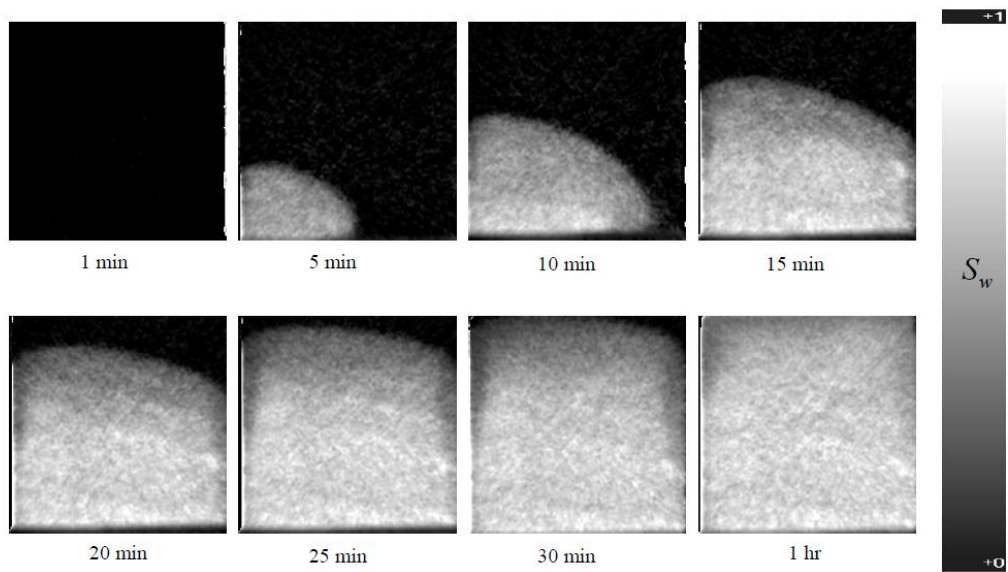


Figure 19: CT images for "filling-fracture" system for different times. This regime shows a plane source that grows with time due to relatively slow water flow through fractures. Fracture initially air-filled. Dark shading indicates zero water saturation while white indicates fully water saturated. Water injection at 1cc/min in a fracture 0.1mm thick. Injection is from lower left corner and production from lower right corner (from Rangel-German, 2002 [168]).

1.9 FLOW EXPERIMENTS VISUALIZED WITH CT

and water-oil displacements (fig. 20). They could show how oil droplets form on the fracture surface at moderately oil-wet conditions. The droplets contribute significantly to fluid transfer across open fractures, as droplets bridge capillary pressure. The assumption of a uniform pressure distribution in the fracture, the fracture flow, and that the fracture is instantly water-filled during waterfloods has to be questioned. In a similar study Ferno et al., 2013 [67] monitor the displacement of oil by spontaneous imbibition of brine into fully oil-saturated cores of limestone, sandstone and chalk composite. They find that heterogeneities in core properties have a dominant effect on the imbibition mechanism, especially differences in end-face bubble pressures. The NMRI images also show that, in the initial stage, brine invades the oil-saturated core spherically only from a few localized points and only later merges to form a piston-like flow front.

- The same group also combines imaging techniques to visualize enhanced oil recovery (EOR) processes in fractured reservoirs: In Erslund et al., 2010 [64] NMRI is combined with nuclear tracer imaging (NTI) to monitor waterflood mechanisms into and across an open fracture in low permeability chalk cores of different wettabilities, where oil production is governed by spontaneous imbibition. NMRI has a high spatial resolution, and fractures less than 1mm wide can be visualized, whereas NTI is used to visualize the macro-scale saturation distribution in the fractured system. The complementary imaging allows for a detailed explanation of fluid flow mechanisms, where large scale phenomena are controlled by small scale heterogeneities. The study concludes for example that water liquid bridges across the open fracture, which form from growing water droplets at the fracture face, at moderately water-wet conditions accelerate fluid transport across the fracture, and result in exceeding the spontaneous imbibition potential for oil recovery.
- In Ferno et al., 2015 [65] positron emission tomography (PET) is combined with CT imaging for the first time to quantify the development of local fluid saturations in sandstone and chalk. CT is used to visualize the structural rock information, whereas PET is used to visualize

1.9 FLOW EXPERIMENTS VISUALIZED WITH CT

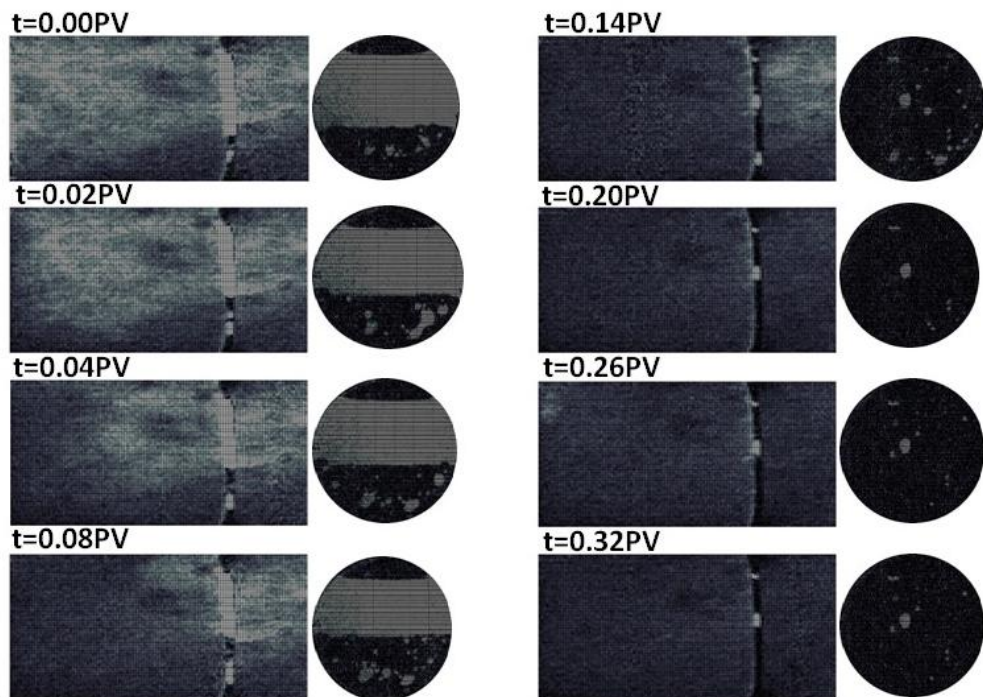


Figure 20: Two-dimensional oil distribution development during waterflooding of a moderately oil-wet core. NMRI images at orthogonal directions. Each time step has a longitudinal image showing the stacked cores (inlet core, fracture, outlet core) and a transverse image of the fracture. Oil appears bright and lack of color equals reduced oil saturation. Oil was produced from the inlet core in the form of droplets growing on the fracture surface (from [66]).

1.9 FLOW EXPERIMENTS VISUALIZED WITH CT

the explicit fluid saturation. They demonstrate the possibility of this new approach to investigate miscible displacement processes to study flow variations (e.g. development of preferred flow paths) related to local heterogeneities. They also injected CO₂ into water-saturated core plugs to show that PET captures the fluid front progression well, where CT allows for additional direct measurement of the rock structure. The combined PET/CT method therefore provides complimentary information superior to each method alone.

- Dijk et al., 1999 [59] used NMRI to present a direct measurement of flow velocities in water-saturated fractures in a limestone sample to investigate a variety of geometric and hydraulic features (e.g. flow and stagnant regions in the fracture) and to examine the applicability of the cubic law. Compared to more recent studies, though, the image resolution has been poor and the fracture was artificially widened (mean fracture aperture $\sim 2.3 \pm 1.0$ mm).
- Detwiler and Rajaram, 2001 [55] used a transparent fracture model to investigate the fluid flow and transport of nonaqueous-phase-liquid (NAPL) in fractures using light transmission techniques (cf. Detwiler et al., 1999 [56]). They compared the physical experiment with simulations, which showed close agreement.
- A similar study of fracture replicas of sandstone and granite fractures has been conducted by Nowamooz et al., 2013 [149]. They investigate breakthrough curves for miscible tracer displacement. They found the transport behaviour to be non-Fickian (anomalous diffusion), so that the classical advection-dispersion equation is not appropriate to describe early breakthrough and long-time tailing in fractured cores.
- Bertels et al., 2001 [21] measured fracture aperture distribution, in-situ saturation of gas and water for gas/water drainage in the fractured impermeable basalt sample with μ -CT, along with relative permeabilities and capillary pressures. They found channelling areas for the gas phase and retained water in the fracture, and linked the manner the capillary pressure changed to the local behaviour of the fluid flow in the fracture.

1.9 FLOW EXPERIMENTS VISUALIZED WITH CT

- Polak et al., 2003 [162] investigated the tracer diffusion from a vertical fracture into the surrounding matrix for which they used a second-generation medical scanner. They could only acquire 28 images, but could visualize the vertical tracer distribution and show that although transport is dominated by diffusion, advection plays also a significant role in the matrix when vertical density differences occur in the fluids.
- Wanatabe et al., 2011 [204] used the *peak height (PH)* method, also used in this work (see 2.5), to locate and measure fractures in granite core samples. They later apply a local cubic law (LCL) (eq. (5)) based single-phase fracture flow model to calculate permeabilities. Unfortunately, their fracture model from the CT measurements was not accurate enough to reproduce the experimentally obtained permeabilities. On the other hand, they were able to calculate and show preferred flow paths within a fracture network.

The original motivation for our research were the studies carried out by Karpyn and co-workers at Pennsylvania State University. She pioneered the visualization of immiscible displacement using μ -CT in various set-ups (Karpyn et al., 2007 [106]). In some studies, Karpyn used a line scanner (an X-ray detector consisting of a single pixel row) in a parallel beam architecture for faster imaging resulting in a time series of cross sections during fluid invasion (Lee and Karpyn, 2010 [119]). The advantage of such a device is the much faster image acquisition time, on the other hand only single image slices can be produced of the 3D core. She studied the effects of the fracture morphology on the distribution and transport of two immiscible fluids (oil and water) and could observe various flow mechanisms such as trapped oil (fig. 21), preferred flow paths, and snap-off effects during two-phase flow experiments. Karpyn and Piri et al., 2007 [161, 104, 106] also combined μ -CT successfully with an equivalent two-dimensional pore-scale network model of the fractured sandstone to predict fluid occupancy and multiphase flow properties during primary drainage, imbibition, and secondary drainage. Simulation results were compared to the above two-phase X-ray CT flow experiments and showed good agreement. Karpyn et al., 2009 [105] and Landry et al. 2014 [118] recently studied the relationship between fracture conductivity and matrix porosity, which includes sequential CT images,

1.10 REVIEW SUMMARY

images of flow through core samples, or flow through fractured glass bead packs.

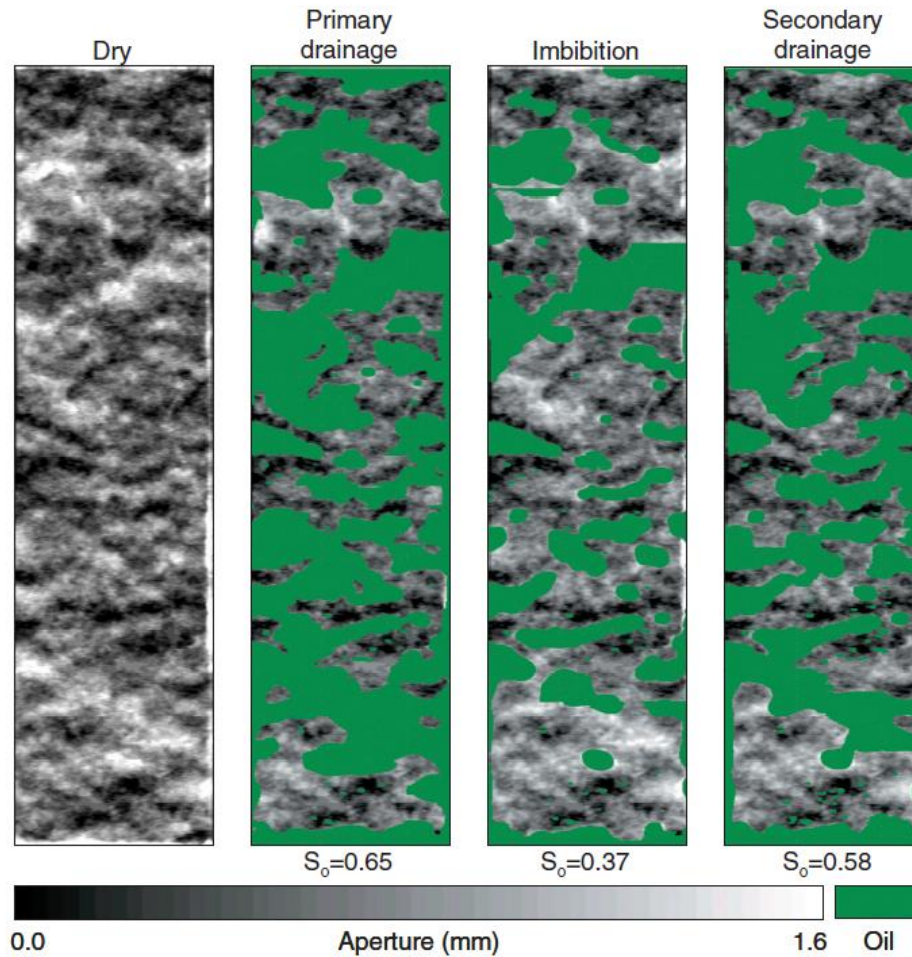


Figure 21: Green: Oil residence relative to local fracture aperture (dark and light grey represent small and large apertures, respectively) generated by x-ray microtomography at the end of different experimental stages (from Piri and Karpyn, 2007 [161]).

1.10 REVIEW SUMMARY

As naturally fractured reservoirs (NFR) play a significant role in hydrocarbon production, carbon capture storage (CCS), groundwater contamination, and other geologic research fields, the understanding of how a single fracture, or fracture networks, respectively, influence the physics of flow in these reservoirs is of dominant importance for real-world applications. The

1.10 REVIEW SUMMARY

problem of considering several scales of complex heterogeneous geometries at once (from pore scale up to reservoir scale) is intrinsic and has been overcome only by upscaling properties, trying to retain the overall effects of smaller discontinuities. The characteristics of carbonates as porous medium herein have been quite well understood, but their heterogeneous nature renders it even more difficult to predict flow in carbonates. Fractures add to this complexity. Experimental work investigating the influence on flow of a single non-uniform fracture in carbonates has been limited so far.

Dual porosity/dual permeability and Discrete Fracture Models (DFM) aim to overcome these scale-dependent problems imposed by fractures being present in geologic formations by incorporating both, rock matrix and fractures, for simulation models. DFM though can account explicitly for the natural geometry of fractures. As simulator, CSMP++ is, amongst others, able to realize DFM as modelling approach, and as computers are becoming more powerful, resolvable grid resolutions are becoming larger. CSMP++ has successfully been used to describe single- and multiphase flow in complex geometries.

Verification of these simulations is difficult. As one of the necessary steps, the influence of non-uniform fractures on recovery processes like imbibition, drainage, or fluid exchange between fracture and rock matrix in general, has to be investigated.

By now, X-ray computer tomography (CT) has become a standard tool for visualization and quantification of geomaterials – from pore-scale imaging to investigating larger features like compaction bands, etc. The imaging of fluid flow through porous rocks has predominantly been covering limestones, sandstones, chalk, or synthetic materials. Especially in multiphase flow unexpected effects could be shown.

With these preconditions in place, a high-resolution survey of a natural fracture in an inhomogeneously porous carbonate sample, accompanied by an experimental flow study through the same sample, could be – if adequately processed – used to compare DFM simulations qualitatively and quantitatively with real-world experiments.

The overarching aim of this thesis is hence to visualize flow in a fractured carbonate using X-ray CT and develop a strategy for how the fracture

1.11 OBJECTIVES AND STRUCTURE OF THE THESIS

geometry could be represented in a DFM model to compare experiments and simulations.

1.11 OBJECTIVES AND STRUCTURE OF THE THESIS

Primary aim of this thesis was to develop a suite of μ -CT experiments and simulations for fractured carbonates and find a way of how the fracture and matrix geometry could be used for further simulation using DFM methods and validation flow experiments. An initial task was to design and build a high-resolution X-ray CT system to suit our experimental needs.

Based on this overarching aim, the objectives of this research, which build up on each other step by step, are as follows:

- A highly flexible CT scanner system is built from scratch, including a versatile control software, to allow for high-resolution 3D scans of fractures in carbonate materials on the one hand, and for visualization of flow experiments in these materials on the other hand. The new and precise remote control program to synchronize the separate scanner parts is developed, implemented, and optimized for accurate data acquisition. The data collection process is then optimized regarding measurement accuracy for carbonate samples including an open fracture. This new setup allows to investigate fracture aperture distributions in detail on fractured carbonate core samples with up to about 4cm in diameter and about 10cm length.
- To characterize the fracture aperture distribution of two different fractured carbonate cores with high resolution, a combination of image processing methods and calibration measurements leads to a detailed quantitative description of the fracture topology and a corresponding aperture distribution. The smallest resolvable aperture is $75\mu\text{m}$.
- An interface is then developed to implement these fracture apertures and the topology as direct input into DFM flow simulations. The 3D fracture geometry data is therefore generated as a 2D geometrical representation in form of a point cloud in 3D space and a cohering aperture value at each position. For the input for a DFM simulation, an averaging procedure of the high-resolution data is applied, and

1.11 OBJECTIVES AND STRUCTURE OF THE THESIS

differently fine meshes, representing the rock matrix as 3D finite elements and the fracture as 2D finite elements, are generated.

- The CT scanner set-up and developed control software can (due to their flexibility) be changed to image flow experiments on the same samples used for the accurate aperture distribution measurements. For this, a special X-ray transparent flow cell is constructed. Different tracers added to the water and oil phases are tested in terms of image contrast. A set of single and two-phase flow experiments is carried out on both different rock samples.
- DFM single-phase flow simulations are carried out on the fracture mesh, employing the CSMP++ simulator. It is shown that the simulations can be run on the full hybrid 2D/3D model as well.
- In the end, a qualitative comparison of flow simulations with experiments on the same geometries is discussed leading to the identification of open questions.

Aside from the current chapter (Chapter 1), which served to give a brief overview of flow simulations in fractured porous media, computer tomography for geomaterials and flow experiments in limited carbonate studies, this thesis contains 6 more chapters – 7 chapters in total:

- Chapter 2 presents the methods used to achieve the research objectives. It discusses the preparation of the carbonate samples, the imaging equipment including the development of the CT scanner system, how the image acquisition and reconstruction of the CT data has been carried out, the measurement methods of the fracture apertures, the numerical modelling approach and the simulation methods, and we discuss how the single and two phase flow experiments have been designed and conducted.
- Chapter 3 describes a particular new image correction method to be used on the scanned 2D images before reconstructing the 3D images. The method was developed to allow for a non-linear imaging error, which is inherent to the type of X-ray camera of the in-house built CT scanner.

1.11 OBJECTIVES AND STRUCTURE OF THE THESIS

- Chapter 4 gives a detailed description of how the fracture apertures were measured, and presents the analysis of the aperture distributions.
- In Chapter 5 we present the results of the single and two-phase flow experiments, which clearly show heterogeneous flow patterns in fracture and rock matrix for both, single and two-phase flow.
- Chapter 6 presents the results of the single-phase flow simulations, and shows the feasibility for the simulations to be extended from 2D to 3D simulations. The results are compared with the experimental results. Probable causes for differences are discussed in the end of the chapter.
- Chapter 7 concludes the thesis with a discussion of the results followed by recommendations for future work.

METHODOLOGY

2.1 INTRODUCTION

We combine DFM simulation and μ -CT, for a comparison study of single-phase flow through fractured core samples. On the one hand, we utilize the CT to measure fracture aperture distributions in fractured core samples. Also, the CT is used to visualize single- and two-phase flow experiments on the same core samples. On the other hand, single-phase flow simulations with DFM are carried out on computer models of the previously measured core samples. The measured fracture surface topology and fracture apertures for input into CSMP++ are derived from the CT studies. A novel flow cell is designed and built in-house. The static and flow experiments were carried out using the new X-ray CT instrument built in-house at the School of Geosciences, University of Edinburgh. The research includes the optimization and standardization of the data collection process and the experimental design. This also includes the development and optimization of the control software to operate the rotation and imaging equipment of the CT system, as well as several studies to improve the image quality. An essential task in this study was to design an efficient data interface to quantify the CT data for the numerical model by digital image processing, and enable a discussion of methods to compare the experimental and simulation results.

2.2 CARBONATE SAMPLES

The considered samples are Baker Dolomite (BD), and San Andreas carbonate (SAC) provided by ExxonMobil (see fig. 22). The two types of carbonate

2.2 CARBONATE SAMPLES

rocks that differ in porosity and mineralogy have been characterised in the laboratory at Heriot-Watt University, School of Energy, Geoscience, Infrastructure and Society, using a combination of several techniques used in conventional routine core analysis, having been measured in-house at Heriot-Watt University¹. These include petrography thin sections analysis, scanning electron microscopy (SEM) and X-ray diffraction (XRD). The porosity of these two types of carbonate rocks has been measured using a helium gas porosimeter. These four complementary techniques have been employed in this study to characterize two carbonate core samples (from BD and SAC). This strategy allows a full range of characteristics to be determined and the results of the different methods used were found to be consistent with each other.

This study has shown that the rock sample of the BD core is homogeneous, composed by dolomite. No clay minerals have been identified; however 2 to 3% of the rock are represented by celestine-barite particles. The presence of these crystal deposits can be explained by a precipitation as a result of the mix of seawater and formation water. The high porosity value of the rock material (28.6 to 29.6%) is explained by the absence of cement in this rock. The rock sample of one part of the SAC core (SAC6) is heterogeneous; sample SAC6C is composed by 72% of dolomite, 23% of calcite and 1% of quartz. The cement is composed by kaolinite, which represents 4% of the rock. Another sample of the same core sample (SAC6F) is composed by 89% of dolomite and 2% of quartz. The cement is composed by dickite-kaolinite, which represents 9% of the rock. The porosity is 23.0%. The rock material of another core sample (SAC19) represents a similar mineralogy as sample SAC6C. The rock material is composed by 78% of dolomite, 14% of calcite and 6% of quartz. The cement is composed by kaolinite, which represents 4% of the rock. The porosity of the rock material is lower than the porosity of the rock material of sample SAC6 (20.3% and 23.0%, respectively). This confirms the heterogeneity of the rock material of sample SAC.

The San Andreas Carbonate (SAC) has a porosity of $\phi = 20.3$ to 23.0% and a permeability of $k = 30\text{mD}$ (NB: rock is very variable and permeability is likely to be higher or lower for other samples). The Baker Dolomite has

¹ The internal laboratory report may be queried via Sebastian Geiger, School of Energy, Geoscience, Infrastructure and Society (EGIS), Heriot-Watt University, Edinburgh (UK).

2.3 IMAGING EQUIPMENT

a porosity of $\phi = 28.6$ to 29.6% and a permeability of $k = 61\text{mD}$ (room temperature) to 57mD (90°C), respectively.

Twin samples each a 3.81cm diameter core (length 10cm) from the same blocks are used for fracture aperture measurements and single and two-phase flow experiments. For this, each sample was artificially fractured: Using a modified Brazilian test (see fig. 23) a single centered fracture was created over the whole length of the core.

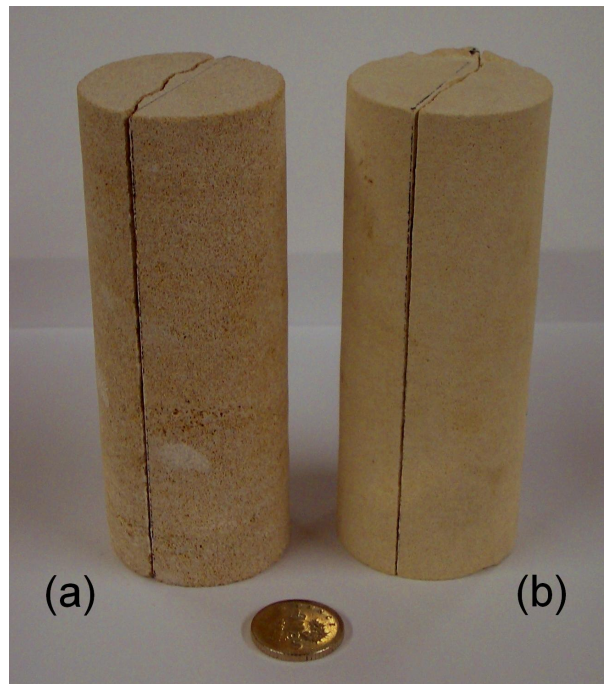


Figure 22: Carbonate Samples: (a) San Andreas Carbonate (SAC), (b) Baker Dolomite (BD) cores with a single artificial fracture. Diameter 3.81cm .

2.3 IMAGING EQUIPMENT

2.3.1 Background of $\mu\text{-CT}$

In general, X-ray CT is a non-destructive imaging technique which derives three-dimensional data of the inner structure of an object from a set of two-dimensional projection images. Each 3D volume data element is called a *voxel*. The general principle of a CT scanner is to position the object of interest between an X-ray source and an X-ray detector. A sequence of

2.3 IMAGING EQUIPMENT

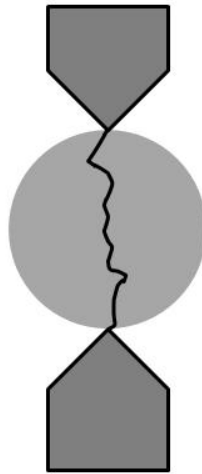


Figure 23: Modified Brazilian test. The cylindrical rock cores are clamped between two wedges. The vertical pressure is slowly increased until a fracture forms along the length of the core sample.

radiographic images is taken of the sample as it is rotated in equal angular steps (fig. 24). The three-dimensional image is then calculated from the projection images.

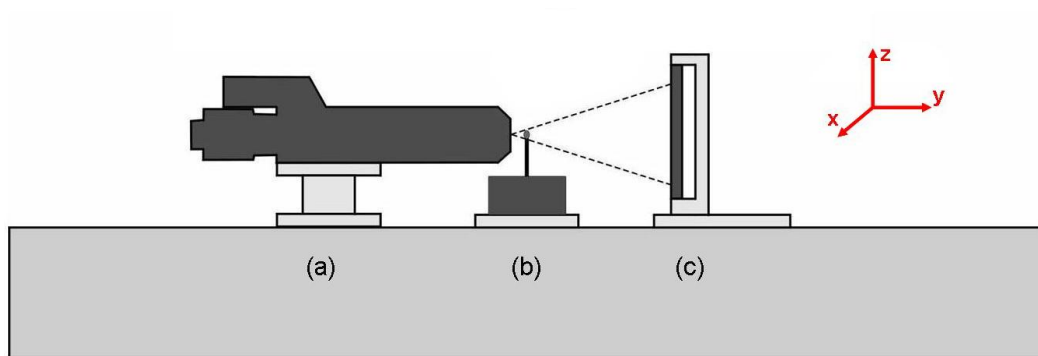


Figure 24: Initial configuration of a CT Scanner; (a) X-ray source, (b) rotary table for sample, (c) X-ray camera/detector (by Ian Butler).

Thus, the CT procedure comprises two key steps: First, acquiring a set of 2D projection images (in the x - z -plane) from different angles around a single axis (z) by a rotation of the object. Second, a mathematical reconstruction procedure to create a stack of cross-sectional images (in the x - y -plane) of the object (fig. 25).

The x - z -projections are a 2D distribution of line integral values which are corresponding to the total, i.e. accumulated, attenuation of X-rays as they

2.3 IMAGING EQUIPMENT

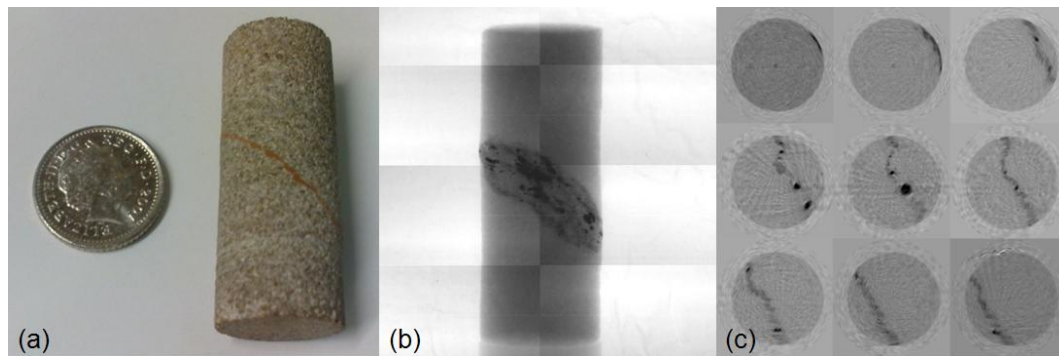


Figure 25: Typical radiograph and stack of cross sections (a) Indiana limestone sample containing an artificial fracture (diagonal to the core length) filled with lead oxide loaded epoxy particles (diameter 1.27cm). (b) Single 2D X-ray projection of the same sample (in the x - z -plane), (c) example images out of 900 of the stack of reconstructed tomographic cross-sections (in the x - y -plane) acquired from 50 projections from different angles.

propagate through the material (Radon transformations). One algorithm which is currently used in many applications to reconstruct the x - y -cross-sections is the *filtered backprojection (FBP)*. The idea is to separate the 2D distribution into a set of horizontal information (in x -direction) and then to "smear" the information again from the same angles as they were taken onto the x - y -cross-section plane (for a detailed description see Kak, 1999 [101], section 3.6).

Magnification of the image relative to the source is a geometric factor determined by the ratio of source-to-sample-distance versus source-to-detector-distance. Crucial for the quality of the results is the cross-sectional resolution and the magnification level. However, the final resolution depends on the detector and the number of exposure pixels, respectively. The quality of the data reconstructed from CT scans and the resolution which can be obtained depends on a number of factors. Ultimate image resolution is governed by both the X-ray source spot size and the detector properties.

The X-rays are generated in the source by the impact of an electron beam on a metal target. Both the electron beam and the subsequent X-ray generation volume are of finite size. Thus, any sharp edge in the sample will be imaged as unsharp at the detector plate and the unsharpness will be

2.3 IMAGING EQUIPMENT

directly related to the geometric magnification². The detector itself impacts image quality since the image is generated from a set of detector elements of finite size in the detector plate. Each resultant pixel is $x \times y$ micron and the whole image is built up from $n \times m$ such elements (1 micron = 1 μm). Because of this pixellation the image at the detector cannot be sampled to more than the corresponding resolution x , or y respectively, in this direction. The best resolution in the overall system results from matching image unsharpness from the source spot size to the detector pixel size (see e.g. Kak, 1999 [101]; Desrues et al., 2006 [54]). Although the source spot size and detector pixellation determine the ultimate resolution of the CT system, other factors, such as the X-ray scattering properties and density contrast range in the sample, also have practical impact. The art of CT experimentation is hence to balance the various factors to obtain the best possible experimental data from the system.

The basic quantity measured by CT is the *linear attenuation coefficient*, μ . It is used to quantify different media, according to the amount of extinction of the beam intensity. The attenuation is an exponential function of the path-length, which the beam has travelled through the medium. It is defined by the *Beer-Lambert-Law*

$$\frac{I}{I_0} = \exp\left(-\left(\frac{\mu}{\rho}\right)\rho x\right) = \exp(-\mu x) \quad (10)$$

I_0 is the incident beam intensity, I is the transmitted beam intensity remaining after passing the path length x in the material. ρ is the density of the material, and $\left(\frac{\mu}{\rho}\right)$ is the mass attenuation coefficient. The attenuation of the transmitted beam is caused by interaction of the X-ray photons (Compton effect, photoelectric effect, Rayleigh scattering) with the matter. For an overview of attenuation coefficients for different materials and energies see Wiedenbeck, 1962 [206] and McCrary et al., 1967 [132]. A higher energy corresponds to a lower attenuation coefficient, but the relation is non-linear.

In the literature, instead of the attenuation coefficient, the CT number on the *Hounsfield scale (HU)* is often applied. It is a normalised value of the

² For example, a one micron source spot size, used to image an edge on the sample magnified ten to one at the detector, will give an unsharpness in the image of ten microns, and this is the best resolution obtainable, whatever post-processing is used.

2.3 IMAGING EQUIPMENT

linear attenuation coefficient and is directly proportional to the density of the scanned object (Vinegar and Wellington, 1987 [196]).

The Beer-Lambert-Law assumes a couple of prerequisites, for example parallel rays for the incident radiation, a narrow X-ray beam, a monochromatic X-ray spectrum, etc. In reality, the emission curve of an X-ray tube consists of a polychromatic spectrum³. On the other hand, the energy spectrum defines the penetration level of the X-ray source. High-energy X-rays penetrate more effectively, whereas low-energy X-rays are absorbed completely. Therefore, the remaining beam at the outlet has a richer percentage of high-energy photons (hard X-rays). This effect is called *beam hardening* (see Kak, 1999 [101], section 4.1) and causes the average density to be interpreted lower (darker area). The effect occurs mostly in the center of the sample as the absorption corresponds to the thickness of the object. Additionally, artefacts like streaks appearing around objects with a higher density, and a variety of other artefacts, like ring artefacts or star artefacts, can occur (fig. 26). Most artefacts and noise can be avoided by using filters (for example inserting a lead or copper sheet between sample and detector to filter the low-energy X-rays to minimise beam hardening), or by application of correction algorithms after exposure (e.g. by simulation of streaks (De Man et al., 1999 [?]), or by advanced gain correction methods to remove beam hardening artefacts (Ketcham and Hanna, 2014 [112])). Both procedures can be quite time expensive. For an overview of artefact correction methods see e.g. Ketcham and Carlson, 2001 [111], and recent developments can be found in e.g. Desrues et al., 2006 [54]; proceedings of the ICTMS conference 2013, 2015 [89, 90].

³ X-rays are generated by accelerated electrons, released by a cathode in a vacuum tube, which are striking a target material (anode). Two effects occur: a) The electrons are scattered, they emit a continuous radiation, the so called *bremstrahlung*. b) Electrons with enough energy can shift an electron from a target atom of the anode to another orbit. A higher energy electron then swaps to the vacant place and emits an X-ray photon. This gives an additional material specific, discrete spectrum, the *characteristic lines*. The resulting wavelength of X-rays is in the range of 10^{-8} to 10^{-12} m, with anode specific spectral peaks, and photon energies from ca. 0.1keV up to the range of MeV.

2.3 IMAGING EQUIPMENT

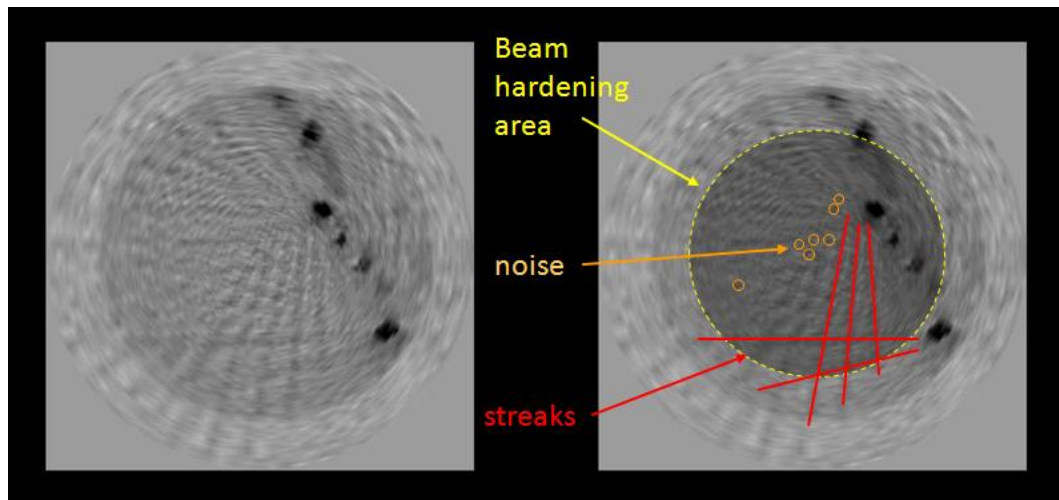


Figure 26: Reconstruction of an example object consisting of an Indiana limestone sample containing an artificial fracture (diagonal to the core length) filled with lead oxide loaded epoxy (fig. 25) acquired from 50 projections. Dark streaks are caused by beam hardening, which can also cause the outer areas to be brighter. Further streak (or star) artefacts can be caused by too little projections. The cause for ring artefacts lies usually in defect pixels at the detector which are then "reconstructed" over the whole cross-section (Kak, 1999 [101]).

2.3.2 CT scanner development

The CT scanner (see fig 27) at the Edinburgh Experimental Geoscience laboratories was built in-house from scratch, modelled after the design of the cone-beam scanner architecture of a microtomograph used at the Centre for X-ray Tomography of Ghent University, Belgium (UGCT). When I started my PhD, the scanner components had not been in use so far. My co-supervisors, Ian Butler and Stephen Elphick, planned and realised the technical installation of the separate components and the design of the mounting. My work included the installation and commissioning of the software programs provided with the equipment as well as the development of a control software (see 2.3.3) to synchronize the separate scanner parts. We then concentrated on the optimisation and standardisation of data collection and the design of single and multiphase coreflood experiments. The setup was implemented using commercial components in a full room installation which keeps costs minimal and design freedom maximal. The benefit of a full room installation comes from the extra thick and X-Ray adsorbing

2.3 IMAGING EQUIPMENT

walls of the laboratory originally designed to contain high pressure gas experiments. Many other laboratories use ready-made CT scanner systems (e. g., desktop systems) or medical CTs. While these tend to work out of the box, one key disadvantage is that they are less flexible with respect to experimental set-ups and tend to have a lower spatial image resolution. One of the key advantages of our custom-built system is that we can exchange the separate parts of the configuration or change their position, which allows us to use a wide range of imaging options. We can switch between a directional source (high brightness, good resolution of 3-300 μm) and a transmission source (low brightness, very high resolution of 0.9 μm) for small or low-density samples. The camera is a large area X-ray camera with a resolution of 2000 \times 2000 pixels, a 10-160keV sensitivity (matched to the sources) consisting of a panel of eight active-pixel CMOS photodiodes coupled with a scintillator (Graeve and Weckler, 2001 [79]). The instruments are placed on a granite surface table for shock resistant mounting. The reconstruction software is Octopus (Dierick et al., 2004 [58]), which is a scanner independent tomography reconstruction package, developed at the UGCT. Octopus covers the main reconstruction algorithm, as well as pre-processing steps like normalization, standard image corrections for noise and artefacts reduction, such as artefact from beam-hardening and ring-artefacts (Cnudde et al., 2006 [46]).

2.3.3 *CT Control Software Development*

In the initial research of this thesis I focussed on the design, implementation, and optimization of a new and precise remote control program to synchronize the rotating table movements and the image capturing by the camera which ensures an accurate data acquisition for 360 $^\circ$ images. Each piece of equipment was provided with its own standalone demonstration software. The X-ray source (fig. 27.a) is in constant operation during the whole experimental run. The rotary table (fig. 27.b) and the X-Ray camera (fig. 27.c) had to be synchronised to ensure accurate data acquisition for 360 $^\circ$ images. Therefore, I developed a parent automated control program with

2.3 IMAGING EQUIPMENT

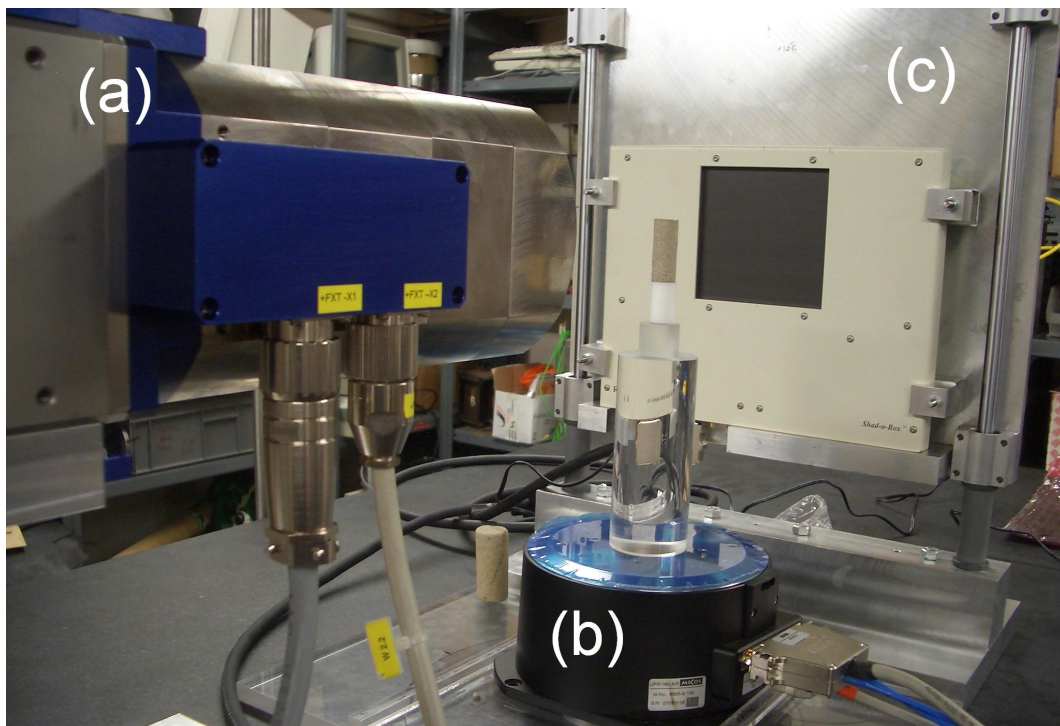


Figure 27: X-Ray CT scanner components: (a) X-ray source (Feinfocus dual head transmission/directional nano/microfocus tube), (b) Air-bearing rotary table (Micos UPR-160F SMC Pegasus with Taurus motion controller), (c) 4 MP Gadox X-ray camera (Rad-ikon Shad-o-Box) with vertical adjustable mounting.

2.3 IMAGING EQUIPMENT

the commercial software tool Testpoint⁴. The developed program operated the rotating table controller directly via the parallel port, the camera on the other hand was called via its software interface. Therefore, the overhead to produce one single projection was about 15sec. additional to the exposure time, during which the actual image is recorded by the camera. This overhead was in this case essential for the program to function in a stable fashion in the Windows environment using the Testpoint control. However, a new program was written for this study by me because this additional time is crucial for fast CT measurements, and to allow more scans being taken with each source filament – a high resolution 3D image acquisition can consist of more than 1000 projections for each complete 360° turn. To allow for a speedup, a new approach was to call the camera and frame grabber library directly via a newly designed C++ program, which could then be called from Testpoint. The external C++ program now consists of the following procedures:

- opening the frame grabber and camera library structures and providing the necessary object and pointer structure,
- reading an initialization file, which contains the exposure time, the image acquisition method, and the image file name - this file is created in Testpoint for each external program call and provides the communication interface between Testpoint and the C++ executable file,
- configuration of the frame grabber objects (initialization, camera configuration, buffer allocation, etc.),
- the actual image acquisition procedure, which consists of grabbing the image into the frame grabber object, image deinterlacing (accounts for the camera being built of eight different panels), a pixel map correction to eliminate factory-caused pixel defects, a bite-swap routine to change the image format for visualization (little-endian to big-endian),
- and saving the image to a file under a given name with a consecutive number.

⁴ Testpoint is a software development environment which can (inter alia) control other programs via their graphical user interface (GUI), execute C++ written programs, or call directly Dynamic Link Library (DLL) functions.

2.3 IMAGING EQUIPMENT

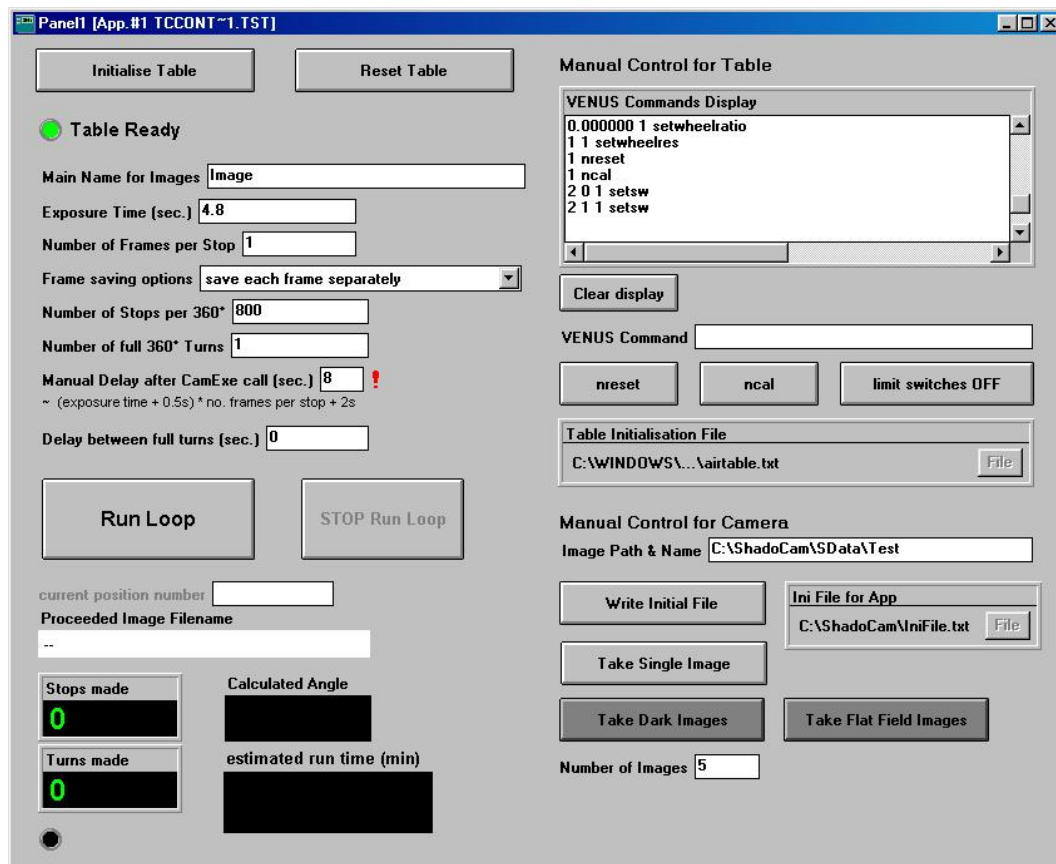


Figure 28: Graphical User Interface (GUI): The developed Testpoint front end provides a user friendly interface for the operation of the CT. It operates the camera and the rotating table in the background by calling the developed external C++ routine to control the camera, and piloting the hardware controller of the table via the parallel port.

With this new approach it was possible to reduce the overhead time to about 6sec., which was a great achievement considered the large number of projections required for high-resolution imaging. Another advantage was that the initial graphical user interface, which were developed for optimal user-friendliness (fig. 28), needed to be changed just slightly, as the table related parts could remain the same, and the former camera functionalities could be either reproduced or improved. The new hybrid C++/Testpoint program allows us now to control both instruments manually to obtain the samples in the required position and take single pictures. It also allows us to run a whole experimental loop of several 360° turns in an acceptable time (approximately 300 - 350 projections per hour) with a few prescribed values to define the amount of pictures taken, the stop positions

2.3 IMAGING EQUIPMENT

for the correct illumination angles, and pre-set time intervals. Additionally, I implemented the possibility to take several pictures at each stop position and accumulate them by addition or averaging to increase the information content at low X-Ray intensities and to reduce image noise. The complete program documentation can be found in the appendix A.3.

2.3.4 *Optimization of Data Collection*

2.3.4.1 *1st experiment: Indiana Limestone*

The first images that were recorded with the new software came from a dry, fractured Indiana limestone core. This image acquisition enabled the testing of the CT system. To enhance the contrast between rock matrix and void space, the fracture was filled with lead oxide loaded epoxy (see fig. 29). On the X-Ray projection (fig. 29.b), the fracture is clearly visible. The images were acquired with the transmission source with a power level of 115kV.

50 projections from different angles around the sample object were taken, additional to flat field and offset correction images, to reconstruct tomographic cross-sections (see fig. 30) with the commercial tomography reconstruction package Octopus. Fig. 31 shows some of the results after applying a rendering procedure to the volume data.

In these results, several artefacts caused by beam-hardening and image noise can be observed (streak and ring artefacts, seemingly less dense material in core center, scattered noise around the object). Given just 50 recorded projections, a very high density contrast, and since it was the very first scan carried out on the newly constructed instrument, the observed artefacts were not unexpected. To overcome these problems, experiments to optimise the data collection were carried out.

2.3.4.2 *X-ray CT imaging of Baker Dolomite and San Andreas carbonate*

To compare the CT response from carbonate samples that are used in the flow experiments, and to obtain datasets that enable the quantification of fracture topology and aperture, experiments were carried out to test the calibration and settings of the CT system (exposure times, hardware and software filters, etc.). For the data acquisition, the two core halves (fig.

2.3 IMAGING EQUIPMENT

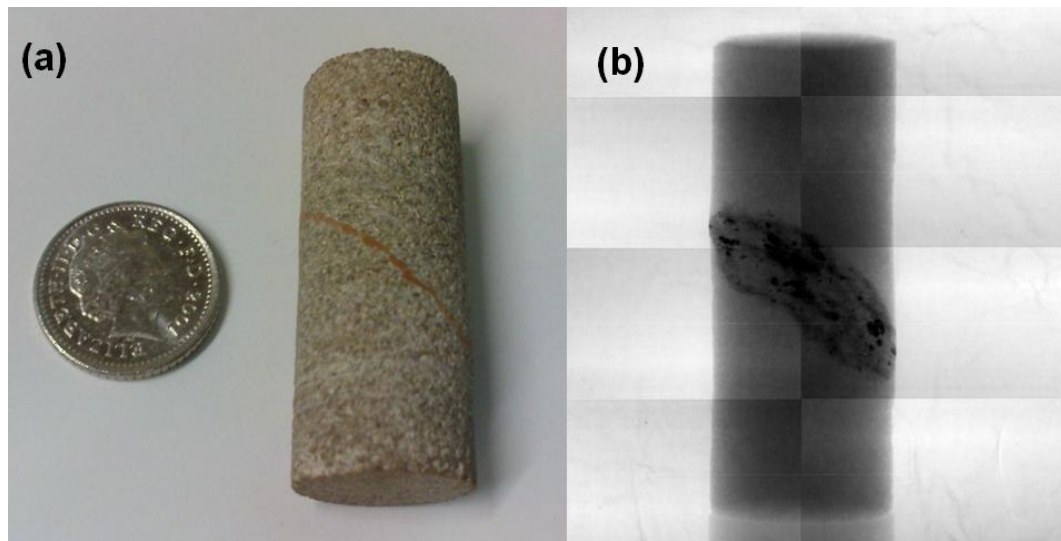


Figure 29: (a) Indiana limestone sample containing an artificial fracture (brown line in the centre of the core, diagonally to the core length), diameter 1.27cm. (b) Single 2D X-ray projection of the same sample. Dark areas mark a higher cumulative density as the X-rays are attenuated relating to the material density and the path length the X-rays travel through the sample object. The rectangular pattern across the image is caused by the camera consisting of an array of eight image sensors. Note that the example of a fractured Indiana Limestone is for illustration only - the location of the fracture is not suitable for flow experiments. A linear fracture through the center of a core plug had to be manufactured for the subsequent studies.

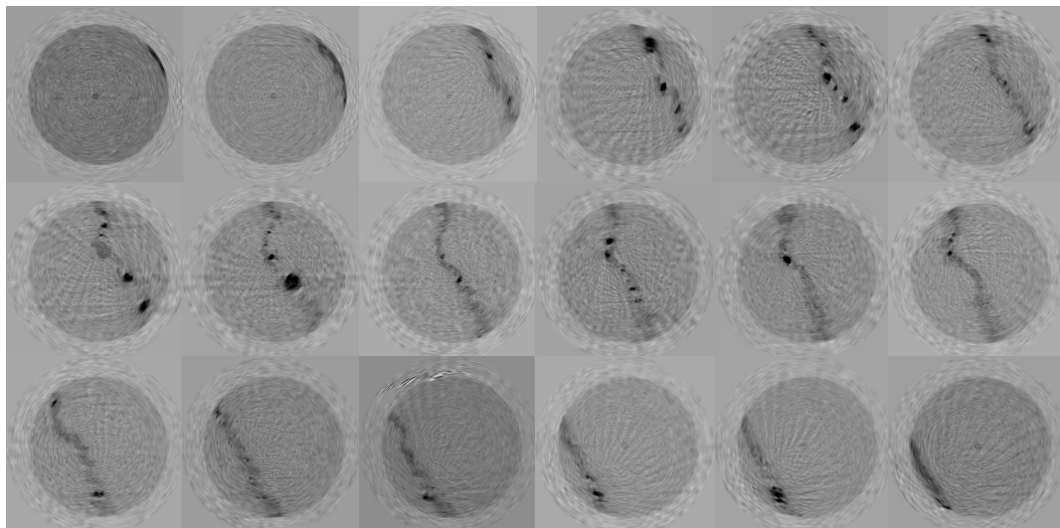


Figure 30: 18 example images out of 900 of the stack of reconstructed tomographic cross-sections acquired from 50 projections from different angles around the sample object in fig. 29. Each image corresponds to a slice of the object and to one pixel row on the detector. Realization with Octopus.

2.3 IMAGING EQUIPMENT

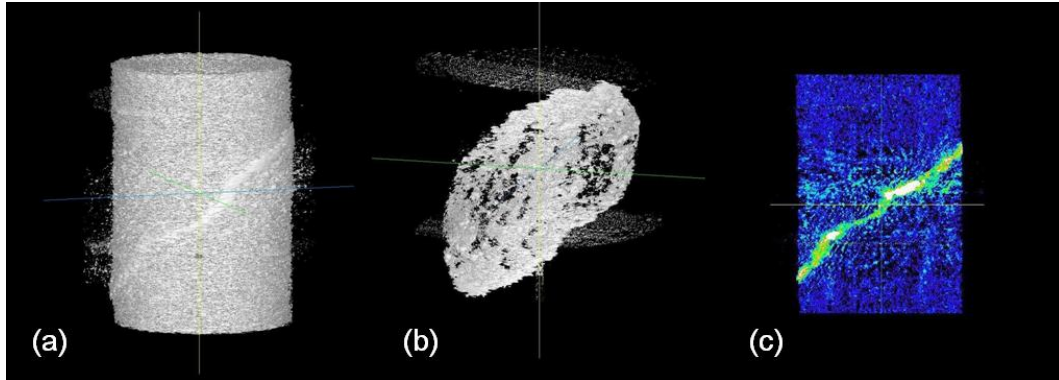


Figure 31: Rendered 3D computer model of the sample object in fig. 29 built from the stack of cross-sections from fig. 30. (a) Complete 3D model of the limestone core. The fracture is clearly recognizable diagonal to the core length. The scattered voxels around the object refer to "bad pixels" on the camera. (b) Visualization of only the lead-epoxy filled fracture by excision of brighter voxels referring to less dense material. (c) Cross-section in the x-plane through the 3D model. Dark blue color refers to less dense areas in the object, white areas mark high density. Any possible slicing and any data extraction depending on the gray value of the voxels can be realized. Rendering and visualization software: Octopus 3D Viewer.

22) were gapped out by about 1mm with melinex strips to increase the image contrast, and held together by elastic bands. The images were as well recorded with the transmission source, with an exposure time of 6.5sec. and a power level of 120kV. The voxel resolution is calculated to $(0.0236 \text{ mm})^3$.

The actual voxel resolution for the reconstructed volume from a CT scan can be derived by applying the interception theorem. It states that the ratio of the distance from source to camera, $a + b$, and the size of a pixel on the detector, p , is equal to the ratio of the distance between source and the rotation axis of the object, a , and the actual mapped sector of the object, d . (cf. fig. 32) The pixels on the detector are equally sized in horizontal and vertical direction. Therefore, the voxel resolution is

$$d = \frac{p \cdot a}{a + b} \quad (11)$$

for each spatial dimension.

On the reconstructed slices (fig. 33), beam hardening and noise artefacts are still clearly visible (e.g. due to beam hardening, the samples appear to be brighter towards the rim). The attempt to apply software corrections

2.3 IMAGING EQUIPMENT

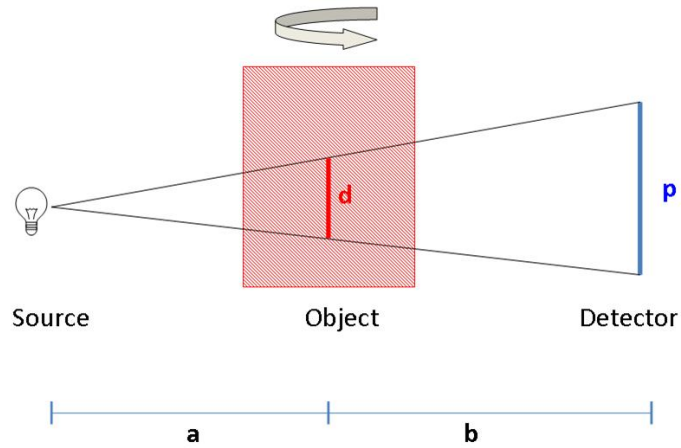


Figure 32: Schematic of CT scanner components to influence magnification.

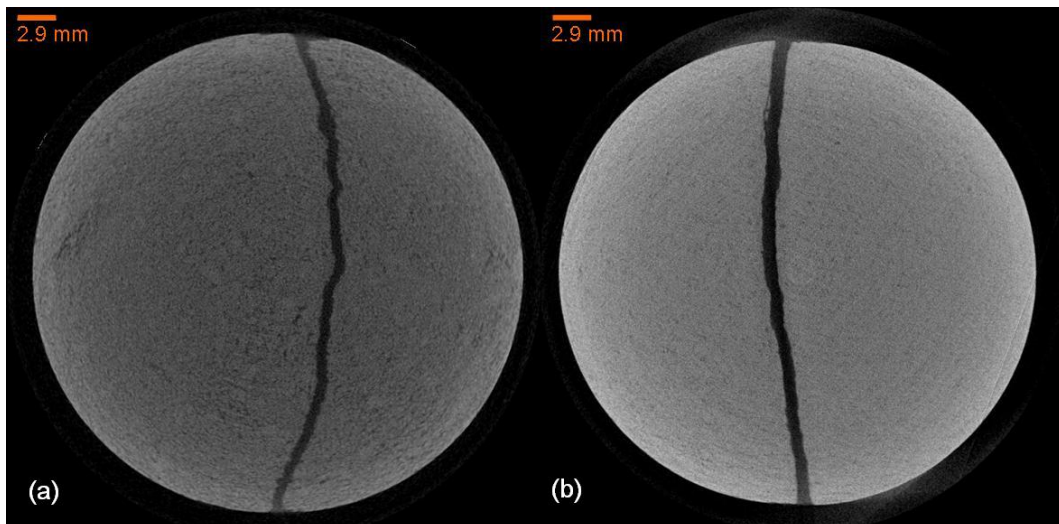


Figure 33: Reconstruction: Reconstructed tomographic cross-sections of the samples in fig. 22 (a) SAC acquired from 360 projections, (b) BD acquired from 700 projections. Due to beam hardening, the samples appear to be brighter towards the rim. Software: Octopus.

2.3 IMAGING EQUIPMENT

after the image acquisition during the reconstruction process with the provided features by Octopus (vertical smoothing, beam hardening correction, noise and ring filters) showed insufficient results. Therefore, the next steps comprised further studies to find optimal hardware filters (copper and lead in various thicknesses) to minimize beam hardening artefacts, further tests with software-based noise filters, and improved imaging techniques as for example image accumulation to average pixel failures.

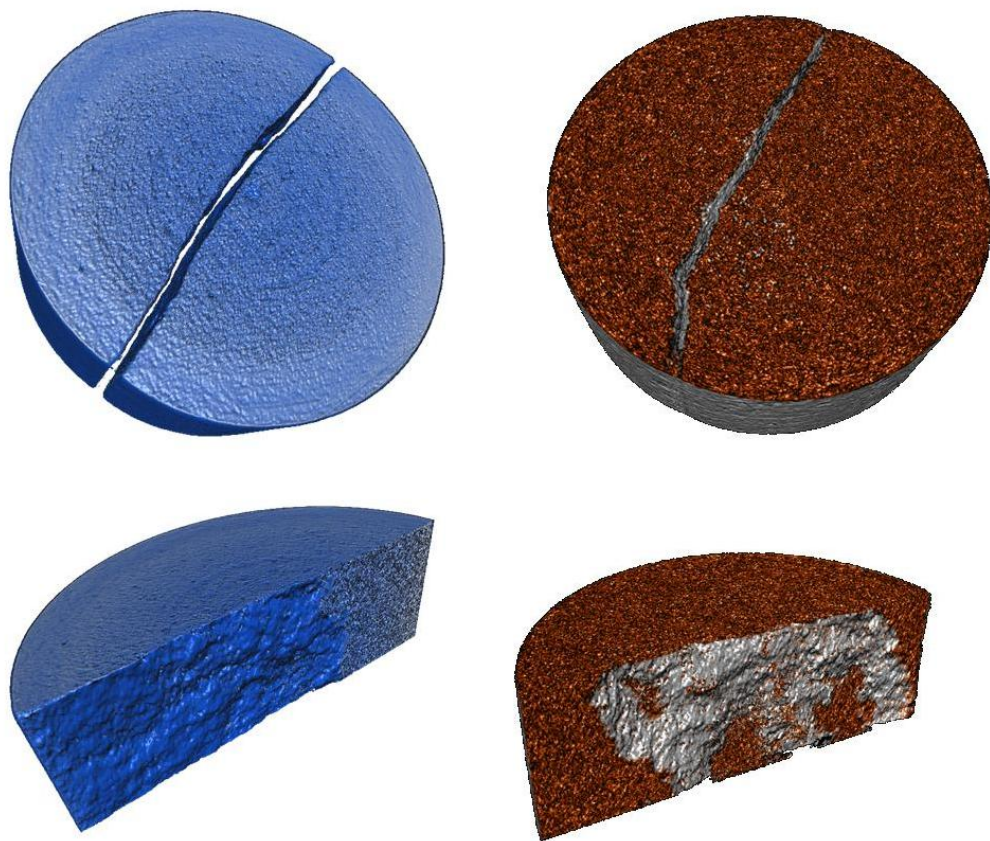


Figure 34: Rendered 3D computer model: Comparison of SAC (left, blue) and BD (right, red). Top: 3D visualisation of a slice of the reconstructed core. Bottom: Straight cut through the sample with the cutting plane along the fracture. Note that the finer grained material in the SAC is part of the matrix. The fracture is slightly curved (see fig. 33) and hence the straight cut-plane intersects fracture and matrix. Rendering and visualization software: ImageVis3D.

The samples needed to be scanned with a high dynamic range, as we are mainly interested in the (dark) fracture space. Therefore, the dense material surrounding the fracture needed to be bright enough. An exposure time of

2.4 IMAGE ARTEFACT CORRECTION

2sec. at 140kV tube voltage (target current $190\mu\text{A}$, target power 26.6W) was found to give the best results respective image contrast in the reconstructed images. Additionally, a copper filter of 1mm thickness was mounted in front of the camera to mostly remove the beam hardening artefact, which was due to the high energy level.

2.4 IMAGE ARTEFACT CORRECTION

After focusing on finding a good image contrast, the reconstruction procedure had to be optimized. It is common practise to correct the projection images with a *dark current (DC)* – or dark/offset – image and a *flat field (FF)* – or bright – image before the reconstruction. A DC image is recorded without operating X-ray source, a FF image is recorded with operating X-ray source at 100% imaging intensity, though without a sample in front of the camera (FF_{100}). The DC image then contains only information about possible noise originated in the detector itself. The FF image can correct for possible pixel failures and intensity deviation of the detector. Multiple DC and FF images can be averaged to increase the correction. The standard (linear) correction method is then to first subtract all radiographic projections by the (average) DC image, and then divide all projections by the (average) FF image. The images then have to be scaled back to the original value range.

$$x(i) = \frac{y(i) - DC(i)}{FF_{100}(i)} \overline{FF_{100}}, \quad (12)$$

where $x(i)$ is the resulting linear response in pixel i , $y(i)$ is the measured grey value in pixel i of original image, $DC(i)$ is the grey value in pixel i of dark current image, $FF_{100}(i)$ is the grey value in pixel i of flat field image at 100% intensity, and $\overline{FF_{100}}$ is the average value of all pixels in FF_{100} . This image normalization/correction procedure is implemented in Octopus.

However, this approach lead to an artefact that appears only on very dense materials close to the rotational axis of the sample. This artefact expressed itself in variations in grey values from top to bottom four times from white to black. This artefact could not be removed by any changes to the image acquisition, or the reconstruction procedure, respectively (fig. 35). The origin of this artefact was not described in the literature. The artefact

2.4 IMAGE ARTEFACT CORRECTION

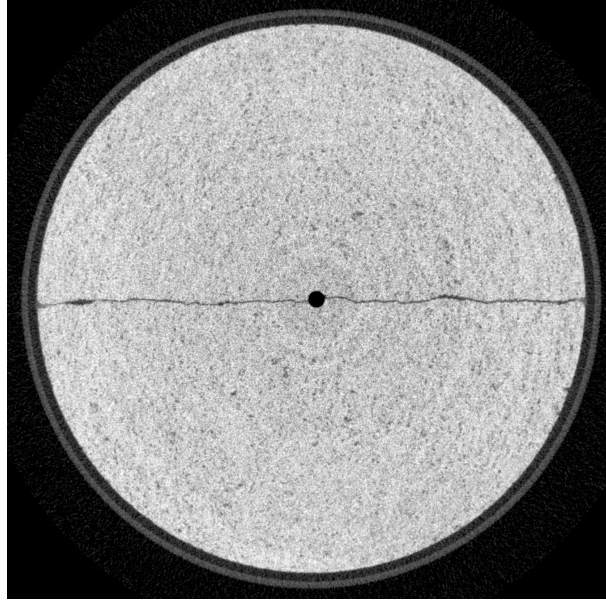


Figure 35: Reconstruction of a scanned BD sample which shows a significant spot artefact in the middle.

was intersecting the fracture in the core samples in some regions, which created a high inaccuracy in the measurements and therefore made the images partially useless for subsequent image analysis to compute fracture aperture distributions. Three root causes for this artefact were identified: (a) the pattern structure of the camera, (b) the non-linear, non-logarithmic response from the CMOS sensors of the detector in very dark image areas, whose intensity is not necessarily consistent at adjacent sides from the diodes, and (c) the reconstruction algorithm of the Octopus software, which turns the interfering camera pattern into 3D circular spot patterns. The camera we use consists of a 2-by-4 array of CMOS photodiode panels (fig. 36). This pattern can be seen on the radiographic projections even after DC/FF correction (fig. 37).

To overcome this problem, a modified DC/FF correction was implemented, which takes the non-linearity of the detector into account (chapter 3). A generalized piecewise polynomial approach was used to fit the response curve of the camera. The inverse function of the approximation curve is then used to correct the images pixel-wise. This approach removes the spot artefact and several ring artefacts completely (fig. 38), and the fracture aperture could be measured with significantly higher accuracy.

2.4 IMAGE ARTEFACT CORRECTION

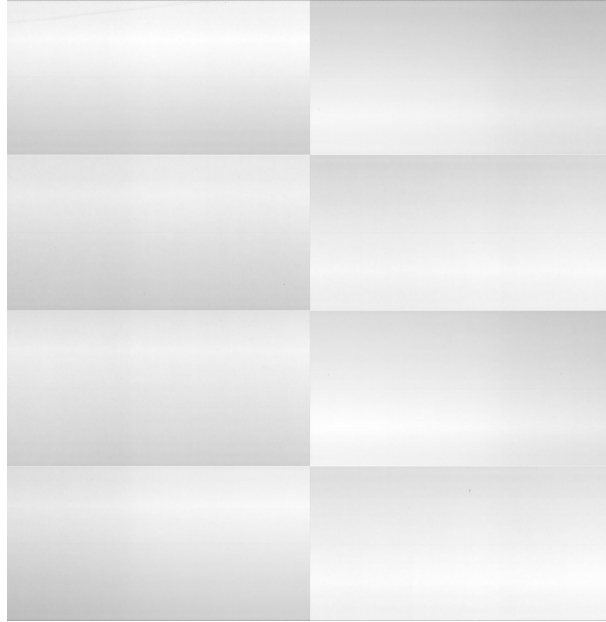


Figure 36: Flat-Field image of the camera showing 2-by-4 panel pattern. The camera consists of a 2-by-4 array of CMOS photodiode panels. A standard image normalization method cannot cancel this evolving pattern.

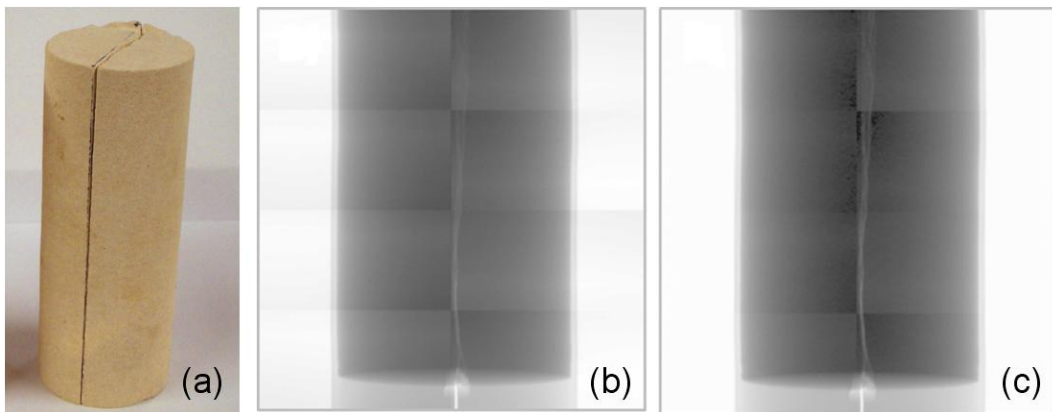


Figure 37: X-ray phantom image of the cylindrical carbonate core with a vertical fracture visible in the centre of the sample. (a) Carbonate sample \varnothing 3.81 cm with a single fracture; (b) Original radiographic image including the artefact that shows the 2-by-4 sensor panels clearly; (c) Standard linear corrected image that does not remove the artefact completely; (Images b and c are gamma corrected by 4.0 for the purpose of clarity. Camera: Shad-o-BoxTM 4K from Rad-icon Imaging Corp (now Teledyne Dalsa).

2.4 IMAGE ARTEFACT CORRECTION

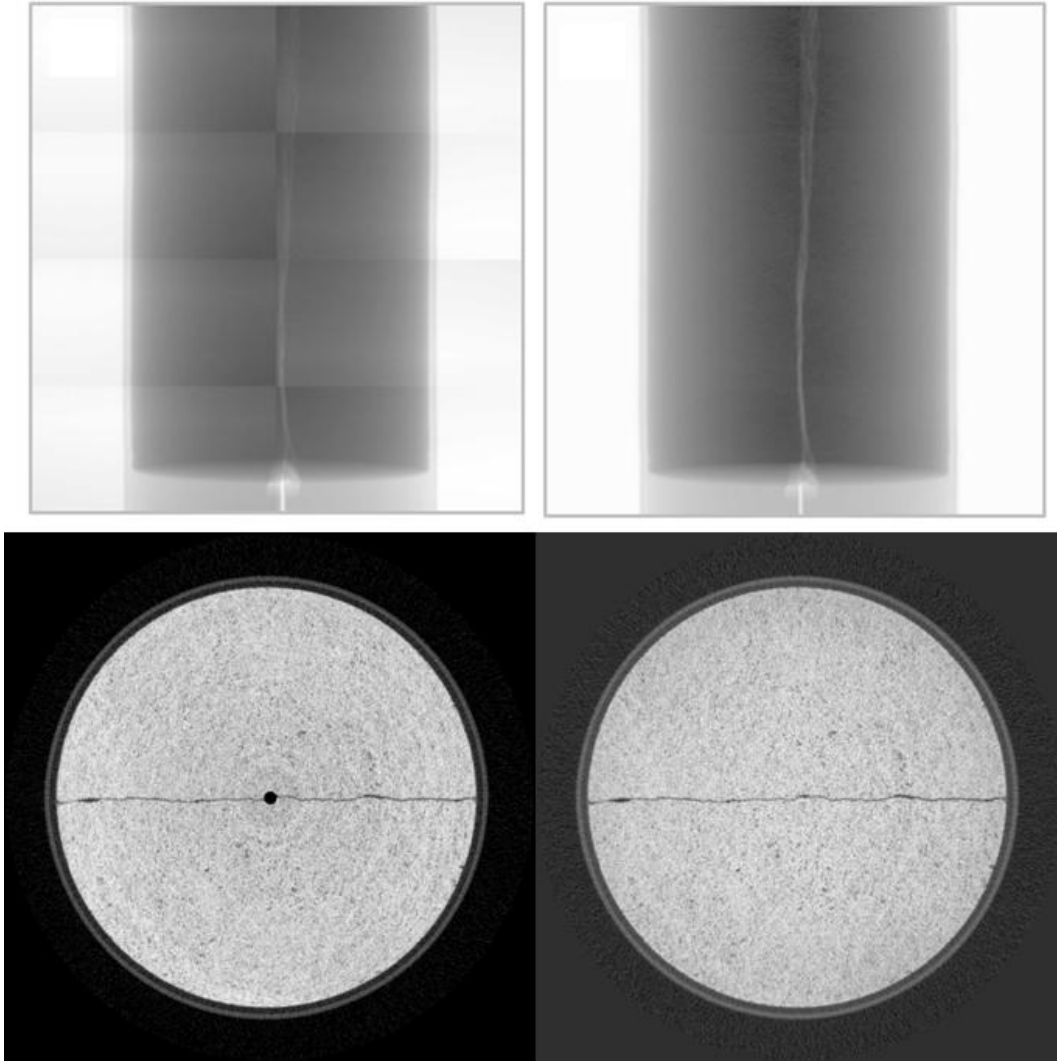


Figure 38: Top: Projection images (left) before and (right) after correction using the piecewise polynomial approach. Bottom: Reconstructed CT images for the (left) uncorrected and (right) corrected projections.

2.5 FRACTURE APERTURE MEASUREMENT

A detailed description of the developed image correction method can be found in chapter 3.

2.5 FRACTURE APERTURE MEASUREMENT

To obtain the best possible results in the subsequent simulations, the focus is on identifying the fracture boundary as accurate as possible, to be able to relate the aperture distribution to perturbations in the flow through the fracture. The fracture aperture distribution was then also used in the flow simulations, for which it had to be mapped onto a 2D plane (cf. Keller, 1998 [108]; Ketcham et al., 2010 [113]; Detwiler et al., 1999 [56]; Power and Durham, 1997 [164]). Because of the limited resolution of the detector, each voxel at a phase boundary can contain information of both adjoining phases, the solid and void phase. This effect is called partial volume effect. It is described in Keller, 1997 [109] and Ketcham and Carlson, 2001 [111]. To measure apertures on the grey values directly, several approaches exist. A simple threshold segmentation would measure the gap width in the profile at a certain height, depending on the threshold. The *peak height (PH)* is defined as the difference in the attenuation coefficient or grey values between the average value of the the fracture surrounding (porous) medium and the attenuation of the peak in the signal. The peak height though does not increase for wider fracture apertures. The *full width at half maximum (FWHM) method* measures across the gap at half the height of the peak height. Another approach is to integrate the signal profile for the whole peak area, the *missing attenuation (MA) area* (Ketcham et al., 2010 [113]; cf. fig. 39).

All these approaches need to be calibrated to measurements of known apertures with polished samples of the same rock types (Johns et al., 1993 [97]). They enable to measure the aperture more accurately than the voxel resolution allows alone, because one can relate the grey value directly to an aperture value as opposed to threshold methods. We combined the PH and the FWHM approach to measure the fracture apertures of the BD and SAC samples.

To facilitate the measurements, a combination of Avizo and Matlab was used, which gave a good collection of pre-implemented image processing

2.5 FRACTURE APERTURE MEASUREMENT

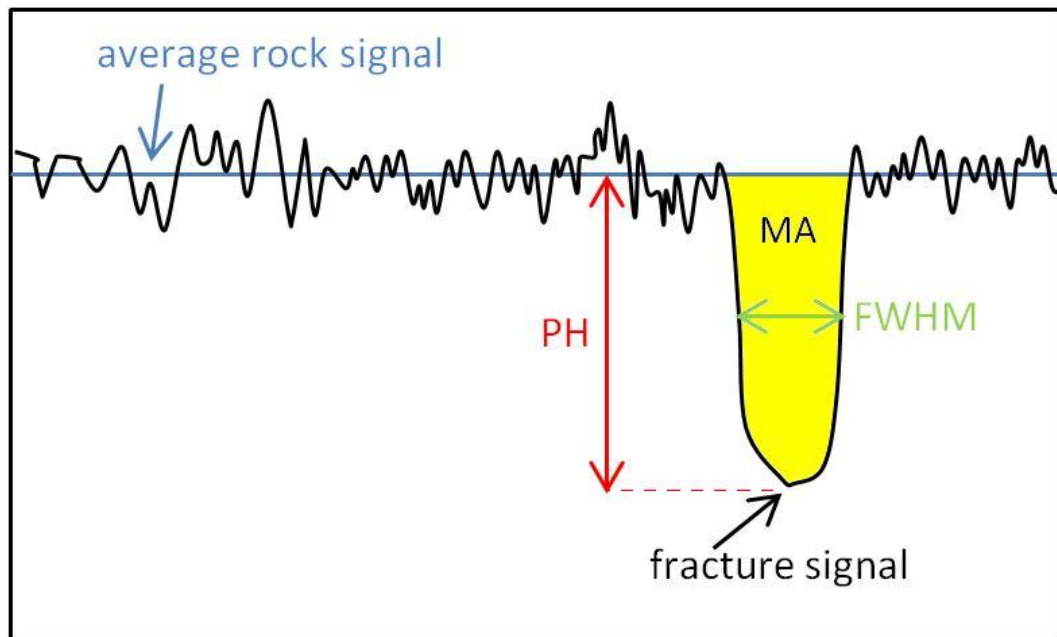


Figure 39: Sketch depicting the different methods to quantify fracture apertures; green: full width at half maximum (FWHM), red: peak height (PH), yellow: missing attenuation area (MA)

methods (volumetric and slicewise). Also, Avizo has a built-in interface to Matlab, which enables switching from one application to the other easily. An example of this processing workflow for a wider fracture in BD is shown in fig. 40.

Simulating fluid flow in the fractured core with the DFM model and the hybrid mesh approach requires a 2D representation of the fracture surface as point cloud with a coinciding aperture value at each 3D coordinate location. Gapping the fracture wide open is not a viable approach to measure the apertures. Instead, the apertures needed to be measured in situ in the flow cell at the apertures used in the subsequent flow experiments. For narrow fractures, a simple segmentation algorithm leads to erroneous results, as the smallest resolvable aperture is limited by the voxel size, and larger apertures are also only measurable in discrete steps of the voxel size. The fracture apertures in the flow cell though are significantly smaller than the voxel size of $\sim 0.025\text{mm}$. Additionally, contact areas in the fracture are highly overestimated.

Due to the partial volume effect occurring at this scale at the fracture boundaries, the approach of Johns et al., 1993 [97] to measure the fracture

2.5 FRACTURE APERTURE MEASUREMENT

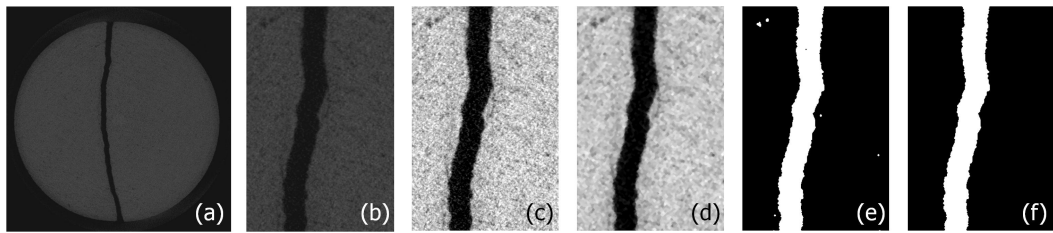


Figure 40: Image Processing Sequence. For a quantitative analysis of the fracture geometry and volume extraction an accurate image segmentation algorithm is crucial. To simplify matters, the two core halves of the BD sample (fig. 33(b)) were gapped out by about 1-2 mm to increase the image contrast. 700 projections were recorded, reconstructed, and segmented to obtain a 3D fracture volume (see fig. 41). (a) Original reconstructed slice, (b) cropped area of (a), (c) histogram based contrast enhancement, (d) application of Median filter (3×3 neighborhood, 10 iterations), (e) binarization with a global threshold, (f) concluding automated cavity removal. A slice-wise treatment of the measured volume was possible due to its clear-cut feature geometry. The sequence works well with this data set as it preserves the fracture roughness well enough while pore and noise information is discarded. For finer fractures and multi-phase images advanced volumetric image processing algorithms are necessary. Realization with Matlab Image Processing Toolbox.

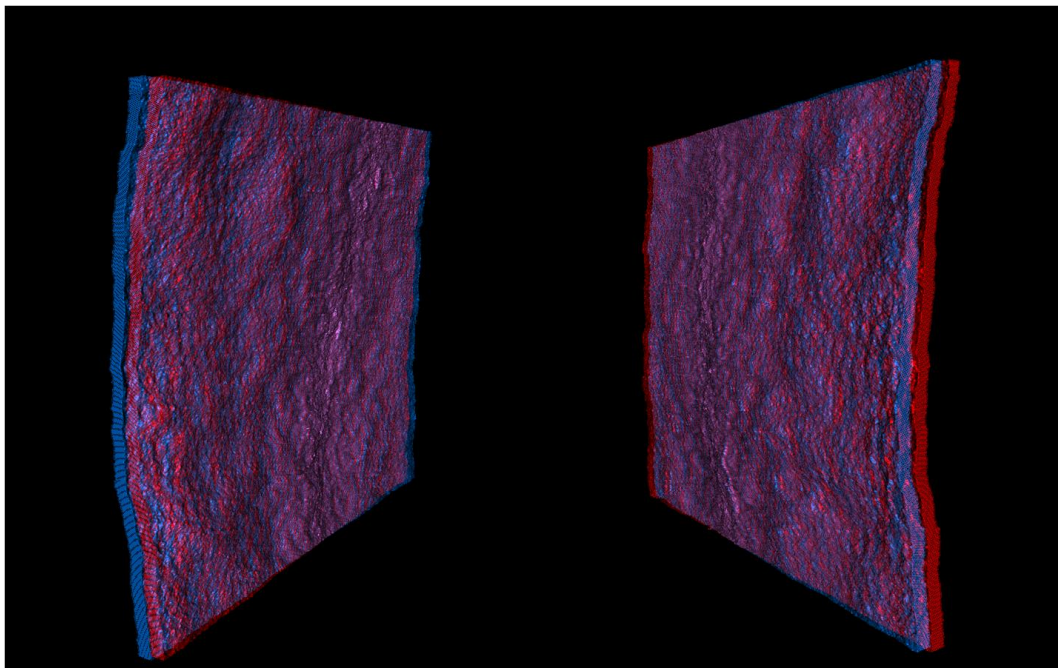


Figure 41: Stereographic 3D Representation of Fracture Volume. Segmented fracture volume of the BD sample (fig. 33(b)) from front and back view, which was implemented in the conceptual flow simulation study (see section 2.7). (Please use red-cyan 3D glasses.) Realization with ImageVis3D.

2.5 FRACTURE APERTURE MEASUREMENT

apertures by applying the peak height (PH) and full width at half maximum (FWHM) approaches and relate them to calibration measurements was followed. Both approaches are not fully able to represent fracture apertures in heterogeneous materials (Ketcham et al., 2010 [113]), but as we are studying mineralogically homogeneous carbonates, the PH and FWHM method, respectively, are valid, and an average rock grey value can be defined. Also, noise and superimposed pores are assumed to be distributed homogeneously in the samples, therefore the average rock grey value takes noise and pores into account.

First, calibration standards of San Andreas carbonate and Baker dolomite were employed, respectively, which were slit and grounded, as suggested by Johns et al., 1993 [97]. These measurement standards were gapped out with melinex strips of different thicknesses, and scanned at the same scanner settings as the original BD and SAC samples. This data was then measured with both, PH and FWHM, methods.

To recount, the low-resolution method (FWHM) measures the width of the fracture at each point, the high-resolution method (PH) uses the grey value of the pixels in the fracture as a reference to estimate the fraction of air/rock in each pixel. The PH method herewith can only measure apertures, where the peak is lower than the grey value for air. From the calibration measurements, the interval in which the PH method is valid is determined by finding the shim size, above which the PH measured aperture does not increase any more. Two calibration curves, one for each measurement method, are calculated – a log function for the PH method, as the PH method is based on the Beer-Lambert law, and a linear function for the FWHM method. The grey value at a fracture location can then be either related directly to an aperture by the PH method, if the grey value is in the PH range, or the aperture is larger, then the FWHM method is applied (details and images see chapter 4). Also, as the rock cores did not fit completely in front of the camera, the top and the bottom part were scanned separately. A rectangular copper marker was attached at the side of the cores to be able to manually align both datasets afterwards in Avizo. The top and bottom datasets were then merged into a single dataset. Each combined dataset is about 3.5GB large. Both datasets were corrected with the advanced gain correction method as described in chapter 3). To

2.6 NUMERICAL FLOW MODELLING

reduce noise, a Gaussian filter was applied to the images with Avizo. Then, the *ridgeline function* implemented in Avizo was employed to detect the 3D fracture position in each slice. This function is basically a path search algorithm, which tries to find a path from the left side to the right side of the image along the darkest pixels. By this algorithm a 3D point cloud with the fracture locations was obtained. With this combination of methods a point cloud which represents the fracture topology and can be implemented in the DFM simulations, and to measure the fracture apertures at each location below the image resolution was acquired. The resulting fracture aperture distributions are shown in fig. 42.

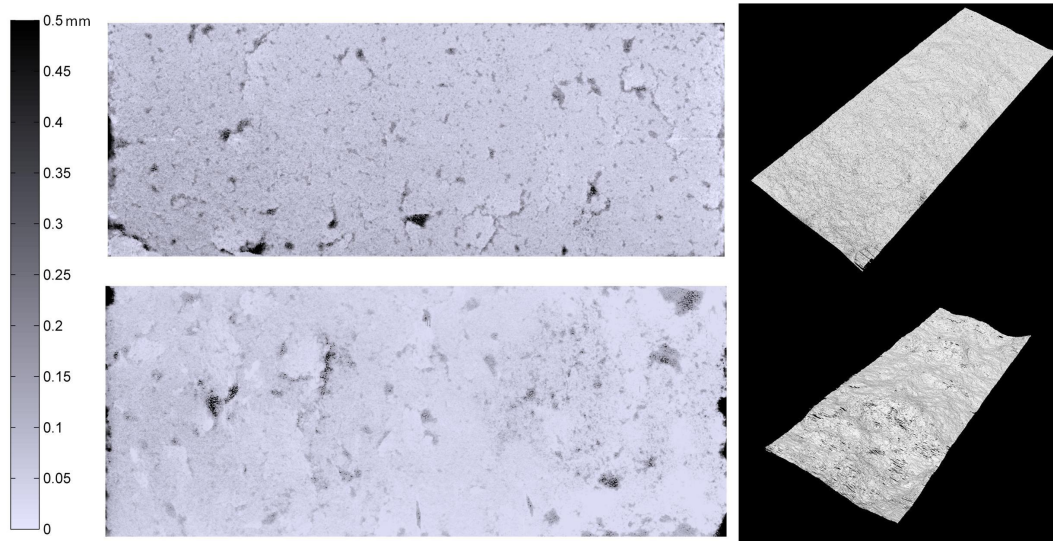


Figure 42: Visual representation of the fracture aperture distributions [mm] (left) and topology (right). Top: Baker Dolomite, Bottom: San Andreas Carbonate (see fig. 22). Voxel resolution $23.6\mu\text{m}$. Dimension of the fractures is 3.8 by ~ 10 cm.

2.6 NUMERICAL FLOW MODELLING

As geometrical input for 3D DFM flow simulations, a finite element mesh is needed, where the fracture is represented by 2D elements (triangles) embedded in the core represented by 3D elements (tetrahedra), or a planar 2D mesh with triangular elements representing the fracture only. An aperture is assigned to each 2D fracture element from which an effective permeability is calculated by the cubic law (CL) (eq. (5)). The fracture elements resolve

2.6 NUMERICAL FLOW MODELLING

the fracture with a smaller resolution, than the fracture apertures were measured, therefore the apertures in the triangular fracture elements are calculated by averaging the apertures inside each element. Several averaging approaches are investigated.

To start with generating a 3D mesh with embedded 2D fracture, the measurements with MATLAB give the apertures at each x - y - z -location in the fracture. The CAD software Rhinoceros 4.0 is employed to generate a geometric surface from the x - y - z -locations. As the finite element mesh is coarser and smoother than the measured fracture due to upscaling, and as the measured point cloud is very dense, we only use each 4th point to create the surface topology in Rhinoceros. After creating the fracture surface from the point cloud, we fit a cylinder around the surface, so that the fracture is located along the cylinder length, and the fracture surface and the core have a continuous intersection line (see fig. 43). The intersection lines at the cylinder top and bottom hereby represent the inlet and outlet for the subsequent fluid flow simulations. The obtained geometry is imported

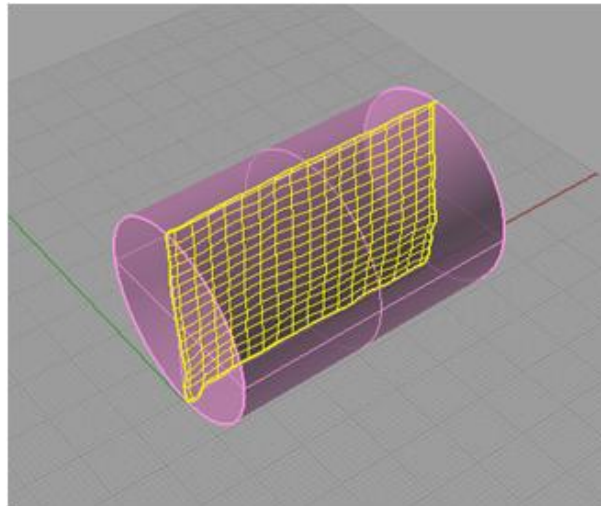


Figure 43: Geometric representation of a 2D fracture embedded in a 3D cylindrical rock core with Rhinoceros 4.0.

into Ansys ICEM 11.0, where we are able to parametrically generate an unstructured mixed-dimensional mesh. The fracture surface is triangulated by 2D elements and is represented as internal surface, i.e. the fracture elements are preserved in the final mesh. The cylindrical core (i.e. the rock matrix) is represented by tetrahedral 3D elements (see fig. 44).

2.6 NUMERICAL FLOW MODELLING

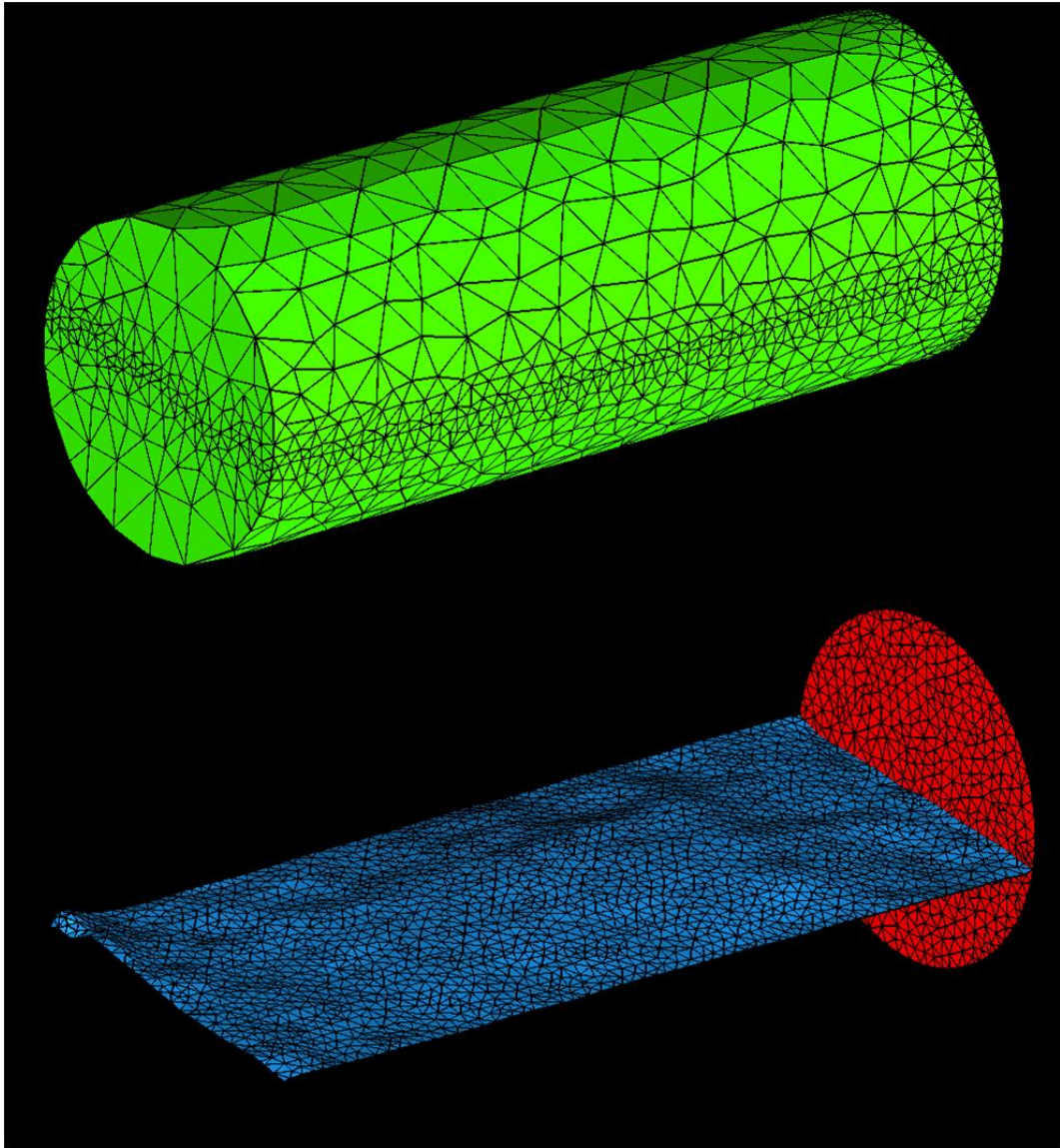


Figure 44: Generated example mesh with about 10000 finite elements, where the fracture contains about 4000 2D finite elements. Software Ansys ICEM.

2.7 SIMULATIONS

The local aperture for each fracture element is assigned after the mesh has been read into CSMP++. This then allows for the calculation of the local fracture permeability.

Note that, as noted above, for computational reasons it is not possible to assign as much fracture elements in the simulation grid as there are fracture aperture measurements. Hence the fracture apertures measured using X-Ray CT are averaged such that each fracture element contains the average fracture aperture of all local measurements that correspond to a given element (see fig. 45 for further details). These calculations are performed in Matlab. In a similar way, 2D planar fracture meshes were created by setting the z-components of the points in the point cloud to zero.

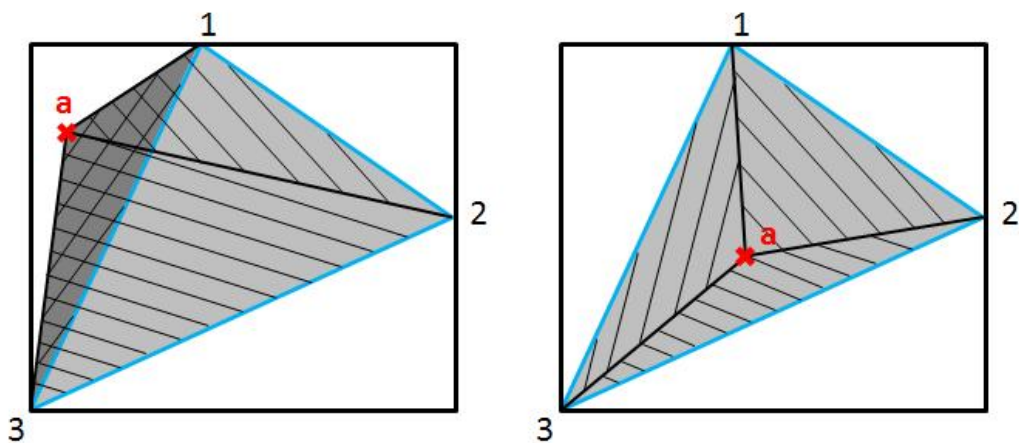


Figure 45: Sketch depicting the test for a measurement point being inside a finite element. Left: Point with aperture measurement (red) outside finite element (blue). The area of the triangles 1-2-a, 2-3-a, 1-3-a sums up to a larger area than the area of the finite element 1-2-3. Right: Point with aperture (red) inside finite element (blue). The area of the triangles 1-2-a, 2-3-a, 1-3-a sums up to the same area as of the finite element 1-2-3.

2.7 SIMULATIONS

This subsection reviews the governing equations for the simulations carried out in this thesis. Although some initial simulations were tested on a full 3D geometry, due to time constraints the key simulations were carried out on a 2D fracture model. They are presented in chapter 6.

2.7 SIMULATIONS

2.7.1 Governing Equations for Single-Phase Flow

As the first experiments were carried out at standard conditions using distilled water containing a tracer that did not affect fluid properties, it is possible to carry out simulations assuming incompressible and isothermal single-phase flow with constant fluid properties. To calculate the pressure field p , the static pressure diffusion equation is solved

$$0 = \nabla \cdot \left(\frac{\mathbf{k}}{\mu} \nabla p \right) + S, \quad (13)$$

where \mathbf{k} is the permeability tensor, and μ the fluid viscosity. The volumetric source term S models the rate of the injected fluid. The corresponding velocity field is then computed in a post-processing step using Darcy's law

$$\mathbf{v} = -\frac{\mathbf{k}}{\mu} \nabla p. \quad (14)$$

To calculate the single-phase tracer transport, the advection dispersion equation for the concentration of the tracer c is solved

$$\phi \frac{dc}{dt} = \text{div}(\mathbf{D} \nabla c) - \text{div}(c \mathbf{v}) + S, \quad (15)$$

with \mathbf{v} is the velocity vector from the steady state diffusion equation (13). $\text{div}(\mathbf{D} \nabla c)$ controls the dispersion, and $-\text{div}(c \mathbf{v})$ the advection part of the fluid motion. \mathbf{D} is the dispersion tensor given by

$$\mathbf{D} = D_p \mathbf{I} + (a_L - a_T) \frac{\mathbf{v}_x \mathbf{v}_z}{|\mathbf{v}|} + a_T |\mathbf{v}| \mathbf{I}, \quad (16)$$

where D_p is the porous-medium diffusivity, a_L and a_T are the longitudinal and transversal dispersivities, respectively, and \mathbf{I} is the identity matrix.

2.7.2 Numerical Formulation

2.7.2.1 Operator Splitting – FEFV combination

The governing equations have mixed elliptic (diffusive) and hyperbolic (advective) character. We use a combination of higher-order FEFV meth-

2.7 SIMULATIONS

ods, similar to Geiger et al., 2006 [73]. The described decoupling in the FEFV method is similar to the implicit pressure explicit saturation (IMPES) approach for modelling immiscible and incompressible two-phase flow (Aziz and Settari, 1979 [9]). In the IMPES method it is allowed to solve the governing equations separately because pressure diffuses faster than concentration advects through the computational domain. Hence, equation (13) and (15) operate on different timescales. Therefore it is possible to solve the pressure equation from the concentration equations separately from each other (Geiger et al., 2006 [73]). Altogether, the hyperbolic sub-equations are then solved by the FV method by surface integration of the flux term over an area A , e.g.

$$\int_A \mathbf{n} \cdot \left[\frac{k}{\mu} \nabla p \right] dA, \quad (17)$$

where \mathbf{n} is the outward-pointing normal of A . The elliptic sub-equations are solved using the FE method by volume integration of the flux term over a volume V , e.g.

$$\int_V [\text{div} \mathbf{D} \nabla c] dV. \quad (18)$$

Further, equation (15) can be split as well into a hyperbolic advection equation and a elliptic diffusion equation by operator splitting (Strangm 1968 [185]). Equation (15) is treated as follows: A partial solution $\hat{c}^{t+\Delta t}$ for the diffusion part $\nabla \cdot (\mathbf{D} \nabla c)$ is obtained by FE methods by solving

$$\phi \frac{\hat{c}^{t+\Delta t} - c^t}{\Delta t} = \nabla \cdot (\mathbf{D} \nabla c^t) + S. \quad (19)$$

The result $\hat{c}^{t+\Delta t}$ is then used to solve the advection part $\nabla \cdot (c \mathbf{v})$ of equation (15) using a FV method

$$\phi \frac{c^{t+\Delta t} - \hat{c}^{t+\Delta t}}{\Delta t} = -\nabla \cdot (\mathbf{v} \hat{c}^{t+\Delta t}). \quad (20)$$

By this we arrive at the final solution $c^{t+\Delta t}$ at time $t + \Delta t$.

The fluid velocities are then calculated from Darcy's law (eq. (14)). Then the advection-diffusion equation for concentration is solved.

2.7 SIMULATIONS

2.7.2.2 Spatial Discretization

The computational domain Ω is divided into two sub-domains, the matrix domain Ω_m and the fracture domain Ω_f . Ω_m is discretised in space using tetrahedral elements for 3D models and triangular elements for 2D models. Ω_f is discretised with one dimension lower elements (fig. 11), that is as triangular elements for 3D models, and as line elements for 2D models. As fractures are represented by lower-dimensional elements, the fracture aperture a , needs to be accounted for when integrating the pressure and concentration equations.

$$\int_{\Omega} X \, dX = \int_{\Omega_m} X \, dX + a \cdot \int_{\Omega_f} X \, dX, \quad (21)$$

where X is the unknown variable p or c . The discretisation of Ω comprises the finite element grid and the complementary finite volume grid. Node-centered finite volumes are constructed on the basis of the finite elements. For this, the centroids of the finite elements are connected with their side-midpoints (fig. 10). This divides the finite element into sectors and by this forms a dual finite volume grid. The nodes of the finite elements correspond thus directly with the nodes of the finite volumes. The permeability and porosity (k , ϕ) are assigned to the FEs and are constant on the FE. Other values such as p and μ are assigned to the FV and are assumed to be constant across the FV. If needed, they can be interpolated though across the FE.

2.7.2.3 Finite Element Method

The pressure equation (13) and the parabolic components of the concentration equation (15) are solved by the Bubnov-Galerkin approach (Geiger et al., 2006 [73]). The computational domain is discretised into a set of finite elements spanning the finite element space \mathcal{V} of continuous linear polynomial functions. \mathcal{V} is comprised of n Lagrange points $\mathcal{N} = \{\mathbf{x}_i\}_{i=1}^n$ and a set of basis functions $\{\Phi(\mathbf{x})\}_{i=1}^n$. The basis functions Φ can be used to approximate equation (19) for a fixed time t . For this, a set of functions

2.7 SIMULATIONS

$c \in \mathcal{V}$ is defined as $c(\mathbf{x}) = \sum_{j=1}^n c_j \Phi_j(\mathbf{x})$. Then from equation (19) follows

$$\int_{\Omega} \phi \frac{\partial c}{\partial t} \Phi_i \, d\mathbf{x} = \int_{\Omega} \mathbf{D} \nabla c \nabla \Phi_i \, d\mathbf{x} + \int_{\Omega} S \Phi_i \, d\mathbf{x} \quad (22)$$

With the decomposition $c(\mathbf{x}, t) = \sum_{j=1}^n c_j(t) \Phi_j(\mathbf{x})$, the coupled system of ordinary differential equations is defined as

$$\sum_{j=1}^n \frac{dc_j}{dt}(t) \mathbf{A}_{ij}(t) = \sum_{j=1}^n c_j(t) \mathbf{K}_{ij}(t) + s_i(t), \quad (23)$$

where the mass matrix \mathbf{A} , stiffness matrix \mathbf{K} , and the right-hand side vector \mathbf{s} are given by

$$\begin{aligned} \mathbf{A}_{ij}(t) &= \int_{\Omega} \phi \Phi_j \Phi_i \, d\mathbf{x}, \\ \mathbf{K}_{ij}(t) &= \int_{\Omega} \nabla \Phi_j \mathbf{D} \nabla \Phi_i \, d\mathbf{x}, \\ \mathbf{s}_i(t) &= \int_{\Omega} S \Phi_i \, d\mathbf{x}. \end{aligned} \quad (24)$$

An implicit Euler time-stepping formulation is used to get from time t to $t + \Delta t$:

$$\sum_{j=1}^n \left(\mathbf{A}_{ij}^{t+\Delta t} + \Delta t \mathbf{K}_{ij}^{t+\Delta t} \right) c_j^{t+\Delta t} = \sum_{j=1}^n \mathbf{A}_{ij}^t c_j^t + \Delta t \mathbf{s}_i^{t+\Delta t}. \quad (25)$$

The fluid velocities are then constant for each finite element, and thus discontinuous between adjacent finite elements. They are though continuous across the face of a node-centered finite volume and conserve mass on the finite volumes (Durlofsky, 1994 [61]).

2.7.2.4 Finite Volume Method

Integration of equation (20) over the finite volume V_i with node i yields

$$\int_{V_i} \phi_i \frac{\partial c}{\partial t} \, dV_i = - \int_{V_i} \nabla \cdot (\mathbf{v}c) \, dV_i \quad (26)$$

2.7 SIMULATIONS

The divergence theorem is applied and an explicit Euler formulation is used to discretize in time

$$c_i^{t+\Delta t} = \hat{c}_i^{t+\Delta t} - \frac{\Delta t}{\phi_i |V_i|} \sum_i^{N_i} \left[A_j \mathbf{v}_j^t \hat{c}_{j^*}^{t+\Delta t} \right] \cdot \mathbf{n}_j, \quad (27)$$

where A_j is the area (or length in 2D) of the finite volume segment j . $|V_i|$ is the volume (or area in 2D) of control-volume i . \mathbf{n}_j is the outward-pointing normal of segment j . N_i is the total number of segments belonging to finite volume i . The subscript j^* denotes that the value of c is taken from the upwind finite volume at segment j . This leads to a second order accurate solution of equation (20) in space and resolves shock-fronts occurring in hyperbolic systems in great detail while maintaining mass conservation for nonlinear systems (Geiger et al., 2004 [77]).

2.7.3 Example simulation of 2D tracer transport

To prove the DFM model implemented in CSMP++ being able to result in the expected complex flow patterns, we compare the effect a non-uniform fracture aperture distribution has on fluid flow with a model where an effective fracture permeability was computed, and calculate a single-phase flow simulation modelling the advance of a tracer inside the planar fracture.

We generated a two-dimensional fracture geometry with a statistically generated aperture distribution (see fig. 46). The statistical fracture data was taken from Piri and Karpyn, 2007 [161]. The aperture distribution was generated with a *random field generator* building a spatially correlated random aperture field using an indicator kriging approach (Lord et al., 2014 [122]). According to the afore mentioned cubic law (CL) (5), a permeability distribution was then derived from the aperture distribution. The resulting permeability field provided the basis for the simulations with CSMP++ (see fig. 47).

To see if the results are in agreement, we compare the breakthrough curves, measured at the model outlet, for the two different cases (Fig. 48). The effective permeability was computed using the following approaches:

- Figure (48 a):

2.7 SIMULATIONS

- (1) the permeability is a direct function of the aperture by applying the cubic law locally, i.e. $k(a(x)) = a(x)^2/12$
- (2) a uniform upscaled permeability k depending on the flow rate q from inverting Darcy's Law, i.e. $k_{up} = q \cdot \mu \frac{\Delta L}{\Delta p}$
- (3) a uniform permeability from the mean aperture of the statistic distribution in (1), i.e. $k_{av} = k(\bar{a})$

- Figure (48 b):

Further improvement of the fit of the breakthrough curves can be obtained using the dispersion tensor

$$\mathbf{D}_i = D_{pi}\mathbf{I} + (\alpha_L - \alpha_T) \frac{\mathbf{v}_i \mathbf{v}_i^T}{|\mathbf{v}_i|} + \alpha_T |\mathbf{v}_i| \mathbf{I}.$$

2.7 SIMULATIONS

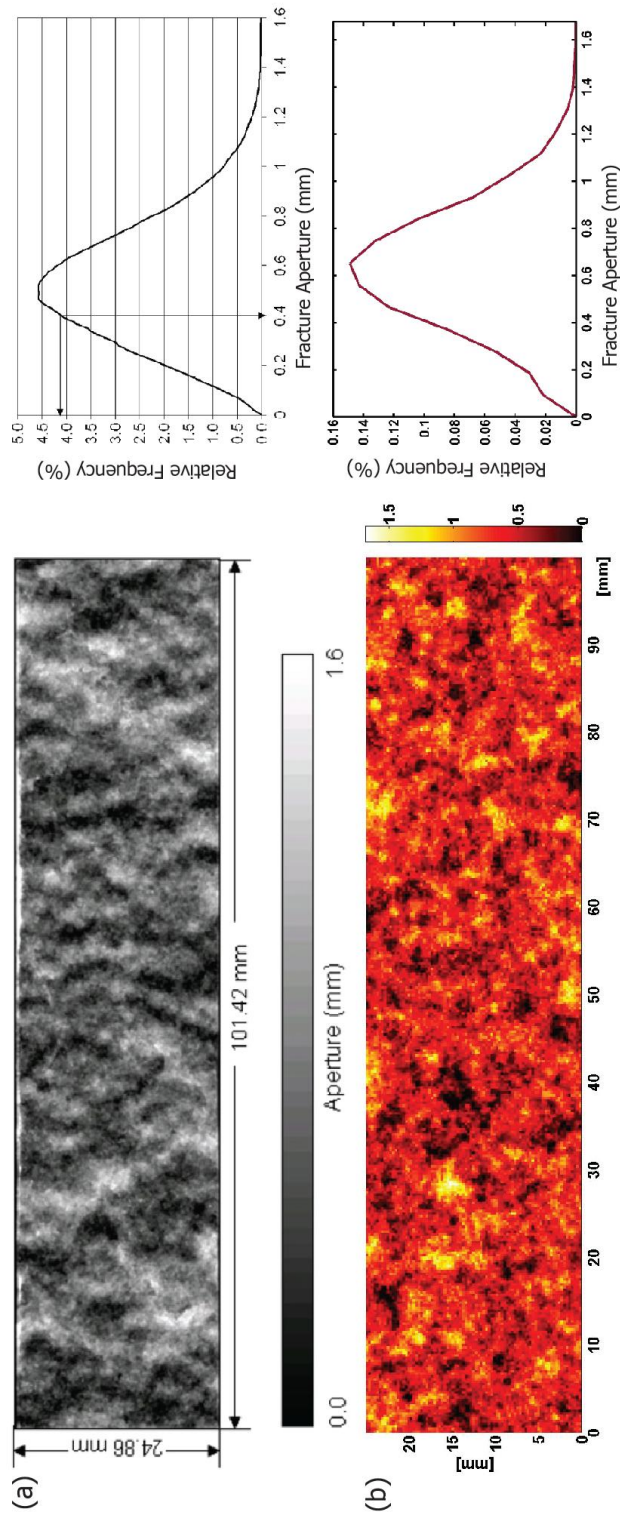


Figure 46: (a) Real fracture aperture measured with High Resolution Computer Tomography (from Karpyn et al., 2007 [106]), min. aperture 0mm, max. aperture 1.6mm, mean aperture 0.58mm, standard deviation 0.25mm. (b) Fracture aperture field with the same statistical properties.

2.7 SIMULATIONS

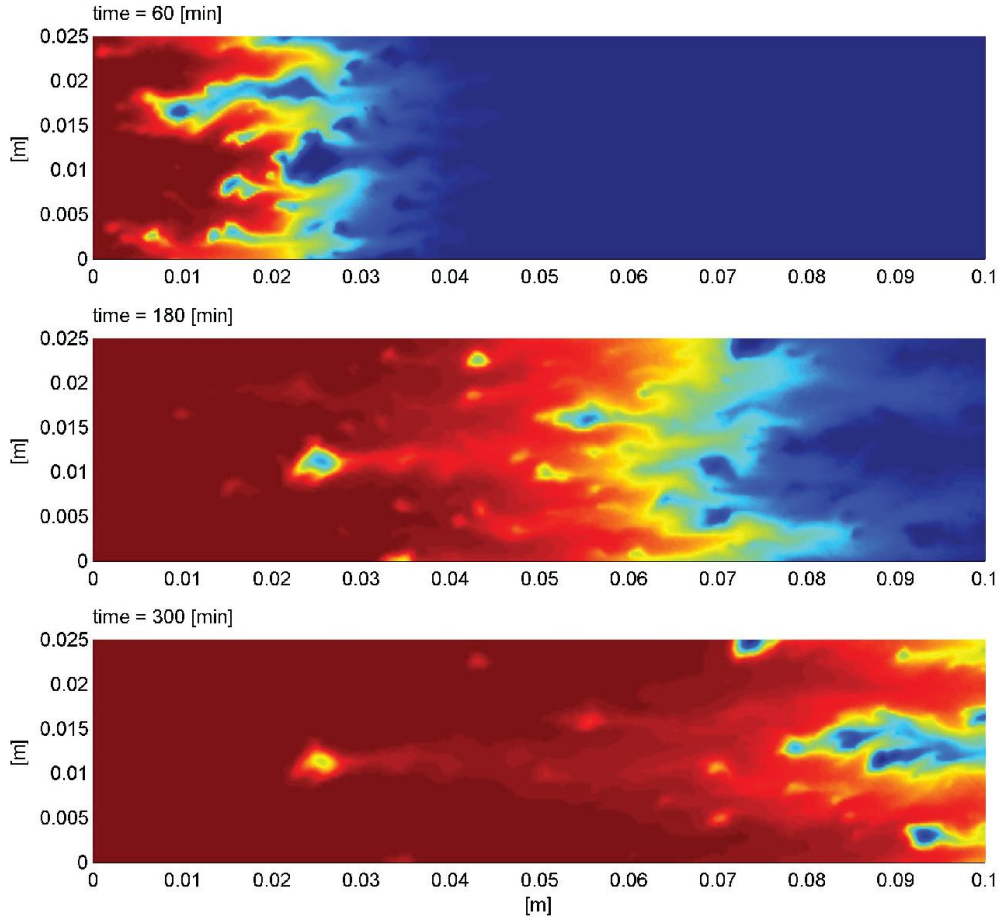


Figure 47: Flow simulation showing the tracer concentration in the statistically generated fracture aperture distribution (Fig. 46 (b)) at different time steps. Flow is from left to right. Red: Concentration $c = 1$, Blue: Concentration $c = 0$. Initially, the concentration in the fracture is zero. Fluid with high concentration enters at the left boundary. Note the stagnant areas where the local aperture is small. We simulated advection and dispersion, assuming that the fracture permeability scales locally with the cube of the fracture aperture.

A heterogeneous flow pattern with stagnant areas can be seen in the flow simulation in the statistically generated fracture aperture distribution (fig. 47), which cannot be covered with the averaged properties. Therefore the breakthrough curves (BTC) (fig. 48) cannot be matched. This shows the significance of calculating flow through fractures with spatially varying apertures to be able to see real effects like fingering or stagnant areas.

2.7 SIMULATIONS

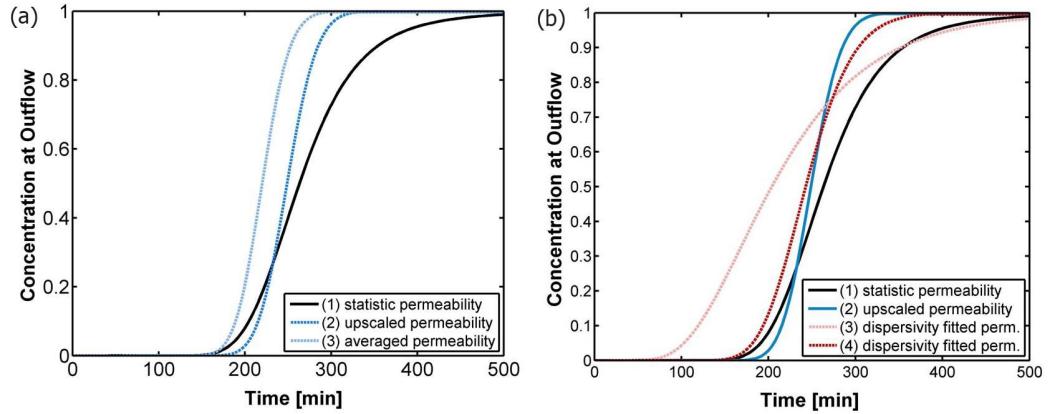


Figure 48: (a) Breakthrough curves showing the concentration at the right boundary for different permeability models: (1) statistically generated fracture with an overlying permeability distribution, (2) fit with uniform mean permeability computed for the flow field by Darcy's Law, (3) fit with uniform upscaled permeability using the cubic law and a mean aperture. (b) Improved fits for the upscaled breakthrough curves: (1) statistically generated fracture, (2) uniform upscaled permeability using the cubic law and a mean aperture, (3) and (4) fit with uniform upscaled permeability and adjusting the longitudinal (α_L) and the transversal (α_T) dispersivity coefficients (1) and (2) $\alpha_L = 3 \cdot 10^{-5}$ m, $\alpha_T = 3 \cdot 10^{-6}$ m, (3) $\alpha_L = 1 \cdot 10^{-2}$ m, $\alpha_T = 2.5 \cdot 10^{-4}$ m, (4) $\alpha_L = 1 \cdot 10^{-3}$ m, $\alpha_T = 1 \cdot 10^{-5}$ m.

2.7.4 Example 3D simulation of tracer transport in a fracture

As in the previous example, a fracture aperture field (for calculation of the permeability field) was generated stochastically but in this example the fracture is a 2D surface embedded in a 3D model (fig. 49). Fig. 50 shows the results of the tracer simulation. In the fracture, flow and transport are much faster than in the rock matrix.

As the fracture is fast filled compared to the surrounding matrix, these example simulations indicate that inflow rates must be chosen carefully in the flow experiments given that a full 360° projection of possibly 400 - 800 images can take up to about 3 hours, and a single image needs about 3 seconds.

2.7 SIMULATIONS

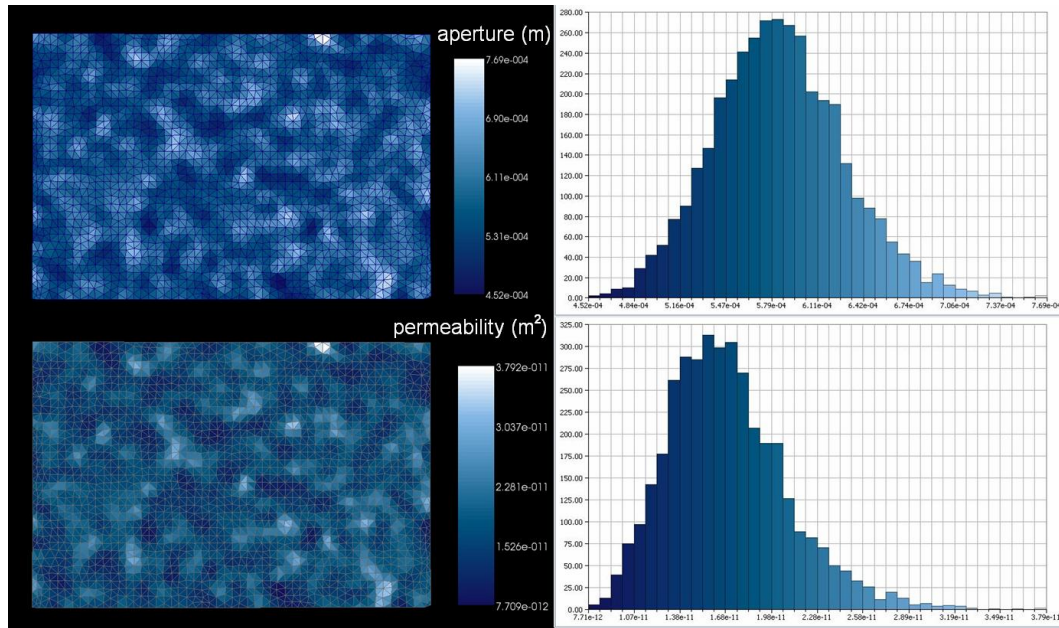


Figure 49: Top: Non-uniform fracture aperture distribution generated with a random field generator algorithm (right: histogram); bottom: Corresponding permeability calculated via cubic law. The fracture is 10 by 15 cm.

2.7.5 2D simulation of tracer transport in fractures in Baker Dolomite and San Andreas Carbonate

Using the aperture measurements from the X-ray CT experiments for BD and SAC, 2D unstructured finite element meshes were constructed. These meshes represent the fracture only, as fluid flow occurs predominantly in the fractures. The afore measured fracture aperture distribution was upscaled to the finite elements of the meshes (cf. section 2.6). Single-phase simulations on BD and SAC were carried out. The simulations were compared with the single-phase flow experiments visually. All simulations are carried out with CSMP++.

A detailed description can be found in chapter 6.

2.7 SIMULATIONS

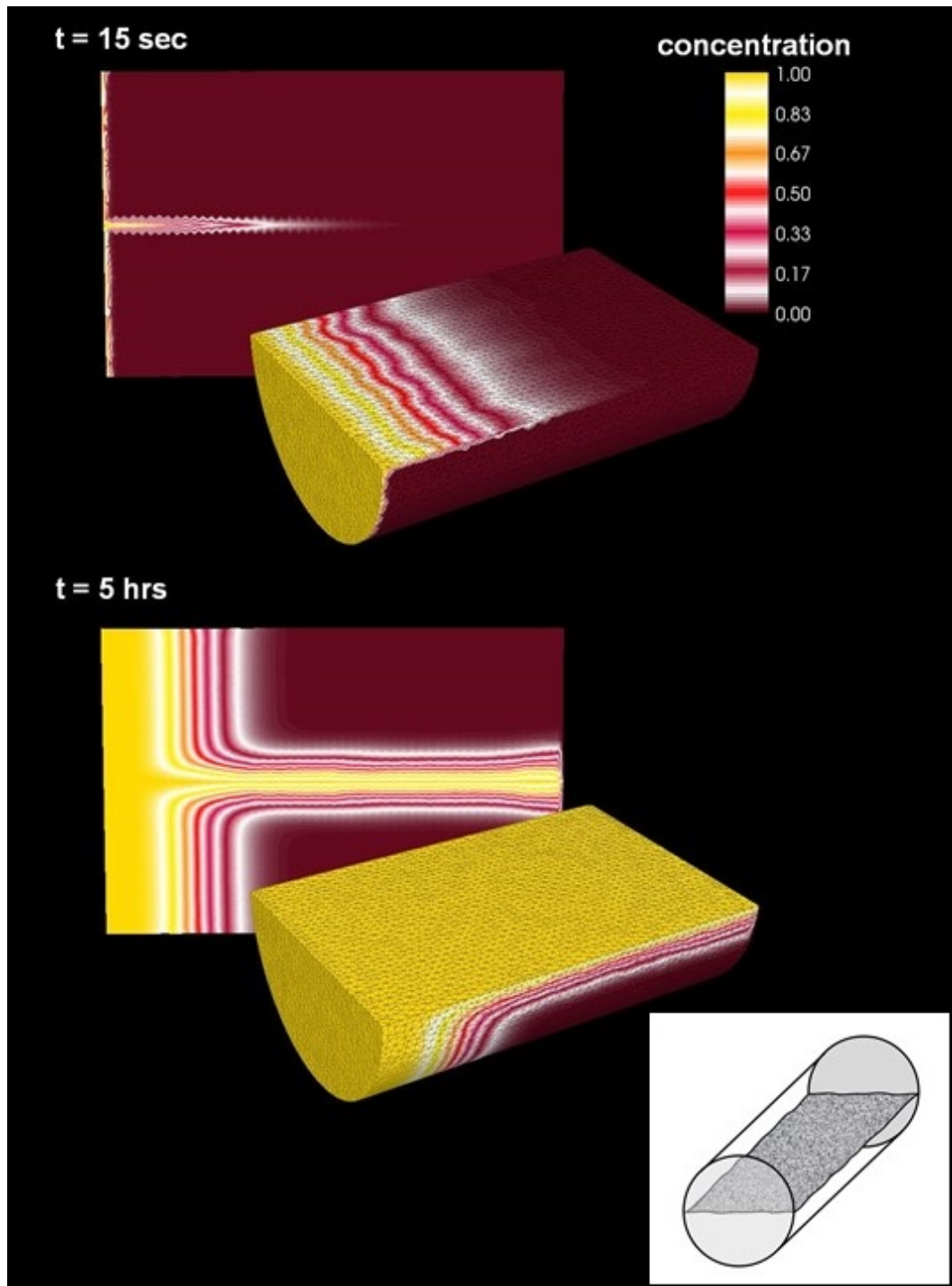


Figure 50: Simulation of a single phase tracer transport in a 3D core geometry with the non-uniform aperture data from fig. 49 mapped onto the 2D fracture embedded along the core length (horizontal and vertical cut through a core at different time steps), as schematically shown in the small inlet box (bottom right). Core diameter 0.1 m, core length 0.15 m, matrix permeability 0.05 D, pressure gradient 5 Pa. Flow is from left to right. Initial tracer concentration in core and fracture is zero.

2.7 SIMULATIONS

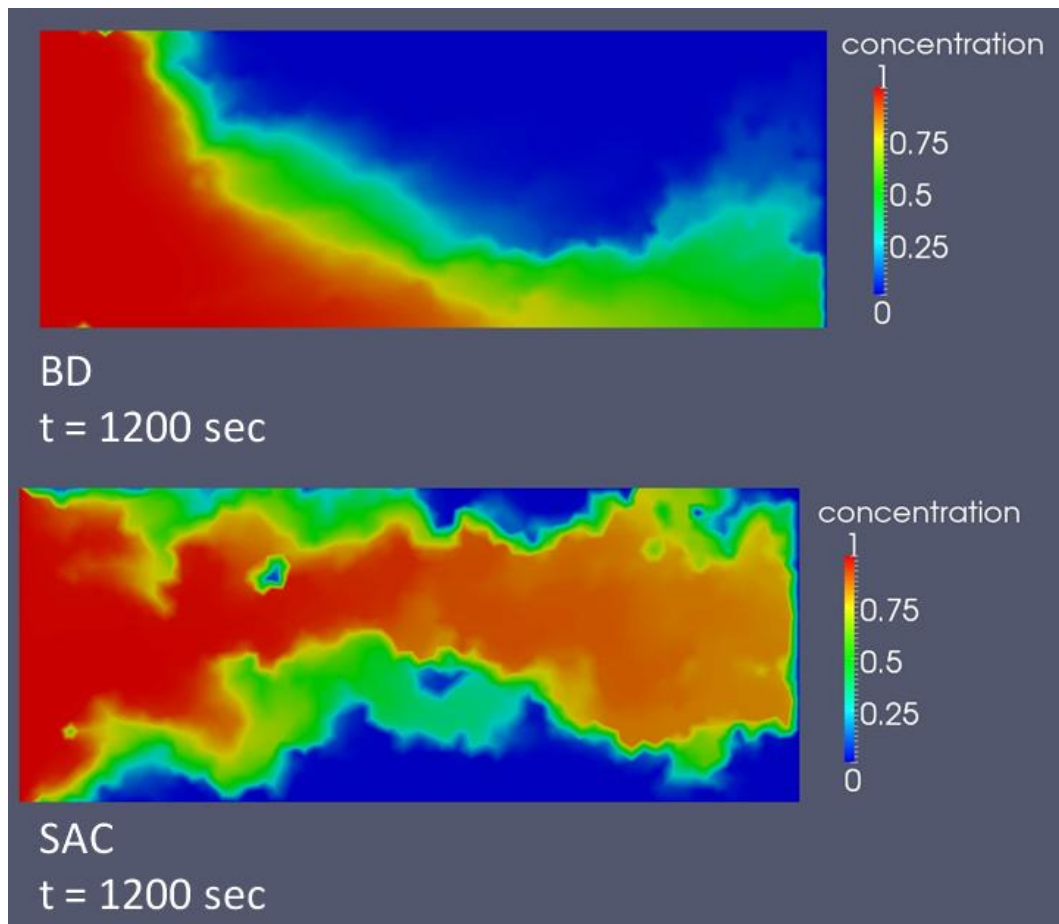


Figure 51: Simulation of a single phase tracer transport in a 2D fracture, frontal view . Top: Baker Dolomite. Bottom: San Andreas Carbonate. Flow is from left to right. The inflow rate is 10ml s^{-1} . Initial concentration in the fracture is zero.

2.8 SINGLE AND TWO PHASE FLOW EXPERIMENTS

2.8 SINGLE AND TWO PHASE FLOW EXPERIMENTS

2.8.1 *Experimental Setup*

A special X-Ray transparent flow cell was designed and constructed for the laboratory experiments because classic pressure vessels consist of materials (e.g aluminium) which are almost impenetrable to X-Rays. Since the experiments are carried out at standard conditions, a much lighter experimental apparatus could be built compared to the traditional core-holders that allow experiments to be carried out at elevated (i.e. reservoir) pressures. The aim was to design a flow cell⁵ which itself creates a minimal and uniform X-ray beam attenuation by minimizing the material around the core. This helps to minimize artefacts and enhance data collection times but does not allow experiments to be run at elevated pressures.

In the constructed flow cell the fractured rock is bonded to two epoxy platens, one at each end, with a thin rubber jacket surrounding the whole apparatus (fig. 52). The epoxy platens on both ends are slit to extend the fracture inside the core along the epoxy and connect it to the inlet and outlet via drainage holes. Tests were carried out to ensure that the epoxy does not react with the injected fluids. On both ends, a glued acetal platen then closes the fracture openings. The design permits control of the inflowing fluid with a syringe pump, or via gravity controlled flow. Separate fluid reservoirs for the fracture fluid and porous medium fluid, held at different heights above the flow cell, permit precise control of the pressure differential between the fracture and the porous medium. The flow direction is vertical and upwards. Initially, the sample is water saturated. The experimental core flood design was loosely based on the studies of Piri and Karpyn, 2007 [161]; Karpyn and Piri, 2007 [104]; Karpyn et al., 2007, 2009 [106, 105].

To establish a good contrast between fluids and rock matrix an examination of attenuation coefficients for different solution concentrations (potassium chloride/iodide) was carried out to find the optimal composition to distinguish clearly between the injected fluids and rock (fig. 53). A solution of 1M KI gives the best contrast. For the two-phase experiments we used

⁵ Designed by Ian Butler and Stephen Elphick.

2.8 SINGLE AND TWO PHASE FLOW EXPERIMENTS

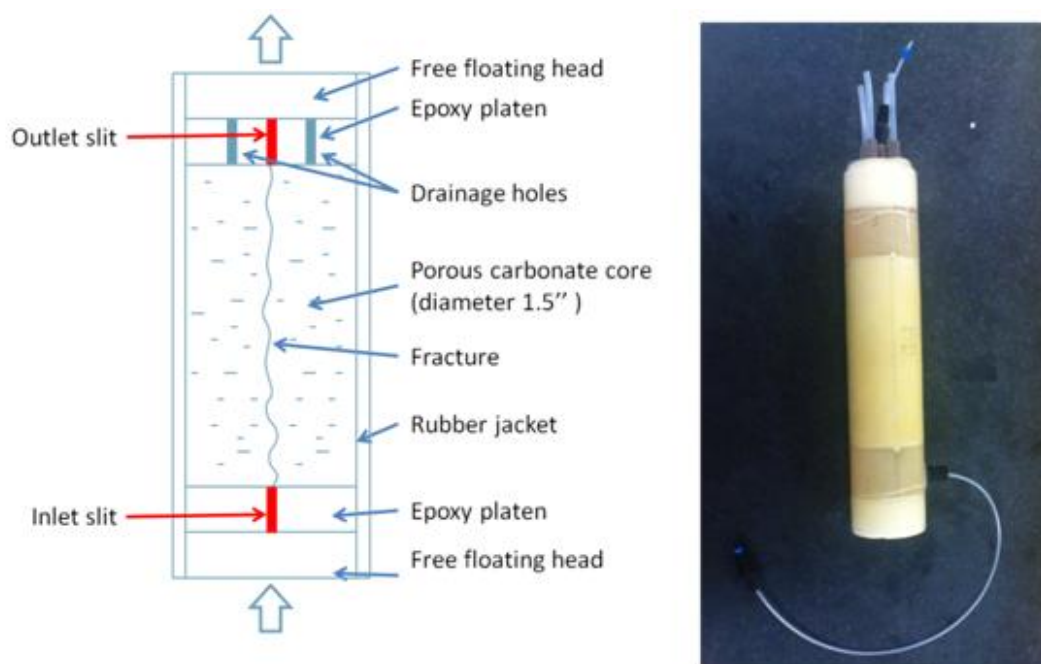


Figure 52: Flow cell suitable for X-Ray CT experiments with minimal beam attenuation and smooth fluid pressure distribution on the inlet and outlet area. The flow cell mainly consists of two epoxy platens simply extending the core, with a thin latex jacket surrounding the core. This creates minimal and uniform X-ray beam attenuation which can minimize artefacts and enhance data collection times.

2.8 SINGLE AND TWO PHASE FLOW EXPERIMENTS

io-dodecane as oil-phase being injected in the bottom of the core.

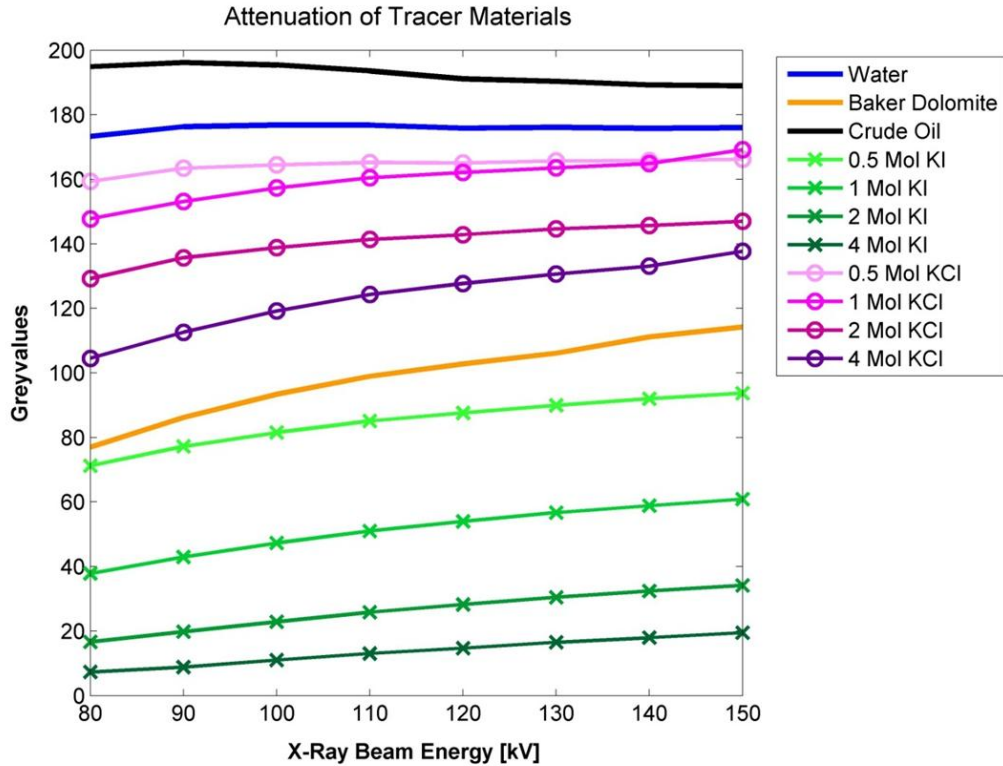


Figure 53: Measured grey values (high values indicate low beam attenuation) from normalized images depending on the beam intensity for potassium iodide (KI), potassium chloride (KCl) solutions, water, oil, and Baker Dolomite.

2.8.2 Flow Experiments

A series of single and two-phase flow experiments was imaged with X-ray radiography, i.e. we only took 2D images in front and side view during the flow process. Recall (section 2.3.3) that a full 3D image cannot be captured during the fluid injection as a full 360° image acquisition of 800 projections takes about one hour. Using the previously measured tracer attenuation profile (fig. 53), the diffusion into the rock matrix can be visualized from the cumulative 2D projections from front and side view. To visualize the advancing fluid, we subtract from each image the initial image of the water saturated sample; therefore the core itself is not visible in the images.

2.8 SINGLE AND TWO PHASE FLOW EXPERIMENTS

Initially, the experiment was carried out twice to obtain both front and side view of the fracture, for later experiments the table was rotated back and forth, as diffusion in the matrix is slow enough to do so. As an example, the images below show a time series of a Baker Dolomite with a single fracture along the flow direction. At the beginning of the experiments, the sample is water saturated. Next, tracer enriched water is injected across the bottom of the sample. The fracture is filled immediately with tracer fluid, whereas diffusion into the matrix occurs relatively slow. An extensive presentation and discussion of the experimental results can be found in chapter 5.

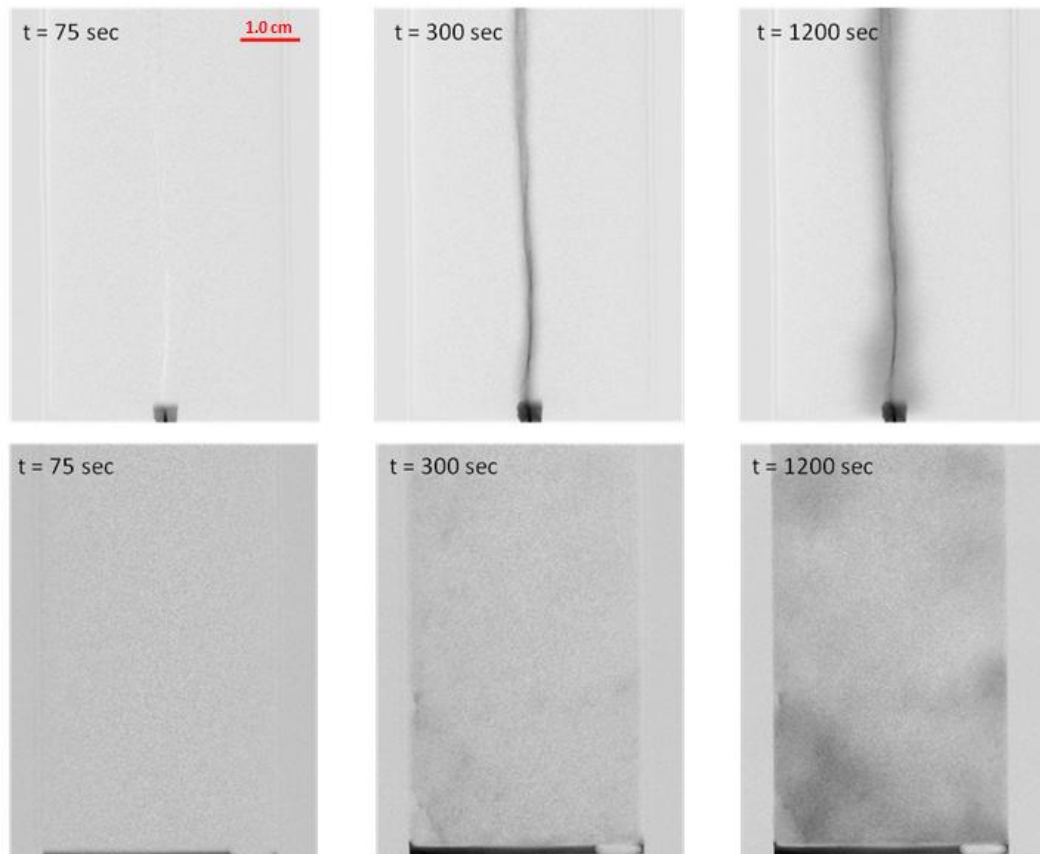


Figure 54: Radiography time series of single-phase tracer transport in a Baker Dolomite core ($\varnothing 3.81$ cm, length 10 cm) with a single artificial fracture. Top row: side view (looking along the fracture surface), bottom row: front view (looking at the fracture surface). Flow is vertically upwards. Approximately 450 images were acquired in the experiments and each image acquisition process took about 3 seconds.

2.9 SUMMARY OF METHODOLOGY

2.9 SUMMARY OF METHODOLOGY

Several steps are involved in the realization of even just a qualitative comparison of flow experiments in fractured carbonates with simulations accounting for the non-uniformity of the fracture. These steps can be divided in, on the one hand, the development and improvement of the newly built X-ray CT system and its application to fracture measurements and flow visualizations, and on the other hand, carrying out DFM based simulation studies. Special attention was needed to be paid for the transition from X-ray CT data to a grid based model as input for the simulations.

First, my supervisors, Ian Butler, Stephen Elphick, and I built a new, highly versatile X-ray CT system in-house. I successfully developed and implemented a fast, stable, and adaptable control software to switch from static full 360° X-ray CT measurements to X-ray radiographic imaging of different angles around the rock samples to be able to visualize in-situ fluid flow.

A large proportion of my research has been done on the development of new and successful image processing routines leading to a high-resolution measurement of fracture topology and aperture distributions for two different rock samples – Baker dolomite (BD) and San Andreas carbonate (SAC). These routines include a new correction method for CMOS sensor based cameras minimizing an artefact, which originates in the non-linear signal response of CMOS sensors, which is especially crucial if – like in our case – the full dynamic range of the camera needs to be used. Also, I was able to successfully combine two existing void space measurement methods for X-ray CT data to be able to cover a wider measurement interval for the apertures. The *peak height method (PH)*, being the finer one, is making use of the partial volume effect intrinsic to all X-ray CT data at material boundaries, whereas the *full width at half maximum (FWHM) method* is based on sharp image segmentation, and is therefore limited in resolution to a minimal unit of 1 pixel. With this approach, we were able to achieve a fracture aperture resolution of down to 75 μ m.

Further, after developing and constructing a nearly X-ray transparent flow cell, and tuning the control software of the CT system to capture front and side views of our samples only, we were able to visualize single- and

2.9 SUMMARY OF METHODOLOGY

two-phase flow experiments in the afore accurately measured core samples. We were able to see how differently fracture and rock matrix are flooded with the tracer induced fluids.

On the simulation side of my research, I first focused on carrying out a feasibility study to apply the DFM simulation approach with CSMP++ to the proposed question by incorporating a stochastically generated fracture aperture distribution in different simulation scenarios. I could show that it is possible to implement a real fracture aperture distribution into the simulation approach of using a hybrid 2D/3D mesh. Actual simulations on the before measured aperture distributions of the rock samples were carried out as well, and will be described in chapter 6.

An overview of how the involved steps of this research built up on each other can be seen in fig. (55).

2.9 SUMMARY OF METHODOLOGY

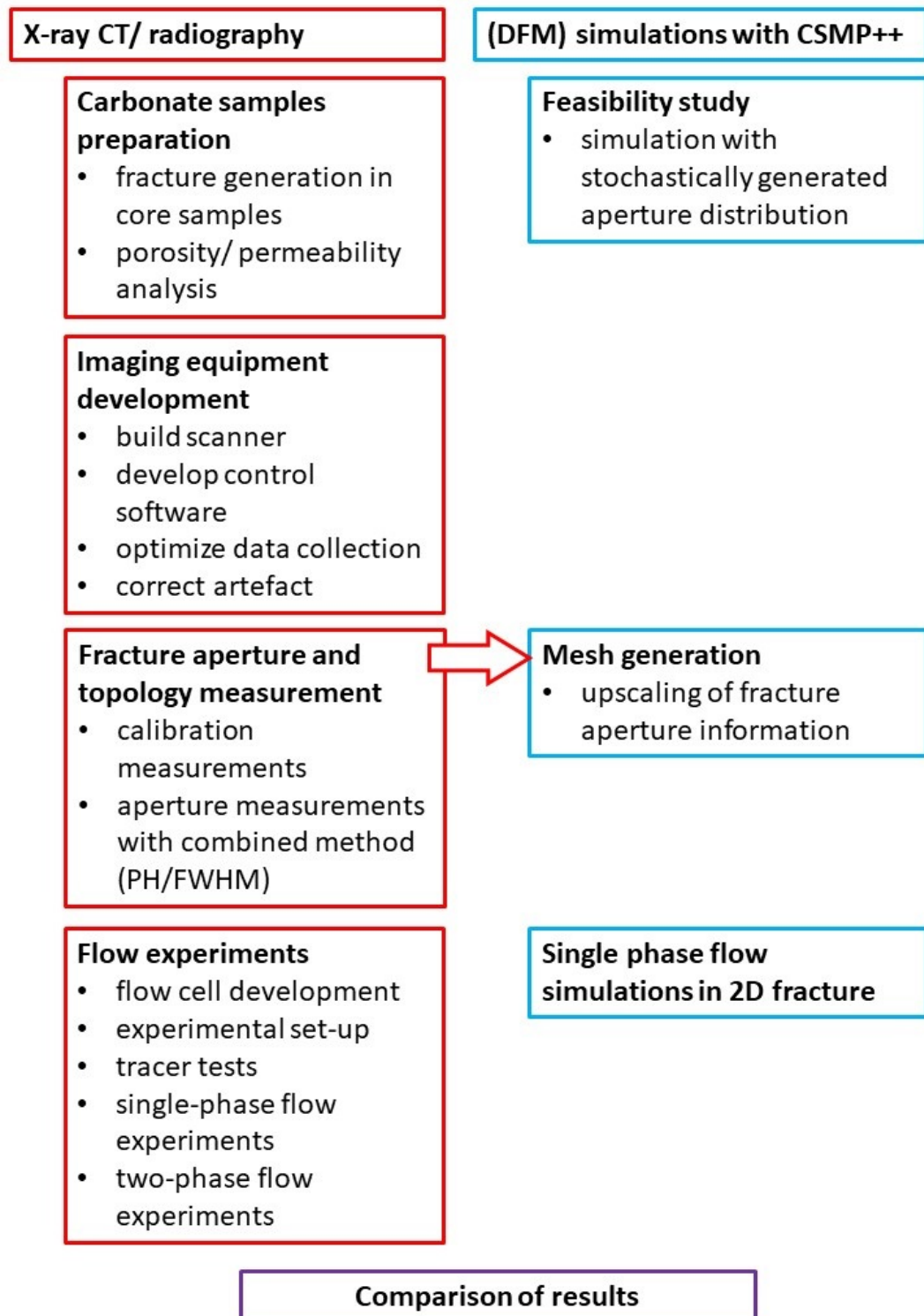


Figure 55: Workflow overview outlining the various steps of the applied methodology to realize a comparison of flow experiments in fractured carbonates with simulations accounting for the non-uniformity of the fracture.

PHOTOGRAPHIC IMAGE CORRECTION FOR CMOS PANEL DETECTORS

3.1 INTRODUCTION

Complementary metal-oxide-semiconductor (CMOS) detectors, also known as active-pixel sensors (APS), are widely used for a variety of applications ranging from digital photography to scientific applications and diagnostic imaging systems. They are state-of-the-art digital photodiodes and are used including cameras from DSLR photography, high-definition/high-speed video cameras, electron microscopy, digital radiography, or Computer Tomography (CT). The intensity dependence of the camera response is usually addressed by a simple pixel-wise linear gain correction method (with a so called flat-field image), which is also usually implemented in the 3D reconstruction software used for CT. The non-linear response nature of CMOS sensors is only relevant for imaging with high dynamic range. The dynamic range denotes the luminance range displayed in an image, or the range a sensor can capture. For capturing a high, or wide dynamic range, the darkest and brightest areas of the image have to be captured both with a sufficient contrast. In general, the non-linear response of CMOS sensors is therefore advantageous for digital photography.

In the Computer Tomography laboratory in the School of Geosciences at Edinburgh University we use a 4 megapixel Gadox X-ray camera, a Shad-o-BoxTM by Rad-icon (now Teledyne Dalsa). This camera consists of a 2-by-4 array of CMOS photodiode panels (fig. 56). Rad-icon's sensors employ only the lower interval of the response curve to resemble a linear signal ratio. As discussed in chapter 2 and depicted in fig. 57a, we record images of

3.1 INTRODUCTION

cylindric carbonate samples with an 1.5 inch diameter. To this end, the Gadox and Shad-o-Box cameras, both with CMOS panels, are used to record the images.

We capture around 1000 radiographic projections which are then used to calculate 3D images. We examine the recorded radiographic projections as well as the reconstructed 3D images. The camera's panel pattern is visible on the projection images in very dark areas (fig. 57b and 57c), which results after reconstruction in an intense spot artefact in the middle of the 3D images (fig. 58) (cf. section 2.4). A conventional flat-field normalization does not remove this artefact because we image across the camera's full dynamic range. Hence the purpose of this chapter is to discuss the development of a modified DC/FF correction.

So, in general, for high-dynamic range CT scanning the imaging error shows as a severe spot artefact in the reconstructed images as well as several ring artefacts.

In the literature the non-linearity of the input-to-output signal is usually described as approximately logarithmic, which can lead to so called Fixed Pattern Noise in very bright image areas (Joseph and Collins, 2002 [99]; Choubey et al., 2007 [42]). To overcome this problem, it has been suggested to adapt the opto-electronic interfaces themselves to linearize the detector signal (e.g. Choubey et al., 2007 [41]). This is impracticable though for many applications. Therefore an image based software correction method has to be applied. In general, the logarithmic response curve can be linearized in good approximation by a least-squares-fit method of a multi-linear regression, if the stochastic error of the pixel responses is independent from sample to sample and underlies a zero-mean Gaussian distribution. Otherwise a full Maximum-Likelihood estimation has to be carried out (Joseph, 2002 [98]).

Seibert et al., 1998 [182] developed a non-linear correction method based on a linear least-square-fit of multiple exposures of flat field images, and that this method can be extended to be fitted with polynomial response curves. Kwan et al., 2006 [117] later use a 4th order polynomial which shows excellent correction results throughout the entire exposure range. With this, the full dynamic range of a CMOS camera can be used for CT imaging.

3.1 INTRODUCTION

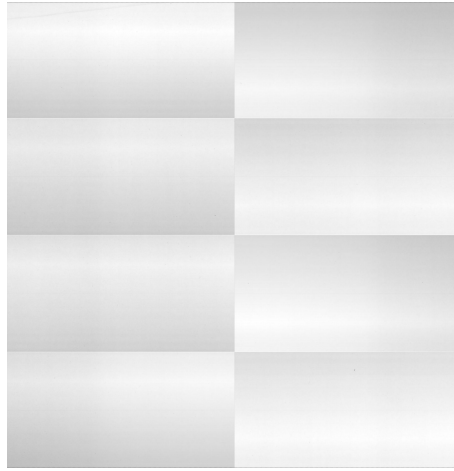


Figure 56: Flat-Field image of camera shows 2-by-4 panel pattern. The camera consists of a 2-by-4 array of CMOS photodiode panels. The image normalization method applied cannot cancel the evolving pattern. (Image shown already in chapter 2 (fig. 36).)

Hofmann et al., 2011 [83] compare different flat-field correction methods, a simple gain correction, a polynomial fit correction, and a piecewise linear interpolation. Both, the polynomial approach, and the piecewise linear interpolation show an improved correction over the simple gain correction method. In contrast, the method that we discuss below combines both, the polynomial approach and the piecewise linear interpolation, to a piecewise polynomial approach.

In our specific case, the luminance for the center region of the samples is even below the intensity at which a logarithmic, or linear approximation can be assumed (fig. 60). Radicon suggests a simple linearisation with a second order polynomial (termed the *fixed correction curve*) (Rad-icon Imaging Corp., 2003 [167] for the CMOS sensor we are using, as it has a characteristic S-shape response, which is a special case of the above mentioned Least-Square-Fit method. Unfortunately, this method did not give satisfying results (fig. 59).

This problem was discussed by Cao and Peter, 2008 [32], who suggest a piecewise second-order polynomial correction. The advantage of this method is that, for each pixel, just five coefficients need to be calculated. The polynomial can then be applied to each of the recorded radiographic projections before the 3D image reconstruction. The presented method though

3.2 NEW IMAGE CORRECTION METHOD

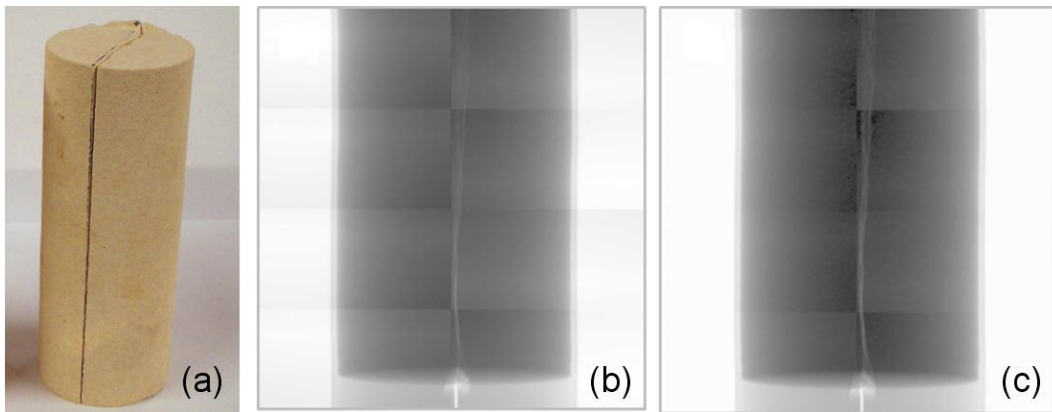


Figure 57: X-ray phantom image of the cylindrical carbonate core with a vertical fracture visible in the centre of the sample. (a) Carbonate sample \varnothing 3.81 cm with a single fracture; (b) Original radiographic image including the artefact that shows the 2-by-4 sensor panels clearly; (c) Standard linear corrected image that does not remove the artefact completely; (Images b and c are gamma corrected by 4.0 for the purpose of clarity. Camera: Shad-o-BoxTM 4K from Rad-Icon Imaging Corp (now Teledyne Dalsa). (Image shown already in chapter 2 (fig. 37).)

expects the intersection point of the two polynomials to be half of the maximal measured intensity, and the inflection points of the polynomials to be at 25%, and 100% of the maximal intensity, respectively. The maximal intensity, i.e. the intensity at which the projections are captured, is determined by the specific set-up of the CT experiment, and hence the shape of the response curve does not necessarily align with the fixed correction curve. We therefore developed a generalized variation of this method by leaving the choice of the intersection and inflection points variable, so the linearisation can be carried out according to the shape of the actual response curve, or the considered interval of the response.

3.2 NEW IMAGE CORRECTION METHOD

In the following we discuss the developed piece-wise polynomial gain approximation in more detail and compare it to the standard linear gain correction algorithm available in commercial tools.

First, we measure the average detector response for a set of flat field images over a complete range of beam intensities (fig. 60). In the case of a

3.2 NEW IMAGE CORRECTION METHOD

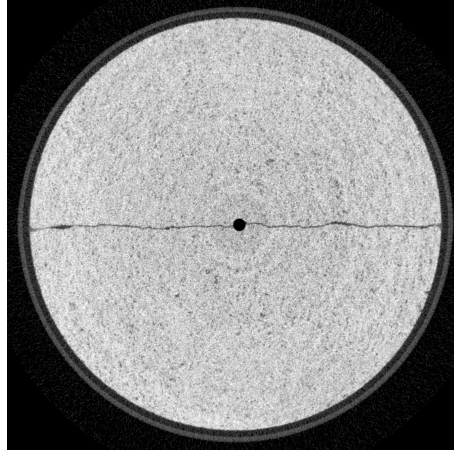


Figure 58: Reconstruction of fig. 2(c) which shows a spot artefact in the middle, and several ring artefacts as a result of the non-linearity of the sensors. (Image shown already in chapter 2 (fig. 35).)

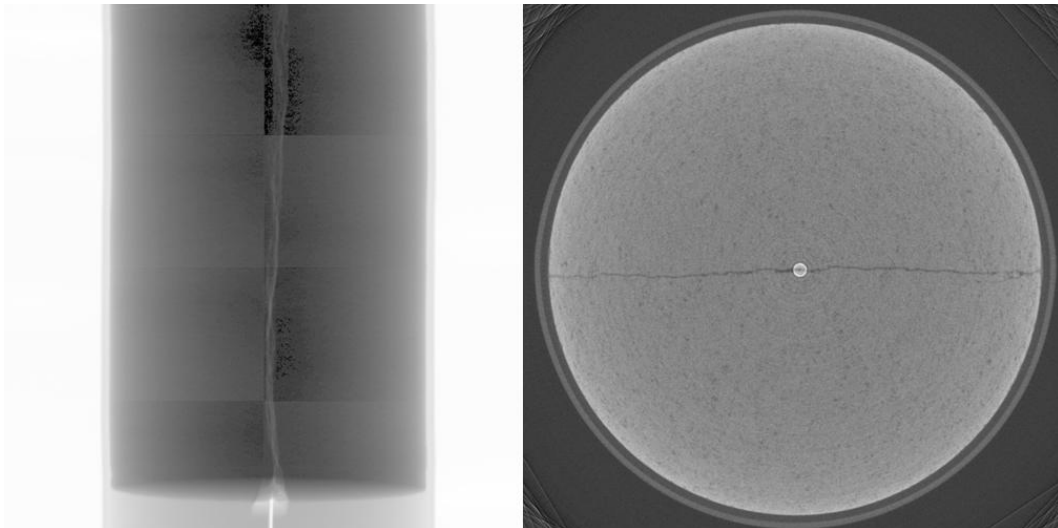


Figure 59: Left: X-ray phantom image of the cylindrical carbonate core after correction with a quadratic fit polynomial. Right: Reconstruction of the quadratic linearisation, which still shows a spot artefact in the middle.

3.2 NEW IMAGE CORRECTION METHOD

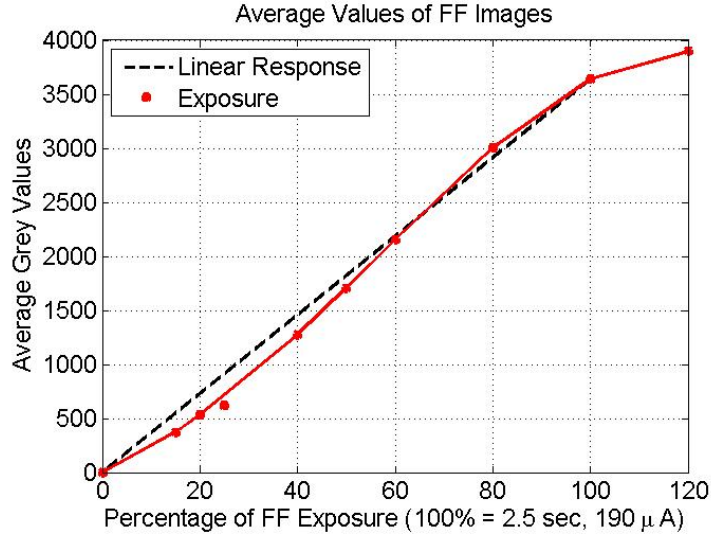


Figure 60: Measured detector response as set of flat field images at different beam intensities. The value at 25% for the exposure time was 0.625 sec, with the 0.005 sec increment not been resolved from the frame grabber.

radiographic application, the intensity can be varied with exposure time [sec] of the camera, or the X-ray tube current [μA], respectively.

3.2.1 Linear gain correction

The standard linear method of image correction is to first subtract all images by an (average) dark current (DC), or offset image, to correct for defect single pixels (offset correction), and then divide all projections by an (average) flat field image at 100% intensity (FF_{100}). The images then have to be scaled back to the original value range. Division and subtraction is carried out pixel-wise based on the assumption that the separate pixels respond mutually independent. We then obtain

$$x(i) = \frac{y(i) - DC(i)}{FF_{100}(i)} \overline{FF_{100}}, \quad (28)$$

where $x(i)$ is the wanted linear response in pixel i , $y(i)$ is the measured grey value in pixel i of original image, $DC(i)$ is the grey value in pixel i of dark current image, $FF_{100}(i)$ is the grey value in pixel i of flat field image at 100% intensity, and $\overline{FF_{100}}$ is the average value of all pixels in FF_{100} .

3.2 NEW IMAGE CORRECTION METHOD

3.2.2 Fit to piecewise quadratic polynomial

The improved method uses a piecewise quadratic polynomial as a fit function to describe the double bend of the response curve better (the basic formulation is similar to Cao and Peter, 2008 [32]). The polynomial is hence defined as

$$\begin{aligned} y(i) &= a_2(i) \cdot x(i)^2 + a_1(i) \cdot x(i) & \forall x(i) \leq x_2 \\ y(i) &= b_2(i) \cdot x(i)^2 + b_1(i) \cdot x(i) + b_0(i) & \forall x(i) > x_2, \end{aligned} \quad (29)$$

with the boundary condition that both polynomials have the same slope at joint x_2

$$2 \cdot a_2(i) \cdot x_2(i) + a_1(i) = 2 \cdot b_2(i) \cdot x_2(i) + b_1(i) . \quad (30)$$

As input, three FF images are needed, called FF_1 , FF_2 , and FF_3 . In Cao and Peter, 2008 [32] they are chosen to be fixed at 25%, 50% and at 100% of the maximal measured intensity, but other options seem to give better results. Principally, the best choice of input values depends only on the shape of the response curve, and on the choice of the maximal intensity, and therefore cannot be generalized.

Following the example in Cao and Peter, 2008 [32], we set the values to

$$\begin{aligned} x_1 &= 0.25 \\ x_2 &= 0.5 \\ x_3 &= 1.0 . \end{aligned} \quad (31)$$

The value x_2 defines the intersection point between the two polynomials. This point should be chosen close to the inflection point of the response curve. Alternatively, depending on which intensity interval is most important for the image acquisition, the "joint" can be selected as the intersection point between the measured response curve and the linear response.

3.2 NEW IMAGE CORRECTION METHOD

We then determine the coefficients $a_2(i)$, $a_1(i)$, $b_2(i)$, $b_1(i)$, $b_0(i)$ for all pixels i . For the example case ($x_1 = 0.25$, $x_2 = 0.5$, $x_3 = 1.0$) we obtain

$$\begin{aligned}
 a_2(i) &= 8 \cdot FF_2(i) - 16 \cdot FF_1(i) \\
 a_1(i) &= 8 \cdot FF_1(i) - 2 \cdot FF_2(i) \\
 b_2(i) &= 16 \cdot FF_1(i) - 16 \cdot FF_2(i) + 4 \cdot FF_3(i) \\
 b_1(i) &= 22 \cdot FF_2(i) - 24 \cdot FF_1(i) - 4 \cdot FF_3(i) \\
 b_0(i) &= 8 \cdot FF_1(i) - 6 \cdot FF_2(i) + FF_3(i) .
 \end{aligned} \tag{32}$$

To provide generality and allow a different choice of input values, the particular equations have been derived in MATLAB.

3.2.3 Gain Correction

The coefficient matrices can now be applied to correct images acquired with the same camera and same X-ray beam intensity as FF_3 .

If $y(i) \leq FF_2(i)$, the value is in the lower polynomial, and the corrected value is calculated as

$$\begin{aligned}
 y_{new}(i) &= \overline{FF}_{100} \cdot \\
 &\frac{-a_1(i) + \sqrt{a_1(i)^2 + 4 \cdot a_2(i) \cdot y(i)}}{2 \cdot a_2(i)} .
 \end{aligned} \tag{33}$$

If $y(i) > FF_2(i)$, the value is in the upper polynomial

$$\begin{aligned}
 y_{new}(i) &= \overline{FF}_{100} \cdot \\
 &\frac{-b_1(i) + \sqrt{b_1(i)^2 + 4b_2(i)y(i) - 4b_2(i)b_0(i)}}{2b_2(i)} .
 \end{aligned} \tag{34}$$

This method shows to be suitable for all values and is versatile enough for an application to a range of different imaging problems. This is a significant improvement compared to the linear correction method and the quadratic fit suggested by the manufacturers of the sensor (Rad-Icon Imaging Corp., 2003 [167]).

3.2 NEW IMAGE CORRECTION METHOD

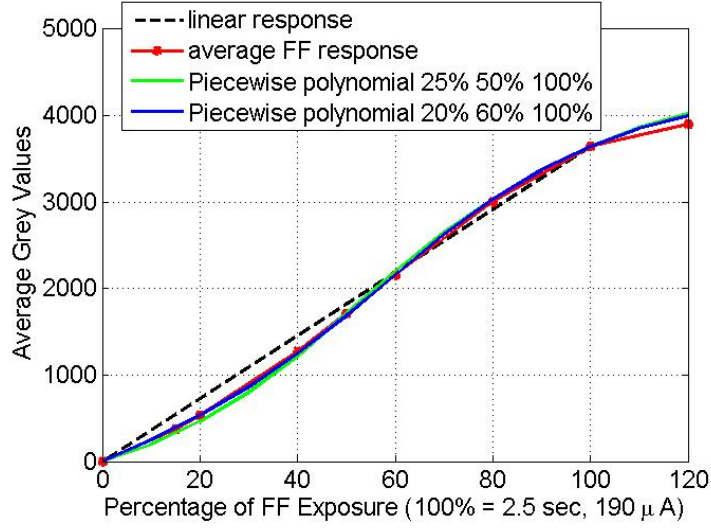


Figure 61: Piecewise polynomial fits for two different sets of input parameters (see legend). Blue 20%-60%, green 25%-50%. The blue curve represents the measured camera response more accurately, especially at lower intensities, which is important for the high density materials we are considering in our CT scans.

3.2.4 Error calculation

To compare different values for x_1 , x_2 , and x_3 , and to best fit the response curve, we calculate imitated FF images based on the coefficient matrices a_2 , a_1 , b_2 , b_1 , b_0 . With $k = 1, \dots, n$ number of measured intensities, and y_k measured intensities of which some equal x_1 , x_2 , and x_3 , we obtain one "fake" FF image Y_k for each measured intensity y_k .

If $y_k \leq x_2$ the pixel i in image Y_k is calculated as

$$Y_k(i) = a_2(i) \cdot y_k^2 + a_1(i) \cdot y_k. \quad (35)$$

If $y_k > x_2$

$$Y_k(i) = b_2(i) \cdot y_k^2 + b_1(i) \cdot y_k + b_0(i). \quad (36)$$

We calculate an average relative error as

$$\delta_n = \frac{1}{n} \sum_{k=1}^n \left| \frac{\overline{Y_k} - \overline{FF_k}}{\overline{FF_k}} \right|, \quad (37)$$

3.2 NEW IMAGE CORRECTION METHOD

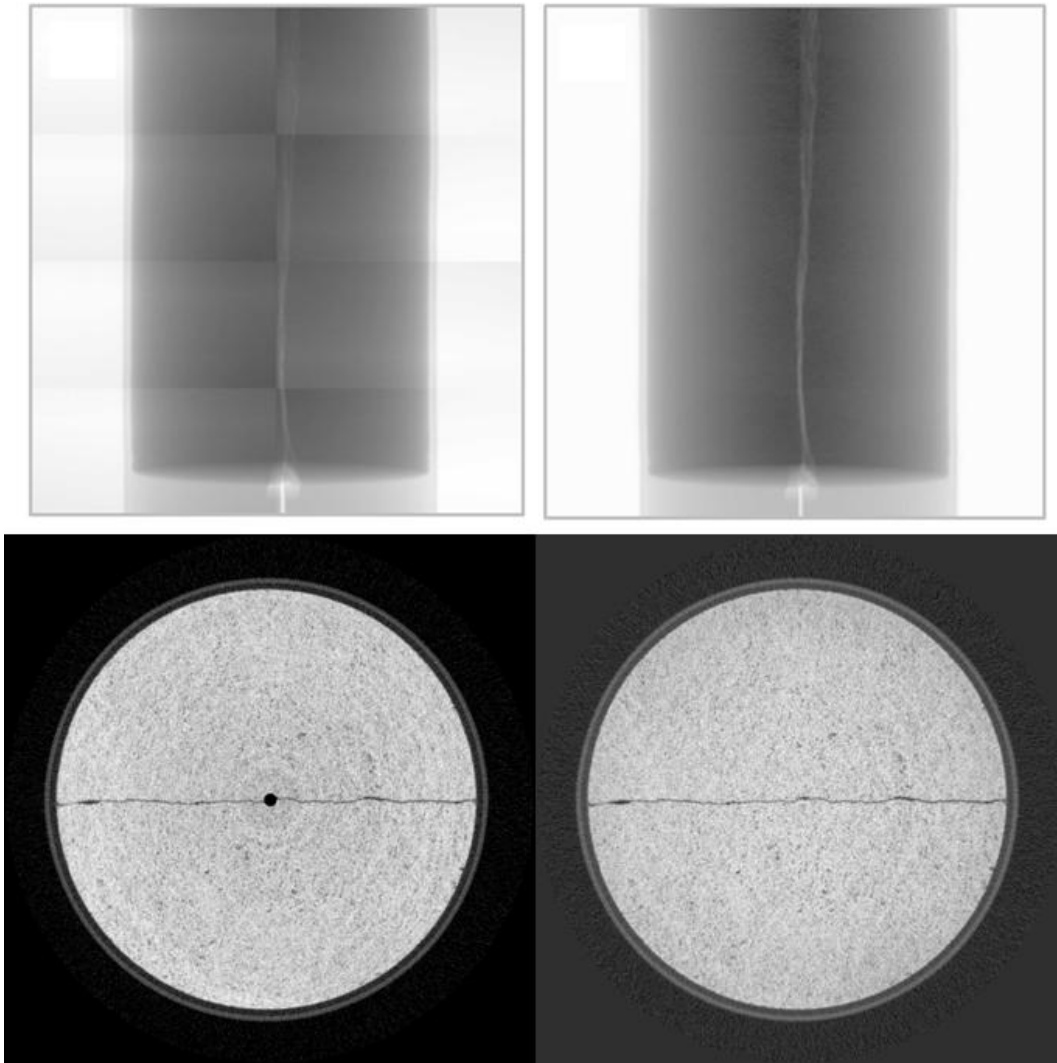


Figure 62: Top: Projection images (left) before and (right) after correction using the piecewise polynomial approach. Bottom: Reconstructed CT images for the (left) uncorrected and (right) corrected projections. (Image shown already in chapter 2 (fig. 38).)

3.3 CONCLUSIONS

where \overline{FF}_k denotes the average value of all pixels in the measured FF image at intensity k , and \overline{Y}_k the average value of all pixels in the "fake" FF image.

CORRECTION METHOD	δ_n [%]
Linear Correction (with 100% FF image)	15.705
Quadratic Correction ($x_1 = 0.5, x_2 = 1.0$)	9.953
Piecewise Polynomial Correction $x_1 = 0.25, x_2 = 0.5, x_3 = 1.0$	5.093
Piecewise Polynomial Correction $x_1 = 0.2, x_2 = 0.6, x_3 = 1.0$	0.996

Table 1: Relative Error of the different correction methods.

Using the piecewise polynomial reconstruction, we are able to reduce the relative error to below 1% compared to a relative error of about 15% from a standard linear FF correction method (table 1). This error analysis strongly suggests that it is beneficial to use FF images for the image correction at beam intensities that fit the actual response curve best.

The implemented MATLAB code can be found in the appendix A.2.

3.3 CONCLUSIONS

We developed a routine that allows us to correct for a non-linear imaging error, which is inherent to all CMOS panel detectors. This error leads to severe artefacts in the recorded images for Computer Tomography (CT) applications. The digital camera we are using to acquire X-ray images for Computer Tomography consists of eight CMOS sensors. These sensors have a non-linear response ratio of input signal to output signal, which is most striking in dark image areas. A standard linear Flat Field correction method cannot remove the panel pattern on the projections, which leads to a fixed pattern artefact on the projection images and severe ring and spot artefacts on the reconstructed CT images (section 2.4). We estimate the error in our case to about 15%. Our correction method is based on a generalized

3.3 CONCLUSIONS

piece-wise polynomial approach. This allows us to correct for the non-linear detector response using a set of three flat-field (FF) images taken across the whole intensity range of the experimental set-up. Averaging the pixel values of each flat-field image yields a camera response curve, which we approximate by two quadratic polynomials. The inverse approximation function can then be used to correct the images pixel-wise. This correction method needs to be applied to all projection images of a full 360° scan instead of the normal FF and DC correction, before the projections are used in the reconstruction procedure to calculate the actual 3D volume.

We were able to successfully develop and implement a program in Matlab to estimate the actual camera response by a piecewise polynomial, and use it to inversely correct for the non-linearity of the camera. The relative error of the correction method is now estimated to be below 1%, and the sensor pattern vanishes completely. With this, we are now able to remove most of the ring and spot artefact in the CT images and produce a far higher accuracy in visualizing and measuring properties using the CT images.

4

CORE FRACTURE ANALYSIS

4.1 INTRODUCTION

To minimize the influence of the measurements on the comparison of flow experiments and simulations, a good estimate of the aperture distribution is needed. Simulating fluid flow in fractured cores using the DFM technique requires a 2D representation of the fracture surface as point cloud with a coinciding aperture value at each 3D coordinate location. We used calibration measurements of standardised samples (Johns et al., 1993 [97]) and subsequently applied two different aperture measurement methods – a low-resolution method measures the width of the fracture at each point, a high-resolution method uses the grey value of the pixels in the fracture as a reference to estimate the fraction of air/rock in each pixel (Ketcham et al., 2010 [113]). The latter approach enables us, in theory, to measure the aperture more accurately than the voxel resolution, because we can relate the grey value of an aperture location directly to an aperture value as opposed to a threshold method alone.

Two carbonate core samples of different heterogeneities including a fracture each were scanned with a micro CT at high resolution at the University of Edinburgh. An aperture distribution needed to be derived to serve as input for a computer model of the scanned samples. The samples are subsequently used for flow experiments. The extensive image processing workflow to derive the aperture distribution is shown in this chapter. From the reconstructed 3D images a measurement method of the fracture aperture is derived by combination of existing methods, which is discussed in detail below.

4.1 INTRODUCTION

The different approaches to measure apertures on the grey values directly are described in the following. The easiest method, which is similar to thresholding the data, is the *full width at half maximum (FWHM) method* (Vandersteen et al., 2003 [193]). The fracture aperture is measured across the gap in the signal at half the height of the peak height (fig. 63). The wider the gap is, the wider is the aperture. The calibration measurement relates this value then linearly to the actual width of the calibration pieces. For very narrow apertures though, when the fracture aperture is less than the voxel resolution, this approach is not valid anymore. The *partial volume effect* is the only reason, why the fracture at this point is still visible in the CT image. The signal for a narrow fracture is a downward peak in the grey value profile, but the lowest point in this valley is lower (i.e. darker) than the grey value of air (fig. 18). In contrast, the *peak height (PH) method* measures the height difference between the average grey value of the fracture surrounding rock (including noise and pores) and the grey value of the peak in the signal (Vandersteen et al., 2003 [193]; fig. 63). The calibration measurements as suggested by Johns et al., 1993 [97] relate this value then to the actual aperture of the fracture. The relation is log-linear due to the Beer-Lambert-Law (eq. 10), as the attenuation of the signal is an exponential function. Another approach is to integrate over the signal profile for the whole peak area, the *missing attenuation area (MA) method* (Ketcham et al., 2010 [113]; fig. 63). This method is not considered further in this chapter, as our data is too noisy.

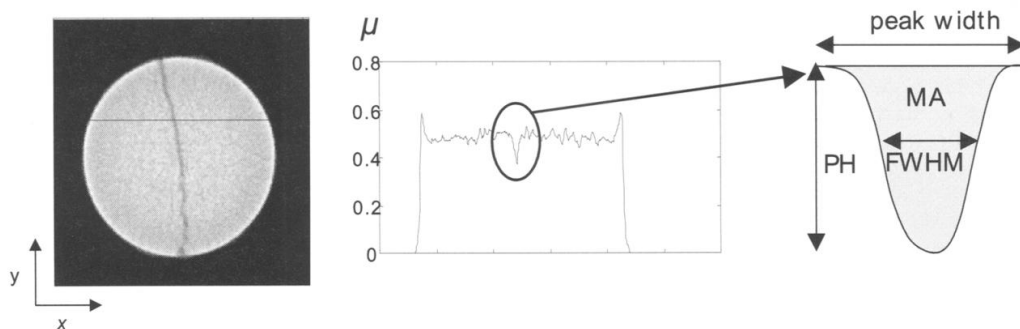


Figure 63: Left: CT image of a limestone sample with variable aperture fracture. Center: Line profile across the fracture. Right: Sketch depicting the different measurement methods (from Vandersteen et al., 2003 [193]).

4.2 FRACTURE APERTURE MEASUREMENTS WITH COMBINED PH AND FWHM METHOD

Crucial for the accurate aperture extraction throughout all steps is a preceding noise reduction procedure (e.g. application of a Median or Gauss filter), as strong noise can distort the rock base line and therefore falsify the calculated results. In general, it is better to use hardware filters (e.g. lead or copper), which provide a better solution by minimizing noise in the first place.

4.2 FRACTURE APERTURE MEASUREMENTS WITH COMBINED PH AND FWHM METHOD

4.2.1 *Calibration measurements*

First, we need a calibration sample, one for each rock type. The calibration samples are cylindrical cores, each about 4cm long with the same diameter as the San Andreas Carbonate (SAC) and Baker Dolomite (BD) samples of 3.81 cm (fig. 22). They were slit in the middle along their length and ground, such that their artificial fracture is as flat as possible. We then use shims of different thicknesses (table 2) to gap out the calibration samples. They were held together with a rubber band. We scanned the calibration samples at the same scanner settings and at the same resolution as the BD and SAC samples at 140 kV tube voltage with an exposure time of 2 sec.

Shim color	Shim thickness [mm]
no shim	0.00
blue shim	0.05
green shim	0.08
dark blue shim	0.13
black shim	0.25
red shim	0.38
yellow shim	0.51

Table 2: Thicknesses of the plastic shims used to gap out the calibration samples

4.2 FRACTURE APERTURE MEASUREMENTS WITH COMBINED PH AND FWHM METHOD

Fig. 64 shows some of the scans obtained from the calibration samples. We notice, that even an aperture of zero shows a "fracture" that can be clearly seen in the images. Assuming, the best reconstruction, artefact removal,

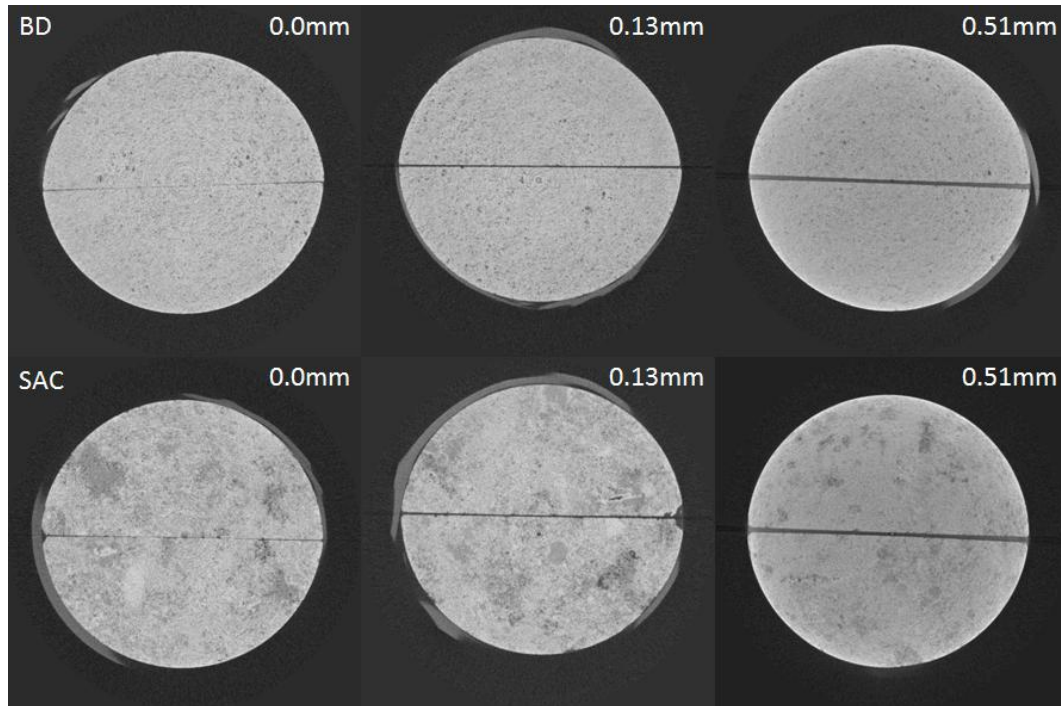


Figure 64: Scans of calibration pieces gapped out with plastic shims of different thicknesses. Top row: Baker Dolomite, bottom row: San Andreas Carbonate.

slice normalization and gain correction (see chapter 3) was applied, we then apply a Gaussian filter to the images to lower the amount of noise present in the images. A Gaussian filter smoothens smaller features, and preserves coarser features at the same time.

The calibration measurements of plastic shims with different thicknesses are then analysed. To calculate the *rock base line* (Vandersteen et al., 2003 [193]), which is the average signal of the corresponding rock type, which also takes noise and pores into account, we manually select a 3D region in the calibration scans in which the slit is not present (with MATLAB's image processing toolbox) to avoid areas with remaining artefacts. We assume the rock with pores/noise to be homogeneous in this volume and calculate the average grey values (table 3).

4.2 FRACTURE APERTURE MEASUREMENTS WITH COMBINED PH AND FWHM METHOD

AVERAGE GREY VALUE		
	BD	SAC
mean	3.6e+4	4.0e+4
stddev	3.9e+3	4.5e+3
n	13.1e+6	4.4e+6

Table 3: Average grey value of rock types – The original images are 16-bit tif images, so the possible greyscale values have a range of 0 - 65535.

A second 3D region is selected manually, in which the slit is present now. The chosen volume is most suitable for aperture measurement, if no large pores or artefacts are visible in the immediate neighbourhood adjacent of the slit, as this could falsify the aperture measurements. Also, the shim itself must not be present in the chosen slices, but the volume should be close to the area where the shim is visible, which is closest to the known given aperture. With this approach, we ensure that the aperture which is being measured is not biased by possible deviations in the slit surface.

To find the locations, where the apertures are measured, we employ a function of Avizo called *ridgeline*. It is a search path algorithm working slice-wise, which tries to find a path in the image from the left to the right border along the darkest pixels. These darkest pixels coincide with the peak locations in the grey value signals across the slit.

At each ridgeline location in the chosen 3D region we now identify the grey value and calculate difference between this grey value and the rock base line, the average rock response. The averages of these grey values then define the calibration values for each shim thickness for the PH method. For the FWHM method on the other hand, at each ridgeline location half the height of the aperture peak is taken into account. We calculate it as half of the difference in grey values between the peak signal and the average rock grey value. We then measure across the gap in the signal how many voxels have a lower grey value than the half measure to arrive at the width of the slit at this height. The average number of voxels, expressed in mm, in the chosen volume defines the calibration value for the FWHM method. The measured values can be seen in fig. 65 and 66.

4.2 FRACTURE APERTURE MEASUREMENTS WITH COMBINED PH AND FWHM METHOD

A log-linear least square fit (LSF) for the PH method and a linear LSF for the FWHM method are calculated over all shim thicknesses. The results of the fit curves can be seen in fig. 65 and 66. The measurement for the dark blue shim (0.13 mm) for the Baker dolomite for the FWHM method could not be used in the analysis, as the values were much brighter than expected, so we defined it as an outlier.

The fit function for the PH method for BD is

$$y = 4.5081 \cdot 10^4 + 1.0527 \cdot 10^4 \ln(x) \quad (38)$$

The fit function for the PH method for SAC is

$$y = 4.8118 \cdot 10^4 + 1.0494 \cdot 10^4 \ln(x) \quad (39)$$

The fit function for the FWHM method for BD is

$$y = 0.0519 + 1.0028 \cdot x \quad (40)$$

The fit function for the FWHM method for SAC is

$$y = 0.0742 + 1.1183 \cdot x \quad (41)$$

Now we can use the fit functions as well to relate the measured grey values of the PH method, or the gap width at half height of the FWHM method, respectively, to actual apertures of shim sizes (tables 4, 5, 6, 7) and calculate a mean absolute error for each measurement method (table 8).

4.2 FRACTURE APERTURE MEASUREMENTS WITH COMBINED PH AND FWHM METHOD

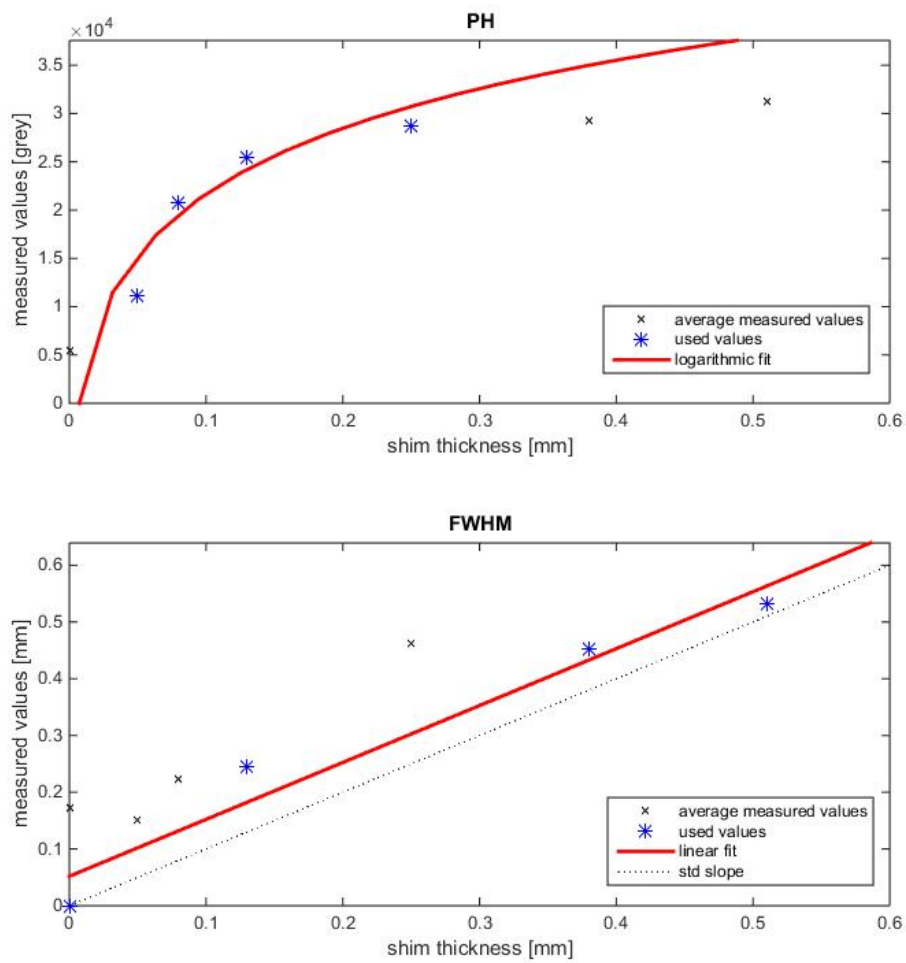


Figure 65: Measured values and fitting curves for the BD calibration sample. Top: PH method. Bottom: FWHM method.

4.2 FRACTURE APERTURE MEASUREMENTS WITH COMBINED PH AND FWHM METHOD

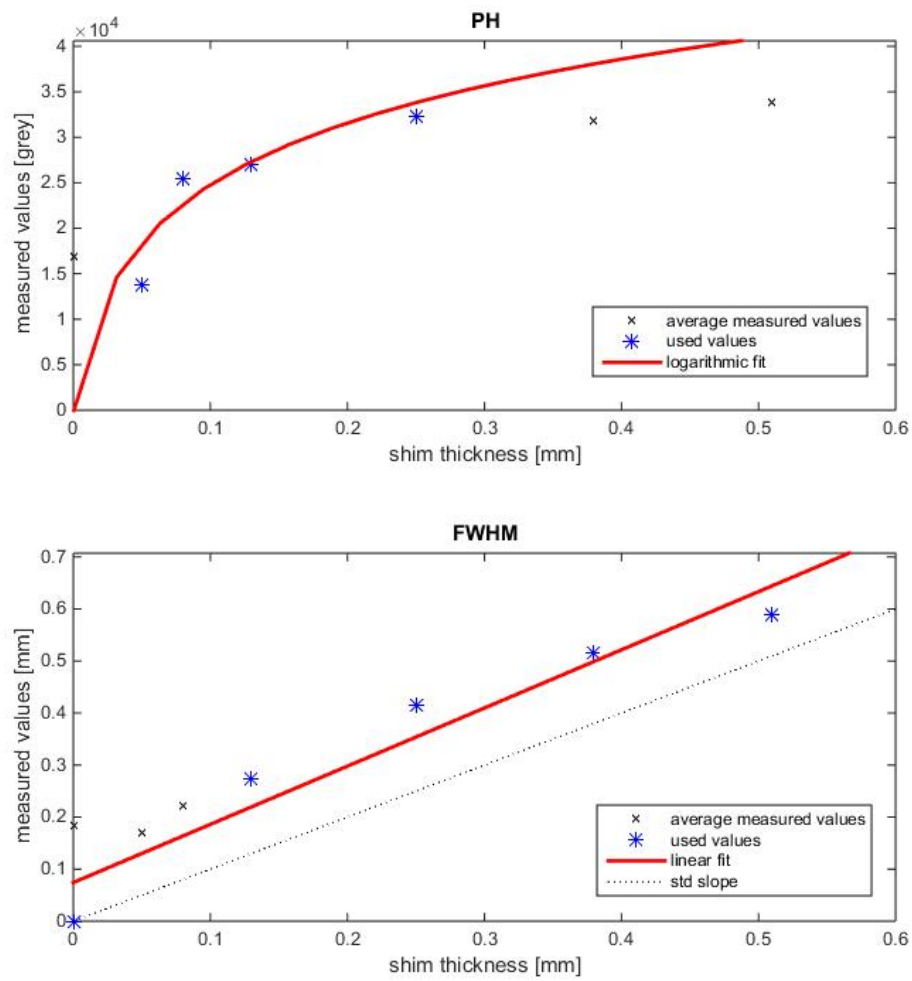


Figure 66: Measured values and fitting curves for the SAC calibration sample. Top: PH method. Bottom: FWHM method.

4.2 FRACTURE APERTURE MEASUREMENTS WITH COMBINED PH AND FWHM METHOD

BAKER DOLOMITE

Shim thickness [mm]	PH mean [mm]	PH std dev [mm]
0.00	0.0244	0.0220
0.05	0.0385	0.0177
0.08	0.0974	0.0169
0.13	0.1543	0.0166
0.25	0.2107	0.0161
0.38	0.2207	0.0164
0.51	0.2679	0.0157

Table 4: Calibration measurement with the PH method for Baker Dolomite

BAKER DOLOMITE

Shim thickness [mm]	FWHM mean [mm]	FWHM std dev [mm]
0.00	0.1215	0.0485
0.05	0.0900	0.0212
0.08	0.1717	0.0221
0.13	0.1916	0.0176
0.25	0.4086	0.0184
0.38	0.3938	0.0168
0.51	0.4796	0.0314

Table 5: Calibration measurement with the FWHM method for Baker Dolomite

4.2 FRACTURE APERTURE MEASUREMENTS WITH COMBINED PH AND FWHM METHOD

SAN ANDREAS

Shim thickness [mm]	PH mean [mm]	PH std dev [mm]
0.00	0.0509	0.0161
0.05	0.0380	0.0160
0.08	0.1158	0.0134
0.13	0.1346	0.0134
0.25	0.2199	0.0127
0.38	0.2120	0.0130
0.51	0.2566	0.0122

Table 6: Calibration measurement with the PH method for San Andreas Carbonate

SAN ANDREAS

Shim thickness [mm]	FWHM mean [mm]	FWHM std dev [mm]
0.00	0.0968	0.0035
0.05	0.0853	0.0245
0.08	0.1313	0.0123
0.13	0.1775	0.0060
0.25	0.3035	0.0134
0.38	0.3947	0.0282
0.51	0.4607	0.0213

Table 7: Calibration measurement with the FWHM method for San Andreas Carbonate

As we see from the calibration data (Tables 4 to 7), the FWHM method always predicts values that are too large for small apertures, whereas the apertures measured with the PH method do not increase significantly anymore for larger calibration apertures.

The mean absolute errors for all rock samples and both calibration methods are listed in table 8.

4.2 FRACTURE APERTURE MEASUREMENTS WITH COMBINED PH AND FWHM METHOD

BD PH	BD FWHM	SAC PH	SAC FWHM
± 0.0740	± 0.0739	± 0.0793	± 0.0498

Table 8: Mean absolute errors of the fit functions respective rock type

The above data shows that we can measure fracture apertures with a resolution of approximately $75\mu\text{m}$. In other words, we cannot resolve fractures below $75\mu\text{m}$. We hence set voxels where the fracture aperture may be lower than $75\mu\text{m}$ to 10^{-22} mm and treat them as areas where the fracture has asperities, i.e. the fracture walls are in contact with each other. The fitting curves further indicate that an aperture of about 0.2 mm is the maximum aperture that can be detected in the PH method. Therefore we have an acceptance interval for the PH method from 0.075 - 0.2 mm. Above this interval, we measure with the FWHM method. Each voxel has a size of 30 microns hence the resolution for the FWHM method is 0.30 microns .

4.2.2 Aperture measurements

The fracture aperture distribution of the actual core samples of SAC and BD can then be analysed. As each sample is approximately 10 cm long and did not fit completely in the camera frame, we scanned the top and the bottom half separately. We employed a rectangular piece of copper foil as a marker glued to the side of the cores, visible in both top and bottom images. The datasets of the top and the bottom half could then be aligned in 3D with Avizo and combined to form a single dataset for each core.

Using the same post-scan refinement procedures in the calibration scans as in the actual sample scans is mandatory as the measurement methods are based on the grey values. We therefore apply the exact same reconstruction, artefact removal, slice normalization and gain correction procedures to the images of the scans of the core samples, as we used for the calibration scans. Also, we apply the same Gaussian filter to remove the same amount of noise in the reconstructed images. The same ridgeline algorithm as for the calibration pieces is then applied slicewise to the 3D data, to obtain the peak valleys of the fracture signal. We assume that the fractures are nearly

4.2 FRACTURE APERTURE MEASUREMENTS WITH COMBINED PH AND FWHM METHOD

perpendicular to the slices which allows to measure the aperture in each ridgeline position in the same direction.

From this procedure the x , y , and z location of the fractures are calculated, resulting in a 3D point cloud representing the fracture topology. This topology can be used later for a 3D representation of the fracture as 2D surface.

Then, each ridgeline location is analyzed. If the grey value is inside the acceptance interval for the PH method, the PH fitting curve is applied to calculate the aperture from the measured grey values. If the difference in grey values is too small, the aperture is below the measurable resolution and the fracture aperture value is set to 10^{-22} mm. This value can be later corrected for and serves as a marker for the contact area of the fracture. If the difference in grey values between PH signal and average rock value is too large, we obtain a measurement close to air. We therefore need to apply the FWHM method. We hence count the voxels across half the height in the signal and use the FWHM fitting curve to relate this value to the actual aperture. The resulting fracture aperture distributions and topologies are shown in fig. 67.

4.2 FRACTURE APERTURE MEASUREMENTS WITH COMBINED PH AND FWHM METHOD

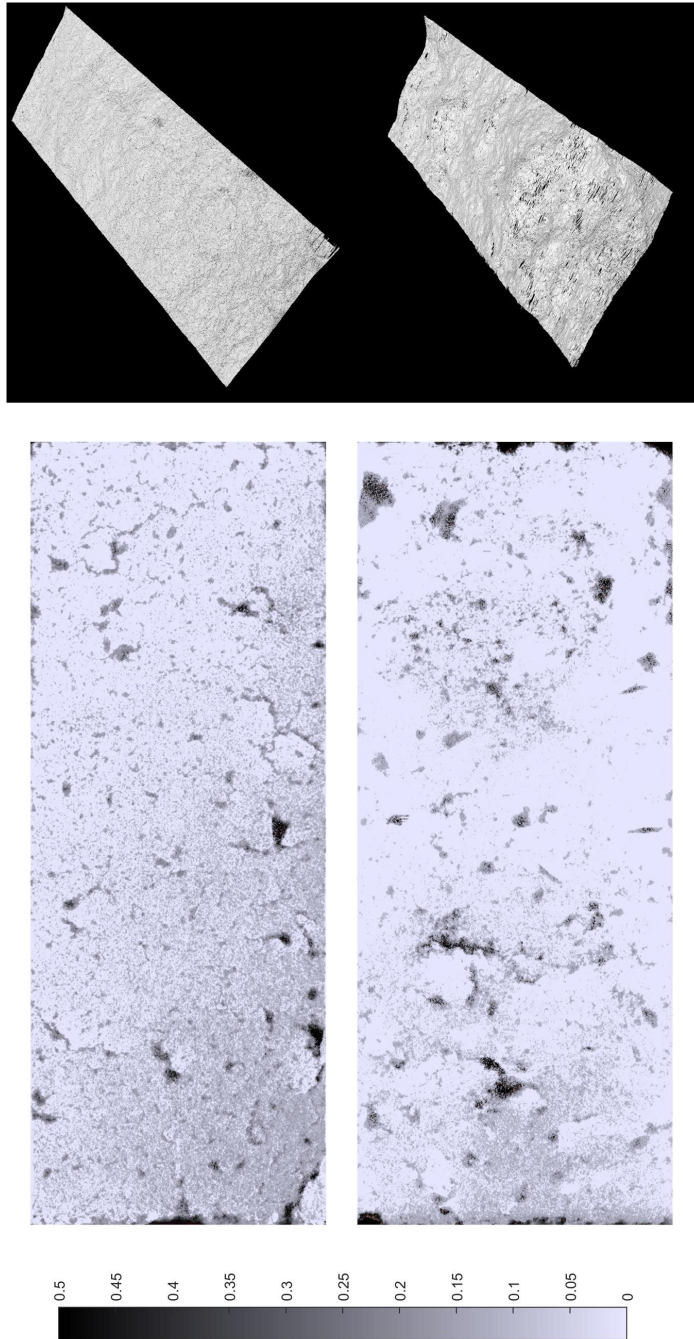


Figure 67: Fracture aperture distributions [mm] (left) and topology (right). Top: BD, Bottom: SAC (see fig. 22). Voxel resolution 23.6 μm . Dimension of the fractures is 3.8 by ~ 10 cm.

4.3 STATISTICAL ANALYSIS OF FRACTURE APERTURE

4.3 STATISTICAL ANALYSIS OF FRACTURE APERTURE

4085741 voxels corresponding to the fracture in the BD core were found. 41.2% of which were measured with the PH method, and 1.7% were measured with the FWHM method. 57.0% of the apertures were measured as 10^{-22} mm, representing the areas where the fracture walls are in contact with each other. 3577779 voxels corresponding to the fracture in the SAC core were found, as the measurement field was a bit smaller. 21.8% of which were measured with the PH method, and 2.6% were measured with the FWHM method. 75.6% of the apertures were measured as 10^{-22} mm.

Using these datasets, we computed the following properties of the fractures: The arithmetic mean aperture for the BD is 0.0500 mm with a standard deviation of 0.0699 mm, for SAC it is 0.0333 mm with a standard deviation of 0.0949 mm. The maximum aperture measured for the BD is 1.1146 mm, and for the SAC 2.8566 mm. The histograms of the apertures are shown in fig. 68. An autocorrelation analysis gives the correlation lengths for which we obtain $x_l = 0.0150$ mm and $y_l = 0.9446$ mm for the BD sample and $x_l = 0.0150$ mm and $y_l = 1.0346$ mm for the SAC sample.

A comparison of the BD and SAC samples regarding the statistical analysis can be found in table 9.

4.3 STATISTICAL ANALYSIS OF FRACTURE APERTURE

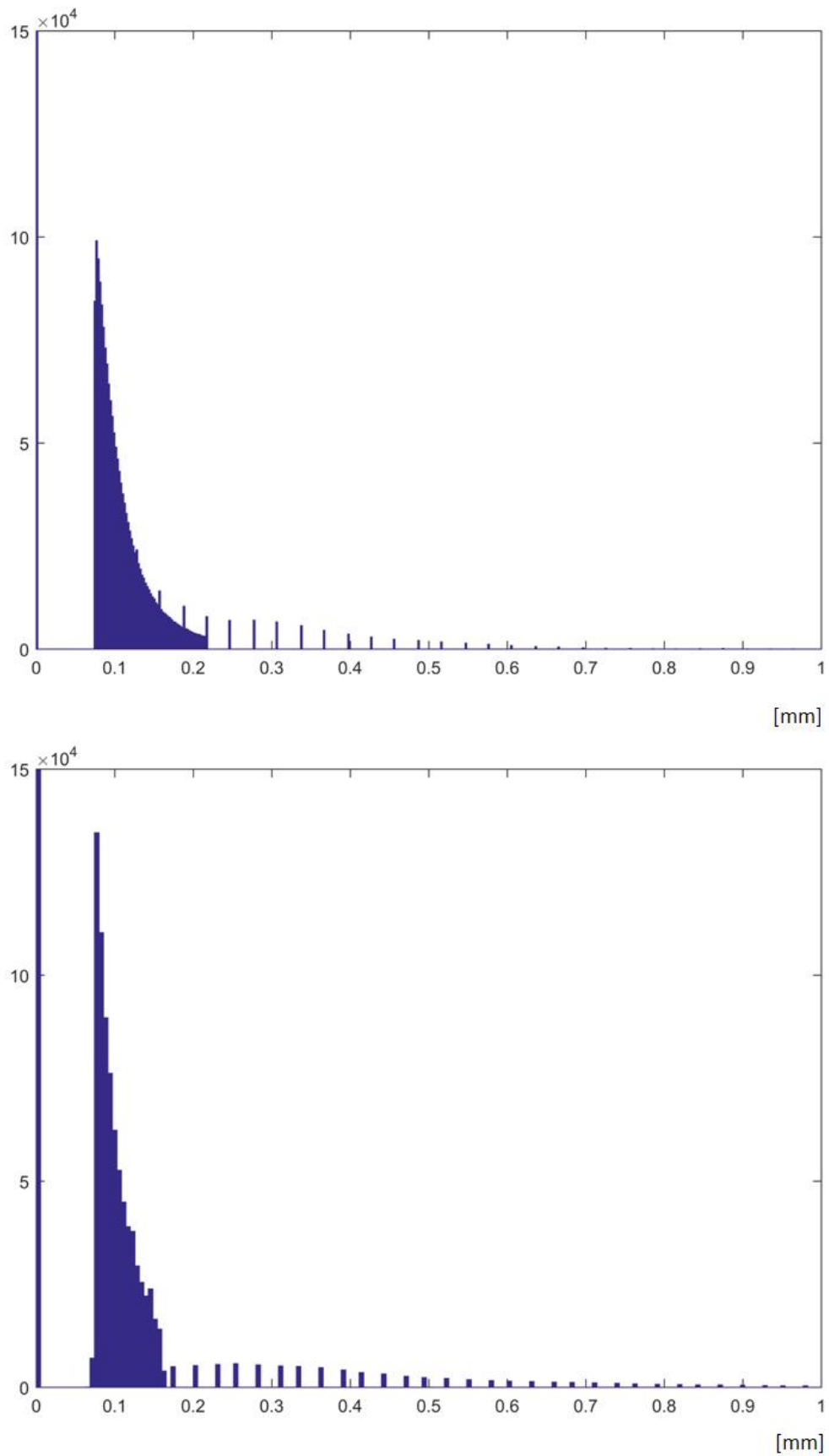


Figure 68: Top: Histogram of apertures measured for BD. Bottom: Histogram of apertures measured for SAC. For clarity, apertures larger than 1 mm are not shown.

4.4 DISCUSSION

	BD	SAC
fracture locations	4085741	3577779
PH portion	41.2%	21.8%
FWHM portion	1.7%	2.6%
zero apertures	57.0%	75.6%
max aperture	1.1146 mm	2.8566 mm
x_l	0.0150 mm	0.9446 mm
y_l	0.0150 mm	1.0346 mm

Table 9: Comparison of BD and SAC regarding the statistical analysis

4.4 DISCUSSION

Both fractures are similar regarding the statistical values. Whereas the BD has a slightly larger mean aperture than the SAC, the maximum measured aperture is larger for the SAC. The samples differ little in their correlation lengths. In general, rough surfaces usually have a short correlation length, while smoother surfaces have a long correlation length. From the obtained values, we assume the surface of the BD to be rougher than the SAC, which is not clear to visibly inspect from the aperture distribution alone in fig. 67. On the contrary, the topology of the fractures indicates that the BD surface is smoother than the SAC surface. This discrepancy is possibly due to relatively high error estimation of the measurement method (see below).

We also see wider apertures along the sides of the core and at the inlet and outlet of the fractures, probably due to the producing process of splitting the core samples with the modified Brazilian test (cf. section 2.2). This may have an influence on the flow patterns evolving in these samples.

In the histograms, we see at the very left one bar depicting the apertures set to 10^{-22} mm. This contains the contact area of the fractures. The apertures themselves seem to follow a gamma distribution. To the right the histogram shows single separate peaks. For larger values the FWHM can only measure in steps of the voxel size, which causes the discrete steps in aperture sizes.

4.4 DISCUSSION

Most striking in the statistical analysis is the large amount of apertures below the acceptance interval for the PH method. 57.0% and 75.6% of the apertures for BD and SAC, respectively, were measured as 10^{-22} mm. The contact areas are included in these portions, but the measurement error of about $75 \mu\text{m}$ plays a significant role also. To ensure a more accurate measurement with better resolution, a larger set of calibration measurements would be needed. We used only seven different aperture sizes to obtain the calibration fit curves, but as the PH method only applies in the lower range and the FWHM method only in the upper range, we have each only 4 values to fit the curves to. Using more shims, or a feeler gauge could decrease the mean absolute error of the measurements.

As we see from the values obtained from the calibration measurements (tables 4 - 7), noise/pores still play a significant role in the data analysis. Applying more severe smoothing filters is problematic, as the slit in the calibration image is a very fine feature and can easily be biased. Kaestner et al., 2008 [100] suggest to use other filters, for example non-linear diffusion filters, which essentially do not smooth the edges of homogeneous areas in images. However, it is unclear how a fine feature such as a slit or fracture would be treated. To avoid noise in the first place, a different scanning method would be advisable. Scanning with a higher resolution for example would lead more accurate results. This could be achieved by using a camera with better resolution, or stronger hardware filters, which would need a higher energy level though to be able to be penetrated. CT scanning at a synchrotron facility would probably lead to improved results, it needs to be accessible though as well for the full 3D scans, as the imaging procedure needs to be the same for the calibration and the actual measurement.

5

FLOW EXPERIMENTS

5.1 EXPERIMENTAL SET-UP

In this chapter the flow experiments are presented, which were carried out on the BD and SAC samples (chapter 4). The aim of the experiments is to analyse how the fracture and the fracture aperture distribution influences the flow of water and oil.

For the flow experiments to be observed with the CT, a special flow cell was constructed (section 2.8). In the flow cell the fractured rock is bonded to two epoxy platens, one at each end, with a thin rubber jacket surrounding the whole apparatus (fig. 69, 70). The epoxy platens on both ends are slit to extend the fracture inside the rock core along the epoxy. The two halves are then separable again, allowing to reuse the core in future experiments.

The experiments were carried out with the sample being initially water saturated. The sample was assembled under water with flowing fluid to ensure that all air bubbles are expelled from the system. Deionized H₂O was used as the pore fluid for all experiments.

For the experimental setup, a syringe pump was attached to the inlet epoxy of the flow cell, ensuring a constant inflow rate of 10 ml hr⁻¹. The porous medium header and fracture header (water tanks) were set up at the same height to ensure a constant pressure differential over porous medium and fracture (fig. 71). A differential pressure gauge was not installed for these experiments. The flow direction of the brine or oil is vertical from bottom to top. Fluid is permitted to flow in the fracture and is freely able to enter into and drain from the porous medium. The flow cell does not

5.1 EXPERIMENTAL SET-UP

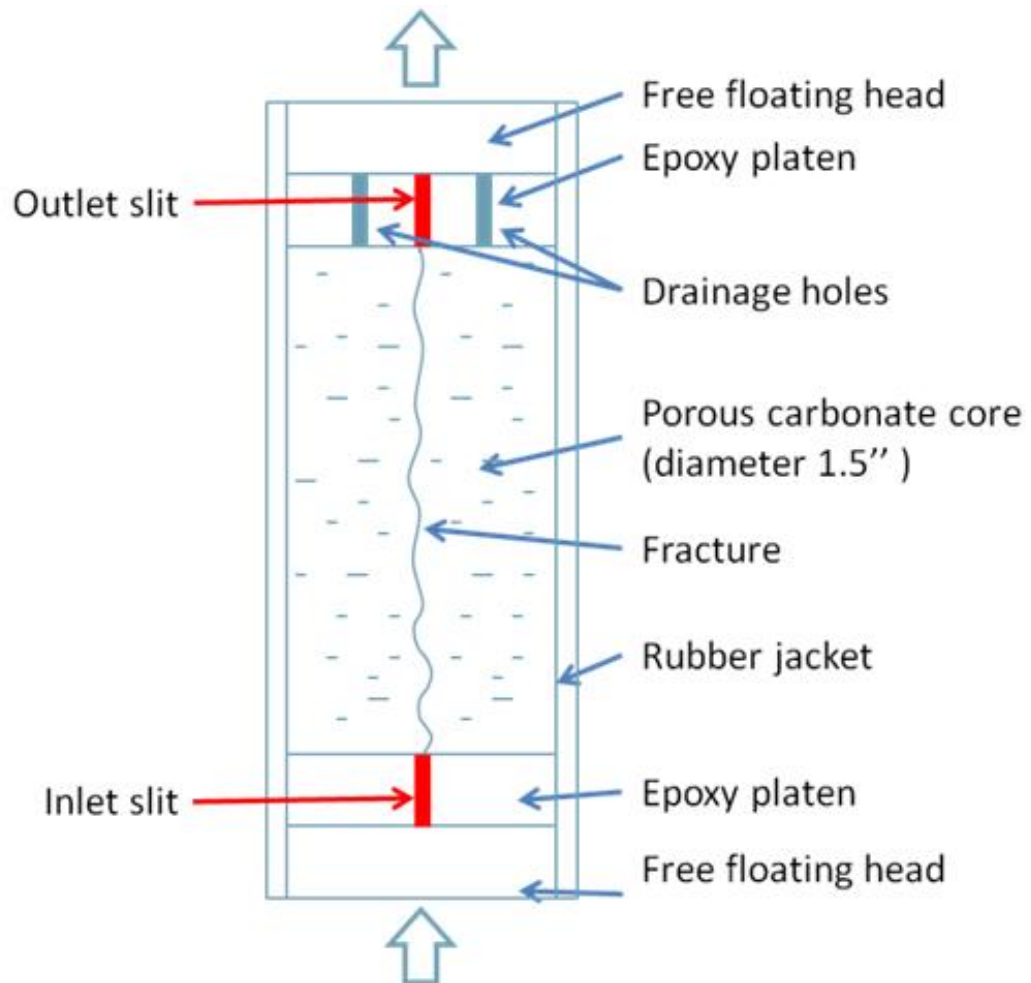


Figure 69: Sketch depicting the flow cell construction. The flow cell mainly consists of two epoxy platens that extend the core. A thin latex jacket surrounds the core.

5.1 EXPERIMENTAL SET-UP



Figure 70: Flow cell with BD sample. The bottom tube connects to the inlet slit, whereas the top tubes comprise the fluid outlet for the fracture and the drainage outlets for the rock matrix.

5.2 SINGLE-PHASE FLOW EXPERIMENTS

fit fully in the camera frame, which is why in the images the fluid outlets cannot be seen.

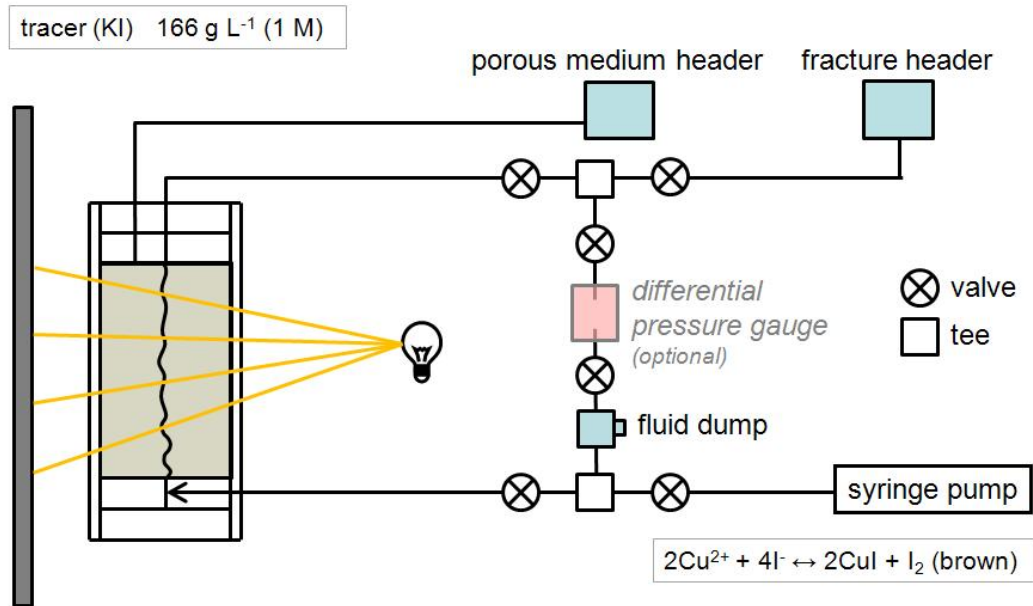


Figure 71: Experimental set-up. A syringe pump ensures a constant inflow rate. The flow direction of the brine or oil is from bottom to top. The porous medium header and fracture header were set up at the same height to ensure a constant pressure differential between fracture and matrix. Copper (II) sulfate (CuSO_4) was used to check for iodine (I^-) at the fracture and porous medium outlets.

5.2 SINGLE-PHASE FLOW EXPERIMENTS

Tracer enriched water was injected into the fluid-saturated sample from the bottom. The sample does not contain a tracer at the start of the experiment. As tracer fluid 1M potassium iodide (KI) solution (166 g L^{-1}) was used for the tracer.

During the experiments we imaged a series of X-ray radiographs, i.e. only 2D images in front and side view were taken during the flow process. For the data collection, 120 kV tube voltage and $670 \mu\text{A}$ tube current were used. The exposure time for a single image was 2 sec. With the overhead of rotating the table and reading out the frame grabber of the camera, each image acquisition time was about 8.8 sec. A 0.5 mm thick copper filter was used in front of the detector. 10 dark current (DC) images were taken with

5.2 SINGLE-PHASE FLOW EXPERIMENTS

the X-ray tube switched off. Also, 10 flat field (FF) images were taken with the flow cell already in place. The new piecewise quadratic procedure then subtracts the core and water information from the images, such that only the tracer fluid is visible in the radiographs.

For the first experiments, two separate runs were carried out, one looking on top of the fracture plane and one looking at the side of the fracture. As the flow was found to be slow enough, the control software was adjusted to alternate the table 90° back and forth. By this, front and side view can be imaged in the same experiment.

For the first set of experiments, the BD sample was used. Water containing the KI tracer was injected at a constant flow rate of 10 mL hr⁻¹. The first experiment ran for 36 min. Two repeat experiments were carried out in front view and three repeat experiments in side view. These experiments ran for 60-65 minutes. (fig. 72, 73). An overview of the experiments can be found in table 10. However, air bubbles have been trapped in the inlets slits in these experiments and hence they were not used for the modelling comparison.

After each run the whole flow system was backflushed with water. Copper (II) sulfate (CuSO₄) was used to check for iodine (I⁻) at the fracture and porous medium outlets. If tested positive, a brown precipitation occurs. After one hour, precipitation could be detected at the fracture outlet, not at the porous medium outlet though, which indicates that the flow in the fracture dominates the flow experiments in BD. Nonetheless, the partial matrix invasion can be seen in the side views (fig. 73 bottom row).

Relative breakthrough curves (BTC) can be calculated from the images by assuming a concentration of 1 at the fracture inlet (in the front views). At the fracture outlet a small stripe of the fracture serves as indicator area. The grey values in this area are averaged and recorded over the experimental run. Results can be seen in fig. 74.

A long run experiment on the BD sample for a flow duration of 2 hrs. 45 min. was carried out to see if matrix fluid invasion could be obtained up to the top of the sample (fig. 75, 76) with one replica experiment showing the same flow pattern evolving. A heterogeneous flow pattern emerges in the fracture as well as in the matrix again. The matrix was drained this time up close to the outlet as can be seen in the side-on views (fig. 75, 76 top row).

5.2 SINGLE-PHASE FLOW EXPERIMENTS

Breakthrough curves were calculated as described above (fig. 77). The flow pattern is contrasted to the fracture aperture distribution in fig. 78.

Experiment	Duration	Images	View	Flow rate
BD ₁	36 min	252	front	10 mL hr ⁻¹
BD ₂	60.8 min	417	front	10 mL hr ⁻¹
BD ₃	64 min	437	front	10 mL hr ⁻¹
BD ₄	60.8 min	422	side	10 mL hr ⁻¹
BD ₅	64 min	434	side	10 mL hr ⁻¹
BD ₆	65 min	442	side	10 mL hr ⁻¹
BD ₈	165 min	1108	front/side	10 mL hr ⁻¹
BD ₉	174 min	1154	front/side	10 mL hr ⁻¹

Table 10: Single-Phase Baker Dolomite Flow Experiments

5.2 SINGLE-PHASE FLOW EXPERIMENTS

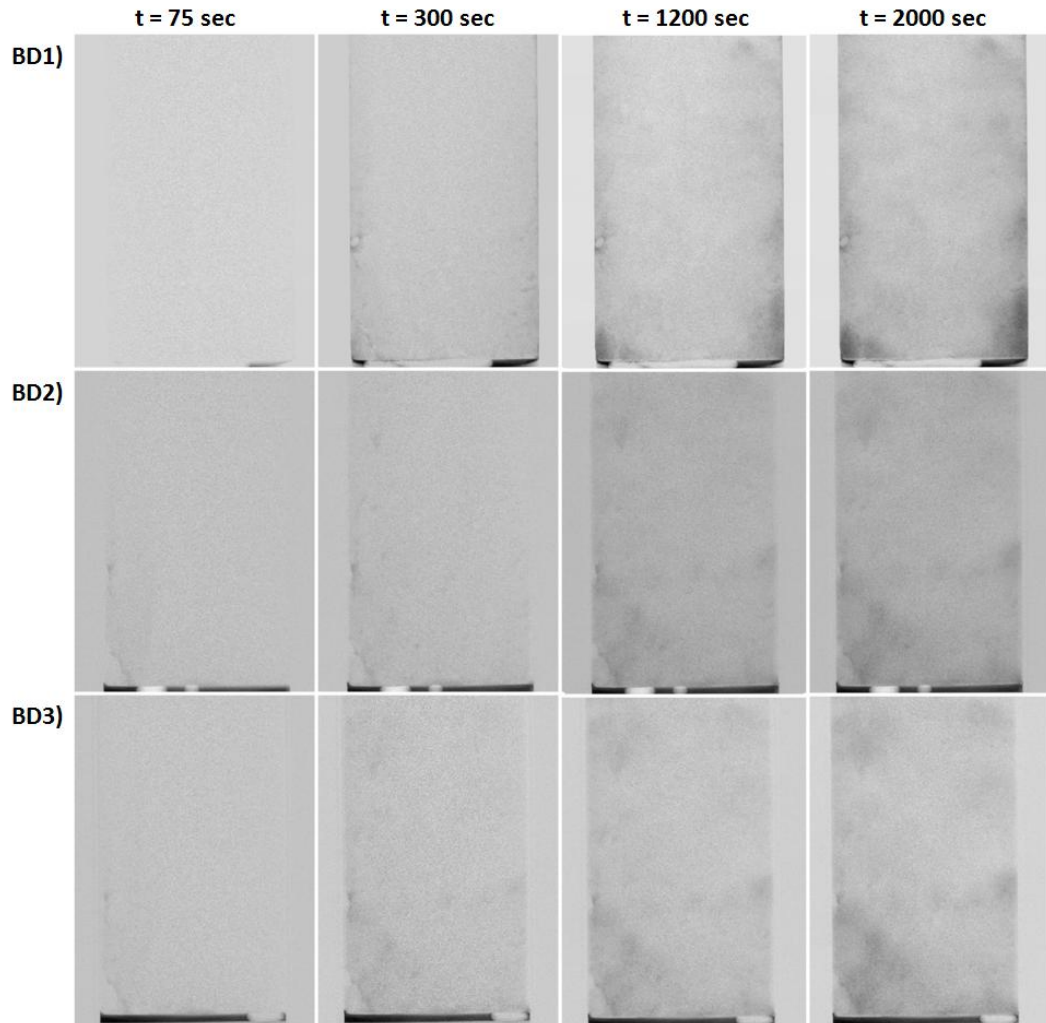


Figure 72: Single-phase flow experiments in BD. Top row: BD1. Middle row: BD2. Bottom row: BD3 (cf. table 10). Each column presents the flow patterns in frontal view of the fracture (i.e. the fracture is located perpendicular to the view plane). The images have been recorded at 75, 300, 1200, 2000 seconds after injection commenced. Darker colours indicate higher concentrations of the KI tracer. Note the different air bubbles present in the inlet slit of the flow cell. The bubbles did not change size or position during the runs.

5.2 SINGLE-PHASE FLOW EXPERIMENTS

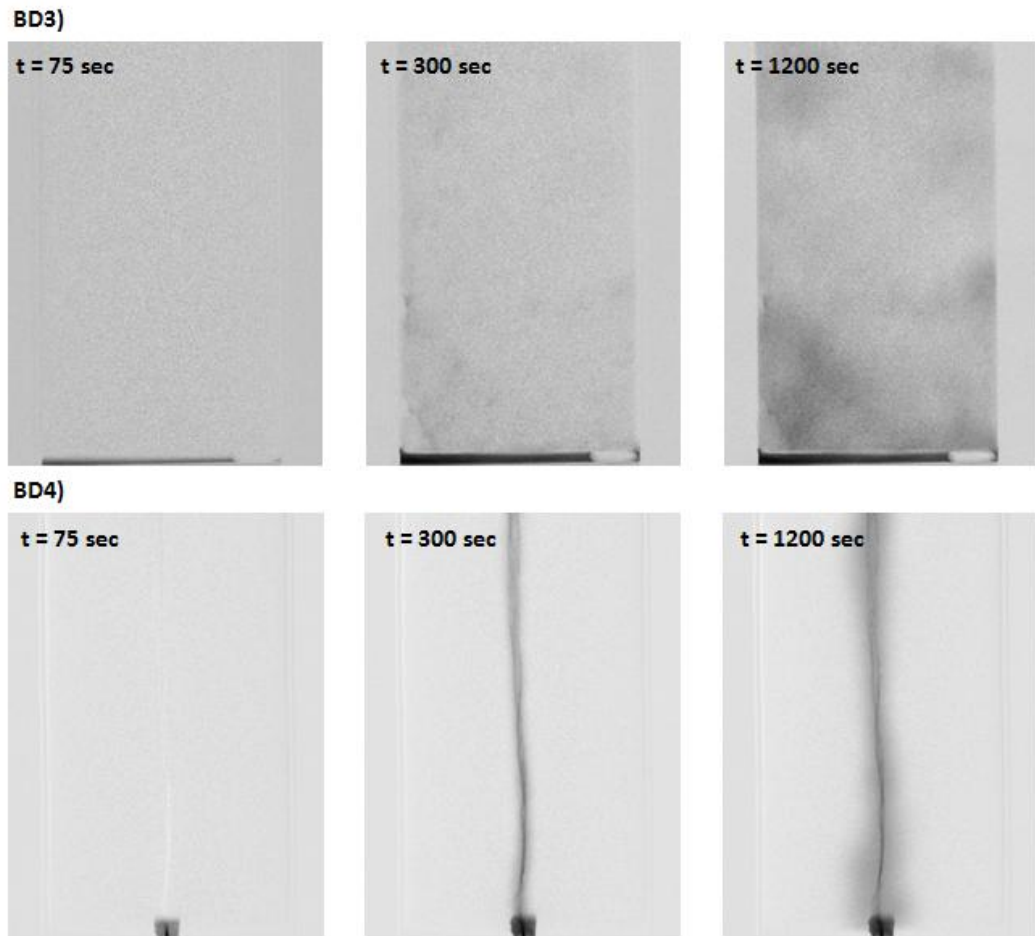


Figure 73: Juxtaposition of experiments BD3 and BD4 (cf. table 10). Each column presents the flow patterns in frontal and side view of the fracture (i.e. the fracture is located perpendicular, or along to the view plane, respectively). The images have been recorded at 75, 300, 1200 seconds after injection commenced. Darker colours indicate higher concentrations of the KI tracer.

5.2 SINGLE-PHASE FLOW EXPERIMENTS

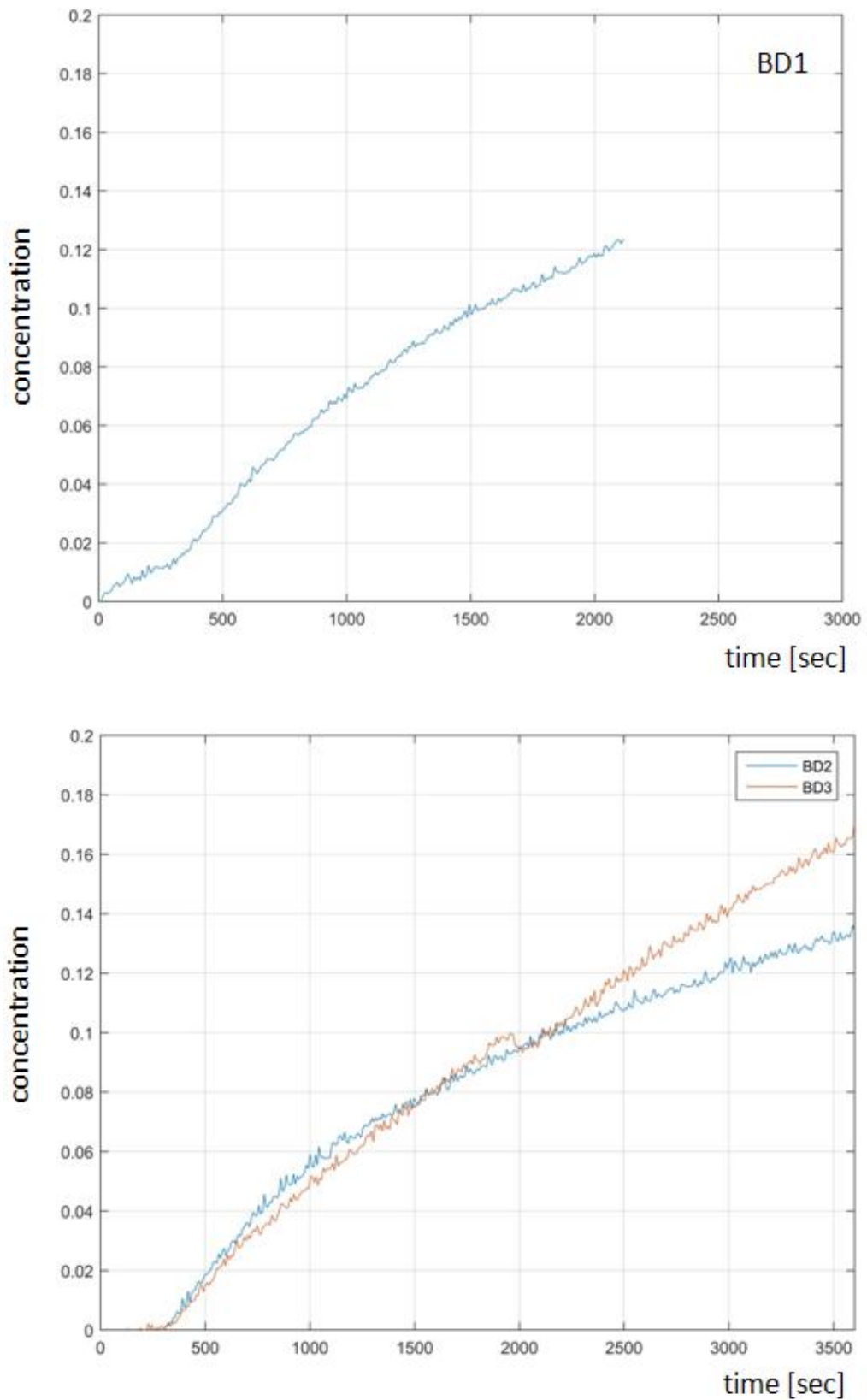


Figure 74: Breakthrough curves (BTC) for experiments BD1 (top) and BD2 and BD3 (bottom) (cf. table 10).

5.2 SINGLE-PHASE FLOW EXPERIMENTS

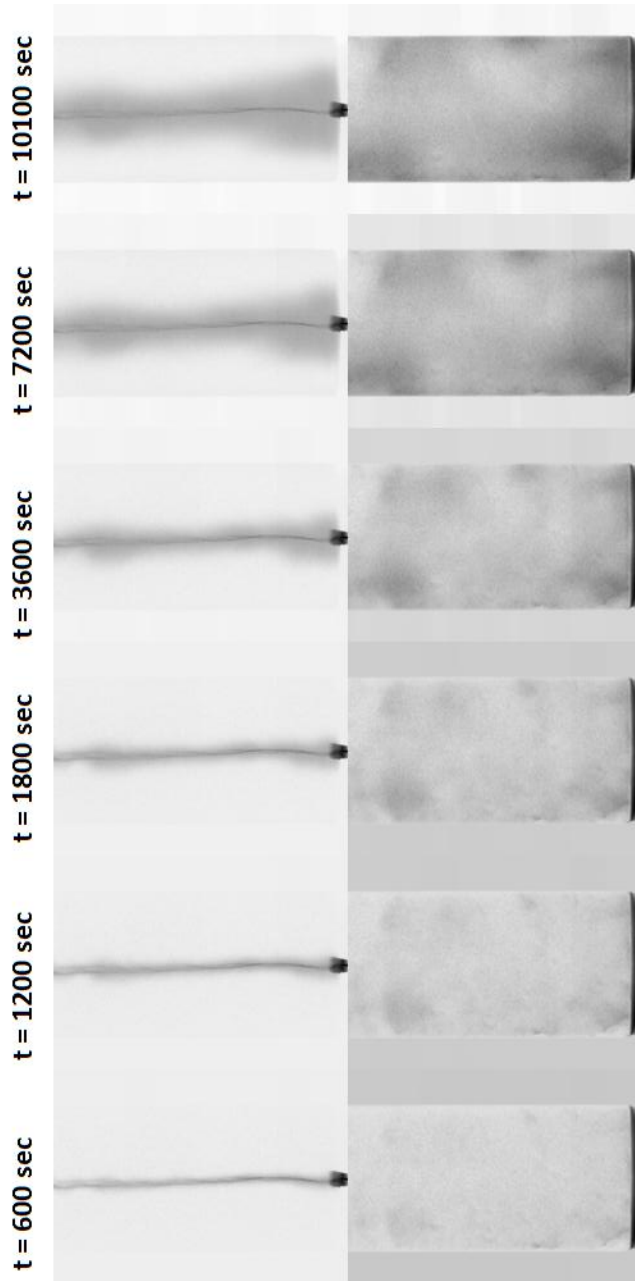


Figure 75: Single-phase flow experiment in BD8 (cf. table 10). Each column presents the flow patterns in frontal and side view of the fracture (i.e. the fracture is located perpendicular, or along to the view plane, respectively). The images have been recorded at 600, 1200, 1800, 3600, 7200, 10100 seconds after injection commenced. Darker colours indicate higher concentrations of the KI tracer. Heterogeneous flow patterns are emerging in matrix and fracture.

5.2 SINGLE-PHASE FLOW EXPERIMENTS

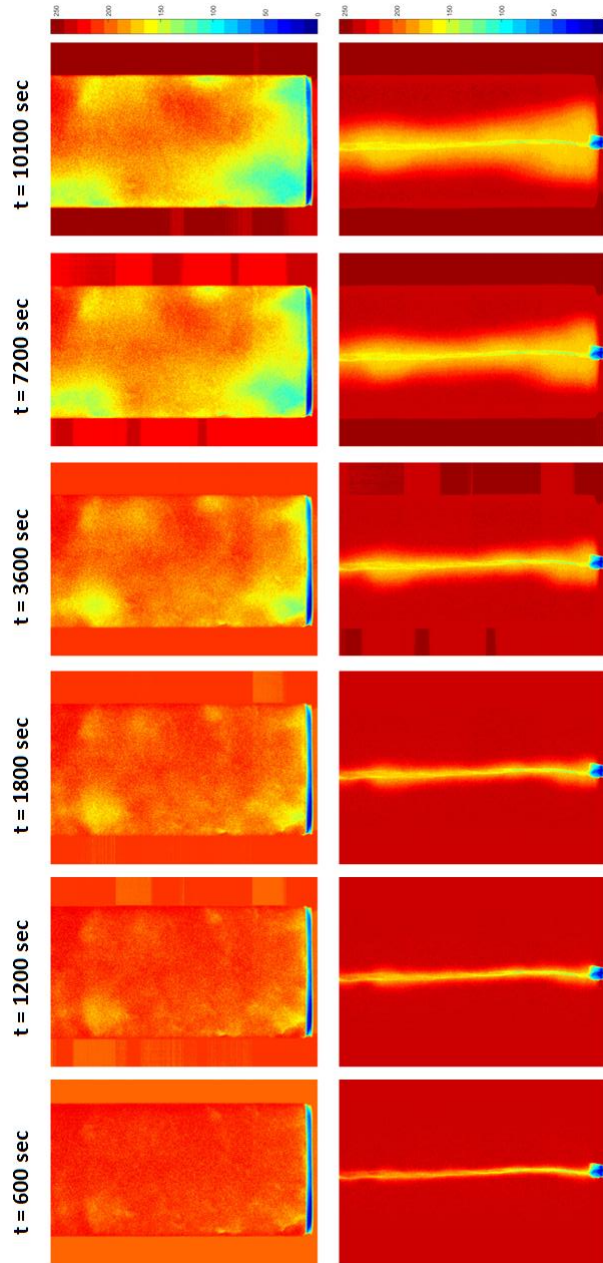


Figure 76: Contour plot of single-phase flow experiment BD8 (cf. table 10). Each column presents the flow patterns in frontal and side view of the fracture (i.e. the fracture is located perpendicular, or along to the view plane, respectively). The images have been recorded at 600, 1200, 1800, 3600, 7200, 10100 seconds after injection commenced. Darker colours indicate higher concentrations of the KI tracer. Colored according to grey values (0 - 255) in images. Heterogeneous flow patterns are emerging in matrix and fracture.

5.2 SINGLE-PHASE FLOW EXPERIMENTS

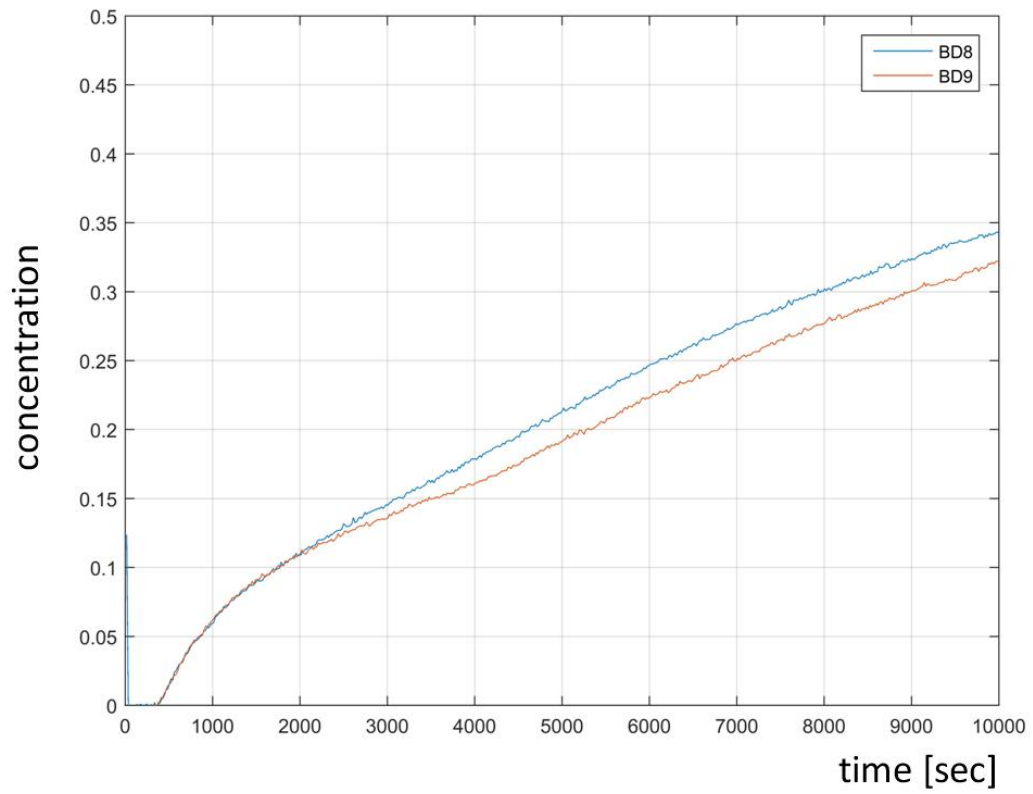


Figure 77: Breakthrough curves (BTC) from experiments BD8 and BD9 (cf. table 10).

5.2 SINGLE-PHASE FLOW EXPERIMENTS

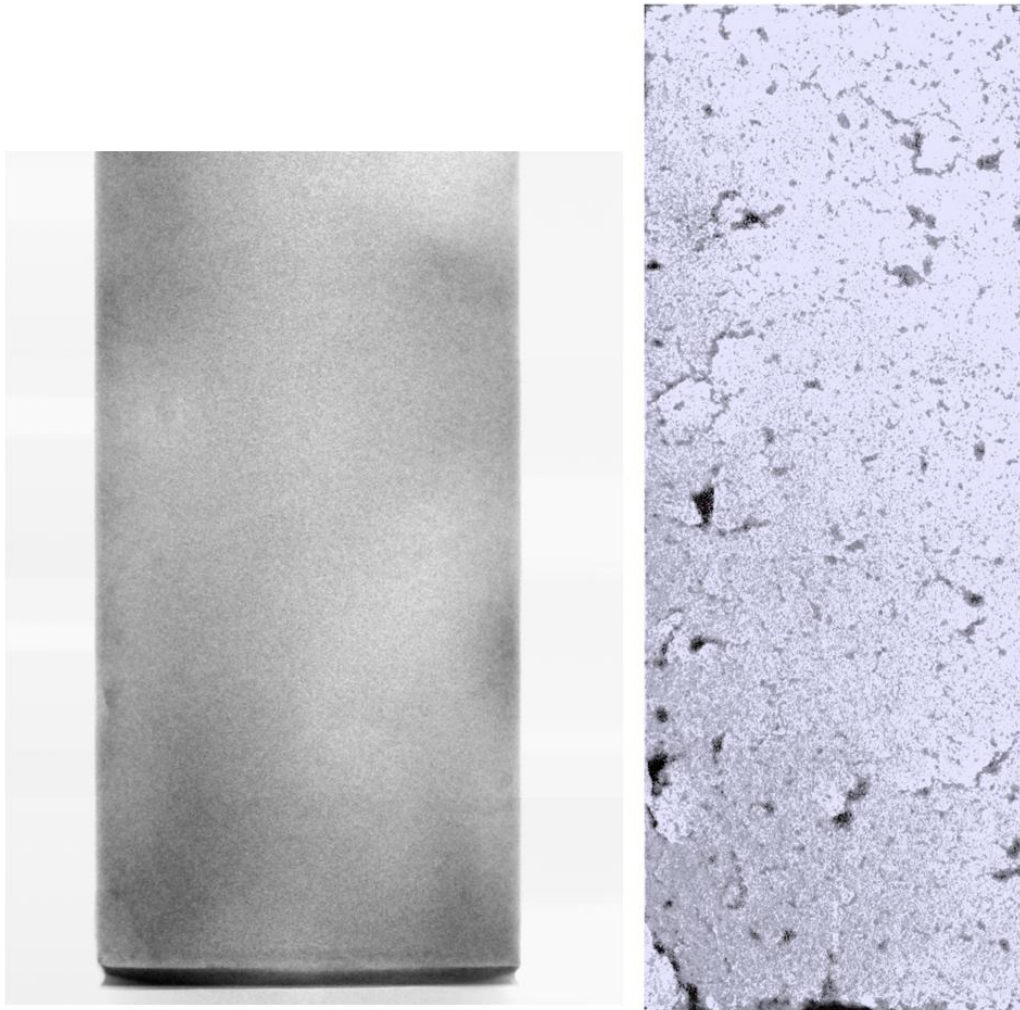


Figure 78: Comparison of tracer distribution after 168 minutes in experiment BD8 (table 10) in frontal view of the fracture and the fracture aperture distribution of the BD sample.

5.2 SINGLE-PHASE FLOW EXPERIMENTS

A second set of experiments was carried out with the SAC sample. The flow rate was again 10 mL hr^{-1} . The experiments ran for 2 hrs. 30 min., and 3 hrs. and 3 min., respectively (fig. 79, 80). Most of the KI tracer exited via the porous medium header, which matches with the observations from the side-on views (fig. 79, 80 bottom row). An overview of the experiments can be found in table 11. The breakthrough curves of SAC₁ and SAC₂ show good agreement with each other (fig. 81). The flow pattern is compared to the fracture aperture distribution in fig. 82.

Experiment	Duration	Images	View	Flow rates
SAC ₁	150 min	995	front/side	10 mL hr^{-1}
SAC ₂	183 min	1233	front/side	10 mL hr^{-1}

Table 11: Single-Phase San Andreas Carbonate Flow Experiments

5.2 SINGLE-PHASE FLOW EXPERIMENTS

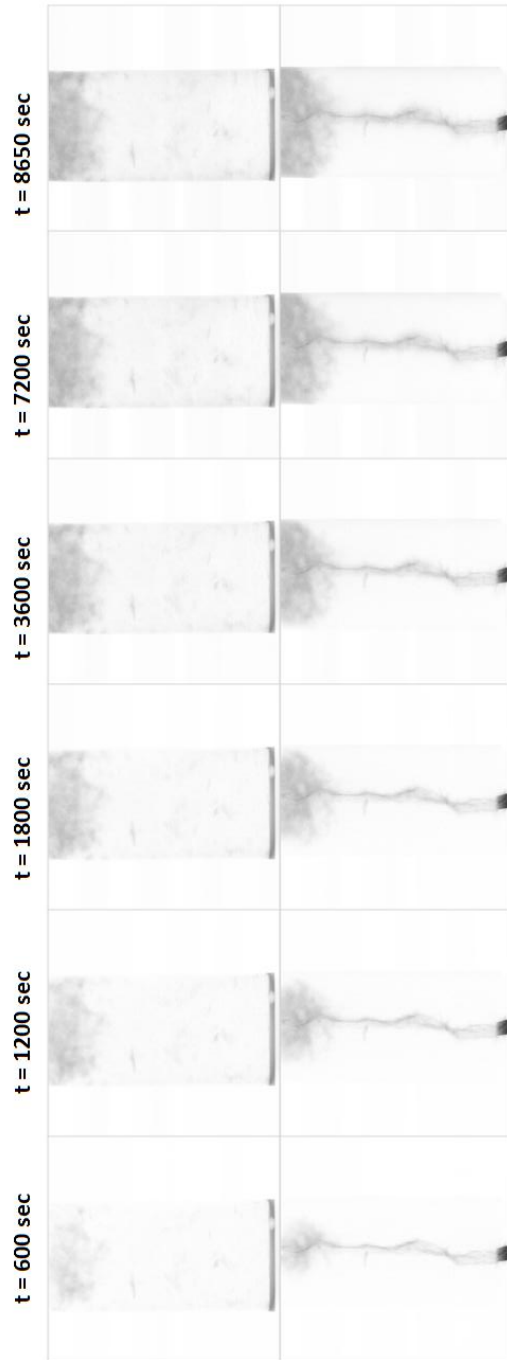


Figure 79: Single-phase flow experiment in SAC₁ (cf. table 11). Each column presents the flow patterns in frontal and side view of the fracture (i.e. the fracture is located perpendicular, or along to the view plane, respectively). The images have been recorded at 600, 1200, 1800, 3600, 7200, 8650 seconds after injection commenced. Darker colours indicate higher concentrations of the KI tracer. Heterogeneous flow patterns are emerging in matrix and fracture. Note how the matrix is invaded preferentially in the top part of the matrix.

5.2 SINGLE-PHASE FLOW EXPERIMENTS

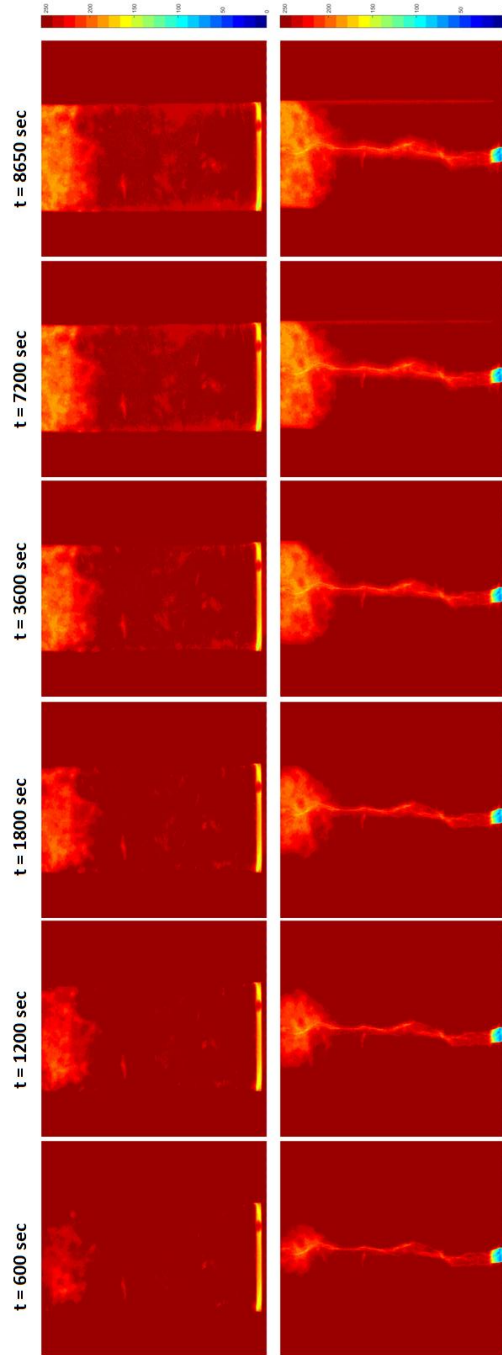


Figure 80: Contour plot of single-phase flow experiment in SAC1. Each column presents the flow patterns in frontal and side view of the fracture (i.e. the fracture is located perpendicular, or along to the view plane, respectively). The images have been recorded at 600, 1200, 1800, 3600, 7200, 8650 seconds after injection commenced. Colored according to grey values (0 - 255) in images. Heterogeneous flow patterns are emerging in matrix and fracture. Note how the matrix is invaded preferentially in the top part of the matrix.

5.3 TWO-PHASE FLOW EXPERIMENTS

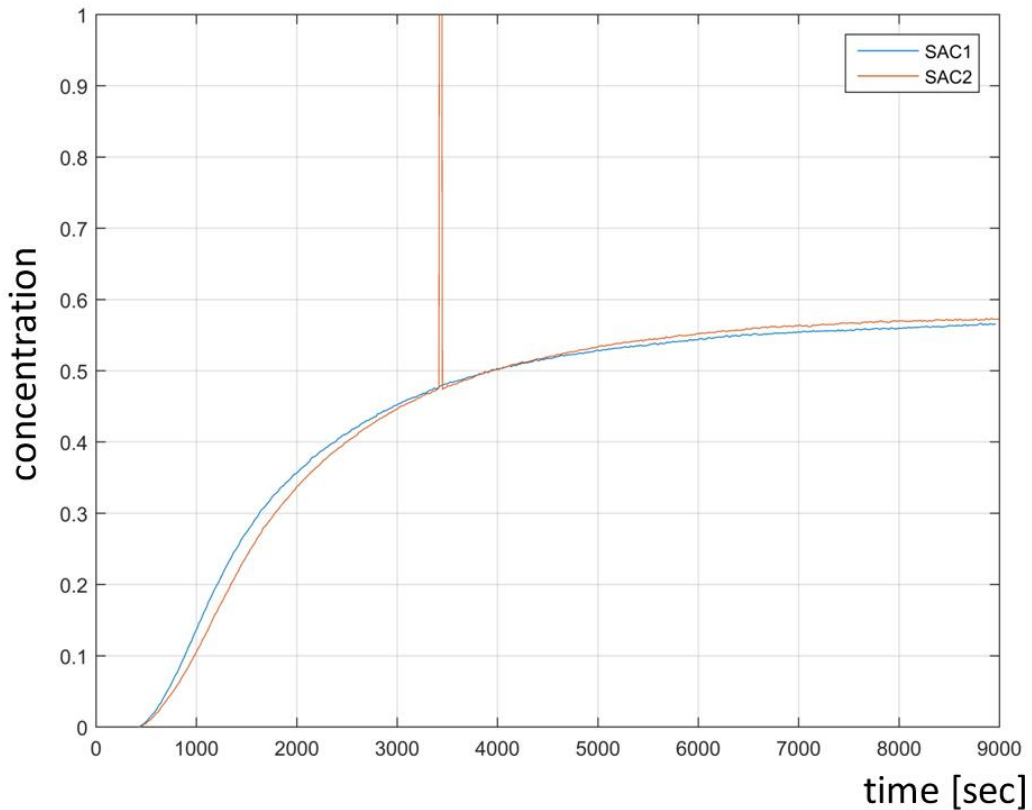


Figure 81: Breakthrough curves (BTC) from experiments SAC1 and SAC2. The outlier in experiment SAC2 is due to the X-ray source losing power for taking a couple of images.

5.3 TWO-PHASE FLOW EXPERIMENTS

The experimental set up was the same as for the single phase flow experiments. The BD sample was initially water saturated. A mixture of 50:50 dodecane-iododecane oil was injected, displacing the water. We used DC and FF images again to visualize the fluid invasion in fracture and core. The governing equations for two-phase flow can be found in the appendix A.1.

The flow rates for the individual runs were varied with floods at 1, 10, 50 mL hr⁻¹. The experiments were carried out in two stages. First, the sample is flooded with dodecane-iododecane. Afterwards the sample is flooded again with water. Initially, a flow rate of dodecane-iododecane of 1 mL hr⁻¹ was applied for 228 minutes. Then the flow rate was increased to 10 mL

5.3 TWO-PHASE FLOW EXPERIMENTS

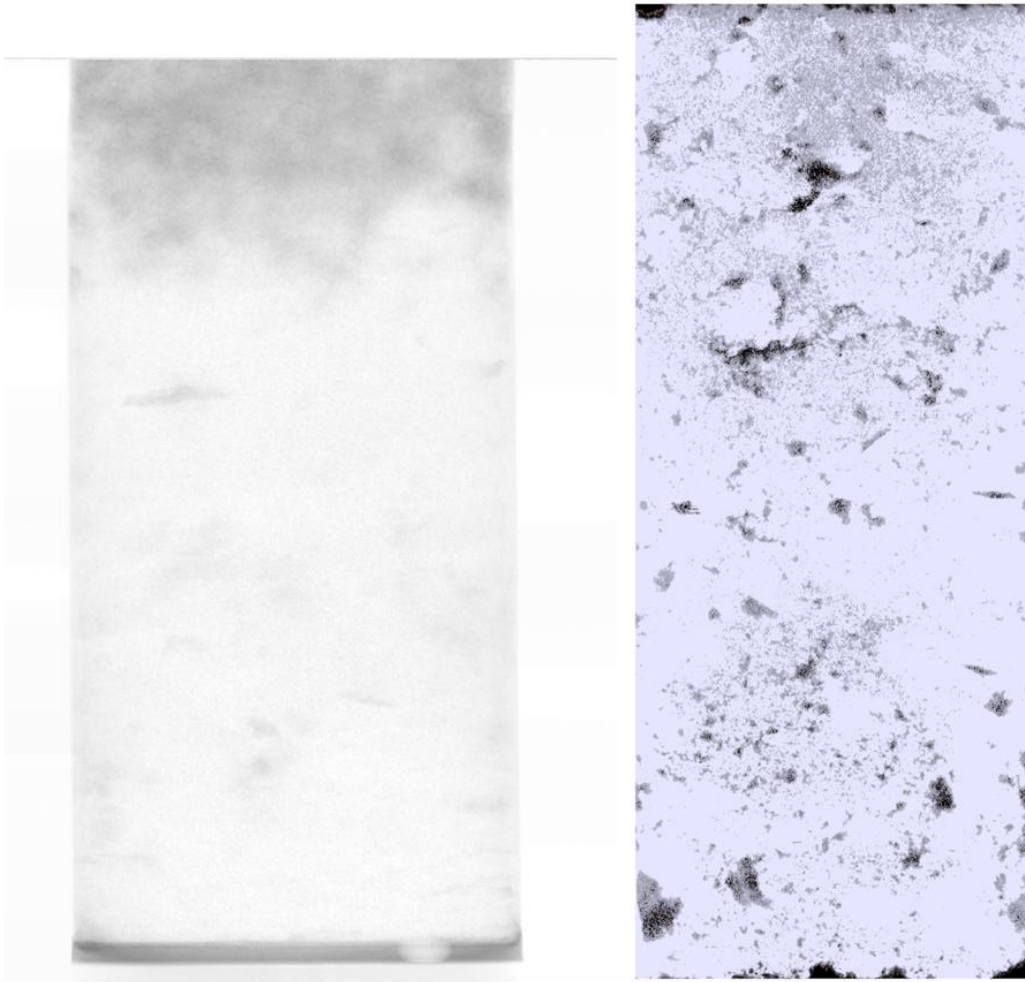


Figure 82: Comparison of tracer distribution after 144 minutes in experiment SAC₁ (table 10) in frontal view of the fracture and the fracture aperture distribution of the SAC sample.

5.3 TWO-PHASE FLOW EXPERIMENTS

hr^{-1} for a duration of 131 min. The sample was then left to rest for 17.5 hrs. Afterwards, the pump was switched on again with a flow rate of 50 mL hr^{-1} dodecane-iododecane for a duration of 31 min. Images were taken looking in frontal view of and along the fracture plane. The results are shown in fig. 83, 84, 85. We see how the fracture was filled first. When the flow rate was increased to 10 mL hr^{-1} the pressure gradient between fracture and matrix became high enough that water could enter the matrix locally due to forced imbibition. Only at a flow rate of 50 mL hr^{-1} water displaced oil in the matrix bottom. Additional flow occurs in the top of the sample.

5.3 TWO-PHASE FLOW EXPERIMENTS

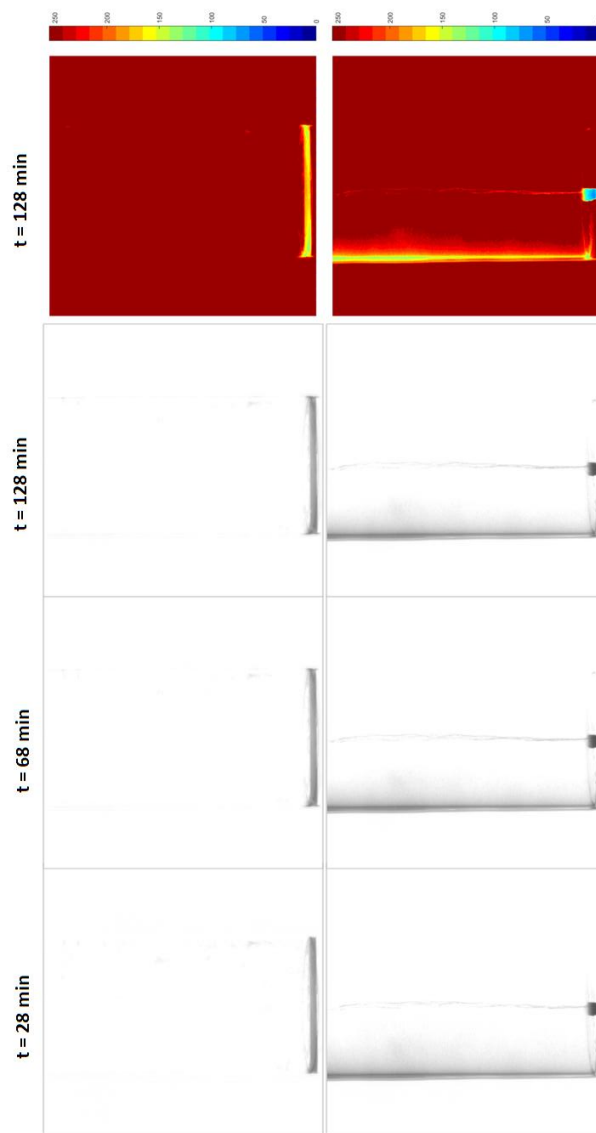


Figure 83: BD flood with dodecane-iododecane with a flow rate of 1 mL hr^{-1} at 28 min, 68 min, 128 min after injection commenced. Each column presents the flow patterns in frontal and side view of the fracture (i.e. the fracture is located perpendicular, or along to the view plane, respectively). Darker colours indicate higher concentrations of dodecane-iododecane. Right column: Contour plot at time 128 min. (colored according to grey values (0 - 255) in images). The fracture is filled slowly. No flow occurs in the BD matrix. The bright area at the left side in the images in the bottom row is due to some misalignment of the core sample.

5.3 TWO-PHASE FLOW EXPERIMENTS

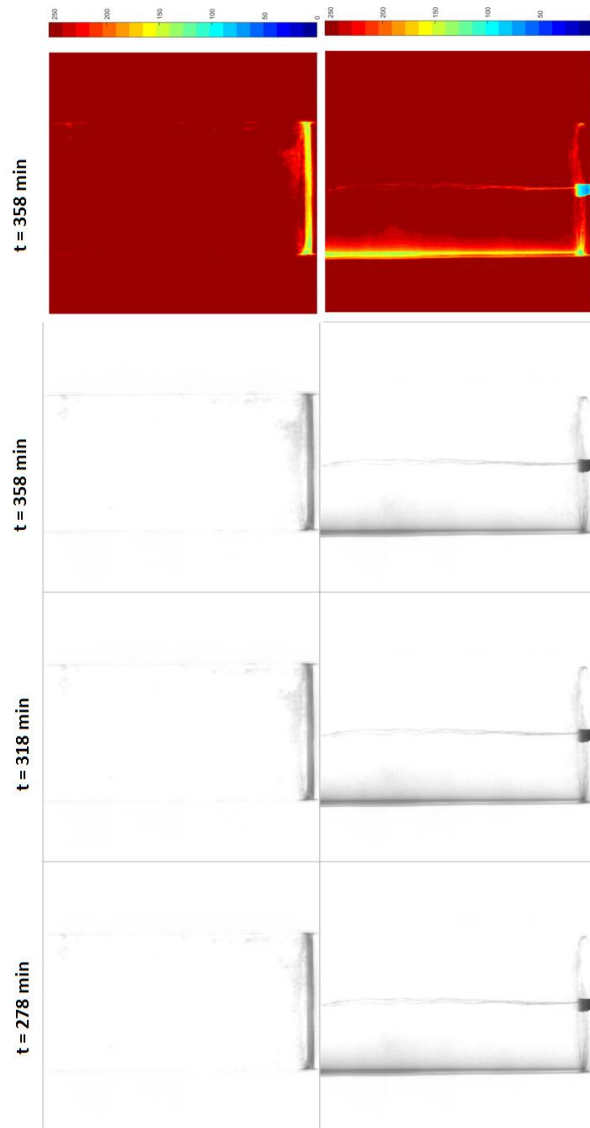


Figure 84: Continued experiment. BD flood with dodecane-iododecane with a flow rate of 10 mL hr^{-1} at 278 min, 318 min, 358 min after injection commenced. Each column presents the flow patterns in frontal and side view of the fracture (i.e. the fracture is located perpendicular, or along to the view plane, respectively). Darker colours indicate higher concentrations of dodecane-iododecane. Right column: Contour plot at time 358 min. (colored according to grey values (0 - 255) in images). The fracture is filled completely. First flow occurs in the BD matrix. The bright area at the left side in the images in the bottom row is due to some misalignment of the core sample.

5.3 TWO-PHASE FLOW EXPERIMENTS

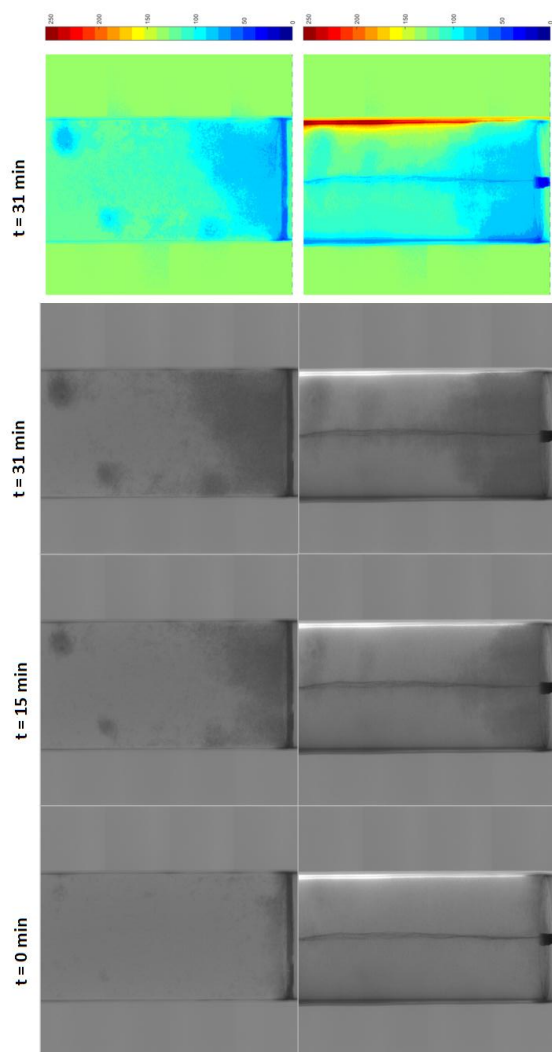


Figure 85: Continued experiment. BD flood with dodecane-iododecane with a flow rate of 50 mL hr^{-1} at 0 min, 15 min, 31 min after leaving the sample to rest for 17.5 hrs. Each column presents the flow patterns in frontal and side view of the fracture (i.e. the fracture is located perpendicular, or along to the view plane, respectively). Darker colours indicate higher concentrations of dodecane-iododecane. Right column: Contour plot at time 31 min. (colored according to grey values (0 - 255) in images). Flow occurs in the matrix and in the fracture. In the bottom of the sample the matrix flow is piston-like, whereas in the top part two patches of dodecane-iododecane form. The bright area at the right side in the images in the bottom row is due to some misalignment of the core sample.

5.3 TWO-PHASE FLOW EXPERIMENTS

In the second stage of the experiment, the sample is flooded with deionized H₂O initially with a flow rate of 1 mL hr⁻¹ for a duration of 254 min. The flow rate was then increased to 10 mL hr⁻¹ for a duration of 124 min. The sample was left to rest for 16 hrs. Afterwards, a flow rate of 50 mL hr⁻¹ was applied for a duration of 126 min. No tracer was added to the water phase. The results are shown in fig. 86, 87, 88. We see how in fracture and matrix the oil was displaced by water simultaneously and the overall oil saturation decreased. Nonetheless some oil remained trapped in the core. The remaining oil pattern is heterogeneous and still resembles the pattern before the waterflood.

One replica experiment was carried out, which showed the same flow patterns emerging. Breakthrough curves could not be obtained due to fluctuations of the x-ray source.

5.3 TWO-PHASE FLOW EXPERIMENTS

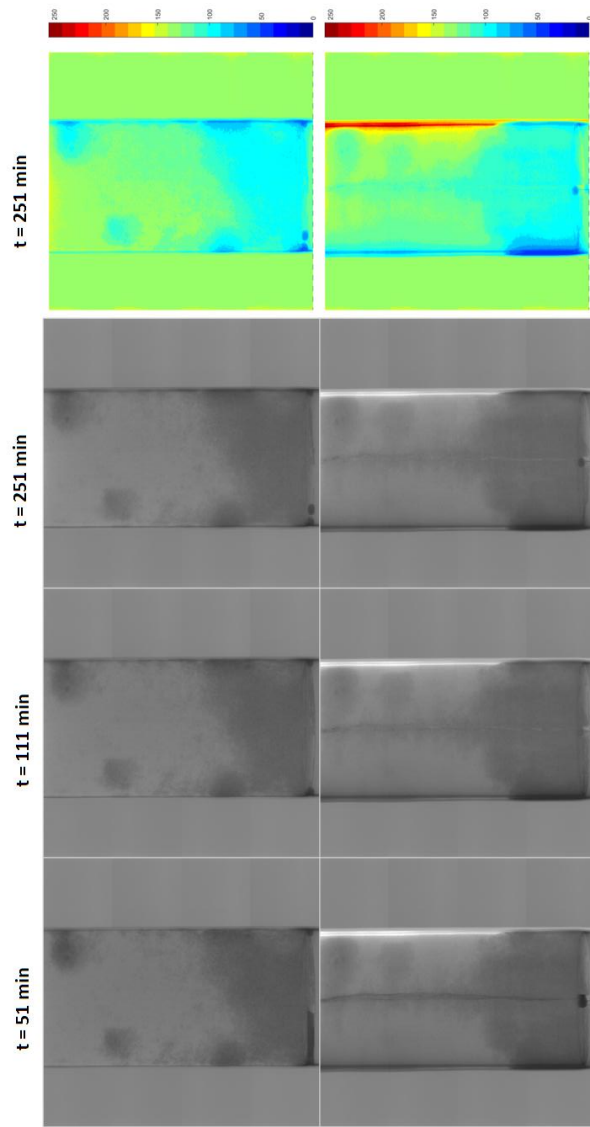


Figure 86: Continued experiment. BD flood with deionized water with a flow rate of 1 mL hr^{-1} at 51 min, 111 min, 251 min, 251 min after water injection commenced. Each column presents the flow patterns in frontal and side view of the fracture (i.e. the fracture is located perpendicular, or along to the view plane, respectively). Darker colours indicate higher concentrations of dodecane-iododecane. Right column: Contour plot at time 251 min. (colored according to grey values (0 - 255) in images). Fracture and matrix oil is replaced simultaneously by water. The bright area at the right side in the images in the bottom row is due to some misalignment of the core sample.

5.3 TWO-PHASE FLOW EXPERIMENTS

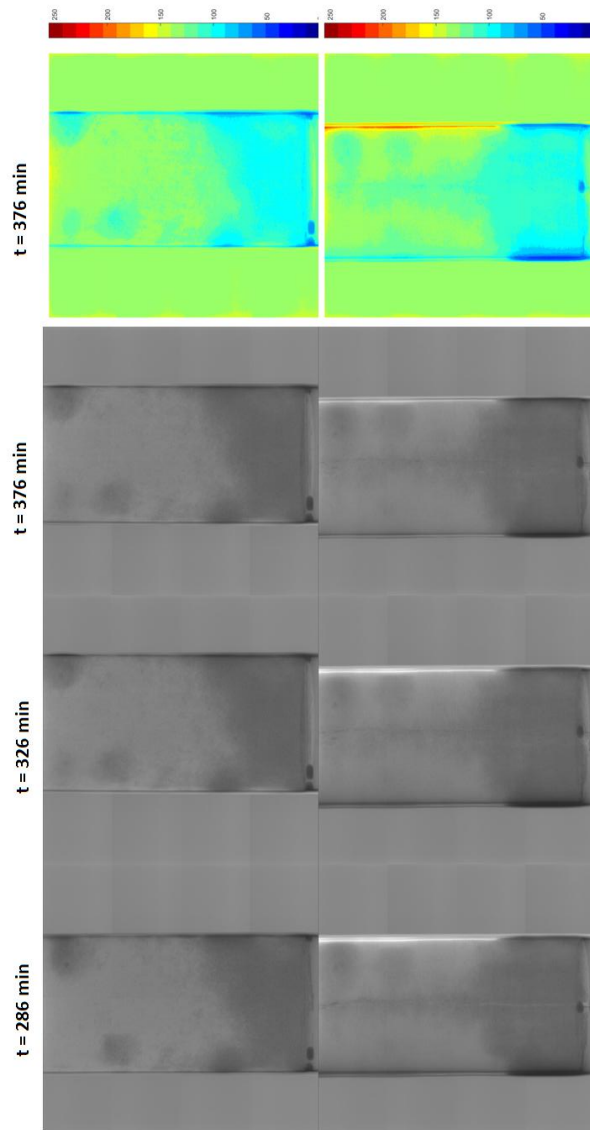


Figure 87: Continued experiment. BD flood with deionized water with a flow rate of 10 mL hr^{-1} at 286 min, 326 min, 376 min after water injection commenced. Each column presents the flow patterns in frontal and side view of the fracture (i.e. the fracture is located perpendicular, or along to the view plane, respectively). Darker colours indicate higher concentrations of dodecane-iododecane. Right column: Contour plot at time 376 min. (colored according to grey values (0 - 255) in images). Further drainage of matrix and fracture can be observed. The oil patches in the top of the sample are reduced. Oil is pushed from the fracture further into the matrix. The bright area at the right side in the images in the bottom row is due to some misalignment of the core sample.

5.3 TWO-PHASE FLOW EXPERIMENTS

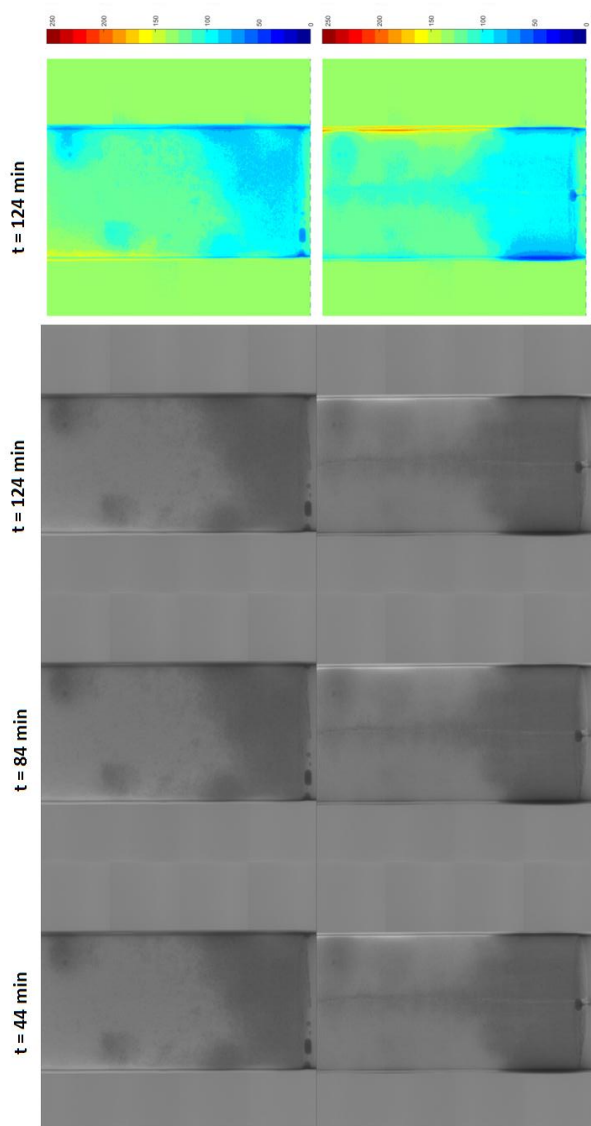


Figure 88: Continued experiment. BD flood with deionized water with a flow rate of 50 mL hr^{-1} at 44 min, 84 min, 124 min after leaving the sample at rest for 16 hrs. Each column presents the flow patterns in frontal and side view of the fracture (i.e. the fracture is located perpendicular, or along to the view plane, respectively). Darker colours indicate higher concentrations of dodecane-iododecane. Right column: Contour plot at time 124 min. (colored according to grey values (0 - 255) in images). Oil remains in the matrix and is still distributed heterogeneously. The bright area at the right side in the images in the bottom row is due to some misalignment of the core sample.

5.4 DISCUSSION

5.4 DISCUSSION

Heterogeneous flow patterns in fracture and matrix for single and two-phase flow can clearly be observed in the experiments. Flow into the matrix seems to occur preferentially in areas with larger fracture apertures where the local permeability is likely to be higher (cf. fig. 78, 82). In general, the fracture filled much faster than the rock matrix. In the BD sample nearly all flow occurs in the fracture, whereas in the SAC sample fluids appear to enter the matrix due to viscous forces, particularly at the top of the sample, where the fracture apertures are larger. In general though, fluid flow occurs predominantly in the fractures.

In the two-phase flow experiment in the BD sample the fracture is filled first with oil as well. Oil patches originating at the fracture form in some areas in the matrix. Only at a high flow rate the matrix is filled over the entire fracture-matrix surface area. When water enters the matrix, it slowly replaces the oil, but oil remains trapped in the fracture and matrix.

USING X-RAY CT DERIVED FRACTURE APERTURES FOR SIMULATING MISCIBLE FLUID FLOW IN FRACTURED CARBONATES

Using the aperture measurements (chapter 4) from the X-ray CT experiments for the Baker Dolomite (BD) and San Andreas Carbonate (SAC), 2D and 3D unstructured finite element meshes were constructed. These meshes represent the rock matrix and the fracture (3D meshes), or the fracture only (2D meshes). Since fluid flow occurs predominantly in the fractures (e.g. fig. 73), only 2D meshes are used for single phase flow simulations. As discussed in chapter 2, all simulations are carried out with CSMP++. The simulations of the BD and SAC samples are compared with the single-phase flow experiments (chapter 5).

6.1 MESH GENERATION

As discussed in chapter 2 the fracture is represented by 2D elements (triangles) and the matrix by 3D elements (tetrahedra). If it is assumed that flow and transport occurs only in the fractures, a planar 3D mesh with triangular elements can be used.

6.1.1 *Upscaling of fracture aperture information*

As discussed in chapter 4, the number of aperture measurements is significantly larger than the number of finite elements that can be handled in the numerical simulations. Hence the aperture measurements need to be averaged for each finite element. The exact procedure was described already

6.2 INFLUENCE OF FRACTURE APERTURES ON FLOW RATES

in section 2.6. With this we can calculate the arithmetic mean, from which we calculate the corresponding permeability field using the Cubic Law (CL) (5). An overview of the meshes can be found in table 12. The upscaled aperture distributions can be found in fig. 89 and 90.

Mesh	FEs	max FE size
coarse BD (Mesh ₁₃)	3346	$2.3 \cdot 10^{-6}$ m
med BD (Mesh ₁₀)	14402	$5.8 \cdot 10^{-7}$ m
fine BD (Mesh ₁₂)	31406	$2.5 \cdot 10^{-7}$ m
coarse SAC (Mesh ₁₄)	3004	$2.2 \cdot 10^{-6}$ m
med SAC (Mesh ₁₁)	12702	$5.5 \cdot 10^{-7}$ m
fine SAC (Mesh ₁₅)	25192	$3.0 \cdot 10^{-7}$ m

Table 12: Meshes generated from the aperture measurements for Baker Dolomite (BD) and San Andreas Carbonate (SAC)

6.2 INFLUENCE OF FRACTURE APERTURES ON FLOW RATES

As suggested by Matthäi and Belayneh, 2004 [131], the ratio of fracture flow to matrix flux q_f/q_m gives a good estimate of the fracture influence on the overall flow. This ratio was calculated in each spatial direction by a 3D simulation. For this a rectangular shaped 3D geometry was constructed around a 2D fracture with the aperture information upscaled to the finite elements. For the BD sample the contribution of the fracture relative to the matrix q_f/q_m is in x-direction: 99.62, in y-direction: 14.41, in z-direction: 123.47. For the SAC sample the contribution of the fracture relative to the matrix q_f/q_m is in x-direction: 42.40, in y-direction: 14.41, in z-direction: 120.23. In both cases, the fracture influence in flow direction (z) is larger than in the other directions. Hence we assume the influence of the flux in the matrix to be negligible, which is also consistent with the experiments, where flow occurred mostly in the fracture (cf. fig 75 and 79). Therefore the simulations are carried out on the fracture in 2D only.

6.2 INFLUENCE OF FRACTURE APERTURES ON FLOW RATES

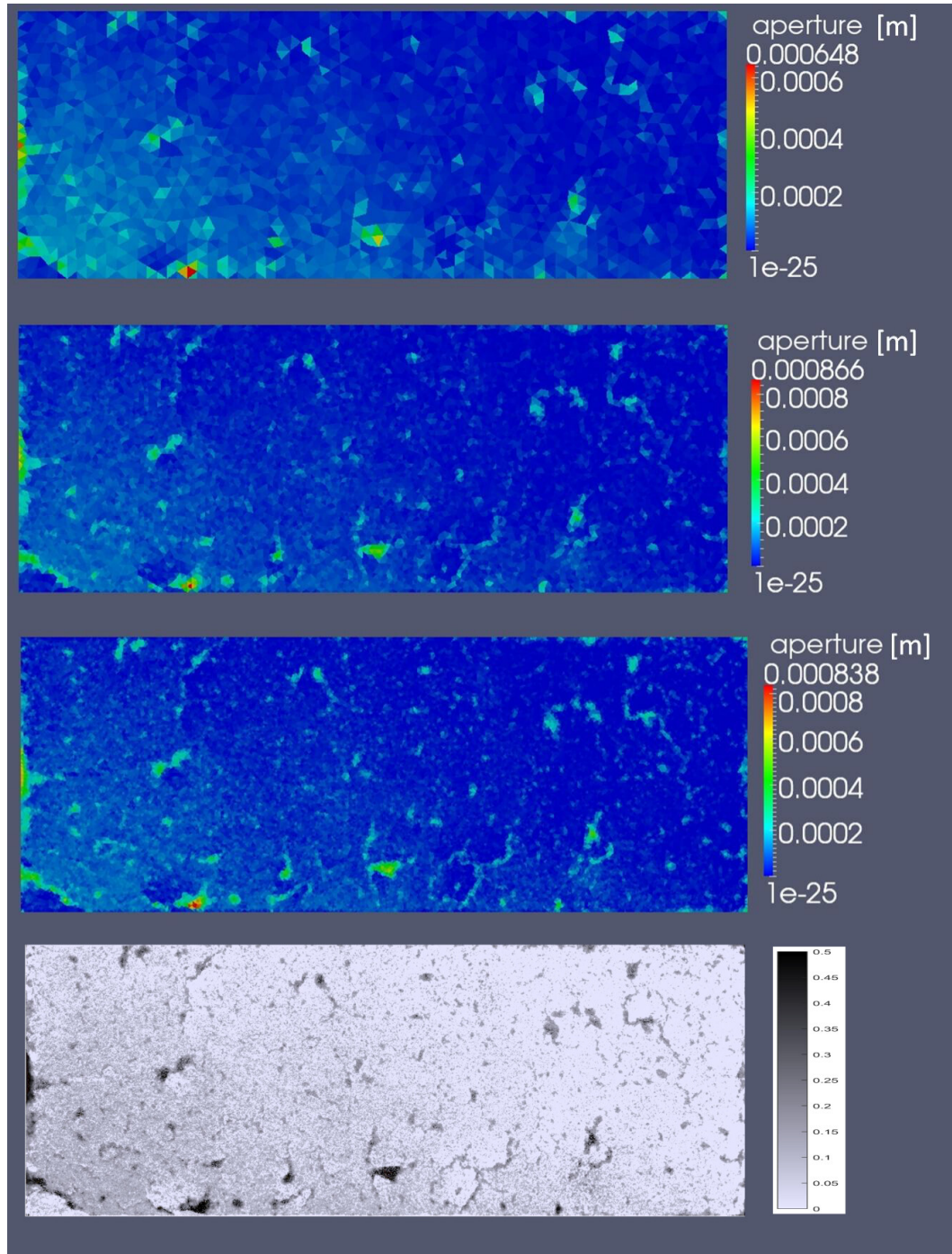


Figure 89: Upscaled fracture apertures measured for the BD sample and mapped to the coarse (Mesh13, top), medium (Mesh10, middle), and fine (Mesh12, bottom) finite element meshes (table 12). The aperture distributions show good agreement with the measured apertures (bottom, cf. fig. 67).

6.2 INFLUENCE OF FRACTURE APERTURES ON FLOW RATES

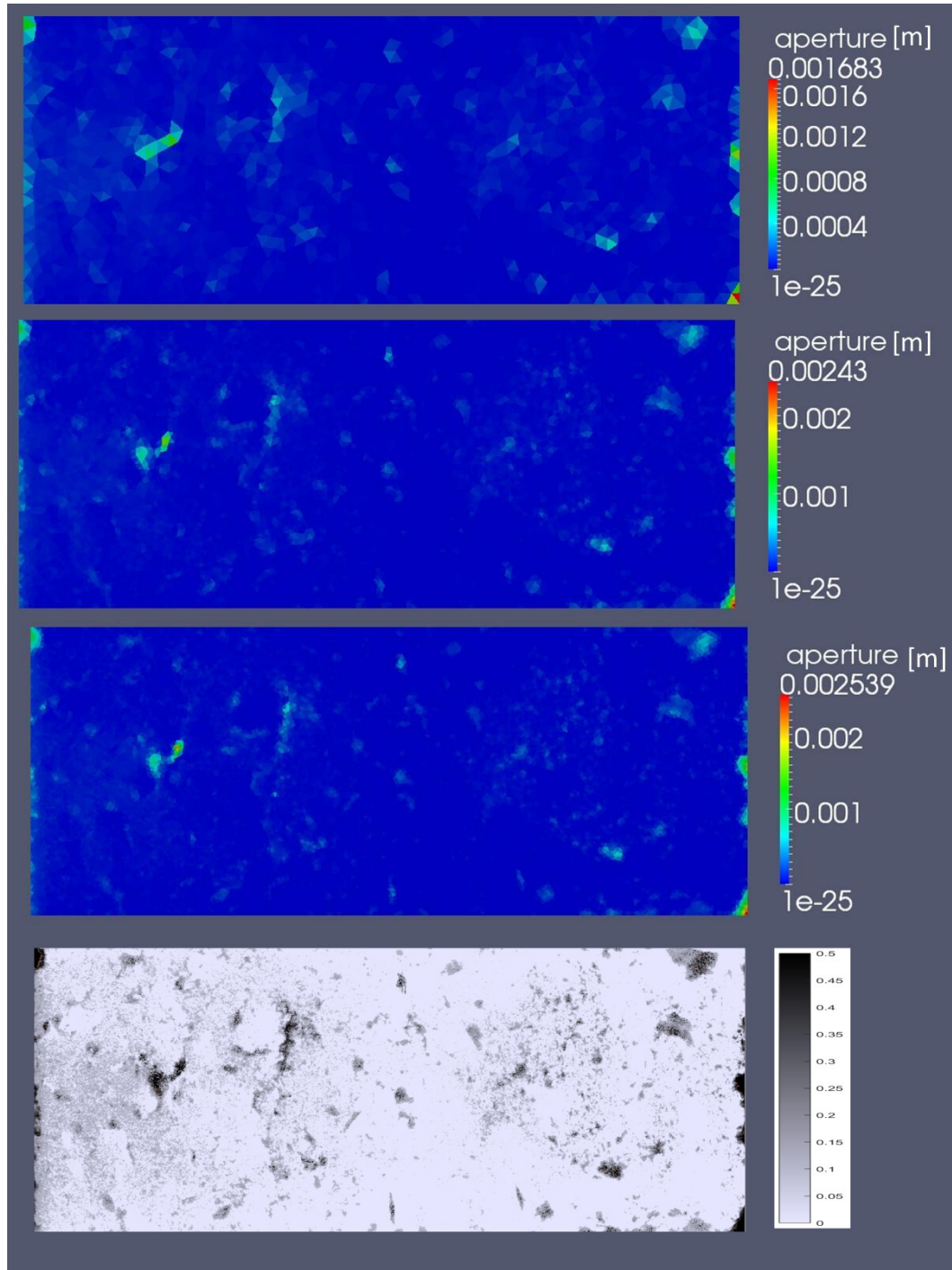


Figure 90: Upscaled fracture apertures measured for the BD sample and mapped to the coarse (Mesh14, top), medium (Mesh11, middle), and fine (Mesh15, bottom) finite element meshes (table 12). The aperture distributions show good agreement with the measured apertures (bottom, cf. fig. 67).

6.2 INFLUENCE OF FRACTURE APERTURES ON FLOW RATES

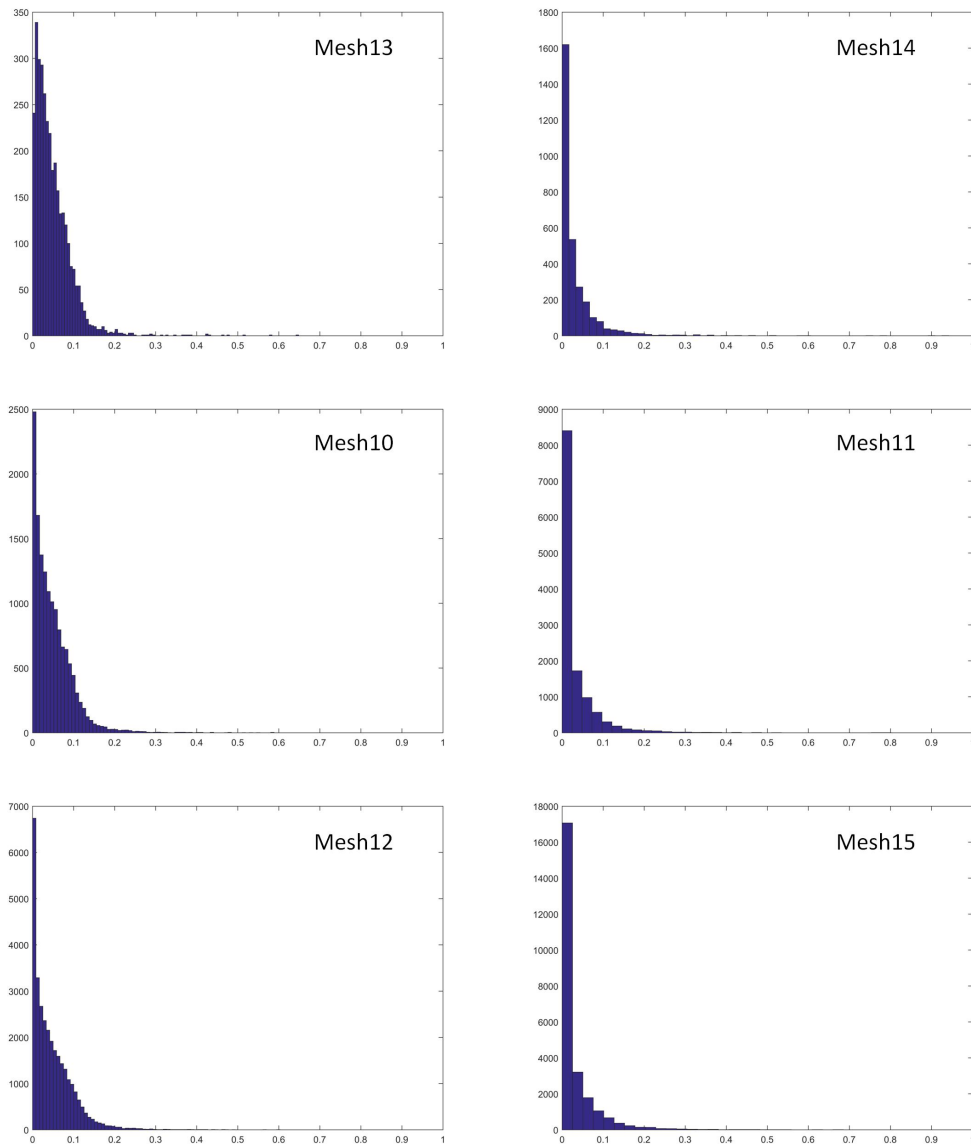


Figure 91: Histograms of the fracture apertures of the BD and SAC meshes in table 12. In comparison to the measured aperture distributions (cf. fig. 68), the extreme values in the long tail of the aperture distribution have decreased. This is an averaging effect. Note that the finer meshes exhibit more finite elements with aperture = 0, which is due to averaging as well.

6.3 SINGLE-PHASE FLOW SIMULATIONS

6.3 SINGLE-PHASE FLOW SIMULATIONS

The governing equations for single-phase flow and the numerical treatment were discussed in section 2.7.

The flow parameters are calculated as follows: The viscosity of KI at 18°C is $\eta = 0.9228 \text{ kg m}^{-1} \text{ s}^{-1}$ [60]. The diffusivity of I^- can be estimated via the Stokes-Einstein relation (Cussler, 1996 [51])

$$D = \frac{k_B T}{6\pi \eta r}, \quad (42)$$

where k_B is the Boltzmann's constant ($k_B = 1.38 \cdot 10^{-23} \text{ J K}^{-1}$), T the absolute temperature ($T = 291.15 \text{ K}$), and r the radius of I^- ($r = 206 \text{ pm}$). The diffusivity then calculates to $1.1213 \cdot 10^{-12} \text{ m}^2 \text{ s}^{-1}$. The porous diffusivity D_p can be estimated via the porosity ϕ as

$$D_p = D \cdot \phi \quad (43)$$

(e.g. Geiger, 2000 [72]). For BD ($\phi = 0.291$) the porous diffusivity is $D_p = 3.2630 \cdot 10^{-13} \text{ m}^2 \text{ s}^{-1}$. For SAC ($\phi = 0.2165$) the porous diffusivity is $D_p = 2.4276 \cdot 10^{-13} \text{ m}^2 \text{ s}^{-1}$. The local permeabilities for BD and SAC are calculated via the CL (eq. 5). The longitudinal and transverse dispersivities are assumed to be 1/10, or 1/100, respectively, of the maximum FE size of the mesh, which implies that dispersion is modelled only below the scale of the grid resolution. Dispersion above the scale of the grid resolution emerges from the heterogeneity in the aperture (i.e. permeability) field. The inflow rate is the same as in the flow experiments $10 \text{ mL s}^{-1} = 2.78 \cdot 10^{-9} \text{ m}^3 \text{ s}^{-1}$. At the fracture outlet, atmospheric pressure of $1.0 \cdot 10^5 \text{ Pa}$ is applied. Dirichlet boundary conditions are applied along the fracture inlet with a concentration of $c = 1$ and $c = 0$ at the fracture outlet. No-slip boundary conditions are applied at the fracture sides.

In the following we consider the coarse meshes only, Mesh13 for BD and Mesh14 for SAC. The pressure distributions of BD and SAC are shown in fig. 92. The magnitudes of the Darcy velocity are shown in fig. 93. In the SAC we can see how a preferred flow path forms, which is not consistent with the experimental observation. The concentration at different timesteps in

6.4 DISCUSSION

BD and SAC are shown in fig. 94 and 95, respectively. Completely different tracer distributions emerge. The tracer in the BD is entering the fracture more uniformly, whereas the SAC fracture is invaded preferentially along its center.

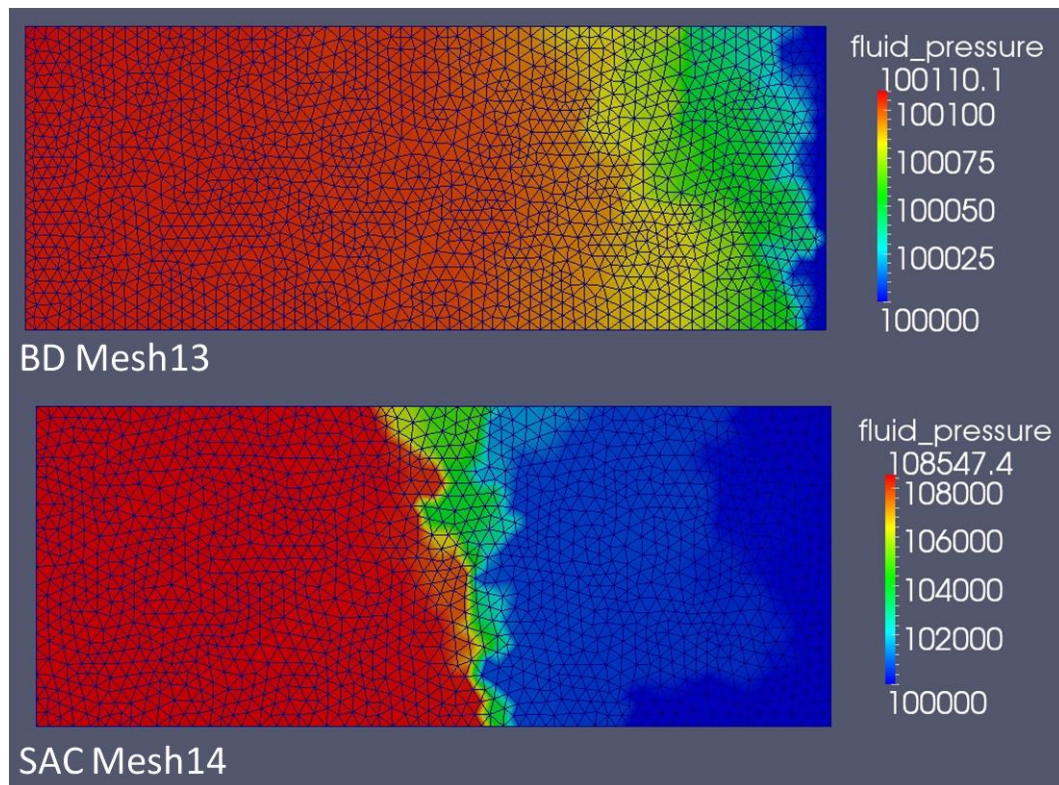


Figure 92: Pressure distributions of BD and SAC. Top: BD Mesh13, Bottom: SAC Mesh14. Flow is from left to right.

The breakthrough curves of BD and SAC show how the SAC is invaded by fluid faster than the BD (fig. 96). The preferential flow path in the SAC simulation is probably the cause.

6.4 DISCUSSION

Aperture data derived from CT measurements of two real-world rock samples were used to set up a 2D finite element model of the fracture. Single-phase flow simulations were successfully performed with these models.

We will now discuss how the results match the physical flow experiments which have been conducted before on the same samples (see chapter 5).

6.4 DISCUSSION

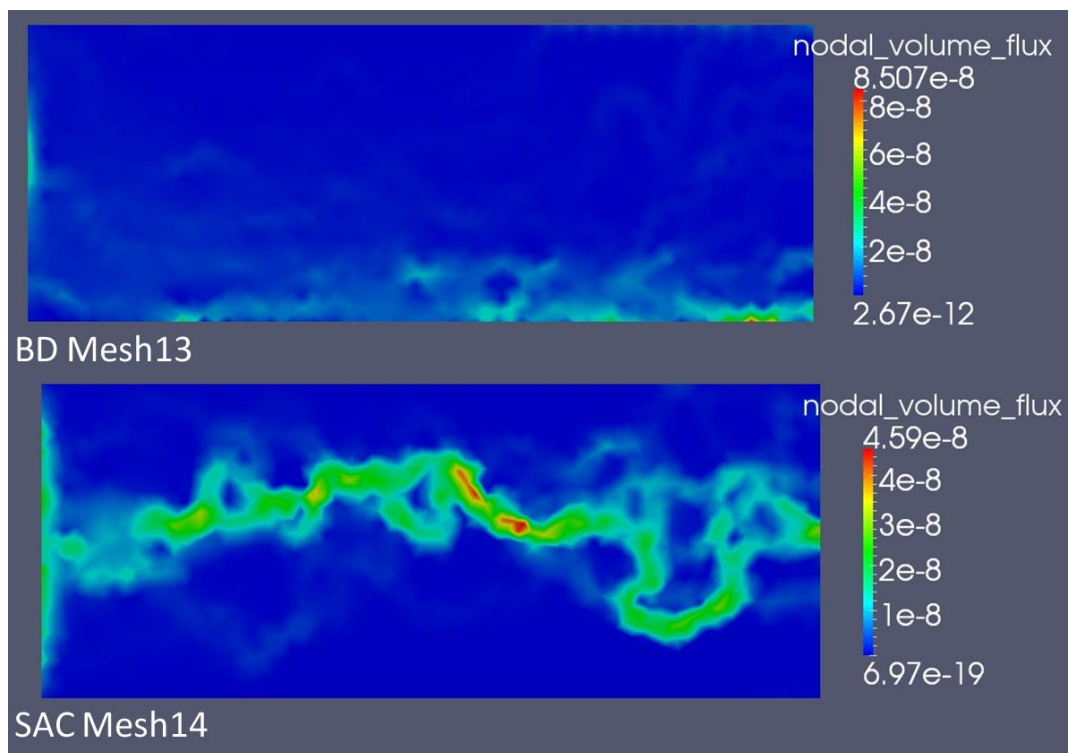


Figure 93: Magnitude of the Darcy velocity of BD and SAC. Top: BD Mesh13, Bottom: SAC Mesh14. Flow is from left to right.

6.4 DISCUSSION

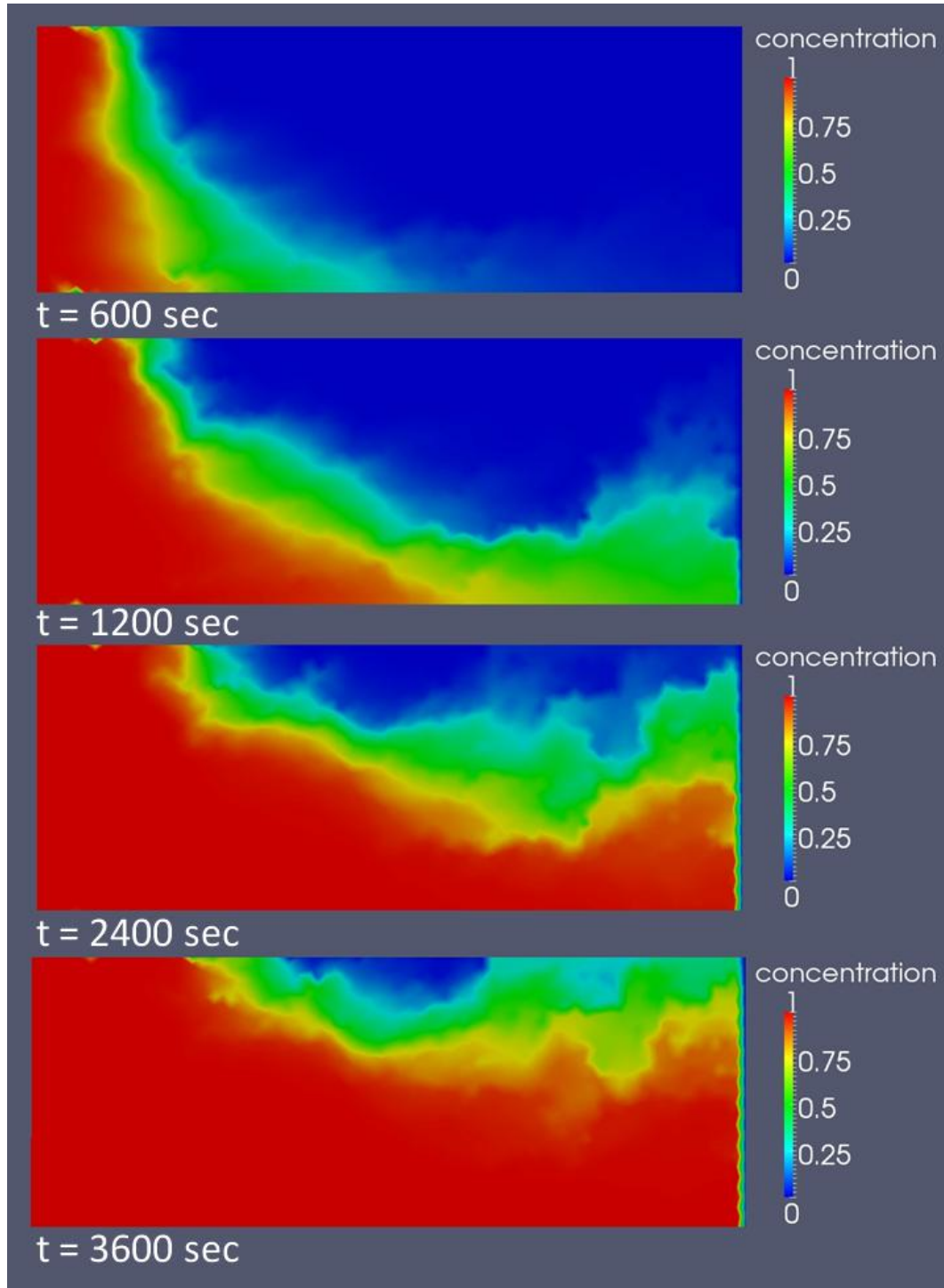


Figure 94: Concentration at different timesteps in the BD sample (BD Mesh₁₃).

6.4 DISCUSSION

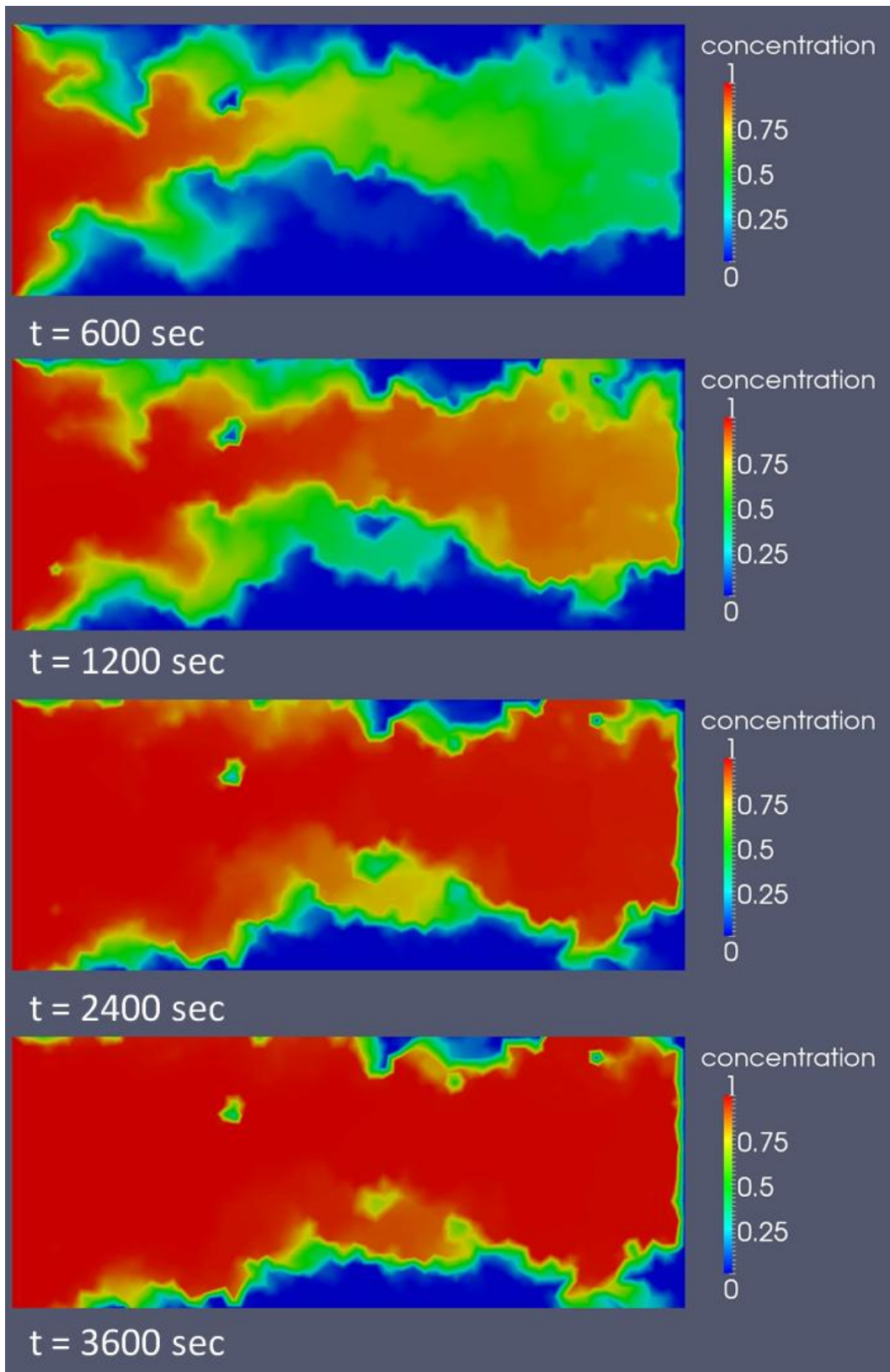


Figure 95: Concentration at different timesteps in the SAC sample (SAC Mesh₁₄).

6.4 DISCUSSION

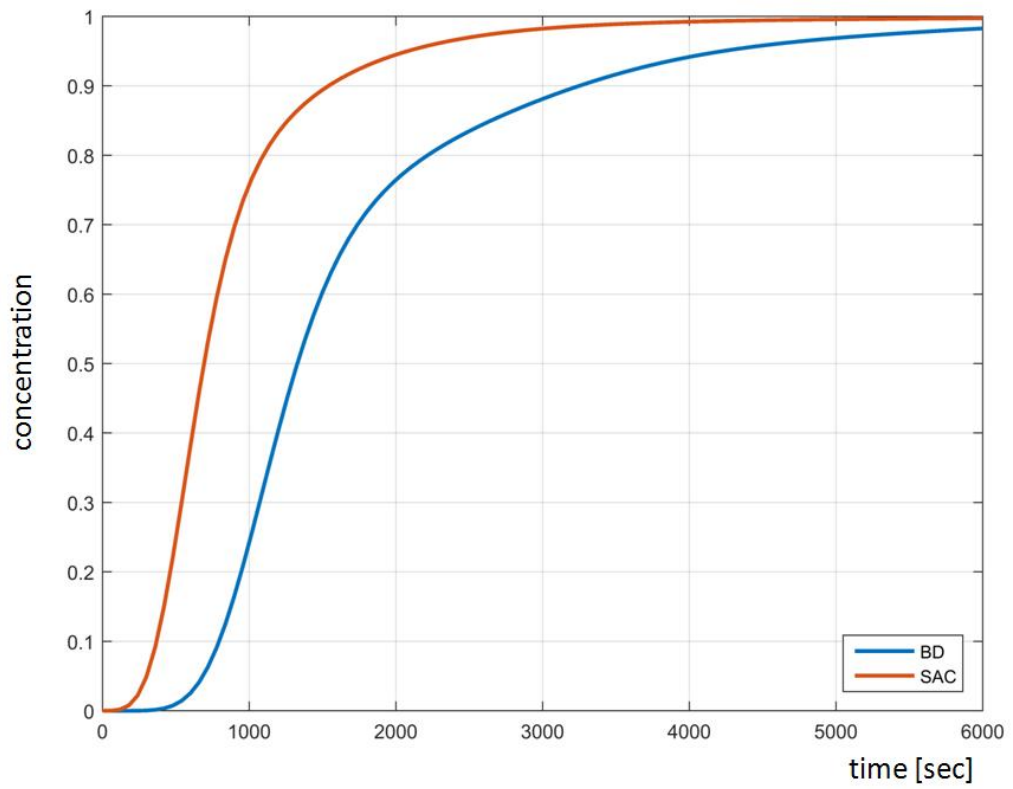


Figure 96: Breakthrough curves for BD and SAC.

6.4 DISCUSSION

Some general aspects of the experiments can be recovered in the simulations while others do not match well or are difficult to compare. Specific discrepancies are expected due to systematic limitations.

Looking at the measured and simulated breakthrough curves (BTCs), the order of the time scales are comparable. To see this, we have to note the different ways of generating the simulated and experimental curves. The former are based on the tracer saturation in the fracture only since the rock matrix is not subject to the simulations. The latter, the experimental curves, in contrast, are based on the cumulated tracer saturation across the entire cross section of the sample as provided by the X-ray projections. In particular, these include the rock matrix where flow velocities are orders of magnitude slower than in the fracture itself. Note that the simulated curves are saturated with $c = 1$ comparably quickly, whereas the experimental curves do not reach $c = 1$ at all within the measured time period, but they rather enter a regime of slow linear increase (see fig. 97 which repeats the experimental data from fig. 77). This linear regime is assumed to represent the infiltration process into the rock matrix when the fracture is already close to saturation. In order to recover the saturation in the fracture only, we can rescale the y-axis of the experimental curves to the point where the linear regime begins. Doing this for the BD and SAC experimental data yields roughly 700 sec. (BD) to 1300 sec. (SAC) as time to 50% saturation (in the fracture only!). The same range of saturation times is seen in the simulated curves (fig. 96).

The fact that the the BD sample is saturated faster than SAC in the experiments seems to be reverse in the simulation. The uncertainties in the complete process chain from experimental data to simulations might be just too large to discriminate the two samples precisely enough. Uncertainties arise from the measurement error of $75\mu\text{m}$ in the aperture width, the simplification of the modelling process (2D only, Darcy flow model, omitting the effects from flow in the matrix), and the limited resolution of the simulation mesh. Also, the BTCs in the experiments are obtained by assuming a concentration of $c = 1$ in the inlet area. This has been an arbitrary reference value prohibiting an absolute comparison of the BTCs.

The comparison of the Darcy velocity and concentration fields (figs. 94, 95) against the X-ray radiographs from the flow experiments (figs. 76, 80) is

6.4 DISCUSSION

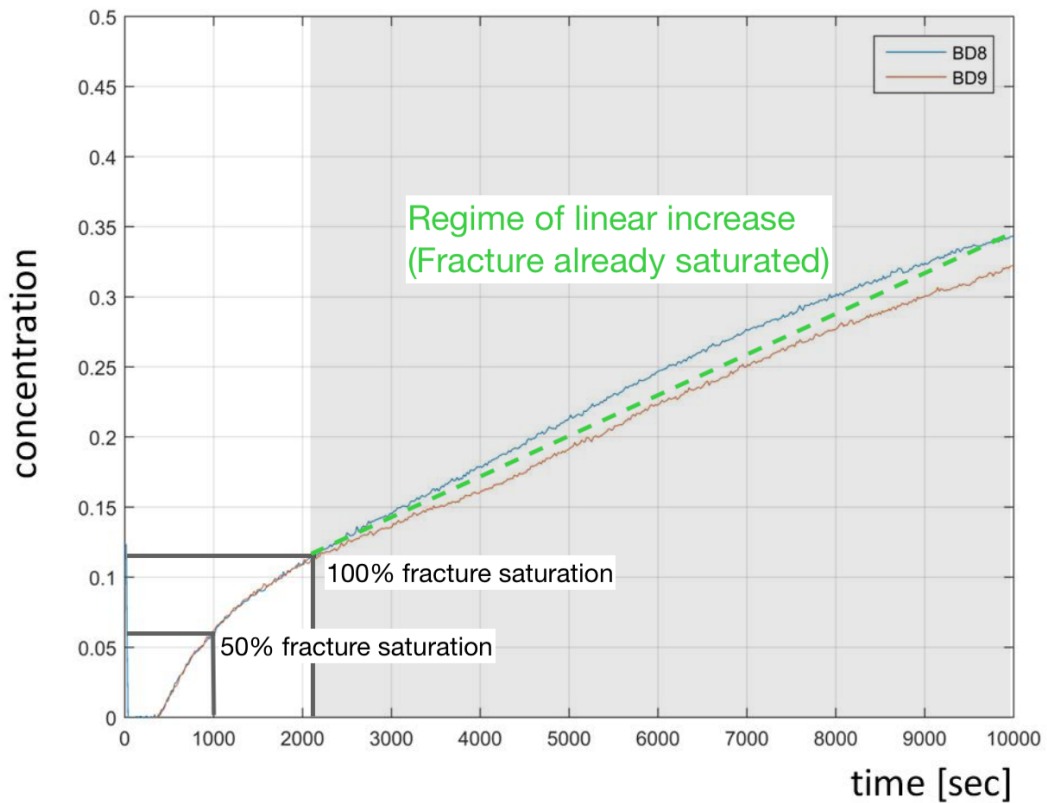


Figure 97: Experimental breakthrough curves for the BD sample (cf. 77). The early process, in which mainly the fracture is filled with tracer fluid, occurs much faster than the diffusion into the porous matrix. It is plausible that the fast slope of the BTC on the left corresponds to this early stage of the flow experiment. Once the fracture is entirely saturated with tracer fluid only diffusion into the matrix remains. The corresponding transition point from steep to linear concentration growth in the BTC has been denoted in the image as 100% fracture saturation. The full saturation of the entire core sample is not reached within the measured time period.

6.4 DISCUSSION

difficult since the X-ray images show a cumulated projection of the tracer density along the direction of view, where tracer substance both in the fracture and in the matrix are overlaid on top of each other. The local tracer concentration in the fracture only cannot easily be reconstructed from the projections. Also, especially in the SAC sample, the contrast in the frontal X-ray images is not high enough to confidently discriminate tracer density variations within the plane of the fracture.

However, some statements can be made:

- The simulated velocity field and tracer concentration in the SAC sample are significantly more inhomogeneous (the flow is following a narrow fractal path) compared to the BD sample where the flow seems to use the full breadth of the fracture (fig. 93, note the different color scales). This corresponds to the patterns seen in the X-ray projections. The BD concentration distribution (see fig. 94, top row) exhibits much smaller spatial frequencies (smooth transitions between areas with high and low concentrations) while the SAC concentration distribution (see fig. 95, top row) shows sharp concentration speckles. However, we do not observe the narrow flow path as seen in the simulation (fig. 93), which could be a result of the limited dynamic range of the radiographs.
- The X-ray projections of the SAC sample (fig. 95, top row) show a pronounced tracer saturation in the rock matrix in the far end of the sample. This is regarded as an effect of a local variation of the permeability of the matrix which is not expected to have a correspondence in the simulations which cover the fracture only. Even if the matrix would have been included in the simulations, the matrix porosity had been assumed to be homogeneous which would be a too strong simplification in this case, also.
- In the SAC sample (see fig. 95, top row), a channelized tracer flow at the lateral borders of the flow cell can be observed. As discussed in paragraph 4.4, this effect is probably caused by void defects occurring at the edges of the fracture as a result of the splitting process of the core samples.

CONCLUSIONS AND DISCUSSION

Within this thesis, a complete workflow was established for the characterization of fractured rock samples using (a) 3D computed tomography (CT) imaging, (b) 2D X-ray monitored flow experiments, and (c) finite element / finite volume simulations. A proof of concept was given using two real-world samples - Baker Dolomite and San Andreas Carbonate.

As a first step, a high-resolution custom X-ray CT system was designed and built from scratch. Control software was developed and optimized for fast and convenient data acquisition (chapter 2). In order to increase the accuracy of the CMOS image detector in the face of non-linear response errors, an imaging correction method had to be developed (chapter 3). The system was used both to acquire high-resolution 3D images of the rock samples, and to monitor a contrast tracer in the flow experiments as time series of 2D X-ray radiographs.

Specific focus was spent on the problem of characterizing the exact shape (aperture distribution and topology) of the rock fracture (chapter 4). An image processing method was developed to measure the fracture aperture distributions of both samples from the CT data. Calibration measurements with sparse data showed that the aperture width can be measured with an uncertainty of about $75\mu m$, which is also the minimum detectable aperture width.

The two rock samples were subject to single- and two-phase flow experiments, in which water and oil distributions could be shown to evolve in fracture and matrix (chapter 5). Breakthrough curves were extracted from the evolution of a tracer substance visualized by X-ray radiographs.

The fracture aperture widths from the CT images were used to set up 2D finite element models for single-phase simulations in the fracture (chapter

CONCLUSIONS AND DISCUSSION

6). For this, the aperture widths were translated into local effective permeabilities using the local cubic law (eq. 5). As results, pressure and velocity fields of the Darcy flow, and the time evolution of a tracer substance are presented. Breakthrough curves based on the simulations are derived.

The simulations and the flow experiments still show some differences, which can in part be attributed to systematic causes:

- (a) The aperture measurements were influenced by the measurement error of a minimum measurable aperture of $75\mu m$.
- (b) The X-ray radiographs always show a combination of tracer substance both in the fracture and the matrix, while the simulation only covers the fracture, which makes a direct comparison difficult — even if the matrix would have been included in the simulations, the matrix porosity had been assumed to be homogeneous which is in case of the SAC, as we can see in the flow experiments, a too strong simplification.
- (c) The coarse meshes used in the simulations simplify the small-scale topology of the fracture which could have significant influence on the flow patterns.
- (d) Assuming the aperture geometry can be homogenized using the local cubic law (eq. 5) is a simplification. Another approach could be to investigate using an hydraulic aperture calculated from the actual mechanical aperture and the joint roughness coefficient (JRC) as proposed by Barton et al. [15].
- (e) The simulation was based on a plane 2D fracture model neglecting the actual 3D topology of the fracture, which is especially significant in the San Andreas Carbonate (SAC) sample.

Hence, future work should address these issues.

- Fracture aperture measurements need to be calibrated with more calibration measurements, especially for very small apertures. Employing marble for the calibration measurements with a very low porosity should be considered.

CONCLUSIONS AND DISCUSSION

- The local fracture apertures should be measured in exact perpendicular direction to the fracture orientation at the corresponding position.
- A camera which produces less noise is recommended to obtain more reliable measurements.
- A camera covering a wider dynamic range is important to improve the resolution of concentration differences in the fracture, as the surrounding rock material absorbs large parts of the X-ray signal.
- A CT scanner which is fast enough to record a full 360° turn in less than 30 sec. could serve to obtain full 3D images during the experimental run, which would help to identify areas in the fracture aperture distribution being most influential to (a) the flow inside the fracture, to observe possible preferred flow paths, and (b) to investigate the actual fluid diffusion into the porous rock matrix.
- Another possibility would be to investigate how to better assess the 3D contraction distribution from the X-ray projections of the sample being imaged in front and side view only. This will help to validate the simulation approach by the experiments.
- During the flow experiments applying a confining pressure to the flow cell should be considered.
- Using multiple samples of BD and SAC should be considered as well.
- To bring experiment and simulation closer together, finer meshes should be considered to show effects of the low-scale structure of the aperture boundaries.
- Simulations should incorporate the rock material in addition to the fracture (3D simulations), as already shown in principle in sections 2.6 and 2.7 (see figs. 44 and 50).
- Gravity should be taken into account for flow simulations.
- Two-phase flow simulations could be carried out to complement the two-phase flow experiments in chapter 5.

BIBLIOGRAPHY

- [1] I. Aavatsmark. An introduction to multipoint flux approximations for quadrilateral grids. *Computational Geosciences*, 6(3):405–432, 2002.
- [2] S.M. Agar and S. Geiger. Fundamental controls on fluid flow in carbonates: current workflows to emerging technologies. *Geological Society, London, Special Publications*, 406:1–59, 2015.
- [3] R.I. Al-Raoush and C.S. Willson. Extraction of physically realistic pore network properties from three-dimensional synchrotron x-ray microtomography images of unconsolidated porous media systems. *Journal of Hydrology*, 300/1:44–64, 2005.
- [4] E. Ando, G. Viggiani, S.A. Hall, and J. Desrues. Experimental micro-mechanics of granular media studied by x-ray tomography: recent results and challenges. *Geotechnique Letters*, 3:142–146, 2013.
- [5] R. Annewandter, I. Main, and S. Geiger. High-resolution numerical simulations of capillary trapping of CO₂ in fractured formations. *Proceedings of SPE Reservoir Characterisation and Simulation Conference and Exhibition*, September:16–18, 2013.
- [6] C.H. Arns, F. Bauget, A. Limaye, A. Sakellariou, T.J. Senden, A.P. Shepard, R.M. Sok, W.V. Pinczewski, S. Bakke, L.I. Berge, and M.A. Knackstedt P.E. Oeren. Pore scale characterisation of carbonates using x-ray microtomography. *SPE Annual Technical Conference and Exhibition, Houston, USA*, 26-29 (SPE 90368):11, 2004.
- [7] A. Assteerawatt. *Flow and Transport Modelling of Fractured Aquifers based on a Geostatistical Approach*. PhD thesis, Universität Stuttgart, 2008.
- [8] H. Auradou. Influence of wall roughness on the geometrical, mechanical and transport properties of single fractures. *Journal of Physics D: Applied Physics*, 42(21):214015, 2009.

BIBLIOGRAPHY

- [9] K. Aziz and A. Settari. *Petroleum reservoir simulation*. Applied Science Publishers, Barking, 1979.
- [10] Bhushan B. *Tribology and Mechanics of Magnetic Storage Devices*, chapter Solid Surface Characterization. Springer, New York, NY, 1996.
- [11] M. Bai, D. Elsworth, and J-C. Roegiers. Multiporosity/multipermeability approach to the simulation of naturally fractured reservoirs. *Water Resources Research*, 29:6:1621–1633, 1993.
- [12] A. Barbu, P.J. Hicks Jr, and A.S. Grader. Experimental three-phase flow in porous media: Development of saturated structures dominated by viscous flow, gravity, and capillarity. *SPE Journal*, 4(4):368–379, 1999.
- [13] G. I. Barenblatt, I. P. Zheltov, and I. N. Kochina. Basic concepts in the theory of seepage of homogeneous liquids in fissurized rocks. *Journal of Applied Mathematics and Mechanics*, 24(5):1286–1303, 1960.
- [14] Choubey V. Barton, N. The shear strength of rock joints in theory and practice. *Rock Mechanics* 10, pages 1–54, 1977.
- [15] Nick Barton. Shear strength investigations for surface mining. *3rd International Conference on Surface Mining, SME 1982, Vancouver*, pages 171–196, 01 1982.
- [16] J. Baruchel, J.-Y. Buffiere, P. Cloetens, M. Di Michiel, E. Ferrie, W. Ludwig, E. Maire, and L. Salvo. Advances in synchrotron radiation microtomography. *Scripta Materialia*, 55/1:41–46, 2006.
- [17] R. P. Batycky, Thiele M. R., and Blunt M. J. A streamline-based reservoir simulation of the house mountain waterflood. *Stanford Center for Reservoir Forecasting (SCRF) Annual Report*, 1997.
- [18] J. Bear. *Dynamics of fluids in porous media*. Elsevier, 1972.
- [19] S. Berg, H. Ott, S.A. Klapp, A. Schwing, R. Neiteler, N. Brussee, A. Makurat, L. Leu, F. Enzmann, J.O. Schwarz, M. Kersten, S. Irvine, and M. Stampanoni. Real-time 3d imaging of haines jumps in porous media flow. *Proceedings of the National Academy of Sciences*, 110/10:3755–3759, 2013.

BIBLIOGRAPHY

- [20] B. Berkowitz. Characterizing flow and transport in fractured geological media: A review. *Advances in Water Resources*, 25 (2002) 861-884:24, 2002.
- [21] S.P. Bertels, D.A. DiCarlo, and M.J. Blunt. Measurement of aperture distribution, capillary pressure, relative permeability, and in situ saturation in a rock fracture using computed tomography scanning. *Water Resources Research*, 37/3:649-662:14, 2001.
- [22] P. Bhattad, C. S. Willson, and K. E. Thompson. Effect of network structure on characterization and flow modeling using x-ray microtomography images of granular and fibrous porous media. *Transp Porous Media*, 0169-3913, 2011.
- [23] M. J. Blunt, B. Bijeljic, H. Dong, O. Gharbi, S. Iglauer, P. Mostaghimi, A. Paluszny, and C. Pentland. Pore-scale imaging and modelling. *Advances in Water Resources*, 51:197-216, 2013.
- [24] M.J. Blunt, M.D. Jackson, M. Piri, and P.H. Valvatne. Detailed physics, predictive capabilities and macroscopic consequences for pore-network models of multiphase flow. *Advances in Water Resources*, 25/8-12:1069-1089, 2002.
- [25] M.J. Blunt, K. Liu, and M.R Thiele. A generalized streamline method to predict reservoir flow. *Petroleum Geosciences*, 2:259-269, 1996.
- [26] E. Bonnet, O. Bour, N. E. Odling, P. Davy, I. Main, P. Cowie, and B. Berkowitz. Scaling of fracture systems in geological media. *Reviews of Geophysics*, 39:347-383, 2001.
- [27] B. Bourbiaux, R. Basquet, M.-C. Cacas, J.-M. Daniel, and S. Sarda. An integrated workflow to account for multi-scale fractures in reservoir simulation models: Implementation and benefits. *Society of Petroleum Engineers*, SPE-78489-MS, 2002.
- [28] L. Brabant, J. Vlassenbroeck, Y. De Witte, V. Cnudde, M.N. Boone, J. Dewanckele, and L. Van Hoorebeke. Three-dimensional analysis of high-resolution x-ray computed tomography data with morpho+. *Microscopy and Microanalysis*, 17(2):252-263, 2011.

BIBLIOGRAPHY

- [29] C. Braithwaite, G. Rizzi, and G. Darke. The geometry and petrogenesis of dolomite hydrocarbon reservoirs: introduction. *Geological Society, London, Special Publications*, 235 (1):1–6, 2004.
- [30] T. Burchette. Carbonate rocks and petroleum reservoirs: a geological perspective from the industry. *Geological Society, London, Special Publications*, 370 (1):17–37, 2012.
- [31] Thibault Candela, François Renard, Yann Klinger, Karen Mair, Jean Schmittbuhl, and Emily E. Brodsky. Roughness of fault surfaces over nine decades of length scales. *Journal of Geophysical Research: Solid Earth*, 117(B8), 2012.
- [32] L. Cao and J. Peter. A practical non-linear gain correction method for high-resolution cmos imaging detectors. In *Deutsches Krebsforschungszentrum, 39. DGMP Tagung, Oldenburg*, 2008.
- [33] M. B. Cardenas, D. T. Slotke, R. A. Ketcham, and J. M. Sharp Jr. Navier-stokes flow and transport simulations using real fractures shows heavy tailing due to eddies. *Geophysical Research Letters*, 34(14):L14404, 2007.
- [34] J. Carmeliet, J.-F. Delerue, K. Vandersteen, and S. Roels. Three-dimensional liquid transport in concrete cracks. *International Journal for Numerical and Analytical Methods in Geomechanics*, 28:671–687, 2004.
- [35] A. Carminati, A. Kaestner, R. Hassanein, O. Ippisch, P. Vontobel, and H. Fluhler. Infiltration through series of soil aggregates: Neutron radiography and modeling. *Advances in Water Resources*, Volume 30, Issue 5:1168–1178, 2007.
- [36] A. Carminati, A. Kaestner, P. Lehmann, and H. Flühler. Unsaturated water flow across soil aggregate contacts. *Advances in Water Resources*, 31/9:1221–1232, 2008.
- [37] L.M. Castanier. *An Introduction to Computerized X-Ray Tomography for Petroleum Research*. Stanford University, Petroleum Research Institute, 1989.

BIBLIOGRAPHY

- [38] F. Catte, P.-L. Lions, J.-M. Morel, and T. Coll. Image selective smoothing and edge detection by nonlinear diffusion. *SIAM J Numer Anal*, 29(1):182–93, 1992.
- [39] E. M. Charalampidou, S. A. Hall, and S. Stanchits. Characterization of shear and compaction bands in a porous sandstone deformed under triaxial compression. *Tectonophysics*, 503(1-2):8–17, 2011.
- [40] Z. Chen, G. Huan, and Y. Ma. *Computational Methods for Multiphase Flows in Porous Media*. Society for Industrial Mathematics, 2006.
- [41] B. Choubey, D. Joseph, S. Aoyama, and S. Collins. Dark current reductions techniques for wide dynamic range logarithmic CMOS pixels. In *30th International Congress of Imaging Science*, 2006.
- [42] B. Choubey, S. Otim, D. Joseph, and S. Collins. Characterization and simple fixed pattern noise correction in wide dynamic range logarithmic imagers. *IEEE Transaction on Instrumentation and Measurement*, 56/5:1910–1916, 2007.
- [43] M.A. Christie. Flow in porous media - scale up of multiphase flow. *Current Opinion in Colloid & Interface Science*, 6 (2001) 236-241:6, 2001.
- [44] M.A. Christie and M.J. Blunt. Tenth spe comparative solution project: A comparison of upscaling techniques. *SPE Reservoir Simulation Symposium*, 2001.
- [45] V. Cnudde and M.N. Boone. High-resolution x-ray computed tomography in geosciences: a review of the current technology and applications. *Earth-Science Reviews*, 123:1–17, 2013.
- [46] V. Cnudde, B. Masschaele, M. Dierick, and et al. Recent progress in x-ray ct as a geosciences tool. *Applied Geochemistry*, 21:826–832, 2006.
- [47] V. Cnudde, J. Vlassenbroeck, Y. De Witte, L. Brabant, M. Boone, J. Dewanckele, L. Van Hoorebeke, and P. Jacobs. Latest developments in 3d analysis of geomaterials by morpho+. *Advances in X-Ray Tomography for Geomaterials (eds. Alshibli, K.A., Reed, A.H.)*, pages 205–212, 2010.

BIBLIOGRAPHY

- [48] P. W. M. Corbett. Petroleum geoengineering: Integration of static and dynamic models. *Society of Exploration Geophysicists, Tulsa, Oklahoma*, 2009.
- [49] D. Crandall, G. Ahmadi, and D.H. Smith. Computational modeling of fluid flow through a fracture in permeable rock. *Transport in Porous Media*, 84(2):493–510, 2010.
- [50] J.P. Crawshaw and E.S. Boek. Multi-scale imaging and simulation of structure, flow and reactive transport for CO₂ storage and EOR in carbonate reservoirs. *Reviews in Mineralogy & Geochemistry*, 77:431–458, 2013.
- [51] E.L. Cussler. *Diffusion: Mass transfer in fluid systems*. Cambridge University Press, 1996.
- [52] B. De Man, J. Nuyts, P. Dupont, G. Marcha, and P. Suetens. Metal streak artifacts in x-ray computed tomography: A simulation study. *IEEE TRANSACTIONS ON NUCLEAR SCIENCE*, 46/3:691–696, 1999.
- [53] B. Dershowitz, P. LaPointe, T. Eiben, and L. Wei. Integration of discrete feature network methods with conventional simulator approaches. *SPE Reservoir Eval. & Eng.*, Vol. 3, No. 2:6, 2000.
- [54] J. Desrues, G. Viggiani, and P. Båsuelle, editors. *Advances in X-ray Tomography for Geomaterials*. Wiley-ISTE, 2006.
- [55] R. Detwiler and R. Harihar. Nonaqueous-phase-liquid dissolution in variable-aperture fractures: Development of a depth-averaged computational model with comparison to a physical experiment. *Water Resources Research*, 37/12:3115–3129, 2001.
- [56] R. Detwiler, S. E. Pringle, and R. J. Glass. Measurement of fracture aperture fields using transmitted light: An evaluation of measurement errors and their influence on simulations of flow and transport through a single fracture. *Water Resources Research*, 35/9:2605–2617, 1999.

BIBLIOGRAPHY

- [57] DiDonato, W. G., Huang, and M. Blunt. Streamline-based dual porosity simulation of fractured reservoirs. *proceedings of 2003 SPE Annual Technical Conference and Exhibition, Denver, 5-8 October, 2003*.
- [58] M. Dierick, B. Masschaele, and L. Van Hoorebeke. Octopus, a fast and user-friendly tomographic reconstruction package developed in labview. *Meas. Sci. Technol.*, 15/7:1366, 2004.
- [59] P. Dijk, B. Berkowitz, and P. Bendel. Investigation of flow in water-saturated rock fractures using nuclear magnetic resonance imaging (nmri). *Water Resources Research*, Vol. 35, no. 2, 347-360:14, 1999.
- [60] N. E. Dorsey. Viscosity of water, sulfuric acid, liquid carbon dioxide and certain organic liquids. *In: International Critical Tables of Numerical Data*, 5, 1929.
- [61] L. J. Durlofsky. Accuracy of mixed and control volume finite element approximations to darcy velocity and related quantities. *Water Resources Research*, 30:965-973, 1994.
- [62] M.G. Edwards. Unstructured, control-volume distributed, full-tensor finite-volume schemes with flow based grids. *Computational Geosciences*, 6(3):433-452, 2002.
- [63] M.G. Edwards and H. Zheng. Double-families of quasi-positive darcy-flux approximations with highly anisotropic tensors on structured and unstructured grids. *Journal of Computational Physics*, 229(3):594-625, 2010.
- [64] G. Ersland, M.A. Ferno, A. Graue, B.A. Baldwin, and J. Stevens. Complementary imaging of oil recovery mechanisms in fractured reservoirs. *Chemical Engineering Journal*, 158(1):32-38, 2010.
- [65] M. A. Ferno, J. Gauteplass, L. P. Hauge, G. E. Abell, T. C. H. Adamsen, and A. Graue. Combined positron emission tomography and computed tomography to visualize and quantify fluid flow in sedimentary rocks. *Water Resources Research*, 51 (9):7811-7819, 2015.

BIBLIOGRAPHY

- [66] M.A. Ferno, A. Haugen, and A. Graue. Wettability effects on the matrix-fracture fluid transfer in fractured carbonate rocks. *Journal of Petroleum Science and Engineering*, 77:146–153, 2011.
- [67] M.A. Ferno, A. Haugen, S. Wickramathilaka, J. Howard, A. Graue, G. Mason, and N.R. Morrow. Magnetic resonance imaging of the development of fronts during spontaneous imbibition. *Journal of Petroleum Science and Engineering*, 101:1–11, 2013.
- [68] Y. Fu, Y. K. Yang, and M. Doe. Three-dimensional, three-phase discrete-fracture reservoir simulation based on control volume finite element (cvfe) formulation. *SPE Reservoir Simulation Symposium*, Houston, Texas, 31 January - 2 February:1, 2005.
- [69] F. Fousseis, X. Xiao, C. Schrank, and F. De Carlo. A brief guide to synchrotron radiation-based microtomography in (structural) geology and rock mechanics. *Structural Geology*, 65:1–16, 2014.
- [70] J. Garland, J. Neilson, S. Laubach, and K. Whidden. Advances in carbonate exploration and reservoir analysis. *Geological Society, London, Special Publications*, 370 (1):1–15, 2012.
- [71] S. Ge. A governing equation for fluid flow in rough fractures. *Water Resources Research*, 33(1):53–61, 1997.
- [72] S. Geiger. *Reactive transport modeling in a discrete fracture: applications to the formation of sericitic hydrothermal alteration at Butte, Montana*. PhD thesis, Oregon State University, 2000.
- [73] S. Geiger, T. Driesner, C. A. Heinrich, and S. K. Matthäi. Multiphase thermohaline convection in the earth's crust: I. a new finite element - finite volume solution technique combined with a new equation of state for nacl-h₂o. *Transport in Porous Media*, 63 (3)::399–434, 2006.
- [74] S. Geiger, Q. Huangfu, F. Reid, S. Matthäi, D. Coumou, M. Belayneh, C. Fricke, and K. Schmid. Massively parallel sector scale discrete fracture and matrix simulations. *SPE*, 118924:15, 2009.

BIBLIOGRAPHY

- [75] S. Geiger, S. Matthäi, J. Niessner, and R. Helmig. Black-oil simulations for three-component - three-phase flow in fractured porous media. *SPE*, 107485:20, 2007.
- [76] S Geiger and S.K. Matthai. What can we learn from high-resolution numerical simulations of single- and multi-phase fluid flow in fractured outcrop analogues? *In: Advances in the Study of Fractured Reservoirs*, eds., Spence G.H., Redfern J., Aguilera R., Bevan T.G., Cosgrove J.W., Couples G.D., Daniel J.M. *Geological Society of London Special Publications*, 374:124–144, 2014.
- [77] S. Geiger, S. Roberts, S. K. Matthäi, C. Zoppu, and A. Burri. Combining finite element and finite volume methods for efficient multiphase flow simulations in highly heterogeneous and structurally complex geologic media. *Geofluids*, 4:284–299, 2004.
- [78] R.C. Gonzalez and R.E. Woods. *Digital Image Processing*. Addison Wesley, Pearson Education, 2008.
- [79] T. Graeve and G.P. Weckler. High-resolution cmos imaging detector. *Physics of Medical Imaging*, SPIE Vol. 4320, 2001.
- [80] S. A. Hall, M. Bornert, N. Lenoir, P. BÃ©suelle, Y. Pannier, G. Viggiani, and J. Desrues. Discrete and continuum analysis of localised deformation in sand using x-ray μ ct and volumetric digital image correlation. *GÃ©otechnique*, 60/5:315–322, 2010.
- [81] R. Helmig. *Multiphase Flow and Transport Processes in the Subsurface*. Springer, 1997.
- [82] A. Hill and G. Thomas. A new approach for simulating complex fractured reservoirs. *Middle East Oil Technical Conference and Exhibition*, Society of Petroleum Engineers, 1985.
- [83] T. Hofmann, J. Claussen, F. Nachtrab, I. Bauscher, and N. Uhlmann. Linearity of flat panel x-ray detectors and comparison of non-linear correction algorithms. *International Symposium on Digital Industrial Radiology and Computed Tomography - Poster 11 20-22 June 2011, Berlin, Germany*, 2011.

BIBLIOGRAPHY

- [84] H. Hoteit and A. Firoozabadi. Multicomponent fluid flow by discontinuous galerkin and mixed methods in unfractured and fractured media. *Water Resources Research*, 41:W11412, 2005.
- [85] H. Hoteit and A. Firoozabadi. An efficient numerical model for incompressible two-phase flow in fractured media. *Advances in Water Resources*, 31(6):891–905, 2008.
- [86] A.N. Houston, S. Schmidt, W. Otten, P. Baveye, and S. Hapca. Effect of scanning and image reconstruction settings in x-ray computed tomography on soil image quality and segmentation performance. *Geoderma*, 207-208:154–165, 2013.
- [87] Hubbard Brook Ecosystem Study. Hubbard Brook Photo Gallery/ Research Projects/ Soils and Geology/ Measuring_fracture_surface_roughness.jpg. <http://data.hubbardbrook.org/photos>, accessed 01.07.2020.)
- [88] R. G. Hughes and M. J. Blunt. Network modeling of multiphase flow in fractures. *Advances in Water Resources*, 4 (2001):409–421, 2000.
- [89] *1st International Conference on Tomography of Materials and Structures (ICTMS 2013): Book of Abstracts. July 1-5 (Ghent, Belgium)*, 2013.
- [90] *2nd International Conference on Tomography of Materials and Structures (ICTMS 2015): Proceedings. June 29 - July 3, (Quebec, Canada)*, 2015.
- [91] S. Iglauer, M.A. Ferno, and and Blunt M.J. Shearing, P. Comparison of residual oil cluster size distribution, morphology and saturation in oil-wet and water-wet sandstone. *Journal of Colloid and Interface Science*, 375:187–192, 2012.
- [92] S. Iglauer, A. Paluszny, and M.J. Blunt. Simultaneous oil recovery and residual gas storage: A pore-level analysis using in situ x-ray micro-tomography. *Fuel* 103, 130:905–914, 2013.
- [93] O. Izgec, D. Zhu, and A.D. Hill. Numerical and experimental investigation of acid wormholing during acidization of vuggy carbonate rocks. (2010),. *Journal of Petroleum Science and Engineering*, 2010.

BIBLIOGRAPHY

- [94] N. P. James and B. Jones. *Origin of Carbonate Sedimentary Rocks*. John Wiley & Sons, 2015.
- [95] J.K. Jasti and H.S. Fogler. Application of neutron radiography to image flow phenomena in porous media. *AIChE Journal*, 38(4):481–488, 1992.
- [96] R. A. Johns and P. V. Roberts. A solute transport model for channelized flow in a fracture. *Water Resources Research*, 27(8):1797–1808, 1991.
- [97] R.A. Johns, J.S. Steude, L.M. Castanier, and P.V. Roberts. Nondestructive measurements of fracture aperture in crystalline rock cores using x ray computed tomography. *Journal of Geophysical Research*, 98/B2:1889–1900, 1993.
- [98] D. Joseph. *Modelling and calibration of logarithmic CMOS image sensors*. PhD thesis, University of Oxford, 2002.
- [99] D. Joseph and S. Collins. Modeling, calibration, and correction of non-linear illuminationdependent fixed pattern noise in logarithmic CMOS image sensors. *IEEE Transaction on Instrumentation and Measurement*, 51/5:996–1001, 2002.
- [100] A. Kaestner, E. Lehmann, and M. Stampanoni. Imaging and image processing in porous media research. *Advances in Water Resources*, 31:1174–1187, 2008.
- [101] A. C. Kak and M. Slaney. *Principles of Computerized Tomographic Imaging*. IEEE PRESS, 1999.
- [102] M. Karimi-Fard, L.J. Durlofsky, and K. Aziz. An efficient discrete-fracture model applicable for general-purpose reservoir simulators. *SPE Journal*, 9(2):227–236, 2004.
- [103] M. Karimi-Fard and A. Firoozabadi. Numerical simulation of water injection in fractured media using the discrete-fracture model and the galerkin method. *SPE Reservoir Evaluation & Engineering*, 6(2):117–126, 2003.
- [104] Z. T. Karpyn and M. Piri. Prediction of fluid occupancy in fractures using network modeling and x-ray microtomography. ii: Results. *PHYSICAL REVIEW*, E 76, 016316 (2007):11, 2007.

BIBLIOGRAPHY

- [105] Z.T. Karpyn, A. Alajmi, F. Radaelli, P.M. Halleck, and A.S. Grader. X-ray ct and hydraulic evidence for a relationship between fracture conductivity and adjacent matrix porosity. *Engineering Geology*, 103:139–145, 2009.
- [106] Z.T. Karpyn, A.S. Grader, and P.M. Halleck. Visualization of fluid occupancy in a rough fracture using micro-tomography. *Journal of Colloid and Interface Science*, 307 (2007):181–187, 2007.
- [107] H. Kazemi, L. S. Merrill, K. L. Porterfield, and P. R. Zeman. Numerical simulation of water-oil flow in naturally fractured reservoirs. *Society of Petroleum Engineers Journal*, 16(6):317–326, 1976.
- [108] A. Keller. High resolution, non-destructive measurement and characterization of fracture apertures. *International Journal of Rock Mechanics and Mining Sciences*, 35(8):1037–1050, 1998.
- [109] A.A. Keller. High resolution cat imaging of fractures in consolidated materials. *Int. J. Rock Mech. Mining Sci*, 34:358, 1997.
- [110] R.A. Ketcham. Computational methods for quantitative analysis of three-dimensional features in geological specimens. *Geosphere*, 1(1):32–41, 2005.
- [111] R.A. Ketcham and W.D. Carlson. Acquisition, optimization and interpretation of x-ray computed tomographic imagery: applications to the geosciences. *Computers and Geosciences*, 27:381–400, 2001.
- [112] R.A. Ketcham and R.D. Hanna. Beam hardening correction for x-ray computed tomography of heterogeneous natural materials. *Computers and Geosciences*, 67:49–61, 2014.
- [113] R.A. Ketcham, D.T. Slottke, and J.M. Sharp. Three-dimensional measurement of fractures in heterogeneous materials using high-resolution x-ray computed tomography. *Geosphere*, 6:499–514, 2010.
- [114] M.J. King and A. Datta-Gupta. Streamline simulation: A current perspective. *In Situ*, 2:910–140, 1998.

BIBLIOGRAPHY

- [115] M. Krause, J.-M. Hausherr, and W. Krenkel. (micro)-crack detection using local radon transform. *Materials Science and Engineering: A*, 527/26:7126–7131, 2010.
- [116] V.A. Kuuskraa, G.J. Koperna, J.W. Schmoker, and J.C. Quinn. Barnett shale rising star in fort worth basin. *Oil & Gas Journal*, 96(21):67–76, 1998.
- [117] A. L. C. Kwan, J. A. Seibert, and J. M. Boone. An improved method for flat-field correction of flat panel x-ray detector. *Med. Phys.*, 33:391, 2006.
- [118] C.J. Landry, Z.T. Karpyn, and O. Ayala. Pore-scale lattice boltzmann modeling and 4d x-ray computed microtomography imaging of fracture-matrix fluid transfer. *Transp Porous Med*, 103:449–468, 2014.
- [119] C.H. Lee and Z.T. Karpyn. Experimental investigation of rate effects on two-phase flow through fractured rocks using x-ray computed tomography. *Advances in X-Ray Tomography for Geomaterials*, (eds. Alshibli, K.A. & Reed, A.H. - John Wiley & Sons):230–237, 2010.
- [120] K.A. Lie, S. Krogstad, I.S. Ligaarden, J.R. Natvig, H.M. Nilsen, and H. Skaflestad. Open-source matlab implementation of consistent discretisations on complex grids. *Computational Geosciences*, 16(2):297–322, 2011.
- [121] W. B. Lindquist, A. Venkatarangan, J. Dunsmuir, and T. Wong. Pore and throat size distributions measured from synchrotron x-ray tomographic images of fontainebleau sandstones. *Journal of Geophysical Research*, 105/B9:21,509–21,527, 2000.
- [122] G. J. Lord, C.E. Powell, and T. Shardlow. *An Introduction to Computational Stochastic PDEs*. Cambridge Texts in Applied Mathematics, 2014.
- [123] H. Lu, G. Di Donato, and M. J. Blunt. General transfer functions for multiphase flow in fractured reservoirs. *SPE Journal*, 102542:9, 2008.

BIBLIOGRAPHY

- [124] F. Lucia. Rock-fabric / petrophysical classification of carbonate pore space for reservoir characterization. *AAPG bulletin*, 79 (9):1275–1300, 1995.
- [125] F. Lucia. Origin and petrophysics of dolostone pore space. *Geological Society, London, Special Publications*, 235 (1):141–155, 2004.
- [126] M. Madadi and M. Sahimi. Lattice boltzmann simulation of fluid flow in fracture networks with rough, self-affine surfaces. *Physics Review E*, 67(2):026309, 2003.
- [127] M. Madadi, C. D. VanSiclen, and M. Sahimi. Fluid flow and conduction in two-dimensional fractures with rough, self-affine surfaces: A comparative study. *J. Geophys. Res.*, 108(B8):2396, 2003.
- [128] C. Maier. *Improved simulation of naturally fractured reservoirs using unstructured grids and multi-rate dual-porosity models*. PhD thesis, Institute of Petroleum Engineering, Heriot Watt University, 2014.
- [129] S. K. Matthäei, S. Geiger, S. G. Roberts, A. Paluszny, M. Belayneh, A. Burri, A. Mezentsev, H. Lu, D. Coumou, T. Driesner, and C. A. Heinrich. Numerical simulation of multi-phase fluid flow in structurally complex reservoirs. *Geological Society, London, Special Publications 2007*, v. 292:405–429, 2007a.
- [130] S. K. Matthäei, A. A. Mezentsev, and M. Belayneh. Finite element - node-centered finite-volume two-phase-flow experiments with fractured rock represented by unstructured hybrid-element meshes. *Society of Petroleum Engineers*, 2007b.
- [131] S.K. Matthäei and M. Belayneh. Fluid flow partitioning between fractures and a permeable rock matrix. *Geophysical Research Letters*, VOL. 31:L07602, 2004.
- [132] J.H. McCrary, E.H. Plassmann, J.M. Puckett, A.L. Conner, and G.W. Zimmermann. X-ray attenuation-coefficient measurements. *Physical Review*, Volume 153, Number 2:6, 1967.

BIBLIOGRAPHY

- [133] D. McDuff, S. Jackson, C. Shuchart, and D. Postl. Understanding wormholes in carbonates: Unprecedented experimental scale and 3d visualization. *Journal of Petroleum Technology*, 62/10:78–81, 2010.
- [134] H.P. Menke, B.R. Bijeljic, M.G. Andrew, and M.J.B. Blunt. Dynamic three-dimensional pore-scale imaging of reaction in a carbonate at reservoir conditions. *Environmental Science and Technology*, 49/7:4407–4414, 2015.
- [135] C Milliotte and S. Matthai. From seismic interpretation to reservoir model: An integrated study accounting for the structural complexity of the vienna basin using an unstructured reservoir grid. *First Break*, 32 (5), 2014.
- [136] R. Mills and J. W. Kennedy. The self-diffusion coefficients of iodide, potassium and rubidium ions in aqueous solutions. *Journal of the American Chemical Society*, 75 (22):5696–5701, 1953.
- [137] A. Moinfar, W. Narr, M.H. Hui, B.T. Mallison, and S.H. Lee. Comparison of discrete-fracture and dual-permeability models for multiphase flow in naturally fractured reservoirs. *SPE Reservoir Simulation Symposium*, 21-23 February, The Woodlands, Texas, USA, 2011.
- [138] B. Montaron. Carbonate evolution. *Oil & Gas Middle East*, 2008.
- [139] J. E. P. Monteagudo and A. Firoozabadi. Comparison of fully implicit and impes formulations for simulation of water injection in fractured and unfractured media. *International Journal for Numerical Methods in Engineering*, 69(4):698–728, 2007.
- [140] J. E. P. Monteagudo and A. Firoozabadi. Control-volume model for simulation of water injection in fractured media: Incorporating matrix heterogeneity and reservoir wettability effects. *SPE Journal*, 12:355–366, 2007.
- [141] J.E.P. Monteagudo and A. Firoozabadi. Control-volume method for numerical simulation of two-phase immiscible flow in two- and three-dimensional discrete-fractured media. *Water Resources Research*, 40(7), 2004.

BIBLIOGRAPHY

- [142] V. Mourzenko, J.-F. Thovert, and P. Adler. Permeability of a single fracture; validity of the reynolds equation. *Journal de Physique II, EDP Sciences*, 5(3):465–482, 1995.
- [143] V. Mourzenko, J.-F. Thovert, and P. Adler. Permeability of self-affine fractures. *Transport in Porous Media*, 45(1):89–103, 2001.
- [144] S. Nakashima, D. Hasegawa, K. Kishida, and H. Yasuhara. Measurement of fracture aperture in granite core using microfocus x-ray ct and laser beam profilemeter. *ISRM International Symposium - 6th Asian Rock Mechanics Symposium, 23-27 October, New Delhi, India*, 2010.
- [145] W. Narr, D.W. Schechter, and L.B. Thompson. *Naturally Fractured Reservoir Characterization*. Society of Petroleum Engineers, 2006.
- [146] R.A. Nelson. *Geologic Analysis of Naturally Fractured Reservoirs*. Gulf Professional Publishing, 2001.
- [147] M.J. Nicholl, H. Rajaram, R.J. Glass, and R. Detwiler. Saturated flow in a single fracture: evaluation of the reynolds equation in measured aperture fields. *Water Resources Research*, 35(11):3361–3373, 1999.
- [148] H. M. Nick and S. K. Matthai. Comparison of three fe-fv numerical schemes for single- and two-phase flow simulation of fractured porous media. *Transport in Porous Media*, 90(2):421–444, 2011.
- [149] A. Nowamooz, G. Radilla, M. Fourar, and B. Berkowitz. Non-fickian transport in transparent replicas of rough-walled roch fractures. *Transport in Porous Media*, 98(3):651–682, 2013.
- [150] P. Nuske, B. Faigle, R. Helmig, J. Niessner, and I. Neuweiler. Modeling gas-water processes in fractures with fracture flow properties obtained through upscaling. *Water Resources Research*, 46(9):W09528, 2010.
- [151] M. Oda, T. Takemura, and M. Takahashi. Microstructure in shear band observed by microfocus x-ray computed tomography. *GÃ©otechnique*, 54:539–542, 2004.
- [152] N. E. Odling. Scaling and connectivity of joint systems in sandstones from western norway. *Journal of Structured Geology*, Vol. 19, No. 10:1257–1271, 1997.

BIBLIOGRAPHY

- [153] W. Oh and W.B. Lindquist. Image thresholding by indicator kriging. *IEEE Trans Pattern Anal Mach Intell*, 21(7):590–602, 1999.
- [154] A.P. Oron and B. Berkowitz. Flow in rock fractures: The local cubic law assumption reexamined. *Water Resources Research*, 34(11):2811–2825, 1998.
- [155] N. Otsu. A threshold selection method from gray-level histograms. *IEEE Trans Syst Man Cybern*, 9(1):62–6, 1979.
- [156] T. Pak, I.B. Butler, S. Geiger, M.I.J. van Dijke, and K.S. Sorbie. Droplet fragmentation: 3d imaging of a previously unidentified pore-scale process during multiphase flow in porous media. *PNAS*, 112(7):1947–1952, 2015.
- [157] N.R. Pal and S.K. Pal. A review on image segmentation techniques. *Pattern Recognition*, 26(9):1277–1294, 1993.
- [158] A. Paluszny, S. K. Matthäi, and M. Hohmeyer. Hybrid finite element-finite volume discretization of complex geologic structures and a new simulation workflow demonstrated on fractured rocks. *Geofluids*, 7:186–208, 2007.
- [159] A. Paluszny and R. W. Zimmerman. Numerical simulation of multiple 3d fracture propagation using arbitrary meshes. *Computer Methods in Applied Mechanics and Engineering*, 200(9-12):953–966, 2010.
- [160] P. Perona and J. Malik. Scale-space and edge detection using anisotropic diffusion. *IEEE Trans Pattern Anal Mach Intell*, 12(7):629–39, 1990.
- [161] M. Piri and Z. T. Karpyn. Prediction of fluid occupancy in fractures using network modeling and x-ray microtomography. i: Data conditioning and model description. *PHYSICAL REVIEW*, E 76, 016315 (2007):13, 2007.
- [162] A. Polak, A.S. Grader, R. Wallach, and R. Nativá. Tracer diffusion from a horizontal fracture into the surrounding matrix: measurement by computed tomography. *Journal of Contaminant Hydrology*, 67(1-4):95–112, 2003.

BIBLIOGRAPHY

- [163] M.L. Porter and D. Wildenschild. Image analysis algorithms for estimating porous media multiphase flow variables from computed microtomography data: a validation study. *Computational Geosciences*, 14/1:15–30, 2010.
- [164] W.L. Power and W.B. Durham. Topography of natural and artificial fractures in granitic rocks: Implications for studies of rock friction and fluid migration. *International Journal of Rock Mechanics and Mining Sciences*, 34(6):979–989, 1997.
- [165] M. Prodanovic, S.L. Bryant, and Z.T. Karpyn. Investigating matrix/fracture transfer via a level set method for drainage and imbibition. *SPE Journal*, 15(1):SPE–116110–PA, 2010.
- [166] M. Prodanovic, W.B. Lindquist, and R.S. Seright. 3d image-based characterization of fluid displacement in a Berea core. *Advances in Water Resources*, 30:214–226, 2007.
- [167] Radicon Imaging Corp. ANo8: Polynomial Gain Correction for Rad-Eye Sensors. *Radicon Imaging Corp (now Teledyne Dalsa)*, 2003.
- [168] E.R. Rangel-German. *Water Infiltration in Fractured Porous Media: In-Situ Imaging, Analytical Model, and Numerical Study*. PhD thesis, Stanford University, 2002.
- [169] E.R. Rangel-German and A.R. Kovscek. Experimental and analytical study of multidimensional imbibition in fractured porous media. *Journal of Petroleum Science and Engineering*, 36:45–60, 2002.
- [170] E.R. Rangel-German and A.R. Kovscek. Matrix-fracture shape factors and multiphase-flow properties of fractured porous media. *SPE Latin American and Caribbean Petroleum Engineering Conference, 20-23 June, Rio de Janeiro, Brazil*, 2005.
- [171] V. Rebuffel and J.-M. Dinten. Dual-energy x-ray imaging: benefits and limits. *Insight NonDestructive Testing and Condition Monitoring*, 49/10:589–594, 2007.

BIBLIOGRAPHY

- [172] V. Reichenberger, H. Jakobs, P. Bastian, and R. Helmig. A mixed-dimensional finite volume method for two-phase flow in fractured porous media. *Advances in Water Resources*, 29:1020–1036, 2006.
- [173] F. Renard, D. Bernard, J. Desrues, and A. Ougier-Simonin. 3d imaging of fracture propagation using synchrotron x-ray microtomography. *Earth and Planetary Science Letters*, 286/1-2:285–291, 2009.
- [174] François Renard, Christophe Voisin, David Marsan, and Jean Schmitbuhl. High resolution 3d laser scanner measurements of a strike-slip quantify its morphological anisotropy at all scales. *Geophysical Research Letters*, 33, 02 2008.
- [175] L. Rudin, S. Osher, and E. Fatemi. Nonlinear total variation based noise removal algorithms. *Physica D*, 60:259–68, 1992.
- [176] A. Sahni, J. Burger, and M. Blunt. Measurement of three phase relative permeability during gravity drainage using CT. *Society of Petroleum Engineers*, SPE-39655-MS, 1998.
- [177] D. J. Sanderson and X. Zhang. Critical stress localization of flow associated with deformation of well-fractured rock masses, with implications for mineral deposits. *Geological Society (London) Special Publication*, 155:69–81, 1999.
- [178] T.H. Sandve, I. Berre, and J.M. Nordbotten. An efficient multi-point flux approximation method for discrete fracture-matrix simulations. *Journal of Computational Physics*, 231(9):3784–3800, 2012.
- [179] P. Sarma and K. Aziz. New transfer functions for simulation of naturally fractured reservoirs with dual-porosity models. *SPE Journal*, 11(3):SPE-90231-PA, 2006.
- [180] K. S. Schmid, S. Geiger, and K. S. Sorbie. Higher order FE-FV method on unstructured grids for transport and two-phase flow with variable viscosity in heterogeneous porous media. *Journal of Computational Physics*, 241:416–444, 2013.

BIBLIOGRAPHY

- [181] C. Schmidgunst, D. Ritter, and E. Lang. Calibration model of a dual gain flat panel detector for 2d and 3d x-ray imaging. *Med Phys.*, 34(9):3649–64, 2007.
- [182] J. A. Seibert, J. M. Boone, and K. K. Lindfors. Flat-field correction technique for digital detectors. *Proc. SPIE 3336, Medical Imaging 1998: Physics of Medical Imaging, 348 (July 24, 1998)*;, 3336, 1998.
- [183] A. Sheppard, R. Sok, and H. Averdunk. Techniques for image enhancement and segmentation of tomographic images of porous materials. *Physica A*, 339:145–51, 2004.
- [184] S.M. Skjaeveland and J. Kleppe, editors. *SPOR Monograph - Recent Advances in Improved Oil Recovery Methods for North Sea Sandstone Reservoirs*. Norwegian Petroleum Directorate, 1992.
- [185] G. Strang. On the construction and comparison of difference schemes. *SIAM Journal on Numerical Analysis*, 5(3):506–517, 1968.
- [186] K. StÅEben. A review of algebraic multigrid. *Journal of Computational an Applied Mathematics*, 128:281–309, 2001.
- [187] K. Thompson. Operations & analysis of voxel data for geosciences. *NSF Sponsored Short Course on CT Imaging in the GeoSciences, February 28, 2010, GeoX 2010*, page 2010.
- [188] K.E. Thompson, C.S. Willson, C.D. White, S. Nyman, J.P. Bhattacharya, and A.H. Reed. Application of a new grain-based reconstruction algorithm to microtomography images for quantitative characterization and flow modeling. *SPE*, 13 (2) SPE-95887-PA:164–176, 2008.
- [189] K.E. Thompson, C.S. Willson, and W. Zhang. Quantitative computer reconstruction of particulate materials from microtomography images. *Powder Technology*, 163/3:169–182, 2006.
- [190] D. Tiab and E. C. Donaldson. *Petrophysics - Theory and Practice of Measuring Reservoir Rock and Fluid Transport Properties*. Elsevier Inc., 2012.

BIBLIOGRAPHY

- [191] Y.W. Tsang and C.F. Tsang. Channel model of flow through fractured media. *Water Resources Research*, 23:467–479, 1987.
- [192] M.L. Turner, L. Knuefing, C.H. Arns, A. Sakellariou, T.J. Senden, A.P. Sheppard, R.M. Sok, A. Limaye, W.V. Pinczewski, and M.A. Knackstedt. Three-dimensional imaging of multiphase flow in porous media. *Physica A*, 339:166–172, 2004.
- [193] K. Vandersteen, B. Busselen, K. Van Den Abeele, and J. Carmeliet. Quantitative characterization of fracture apertures using microfocus computed tomography. *Geological Society, London, Special Publications*, 215:61–68, 2003.
- [194] G. Viggiani, N. Lenoir, P. Besuelle, M.D. Michiel, S. Marelli, J. Desrues, and M. Kretschmer. X-ray microtomography for studying localized deformation in fine-grained geomaterials under triaxial compression. *Comptes Rendus Mécanique*, 332:819–26, 2004.
- [195] V. Vilarrasa, T. Koyama, I. Neretnieks, and L. Jing. Shear-induced flow channels in a single rock fracture and their effect on solute transport. *Transport in Porous Media*, 87(2):503–523, 2011.
- [196] H. J. Vinegar and S. L. Wellington. Tomographic imaging of three-phase flow experiments. *Rev. Sci. Instrum.*, 58:96, 1987.
- [197] J. Vlassenbroeck, M. Dierick, B. Masschaele, V. Cnudde, L. Hoorebeke, and P. Jacobs. Software tools for quantification of x-ray microtomography at the ugct. *Nuclear Instruments and Methods in Physics Research Section A, Proceedings of the 10 th International Symposium on Radiation Physics - ISRP 10*, 580/1:442–445, 2007.
- [198] H.-J. Vogel and K. Roth. Quantitative morphology and network representation of soil pore structure. *Advances in Water Resources*, 24/3-4:233–242, 2001.
- [199] P. Vontobel, E. Lehmann, and W.D. Carlson. Comparison of x-ray and neutron tomography investigations of geological materials. *Nuclear Science, IEEE Transactions*, vol.52, no.1:338– 341, 2005.

BIBLIOGRAPHY

- [200] M. Voorn, U. Exner, and A. Rath. Multiscale hessian fracture filtering for the enhancement and segmentation of narrow fractures in 3d image data. *Computers & Geosciences*, 57:44–53, 2013.
- [201] Maarten Voorna, Ulrike Exnerb, Auke Barnhoorn, Patrick Baudd, and Thierry ReuschlÃ©d. Porosity, permeability and 3d fracture network characterisation of dolomite reservoir rock samples. *Journal of Petroleum Science and Engineering*, 2015.
- [202] L. Wang, M.B. Cardenas, D.T. Slottke, R.A. Ketcham, and J.M. Sharp Jr. Modification of the local cubic law of fracture flow for weak inertia, tortuosity, and roughness. *Water Resources Research*, 51:2064–2080, 2015.
- [203] J.E. Warren and P.J. Root. The behavior of naturally fractured reservoirs. *SPE Journal*, 426:11, 1963.
- [204] N. Watanabe, T. Ishibashi, N. Hirano, Y. Ohsaki, Y. Tsuchiya, T. Tamagawa, H. Okabe, and N. Tsuchiya. Precise 3d numerical modeling of fracture flow coupled with x-ray computed tomography for reservoir core samples. *SPE Journal*, 16(3):SPE-146643-PA, 2011.
- [205] David J. Whitehouse. *Photomechanics, Topics Appl. Phys.* 77, chapter Surface Characterization and Roughness Measurement in Engineering, pages 413 – 461. Springer-Verlag Berlin Heidelberg, 2000.
- [206] M. Wiedenbeck. Total x-ray attenuation coefficients from 40 kev to 412 kev. *Physical Review*, Volume 126, Number 3:2, 1962.
- [207] D. Wildenschild, J. Hopmans, C. Vaz, M. Rivers, D. Rikard, and B. Christensen. Using x-ray computed tomography in hydrology: systems, resolutions, and limitations. *J Hydrol*, 267(3-4):285–97, 2002.
- [208] D. Wildenschild and A. P. Sheppard. X-ray imaging and analysis techniques for quantifying pore-scale structure and processes in subsurface porous medium systems. *Advances in Water Resources*, 51:217–246, 2012.

BIBLIOGRAPHY

- [209] P. A. Witherspoon, J. S. Wang, K. Iwai, and J. E. Gale. Validity of the cubic law for fluid flow in a deformable rock fracture. *Water Resources Research*, 16, No. 6, 1016-1024:1, 1980.
- [210] E.M. Withjack, C. Devier, and G. Michael. The role of x-ray computed tomography in core analysis. *Society of Petroleum Engineers*, SPE-83467-MS, 2003.
- [211] C. Wu, Y. Cheng, Y. Ding, F. Wei, and Y. Jin. A novel x-ray computed tomography method for fast measurement of multiphase flow. *Chemical Engineering Science*, 62:4325 – 4335, 2007.
- [212] Y. Zaretskiy, S. Geiger, K. Sorbie, and M. Färster. Efficient flow and transport simulations in reconstructed 3d pore geometries. *Advances in Water Resources*, 33(12):1508–1516, 2010.
- [213] R. Zimmerman and Ian Main. *Hydromechanical Behavior of Fractured Rocks*, volume 89, pages 363–432. 01 2004.
- [214] R. W. Zimmerman and I.-W. Yeo. Fluid flow in rock fractures: From the navier-stokes equations to the cubic law, in dynamics of fluids in fractured rock. (eds B. Faybishenko, P. A. Witherspoon and S. M. Benson), American Geophysical Union, Washington, D. C.:213–224, 2000.
- [215] R.W. Zimmerman, A. Al-Yaarubi, C. Pain, and C.A. Grattoni. Non-linear regimes of flow in rock fractures. *International Journal of Rock Mechanics and Mining Sciences*, 41(3):163–169, 2004.
- [216] R.W. Zimmerman, D.-W. Chen, and N.G.W. Cook. The effect of contact area on the permeability of fractures. *Journal of Hydrology*, 139(1-4):79–96, 1992.

A

APPENDIX

A.1 GOVERNING EQUATIONS FOR TWO-PHASE FLOW

In general, the flow equations for two-phase immiscible systems are derived from combining material balance with Darcy's law. As the fluids are immiscible, the mass conservation equation and Darcy's law can be applied to each of the two phases, oil and water, separately. The physics take capillary, viscous, and gravitational forces into account.

For a fluid phase, α ($\alpha \in \{W, O\}$ for water or oil, respectively), the mass conservation states that the change of mass of the fluid in a volume over the time equals the flux over the boundaries.

$$\frac{\partial(\Phi\rho_\alpha S_\alpha)}{\partial t} = -\nabla \cdot (\rho_\alpha \cdot \mathbf{v}_\alpha) + \rho_\alpha q_\alpha \quad (44)$$

Here, the mass of phase α in the considered volume is defined by the rock porosity, Φ , the fluid density, ρ_α , and the fluid saturation, S_α . The flux ($\rho_\alpha \cdot \mathbf{v}_\alpha$) describes the transport in the different phases. $\rho_\alpha q_\alpha$ is an additional source term.

Assuming that the fluids are incompressible, i.e. $\frac{\partial\rho_\alpha}{\partial t} = 0$, and the rock porosity is constant, this simplifies to

$$\Phi \frac{\partial S_\alpha}{\partial t} = -\nabla \cdot (\mathbf{v}_\alpha) + q_\alpha \quad (45)$$

As the medium is assumed to be fully saturated, we have the additional constraint

$$S_W + S_O = 1 \quad (46)$$

We sum equation (A.1) for both phases and simplify with

$$\mathbf{v}_t = \mathbf{v}_O + \mathbf{v}_W \quad (47)$$

and

$$q_t = q_O + q_W \quad (48)$$

hence we obtain

$$\Phi \underbrace{\frac{\partial}{\partial t}(S_W + S_O)}_{=0} = -\nabla \cdot (\mathbf{v}_t) + q_t \quad (49)$$

From the constraint (A.1) then follows for incompressible fluids

$$\nabla \cdot \mathbf{v}_t = q_t \quad (50)$$

The phase velocity \mathbf{v}_α in equation (A.1) and (A.1) is given by Darcy's law. Darcy's law states that for fluid flow through porous media the fluid velocity in flow direction is proportional to the pressure gradient

$$\mathbf{v}_\alpha = -\mathbf{k} \frac{k_{r\alpha}}{\mu_\alpha} (\nabla p_\alpha - \rho_\alpha \mathbf{g}) \quad (51)$$

where \mathbf{k} is the permeability tensor, $k_{r\alpha} = k_{r\alpha}(S_\alpha)$ the relative permeability which is depending on the phase saturation, μ_α the fluid viscosity, p_α the fluid pressure of phase α , and $\mathbf{g} = [0, 0, -g]^T$ the gravitational acceleration vector. The relative permeabilities and the fluid viscosity can be combined as phase mobility $\lambda_\alpha = k_{r\alpha} / \mu_\alpha$. The relative permeability $k_{r\alpha}$ is a non-linear function of the saturation S_α .

To complete the equations, we define the capillary pressure, p_c , which is a function of the saturation, as difference between the phase pressures

$$p_c = p_O - p_W \quad (52)$$

Inserting (A.1) into (A.1), and $p_W = p_O - p_c$ from equation (A.1), we get the pressure-diffusion equation for incompressible two-phase flow

$$\nabla \cdot (-\mathbf{k} (\lambda_W + \lambda_O) \nabla p_O + \mathbf{k} \lambda_W \nabla p_c + \mathbf{k} \mathbf{g} (\rho_W \lambda_W + \rho_O \lambda_O)) - (q_W + q_O) = 0 \quad (53)$$

or shorter

$$\nabla \cdot \mathbf{k} (-\lambda_t \nabla p_O + \lambda_W \nabla p_c + \mathbf{g} (\rho_W \lambda_W + \rho_O \lambda_O)) - q_t = 0 \quad (54)$$

which, as a partial differential equation (PDE) to model the oil pressure, and can to be solved numerically. A similar equation can be obtained to model water pressure.

A.2 DEVELOPED MATLAB PROGRAM FOR IMAGE CORRECTION OF CMOS PANEL DETECTORS

The MATLAB program is divided into three parts. First, we initialize variables, i.e. we set the values for x_1 , x_2 , and x_3 , and read the three corresponding FF images taken at different intensities. In the second part, the coefficient matrices are calculated by calling a sub-function `SolvePiecewisePol.m`, which solves the piecewise polynomial approach for the chosen values for x_1 , x_2 , and x_3 . In the third part of the program, a loop runs over all images that will be corrected. The actual image correction takes place in the sub-function `PiecePol_correction.m`.

```
%% Initialization
% choose x values
x1 = 0.2;
x2 = 0.6;
x3 = 1.0;
% image dimensions
row = ...; % number of rows
col = ...; % number of columns
Idim = row*col; % number of pixels
n = ...; % number of images to correct
%% read FF images
% FF image for x1
FF1 = imread(['...tif']);
FF1 = double(FF1)+1;
% FF image for x2
FF2 = imread(['...tif']);
FF2 = double(FF2)+1;
% FF image for x3
FF3 = imread(['...tif']);
FF3 = double(FF3)+1;
% average value of 100% FF image
c = sum(sum(FF3))/(Idim);

%% calculate coefficient matrices
```

```

% initialize coefficient matrices
A = zeros(row, col);
B = A; C = A; D = A; E = A;
% initialize symbolic variables
syms y1 y2 y3
% call subfunction to calculate the inverse functions depending
% on x1, x2, x3
[Asym, Bsym, Csym, Dsym, Esym] = SolvePiecewisePol (x1, x2, x3);
% use symbolic variables to fill the coefficient matrices with
% according values
for i = 1:row
    for j = 1:col
        A(i,j) = subs(Asym, {y1,y2,y3}, {FF1(i,j),FF2(i,j),FF3(i,j)});
        B(i,j) = subs(Bsym, {y1,y2,y3}, {FF1(i,j),FF2(i,j),FF3(i,j)});
        C(i,j) = subs(Csym, {y1,y2,y3}, {FF1(i,j),FF2(i,j),FF3(i,j)});
        D(i,j) = subs(Dsym, {y1,y2,y3}, {FF1(i,j),FF2(i,j),FF3(i,j)});
        E(i,j) = subs(Esym, {y1,y2,y3}, {FF1(i,j),FF2(i,j),FF3(i,j)});
    end
end

%% correct images
% read average offset image
DC = imread('...tif');
% correct images
for i = 1:n
    I = imread([...,num2str(i),'.tif']);
    % offset correction
    I = I - DC;
    I = double(I)+1;
    % call subfunction for gain correction
    II = c*PiecePol_correction(I,FF2,A, B, C, D, E);
    II = uint16(round(II)-1);
    imwrite(II,[...,num2str(i),'.tif'],'Compression','none');
end

```

The subfunction `SolvePiecewisePol.m` uses MATLAB's Symbolic Math Toolbox to calculate the inverse function equations of the piecewise polynomial

fit function, depending on the given values of x_1 , x_2 , and x_3 . The function returns five symbolic variables, which store the inverse function equations.

```
function [a, b, c, d, e] = SolvePiecewisePol (XX1, XX2, XX3)
% calculate general equations
syms a b c d e
syms x1 x2 x3 y1 y2 y3
EQN = solve('y1 = a*x1^2 + b*x1',...
            'y2 = a*x2^2 + b*x2',...
            'y2 = c*x2^2 + d*x2 + e',...
            'y3 = c*x3^2 + d*x3 + e',...
            '2*a*x2 + b = 2*c*x2 + d',...
            'a','b','c','d','e');
a = EQN.a;
b = EQN.b;
c = EQN.c;
d = EQN.d;
e = EQN.e;
a = simplify(a);
b = simplify(b);
c = simplify(c);
d = simplify(d);
e = simplify(e);
a = subs(a, {x1, x2, x3}, {XX1, XX2, XX3});
b = subs(b, {x1, x2, x3}, {XX1, XX2, XX3});
c = subs(c, {x1, x2, x3}, {XX1, XX2, XX3});
d = subs(d, {x1, x2, x3}, {XX1, XX2, XX3});
e = subs(e, {x1, x2, x3}, {XX1, XX2, XX3});
```

The subfunction `PiecePol_correction.m` corrects image `I` with the inverse function of a piecewise quadratic polynomial response fit, saved in the coefficient matrices `A`, `B`, `C`, `D`, `E`, and the inflection point data of Flat Field image FF_2 saved in matrix `Y2`. The function returns the corrected image `II` unscaled.

```
function II = PiecePol_correction(I, Y2, A, B, C, D, E)
% get image dimensions
[row, col] = size(I);
% initialize output image
```

```

II = zeros(row,col);
% loop over all pixels
for i = 1:row
    for j = 1:col
        % save local copies to speed up program
        a = A(i,j);
        b = B(i,j);
        c = C(i,j);
        d = D(i,j);
        e = E(i,j);
        % input pixel
        y = I(i,j);
        % value x2 from middle FF image at input pixel
        y2 = Y2(i,j);
        if (y <= y2) % lower polynomial
            if (a~= 0)
                yy = (-b+sqrt(b^2+4*a*y))/...
                    (2*a);
            elseif (b~=0)
                yy = y/b;
            else
                yy = y; %leave unchanged
            end
        else % y > y2 upper polynomial
            if (c~= 0)
                yy = (-d+sqrt(d^2+4*c*y-...
                    4*c*e))/(2*c);
            elseif (d~=0)
                yy = (y-e)/d;
            else
                yy = y; %leave unchanged
            end
        end
        II(i,j) = yy;
    end
end
end

```

A.3 CT SCANNER – TABLE AND CAMERA CONTROL

```

////////////////////////////////////
// CamExe (Microsoft Visual C++ 6.0 on Windows 98)
//
// devloped for Edinburgh CT Centre for Material Research
// by Claudia Fricke, December 2009
// Update May 2013
// -----
//
// CamExe.exe is written to be called by the Testpoint program
// TCControl.tsp, to control the ShadoCam_4K X-Ray camera.
//
// The program initializes all necessary libraries, variables,
// and objects, some are read from an initialization file.
//
// After the libraries and objects are then configurated,
// several images are grabbed, deinterlaced, and accumulated as
// averaged image into one output file, specified in Testpoint.
// Bad pixels will be corrected by the manufacturers pixel map.
// The output file will be saved in big endian format.
//
// Update: Only Grabbing and saving the images in CamExe as *.crude.
// A new post-process program carries out the image conversions.
// No averaging or summing up images during run possible anymore.
//
// -----
// The executable CamExe.exe has to be in the Folder
// C:\CamExe\Debug
//
// Make sure that the following files are in the given paths
// under the following names:
//
// Cam file:
// C:\ShadoCam\SB4KPX.CAM
//
// Initialization file written by Testpoint
// C:\ShadoCam\IniFile.txt
// This file has to content:
// - 1st line:
//   Name and Path of the current Image
// - 2nd line:
//   Exposure Time
// - 3rd line:
//   Number of frames per stop
//
////////////////////////////////////

#include <iostream>
#include <fstream>

#include <windows.h>
#include <conio.h>

```

```

#include <ctime>

#include <string.h>
#include <stdio.h>

#include "pxd.h"
#include "iframe.h"
#include "Scilib20.h"

using namespace std;

int main()
{
    ////////////////////////////////////////////////// Variables //////////////////////////////////////

    clock_t start_prog(clock());

    PXD pxd;                // pxd library structure
    FRAMELIB framelib;     // frame library structure
    long hFG;              // adress of frame grabber
    FRAME* currentFrame;   // pointer to FRAME object
    short* currentFramePtr; // pointer to start of frame
    FRAME* newFrame;
    long qh;               // handle for grab

    int nWidth  = 2048;    // width of image
    int nHeight = 2000;    // height of image

    CAMERA_TYPE* camType; // pointer to camera object

    const long len = 65536; // length of LUT
    unsigned short nLUT[len]; // LUT

    char camFile[]="C:\\ShadoCam\\SB4KPX.CAM"; // camera setup file

    //help variables
    short* currentTempPtr; // temp pointer
    int i;                 // loop counters

    //read from file
    char output_file[200]; // filename for output *.crude-file
    char ext_output_file[200]; // extended filename for output
    float t = 0.5;        // "exposure" time
    short FramesPerStop = 1; // counter for number of frames per stop

    //open initialization file from Testpoint
    ifstream ini_file("C:\\ShadoCam\\IniFile.txt");
    if (ini_file.is_open())
    {
        ini_file.getline(output_file,199,'\n'); //read name of output file
        for crude-image
    }

```

```

        ini_file >> t;                                     //read "exposure time"
        ini_file >> FramesPerStop;
        ini_file.close();
    }
else
{
    MessageBox(NULL, "Not able to open initialization file.", "CamExe",
        MB_ICONERROR);
    return 0;
}

////////// Configuration //////////

// initialize the Imagenation libraries
if ( !imagenation_OpenLibrary("pxd_32.dll", &pxd, sizeof(PXD)) ) {
    MessageBox(NULL, "Frame grabber library not loaded.", "CamExe",
        MB_ICONERROR);
    return 0; }
if ( !imagenation_OpenLibrary("frame_32.dll", &framelib, sizeof(FRAMELIB
)) ) {
    MessageBox(NULL, "Frame library not loaded.", "CamExe", MB_ICONERROR);
    return 0; }

// request access to frame grabber
if ( !(hFG = pxd.AllocateFG(-1)) ) {
    MessageBox(NULL, "PXD frame grabber not found.", "CamExe",
        MB_ICONERROR);
    imagenation_CloseLibrary(&framelib);
    imagenation_CloseLibrary(&pxd);
    return 0; }

// initialize camera configuration
if ( !(camType = pxd.LoadConfig(camFile)) ) {
    MessageBox(NULL, "Camera configuration not loaded.", "CamExe",
        MB_ICONERROR);
    pxd.FreeFG(hFG);
    imagenation_CloseLibrary(&framelib);
    imagenation_CloseLibrary(&pxd);
    return 0; }

//set exposure time
float ft = pxd.GetFramePeriod(camType);
pxd.SetFramePeriod(camType, t);
ft = pxd.GetFramePeriod(camType);

pxd.SetCameraConfig(hFG, camType);
pxd.ContinuousStrobes(hFG, TRUE); // turn on camera frame sync

// initialize input LUT to shift image data down by two bits
for ( i = 0; i < len; i++) nLUT[i] = i>>2;
pxd.SetInputLUT(hFG, 16, 0, 0, len, nLUT);

```

```

// set up image destination buffers
if ( !(currentFrame = pxd.AllocateBuffer (pxd.GetWidth(hFG), pxd.
    GetHeight(hFG), PBITS_Y16)) ) {
    MessageBox(NULL, "Unable to create image buffer 1.", "CamExe",
        MB_ICONERROR);
    pxd.FreeFG(hFG);
    imagenation_CloseLibrary(&framelib);
    imagenation_CloseLibrary(&pxd);
    return 0; }
if ( !(newFrame = pxd.AllocateBuffer (pxd.GetWidth(hFG), pxd.GetHeight(
    hFG), PBITS_Y16)) ) {
    MessageBox(NULL, "Unable to create image buffer 2.", "CamExe",
        MB_ICONERROR);
    pxd.FreeFG(hFG);
    imagenation_CloseLibrary(&framelib);
    imagenation_CloseLibrary(&pxd);
    return 0; }

// create pointers to image buffer
// note: the configuration file sets up the image buffer to contain
//       an extra column to the left and right of the actual image
// Image Width = 2050
// Image Height = 2000
currentFramePtr = (short *)framelib.FrameBuffer(currentFrame);
currentFramePtr++; // point to first pixel in buffer1

currentTempPtr = currentFramePtr;

////////////////////// Image Aquisition ////////////////////////
clock_t start_aquisition(clock());

if(FramesPerStop == 1)
{
    // grab
    qh = pxd.Grab(hFG, currentFrame, 0);
    if (!qh)
    {
        MessageBox(NULL, "Unable to acquire image.", "CamExe",
            MB_ICONERROR);
        pxd.FreeFG(hFG);
        imagenation_CloseLibrary(&framelib);
        imagenation_CloseLibrary(&pxd);
        return 0; }
    cout << "Grab 1"<<endl;

    //save file
    strcat(output_file, ".crude");
    framelib.WriteBin(currentFrame, output_file, 1);
} //end if(FramesPerStop == 1)

```

```

else //FramesPerStop > 1
{
    for (i=1; i<=FramesPerStop; i++)
    {
        // grab
        qh = pxd.Grab(hFG, currentFrame, 0);
        if (!qh)
        {
            MessageBox(NULL, "Unable to acquire image.", "CamExe",
                MB_ICONERROR);
            pxd.FreeFG(hFG);
            imagination_CloseLibrary(&framelib);
            imagination_CloseLibrary(&pxd);
            return 0; }
        cout << "Grab " << i << endl;

        //save file
        sprintf(ext_output_file, "%s_(%d).crude", output_file, i);
        framelib.WriteBin(currentFrame, ext_output_file, 1);
    } //end for
} //end else (FramesPerStop > 1)

//release extra frame
framelib.FreeFrame(newFrame);

clock_t end_aquisition(clock());

// release frame grabber resources
framelib.FreeFrame(currentFrame);
pxd.FreeConfig(camType);
pxd.FreeFG(hFG);
imagination_CloseLibrary(&framelib);
imagination_CloseLibrary(&pxd);

clock_t end_prog(clock());

cout << "Program ran for " << end_prog - start_prog << "ms" << endl;
cout << "Image Aquisition took " << end_aquisition - start_aquisition <<
    "ms" << endl;

return 1;
// return 0;

}

```


Documentation for MotionPicture.tsp

Aim of the program:

MotionPicture is a software tool written in Testpoint to control the X-ray Camera (c) and the Rotary Table (b) for the use of measuring experimental data with the recently built ECOSSE X-Ray CT scanner in the Grant Institute, University of Edinburgh.

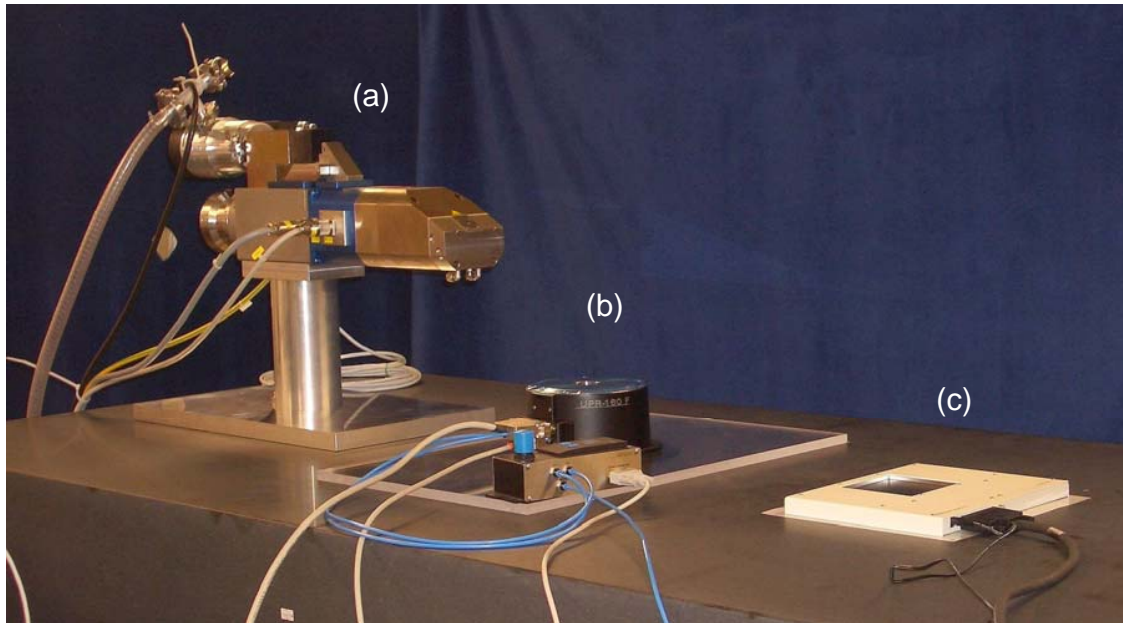
A 3-dimensional CT image is built up from the integration of a number of pictures taken around the object at equal angular intervals. A reconstruction software (e.g. Octopus V8) is then needed to generate a 3-D model from these single images.

The Testpoint program **MotionPicture.tsp** is the integrated and coordinated control of the rotating table and the X-ray camera. The GUI (Graphical User Interface) control connects camera and table, and allows controlling both instruments manually to get the samples in the required position and take single pictures. It also allows running a whole experimental loop of several 360° turns with a few prescribed values to define the amount of pictures taken, the stop positions for the correct illumination angles and preset time intervals.

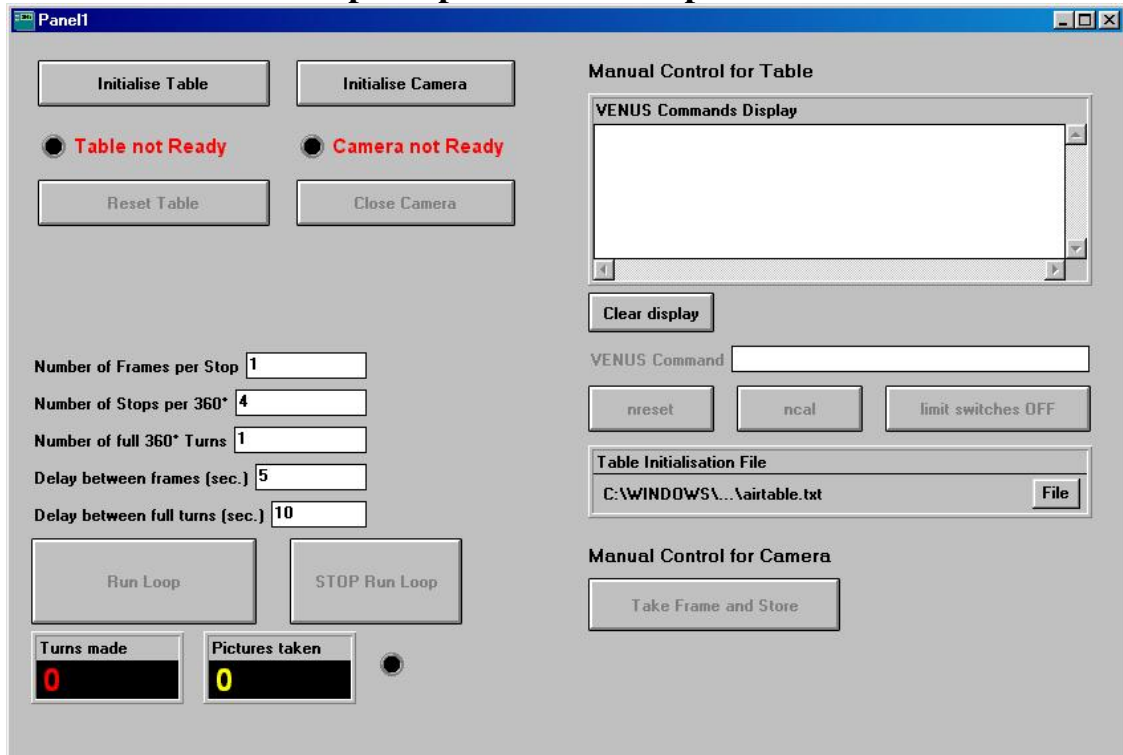
The X-ray source is meant to be in constant operation all along.

ECOSSE X-Ray CT scanner components:

- (a) X-ray source (Feinfocus dual head transmission/directional nano/microfocus tube)
- (b) Air-bearing rotary table (Micos UPR-160F SMC Pegasus with Taurus motion controller)
- (c) 4 MP Gadox X-ray camera (Rad-icon Shad-o-Box)



Screenshot of the Testpoint panel on start-up:



Main use description:

Before any commands can be sent, the table and the camera need to be initialised. At this, the chronological order is not important.

The X-ray source will be in constant operation during a full run.

Table Initialisation

Check first, the **air pressure** connected to the Micos Table is turned on and sufficiently high! Then push “**Initialise Table**” and **wait** until the lamp below the button switches to green. The default initialisation script will be carried out, specified as “Table Initialisation File” in the Manual Control Section on the right-hand side. It sends several VENUS¹ commands via the **COM-1 port** to the motion controller of the table (see attached Table Initialisation File). After the table has been initialised the manual control for the table will be enabled.

Camera Initialisation

In case all folder requirements are observed, pressing the “**Initialise Camera**” button will open the Camera Software **ShadoCam** in a separated window, and then switch back to the Testpoint panel. Please **wait** until the lamp below the button turned green before any other actions are carried out!

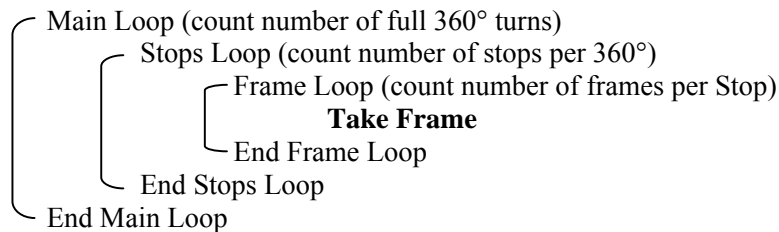
After the camera has been initialised the manual control for the camera will be enabled.

The “**Run Loop**” button is disabled unless the camera and the table are initialised to avoid sending misleading commands to the table or camera software.

¹ VENUS-2 is the interpreter language of the Taurus motion controller for the rotary table by miCos GmbH, Germany.

Run Loop

A complete run consists of three nested loops:



The table will rotate the given **number of full 360° turns** in total.

Per each full 360° circle, the table will move to evenly spaced positions defined by the **number of stops per 360°**, starting at position 0°, proceeding clockwise. After every full circle, the table counter-clockwise moves back to 0° (without taking a picture at 360° to avoid doubled data).

At every stop position, the camera software is then called to take the predefined **number of frames per stop**. Every frame or picture will be saved in the ShadoCam default folder (set to C:\ShadoCam\SData). The single pictures will be continuously numbered as "Image*.raw", starting with Image1.raw.

The Testpoint program will switch to the ShadoCam window and back for every frame taken.

Each set of frames belonging to one full circle then defines a complete data set for a 3-dimensional image.

Two **time delays** can be chosen: Between the frames taken at one position a minimum delay of 5 seconds has to be chosen for the camera software to achieve a proper execution. Between full 360° turns the delay may be varied to observe time changes in the samples.

After a fully completed run the lamp at the bottom will turn green. Another run with different variables might be carried out afterwards without a restart. The numbering of the frames will continue as long as the camera software is not been closed.

A current run can be aborted by pressing the "Stop Loop" button, and should not be stopped differently. Resetting the table and the camera is then recommended.

The two displays at the bottom of the panel monitor the progress of the loop by showing the current number of full 360° turns and the total number of frames being made (corresponding to the image numbering).

Important note:

The taken images are just stored in the ShadoCam default folder. After every restart of the camera software the numbering will start again with Image1.raw. As the Images cannot be overwritten by the Testpoint program, the default folder has to be cleared manually before every new run after the camera software was closed!

Loop Variables

Number of Frames per Stop

defines how many images are taken by the camera software at each stop position.
(default 1, minimum 1, maximum 100)

Number of Stops per 360°

defines the number of stops and therewith the rotation angle or the actual positions the table will stop at, respectively.
(default 4, minimum 1, maximum 2000)

Number of full 360° Turns

defines the number of full circles and therefore the number of 3-dimensional images.
(default 1, minimum 1, maximum 10000)

Delay between frames (sec.)

Between the frames taken at one position a minimum delay of 5 seconds has to be chosen for the camera software to achieve a proper execution.
(default 5, minimum 5)

Delay between full turns (sec.)

Between full 360° turns the delay may be varied to observe time changes.
(default 10, minimum 2)

Folder structure requirements (overview):

Default Table Initialisation File

C:\WINDOWS\Desktop\airtable.txt

Table Taurus motion controller

must be connected to the COM-1 port

ShadoCam Application Location

C:\ShadoCam\Shadocam.exe

Default Folder where all Images are stored

C:\ShadoCam\SData

(how to change the default file see footnote 2 on page 6)

Default Image for Camera Initialisation

C:\ShadoCam\SData\Dummy.raw

(for further details see section "Manual Control")

A detailed print out of the **Program Code** (Action Lists, Cross-References and Object Overviews of MotionPicture.tsp) can be found in the Appendix.

Manual Control:

The program can also be used to control the table or the camera manually and separately. For this purpose the right-hand side of the panel is set up for the manual use with some basic commands.

Basics of the table

All available VENUS commands can be sent via the VENUS Command entry line below the command display after a successful initialisation of the table (for a complete overview see VENUS-2 Handbook).

Basic VENUS positioning commands:

- nm (nmove)** moves the table to the specified position.
Example: 30 1 nm moves the table to position 30°.
Positions below 0° are not possible.
- nr (nrmove)** rotates the table about the specified angle.
Example: 30 1 nr rotates the table clockwise 30° further from the current position.
Positive values signify clockwise, negative values counter-clockwise rotation.
- Whereas the 1 in all commands defines the axis of motion (cannot have another value).

Some important VENUS commands are directly implemented as buttons:

- nreset** resets the table software to the original state
(VENUS Cmd: 1 nreset).
- ncal** calibrates the table at the limit switch at position 0° (the default cal-endswitch), if the limit switches are enabled
(VENUS Cmd: 1 ncal).

Limit switches off

disables both limit switches (the cal- and the rm-endswitch)
with the commands 2 0 1 setsw and 2 1 1 setsw
To enable both limit switches again either push nreset or type
1 0 1 setsw and 1 1 1 setsw

Reset table

sets the table to the similar state as after initialisation
(is similar to pushing nreset, ncal and Limit switches off one after another)

The **VENUS Commands Display** shows the full history of commands sent to the table via the COM-1 port as long as it was not cleared.

The default **Table Initialisation File** is set to `C:\Windows\Desktop\airtable.txt` (in detail see attached print out). The **default table initialisation cannot be carried out correctly**, if this file does not exist or is incorrect, respectively. However it might be useful to change the default file for other purposes.

To chose another initialisation file, chose a path and a suitable initialisation file via the “File” button on the panel to the right of the shown default file.

Basics of the camera

The camera software **ShadoCam** is implemented via the Testpoint program by sending keystrokes to the ShadoCam window itself. Therefore, the **camera software needs to be opened in a separate window the whole time during a run!**

Some general regulations need to be observed:

- The **executable file Shadocam.exe** has to be in the folder C:\ShadoCam\ ...
- The **default folder** in the ShadoCam application has to be C:\ShadoCam\SData.²
- A **default image** named “Dummy.raw” has to be stored at the exact location C:\ShadoCam\SData\Dummy.raw. It is just used to open the camera software correctly and will not be changed.

Change default settings for the camera:

After initialising the camera correctly via the Testpoint panel, it is possible to switch to the ShadoCam window and **change the default settings for the image quality manually**, and then to switch back to the Testpoint panel (via the Windows task bar for example), before a run loop is started. **The ShadoCam window must not be closed manually at all!** Please use the “Close Camera” button on the Testpoint panel.

(Reminder: The ShadoCam default folder has to be cleared manually before every new image taken after the camera software was closed.)

Take single images:

If the camera is initialised and configured properly, single images can be taken manually via the “**Take Frame and Store**” button on the right bottom of the Testpoint panel.

The single pictures will be continuously numbered as “Image*.raw”, starting with Image1.raw. The numbering will continue if a run loop is started afterwards.

² To change the default folder in the ShadoCam application, it is necessary to trick the ShadoCam software:

At first, change the location of the default folder in the ShadoCam window (Menu → Acquisition → Preferences...) to the desired default folder.

Secondly, without closing the ShadoCam program, change the location of the standard Windows “My Documents” folder to the desired folder as well (right click on the My Documents symbol on the desktop and chose the Properties menu, there change the target folder location).

Then close ShadoCam and reopen it to check, if the default folder is still set to the desired folder.

Finally, shut down Windows and restart the computer. The registry entries for the ShadoCam software are then adapted correctly. After a restart of the ShadoCam software the desired folder should be now the default folder.

Setting the path of the “My Documents” folder back to the original location doesn’t influence the ShadoCam setting anymore.

Appendix

Table Initialisation File C:\Windows\Desktop\airtable.txt

```
0 1 nmode
1 nclear
-1 1 snv 1 gne 1 gne 1 gne
1 1 setaxis
1 0 1 setsw
1 1 1 setsw
360.000000000 1 setpitch
180.000000 1 snv
500.000000 1 sna
1 1 setnacelfunc
40 1 1 setncalvel
1 2 1 setncalvel
40 1 1 setnrmvel
1 2 1 setnrmvel
2000.000000 1 setncalaccel
0.0000 1 setncalswdist
0 1 setnpowerup
:version =2.37
:serialno =6914130
1 1 setcloop
0.04000000000000000 1 setclperiod
0.001000 0 1 0 1 setclwindow
0.0012 1 setclwintime
100.000000 700.000000 0.500000 12.000000 3.000000 12.000000
10.000000 0.000000 0.000000 0.000000 10 1 setclpara
1 1 setselpos
2 1 1 setnrefvel
0.01 2 1 setnrefvel
0 1 setref
520 1 setalpha
3900 1 setumotmin
50 1 setumotgrad
2 1 setphases
7 1 setpolepairs
0 1 setmotiondir
80000 3 1 setmotorpara
50.000000 1 setnjoyspeed
5.000000 1 setnjoybspeed
2 1 setnjoytype
2000.000000 1 setnmanaccel
0.000000 1 setwheelratio
1 1 setwheelres
1 nreset
1 ncal
2 0 setsw
2 1 setsw
```

MOTIONPICTURE.TST - Object Overview

Panel1
 TestPoint v4.1, file=C:\WINDOWS\DESKTOP\MOTION~1.TST

Page 1
 14:03 Thu. Feb. 05,2009

Print options: all objects, panels=Y, objectlists=Y, user-defined=N, action-lists=Y, comments=Y,
 data-refs=N, settings=some



Panel1

Objects in panel "Panel1":

- Initialisation
- Main Loop
- manual control
-

Settings for Panel object "Panel1":

X: -1
 Y: -1
 Multitasking mode: Yield at end of loops
 Disable scroll bars: 0



Initialisation (Panel1\Initialisation)

Objects in panel "Initialisation":



 **INI OK** (\Panel1\Initialisation\INI OK)

Settings for Condition object "INI OK":

Expression: x = 1

 **Check INI** (\Panel1\Initialisation\Check INI)

Action list for Pushbutton object "Check INI":

- 1) ----- BUTTONS ON/OFF "OFF"
- 2) Set Run Loop(Enabled) to 0
- 3) Set STOP Run Loop(Enabled) to 0
- 4) Set Initialise Camera(Enabled) to 1
- 5) Set Initialise Table(Enabled) to 1
- 6) Set Close Camera(Enabled) to 0
- 7) Set Reset Table(Enabled) to 0
- 8) Set VENUS Command(Enabled) to 0
- 9) Set Take Frame and Store(Enabled) to 0
- 10) Set nreset(Enabled) to 0
- 11) Set ncal(Enabled) to 0
- 12) Set limit switches OFF(Enabled) to 0
- 13) ----- BUTTONS ON/OFF "ON"
- 14) If/Then INI OK with x=Table Ready
- 15) Set Reset Table(Enabled) to 1
- 16) Set VENUS Command(Enabled) to 1
- 17) Set nreset(Enabled) to 1
- 18) Set ncal(Enabled) to 1
- 19) Set limit switches OFF(Enabled) to 1
- 20) End If INI OK
- 21) If/Then INI OK with x=Camera Ready
- 22) Set Initialise Camera(Enabled) to 0
- 23) Set Close Camera(Enabled) to 1
- 24) Set Take Frame and Store(Enabled) to 1
- 25) End If INI OK
- 26) If/Then INI OK with x=Table Ready
- 27) If/Then INI OK with x=Camera Ready
- 28) Set Run Loop(Enabled) to 1
- 29) End If INI OK
- 30) End If INI OK

Settings for Pushbutton object "Check INI":











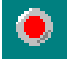
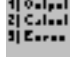

Visible: 0
 Enabled: 0
 Exec. actions at initialize: 1



Initialise Table

(\Panel1\Initialisation\Initialise Table)

Objects in panel "Initialise Table":

	RS232 1		Condition1		Err msg display
	Table Initialisation File		BOOL		Err msg delay
	Initialise Table		Ini Cmd Delay		Reset Table
	IniLoop		Table Ready		
	Load File Line & Send		Comm Errors		



RS232 1

(\Panel1\Initialisation\Initialise Table\RS232 1)

Whenever a CR character arrives, read the incoming line and display it.

Action list for RS232 object "RS232 1":

- 1) Enter from RS232 1 up to 8192 bytes, stop on EOS=CR
- 2) Append to VENUS Commands Displa new line(s)=RS232 1

Settings for RS232 object "RS232 1":

COM port #: 1
Timeout (sec): 5
Event on receiving character:: CR
Input queue size: 1024
Output queue size: 1024
Demo mode: 0



Table Initialisation File

(\Panel1\Initialisation\Initialise Table\Table Initialisation File)

Settings for File object "Table Initialisation File":

Filename initial value: C:\WINDOWS\Desktop\airtable.txt
Update disk on each output: 0
'Save As' style (else 'Open'): 0
Warn on create (if 'Open'): 1
Must exist (if 'Open'): 0
Warn on existing (if 'Save As'): 1
Default extension:
Dialog title:
File name filter:
Visible: 1
Enabled: 1
Execute actions at init: 0



Initialise Table

(\Panel1\Initialisation\Initialise Table\Initialise Table)

Action list for Pushbutton object "Initialise Table":

- | | | | |
|-----|----------|---------------------------|----------------------------------|
| 1) | Open | RS232 1 | |
| 2) | Open | Table Initialisation File | |
| 3) | Set | BOOL | to 1 |
| 4) | Do loop | IniLoop | while BOOL is true (non-zero) |
| 5) | Execute | Load File Line & Send | |
| 6) | Test EOF | Table Initialisation File | |
| 7) | Delay | Ini Cmd Delay | for 0.1 seconds |
| 8) | If/Then | Condition1 | with x=Table Initialisation File |
| 9) | Set | BOOL | to 0 |
| 10) | End If | Condition1 | |
| 11) | End | IniLoop | |
| 12) | Delay | Ini Cmd Delay | for 10 seconds |
| 13) | Close | Table Initialisation File | |
| 14) | Set | Table Ready | to 1 |
| 15) | ----- | BUTTONS ON/OFF | --- |
| 16) | Push | Check INI | |

Settings for Pushbutton object "Initialise Table":

Visible: 1
Enabled: 1
Exec. actions at initialize: 0



Load File Line & Send

(\Panel1\Initialisation\Initialise Table\Load File Line & Send)

Action list for Action object "Load File Line & Send":

- 1) Input from Table Initialisation File up to 1 "lines", stopping at ____
- 2) Store in VenusCmd from Table Initialisation File
- 3) Execute Send VENUS Command

Settings for Action object "Load File Line & Send":

Action parameter phrase:
Action Name: Execute



Condition1

(\Panel1\Initialisation\Initialise Table\Condition1)

Settings for Condition object "Condition1":

Expression: x



BOOL

(\Panel1\Initialisation\Initialise Table\BOOL)

Settings for Math object "BOOL":

Formula: x



Ini Cmd Delay

(\Panel1\Initialisation\Initialise Table\Ini Cmd Delay)

Settings for Time object "Ini Cmd Delay":

Time format: HH:MM:SS



Table Ready

(\Panel1\Initialisation\Initialise Table\Table Ready)

Settings for Indicator object "Table Ready":

Visible: 1
Initial Value: 0

 **Comm Errors** (\Panel1\Initialisation\Initialise Table\Comm Errors)

Catches COM errors and displays a message for 2 seconds, using a Timer object to produce a 2 second delay.

Action list for Error-Handler object "Comm Errors":

- 1) Set Err msg display to Comm Errors:1
- 2) Continue after Comm Errors with data=___
- 3) Start Err msg delay interval=2

Settings for Error-Handler object "Comm Errors":

Min. error #: 270
Max. error #: 279



Err msg display (\Panel1\Initialisation\Initialise Table\Err msg display)

Settings for Display object "Err msg display":

Type: Text
Number Format: Auto
digits: 5
Text if no data:
Visible: 1
Initial Value:



Err msg delay (\Panel1\Initialisation\Initialise Table\Err msg delay)

Action list for Time object "Err msg delay":

- 1) Set Err msg display to ___
- 2) Stop Err msg delay

Settings for Time object "Err msg delay":

Time format: HH:MM:SS



Reset Table

(\Panel1\Initialisation\Initialise Table\Reset Table)

Action list for Pushbutton object "Reset Table":

- 1) Set Table Ready to 0
- 2) Store in VenusCmd from "1 nreset"
- 3) Execute Send VENUS Command
- 4) Store in VenusCmd from "1 ncal"
- 5) Execute Send VENUS Command
- 6) Delay VenusDelay for 5 seconds
- 7) Store in VenusCmd from "2 0 1 setsw"
- 8) Execute Send VENUS Command
- 9) Store in VenusCmd from "2 1 1 setsw"
- 10) Execute Send VENUS Command
- 11) Delay VenusDelay for 2 seconds
- 12) Set Table Ready to 1
- 13) Push Check INI

Settings for Pushbutton object "Reset Table":

Visible: 1
Enabled: 0
Exec. actions at initialize: 0



Initialise Camera

(\Panel1\Initialisation\Initialise Camera)

Objects in panel "Initialise Camera":

	ShadoCamDDE		TPWindow		Go to TP Window
	ShadocamExec		Initialise Camera		WindowDelay
	GetActiveWindow		Get TP Window		Camera Ready
	SetActiveWindow		Open ShadoCam		Take Frame & Store
	ShadoCamWindow		Go to ShadoCam Window		Close Camera



ShadoCamDDE

(\Panel1\Initialisation\Initialise Camera\ShadoCamDDE)

Settings for DDE object "ShadoCamDDE":

Application name: Shadocam
Topic name: C:\ShadoCam\Shadocam.exe
Auto-run: 0
Timeout (sec.): 10



ShadocamExec

(\Panel1\Initialisation\Initialise Camera\ShadocamExec)

Settings for Code object "ShadocamExec":

DLL Filename: KERNEL
Subroutine Name: WinExec
Argument Types: string, integer
Return Type: integer
Preload: 1



GetActiveWindow

(\Panel1\Initialisation\Initialise Camera\GetActiveWindow)

Settings for Code object "GetActiveWindow":

DLL Filename: USER
Subroutine Name: GetActiveWindow
Argument Types:
Return Type: word
Preload: 1



SetActiveWindow

(\Panel1\Initialisation\Initialise Camera\SetActiveWindow)

Settings for Code object "SetActiveWindow":

DLL Filename: USER
Subroutine Name: SetActiveWindow
Argument Types: word
Return Type: word
Preload: 1



Initialise Camera

(\Panel1\Initialisation\Initialise Camera\Initialise Camera)

Action list for Pushbutton object "Initialise Camera":

- 1) Execute Get TP Window
- 2) Execute Open ShadoCam
- 3) Set Camera Ready to 1
- 4) ----- BUTTONS ON/OFF ___
- 5) Push Check INI

Settings for Pushbutton object "Initialise Camera":

Visible: 1
Enabled: 1
Exec. actions at initialize: 0



Get TP Window

(\Panel1\Initialisation\Initialise Camera\Get TP Window)

Action list for Action object "Get TP Window":

- 1) Call GetActiveWindow
- 2) Store in TPWindow from GetActiveWindow

Settings for Action object "Get TP Window":

Action parameter phrase:
Action Name: Execute



Open ShadoCam

(\Panel1\Initialisation\Initialise Camera\Open ShadoCam)

Action list for Action object "Open ShadoCam":

- 1) Call ShadocamExec with "C:\ShadoCam\SHADOCAM.EXE
C:\ShadoCam\SDData\Dummy.raw",1
- 2) Delay WindowDelay for 2 seconds
- 3) Send keys to ShadoCamDDE keys="@VL"
- 4) Delay WindowDelay for 2 seconds
- 5) Send keys to ShadoCamDDE keys="@FC"
- 6) Delay WindowDelay for 2 seconds
- 7) Call GetActiveWindow
- 8) Store in ShadoCamWindow from GetActiveWindow
- 9) Delay WindowDelay for 2 seconds
- 10) Call SetActiveWindow with TPWindow
- 11) Delay WindowDelay for 2 seconds

Settings for Action object "Open ShadoCam":

Action parameter phrase:
Action Name: Execute



Go to ShadoCam Window

(\Panel1\Initialisation\Initialise Camera\Go to ShadoCam Window)

Action list for Action object "Go to ShadoCam Window":

- 1) Call SetActiveWindow with ShadoCamWindow
- 2) Delay WindowDelay for 1 seconds

Settings for Action object "Go to ShadoCam Window":

Action parameter phrase:
Action Name: Execute



Go to TP Window (\Panel1\Initialisation\Initialise Camera\Go to TP Window)

Action list for Action object "Go to TP Window":

- 1) Call SetActiveWindow with TPWindow
- 2) Delay WindowDelay for 1 seconds

Settings for Action object "Go to TP Window":

Action parameter phrase:
Action Name: Execute



WindowDelay (\Panel1\Initialisation\Initialise Camera\WindowDelay)

Settings for Time object "WindowDelay":

Time format: HH:MM:SS



Camera Ready (\Panel1\Initialisation\Initialise Camera\Camera Ready)

Settings for Indicator object "Camera Ready":

Visible: 1
Initial Value: 0



Take Frame & Store (\Panel1\Initialisation\Initialise Camera\Take Frame & Store)

Action list for Action object "Take Frame & Store":

- 1) Execute Go to ShadoCam Window
- 2) Delay WindowDelay for 1.5 seconds
- 3) Send keys to ShadoCamDDE keys="@AS"
- 4) Delay WindowDelay for 2 seconds
- 5) Send keys to ShadoCamDDE keys="@FS"
- 6) Delay WindowDelay for 1.5 seconds
- 7) Send keys to ShadoCamDDE keys="@S"
- 8) Delay WindowDelay for 1.5 seconds
- 9) Send keys to ShadoCamDDE keys="@FC"
- 10) Execute Go to TP Window

Settings for Action object "Take Frame & Store":

Action parameter phrase:
Action Name: Execute



Close Camera

(\Panel1\Initialisation\Initialise Camera\Close Camera)

Action list for Pushbutton object "Close Camera":

- 1) Execute Go to ShadoCam Window
- 2) Send keys to ShadoCamDDE keys="@FX"
- 3) Execute Go to TP Window
- 4) Set Camera Ready to 0
- 5) Push Check INI

Settings for Pushbutton object "Close Camera":

Visible: 1
Enabled: 0
Exec. actions at initialize: 0



Main Loop

(\Panel1\Main Loop)

Objects in panel "Main Loop":

Run Loop	FrameLoop	-----make pictures
Loop Initialisation	StopsLoop	-----
Monitoring	MainLoop	TimeDelay
Abort Loop	----- calibrate at 0 deg.	
Variables	-----move table	



Run Loop (\Panel1\Main Loop\Run Loop)

Action list for Pushbutton object "Run Loop":

- | | | | |
|-----|---------------|---------------------------|---|
| 1) | Execute | Disable Buttons RUN | |
| 2) | Set | Finish Lamp | to 0 |
| 3) | Set | abort | to 0 |
| 4) | Execute | Loop Initialisation | |
| 5) | Linear series | MainLoop | from 1 to NoTurns, step by 1 |
| 6) | If/Then/Else | BOOLisONE | with x=abort |
| 7) | ----- | ABORT | "go to end of Main Loop" |
| 8) | Else if not | BOOLisONE | |
| 9) | Calculate | TurnCounter | |
| 10) | ----- | ----- calibrate at 0 deg. | "(might be changed later with ncal)" |
| 11) | Store in | VenusCmd | from "0 1 nm" |
| 12) | Execute | Send VENUS Command | |
| 13) | Delay | TimeDelay | for 1 seconds |
| 14) | Set | Position | to 0 |
| 15) | Set | StopCounter | to 0 |
| 16) | ----- | -----make pictures | "at position 0" |
| 17) | Linear series | FrameLoop | from 1 to NoFrames, step by 1 |
| 18) | If/Then/Else | BOOLisONE | with x=abort |
| 19) | ----- | ABORT | "go to end of Frame Loop" |
| 20) | Else if not | BOOLisONE | |
| 21) | Execute | Take Frame & Store | |
| 22) | Calculate | PicCounter | |
| 23) | Set | Pictures taken | to PicCounter |
| 24) | Delay | TimeDelay | for Delay between frames (sec.) seconds |
| 25) | End If | BOOLisONE | |
| 26) | End | FrameLoop | |
| 27) | ----- | ---- | ----- |
| 28) | Linear series | StopsLoop | from 2 to NoStops, step by 1 |
| 29) | If/Then/Else | BOOLisONE | with x=abort |
| 30) | ----- | ABORT | "go to end of Stops Loop" |
| 31) | Else if not | BOOLisONE | |
| 32) | ----- | -----move table | ----- |
| 33) | Calculate | StopCounter | |
| 34) | Calculate | Position | with x=Angle y=StopCounter |
| 35) | Calculate | Command | with x=Position |
| 36) | Store in | VenusCmd | from Command |
| 37) | Execute | Send VENUS Command | |
| 38) | Delay | TimeDelay | for 1 seconds |
| 39) | ----- | -----make pictures | "all other positions <360" |
| 40) | Linear series | FrameLoop | from 1 to NoFrames, step by 1 |
| 41) | If/Then/Else | BOOLisONE | with x=abort |
| 42) | ----- | ABORT | "go to end of Frame Loop" |
| 43) | Else if not | BOOLisONE | |
| 44) | Execute | Take Frame & Store | |
| 45) | Calculate | PicCounter | |
| 46) | Set | Pictures taken | to PicCounter |
| 47) | Delay | TimeDelay | for Delay between frames (sec.) seconds |
| 48) | End If | BOOLisONE | |
| 49) | End | FrameLoop | |
| 50) | ----- | ---- | ----- |
| 51) | End If | BOOLisONE | |
| 52) | End | StopsLoop | |
| 53) | If/Then/Else | BOOLisONE | with x=abort |
| 54) | ----- | ABORT | "go to end of Frame Loop" |

Action list for Pushbutton object "Run Loop": ...continued

- | | | | |
|-----|-------------|--------------------|----------------------|
| 55) | Else if not | BOOLisONE | |
| 56) | Set | Turns made | to TurnCounter |
| 57) | Delay | TimeDelay | for Delay360 seconds |
| 58) | End If | BOOLisONE | |
| 59) | End If | BOOLisONE | |
| 60) | End | MainLoop | |
| 61) | Set | Finish Lamp | to 1 |
| 62) | Execute | Enable Buttons RUN | |

Settings for Pushbutton object "Run Loop":

Visible: 1
Enabled: 0
Exec. actions at initialize: 0



Loop Initialisation

(\Panel1\Main Loop\Loop Initialisation)

Action list for Action object "Loop Initialisation":

- | | | | |
|-----|-----------|-------------|--------------------------------------|
| 1) | ----- | ----- | "Initialise Table Values" |
| 2) | Store in | NoStops | from Number of Stops per 360° |
| 3) | Store in | NoTurns | from Number of full 360° Turns |
| 4) | Store in | Delay360 | from Delay between full turns (sec.) |
| 5) | Calculate | Angle | with x=NoStops |
| 6) | Set | PicCounter | to 0 |
| 7) | Set | TurnCounter | to 0 |
| 8) | Set | Position | to 0 |
| 9) | ----- | ----- | "Initialise Camera Values" |
| 10) | Store in | NoFrames | from Number of Frames per Stop |

Settings for Action object "Loop Initialisation":

Action parameter phrase:
Action Name: Execute



TimeDelay

(\Panel1\Main Loop\TimeDelay)

Settings for Time object "TimeDelay":

Time format: HH:MM:SS



Monitoring

(\Panel1\Main Loop\Monitoring)

Objects in panel "Monitoring":



Pictures taken



Turns made



Finish Lamp



Pictures taken (\Panel1\Main Loop\Monitoring\Pictures taken)

Settings for Display object "Pictures taken":

Type: Text
Number Format: Auto
digits: 5
Text if no data:
Visible: 1
Initial Value: 0



Turns made (\Panel1\Main Loop\Monitoring\Turns made)

Settings for Display object "Turns made":

Type: Text
Number Format: Auto
digits: 5
Text if no data:
Visible: 1
Initial Value: 0



Finish Lamp (\Panel1\Main Loop\Monitoring\Finish Lamp)

Settings for Indicator object "Finish Lamp":

Visible: 1
Initial Value:



Abort Loop (\Panel1\Main Loop\Abort Loop)

Objects in panel "Abort Loop":



STOP Run Loop



BOOLisONE



Disable Buttons RUN



abort



ABORT



Enable Buttons RUN



STOP Run Loop

(\Panel1\Main Loop\Abort Loop\STOP Run Loop)

Action list for Pushbutton object "STOP Run Loop":

- 1) Set abort to 1
- 2) Delay TimeDelay for 2 seconds
- 3) Execute Enable Buttons RUN
- 4) Push Check INI

Settings for Pushbutton object "STOP Run Loop":

Visible: 1
Enabled: 0
Exec. actions at initialize: 0



abort

(\Panel1\Main Loop\Abort Loop\abort)

abort = 1 => TRUE (STOP LOOP)
abort = 0 => FALSE

Settings for Math object "abort":

Formula: x



BOOLisONE

(\Panel1\Main Loop\Abort Loop\BOOLisONE)

Settings for Condition object "BOOLisONE":

Expression: x = 1



Disable Buttons RUN

(\Panel1\Main Loop\Abort Loop\Disable Buttons RUN)

Action list for Action object "Disable Buttons RUN":

- 1) Set Run Loop(Enabled) to 0
- 2) Set STOP Run Loop(Enabled) to 1
- 3) Set Initialise Table(Enabled) to 0
- 4) Set Reset Table(Enabled) to 0
- 5) Set VENUS Command(Enabled) to 0
- 6) Set nreset(Enabled) to 0
- 7) Set ncal(Enabled) to 0
- 8) Set limit switches OFF(Enabled) to 0
- 9) Set Initialise Camera(Enabled) to 0
- 10) Set Close Camera(Enabled) to 0
- 11) Set Take Frame and Store(Enabled) to 0

Settings for Action object "Disable Buttons RUN":

Action parameter phrase:
Action Name: Execute



Enable Buttons RUN (\Panel1\Main Loop\Abort Loop\Enable Buttons RUN)

Action list for Action object "Enable Buttons RUN":

- 1) Push Check INI

Settings for Action object "Enable Buttons RUN":

Action parameter phrase:
 Action Name: Execute



Variables (\Panel1\Main Loop\Variables)

Objects in panel "Variables":

	StopCounter		Command		Delay between full turns (sec.)
	TurnCounter		Number of Frames per Stop		NoFrames
	PicCounter		Number of Stops per 360°		NoStops
	Position		Number of full 360° Turns		NoTurns
	Angle		Delay between frames (sec.)		Delay360



StopCounter (\Panel1\Main Loop\Variables\StopCounter)

Settings for Math object "StopCounter":

Formula: Previous() + 1



TurnCounter (\Panel1\Main Loop\Variables\TurnCounter)

Settings for Math object "TurnCounter":

Formula: Previous() + 1



PicCounter (\Panel1\Main Loop\Variables\PicCounter)

Settings for Math object "PicCounter":

Formula: Previous() + 1



Position (\Panel1\Main Loop\Variables\Position)

Settings for Math object "Position":

Formula: $x * y$



Angle (\Panel1\Main Loop\Variables\Angle)

Settings for Math object "Angle":

Formula: $360 / x$



Command (\Panel1\Main Loop\Variables\Command)

Settings for Math object "Command":

Formula: $x \& " 1 \text{ nm}"$



Number of Frames per Stop (\Panel1\Main Loop\Variables\Number of Frames per Stop)

Settings for Data-Entry object "Number of Frames per Stop":

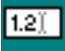
Visible: 1
Enabled: 1
Exec. actions at initialize: 0
Initial Value: 1
Numeric: 1
Min. value: 1
Max. value: 100
Multi-line: 0



Number of Stops per 360° (\Panel1\Main Loop\Variables\Number of Stops per 360°)

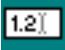
Settings for Data-Entry object "Number of Stops per 360°":

Visible: 1
Enabled: 1
Exec. actions at initialize: 0
Initial Value: 4
Numeric: 1
Min. value: 1
Max. value: 2000
Multi-line: 0

 **Number of full 360° Turns** (\Panel1\Main Loop\Variables\Number of full 360° Turns)

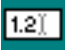
Settings for Data-Entry object "Number of full 360° Turns":

Visible: 1
Enabled: 1
Exec. actions at initialize: 0
Initial Value: 1
Numeric: 1
Min. value: 1
Max. value: 10000
Multi-line: 0

 **Delay between frames (sec.)** (\Panel1\Main Loop\Variables\Delay between frames (sec.))

Settings for Data-Entry object "Delay between frames (sec.)":

Visible: 1
Enabled: 1
Exec. actions at initialize: 0
Initial Value: 5
Numeric: 1
Min. value: 5
Max. value:
Multi-line: 0









 **Delay between full turns (sec.)** (\Panel1\Main Loop\Variables\Delay between full turns (sec.))

Settings for Data-Entry object "Delay between full turns (sec.)":

Visible: 1
Enabled: 1
Exec. actions at initialize: 0
Initial Value: 10
Numeric: 1
Min. value: 2
Max. value:
Multi-line: 0

 **manual control** (\Panel1>manual control)

Objects in panel "manual control":

- | | | |
|--|--|--|
|  Table manual |  ncal |  Camera manual |
|  VENUS Commands |  limit switches OFF |  Take Frame and Store |
|  nreset |  Send VENUS Command | |



nreset (\Panel1\manual control\nreset)

Action list for Pushbutton object "nreset":

- 1) Store in VenusCmd from "1 nreset"
- 2) Push Send VENUS Command

Settings for Pushbutton object "nreset":

Visible: 1
Enabled: 0
Exec. actions at initialize: 0



ncal (\Panel1\manual control\ncal)

Action list for Pushbutton object "ncal":

- 1) Store in VenusCmd from "1 ncal"
- 2) Push Send VENUS Command

Settings for Pushbutton object "ncal":

Visible: 1
Enabled: 0
Exec. actions at initialize: 0



limit switches OFF (\Panel1\manual control\limit switches OFF)

Action list for Pushbutton object "limit switches OFF":

- 1) Store in VenusCmd from "2 0 1 setsw"
- 2) Push Send VENUS Command
- 3) Store in VenusCmd from "2 1 1 setsw"
- 4) Push Send VENUS Command

Settings for Pushbutton object "limit switches OFF":

Visible: 1
Enabled: 0
Exec. actions at initialize: 0



Send VENUS Command

(\Panel1\manual control\Send VENUS Command)

Action list for Pushbutton object "Send VENUS Command":

- 1) Set VENUS Command to VenusCmd
- 2) Delay VenusDelay for 0.1 seconds
- 3) Set VENUS Command to ____

Settings for Pushbutton object "Send VENUS Command":

Visible: 0
Enabled: 0
Exec. actions at initialize: 0



Take Frame and Store

(\Panel1\manual control\Take Frame and Store)

Action list for Pushbutton object "Take Frame and Store":

- 1) Execute Go to ShadoCam Window
- 2) Delay WindowDelay for 1.5 seconds
- 3) Send keys to ShadoCamDDE keys="@AS"
- 4) Delay WindowDelay for 2 seconds
- 5) Send keys to ShadoCamDDE keys="@FS"
- 6) Delay WindowDelay for 1.5 seconds
- 7) Send keys to ShadoCamDDE keys="@S"
- 8) Delay WindowDelay for 1.5 seconds
- 9) Send keys to ShadoCamDDE keys="@FC"
- 10) Execute Go to TP Window
- 11) Delay WindowDelay for 1.5 seconds

Settings for Pushbutton object "Take Frame and Store":

Visible: 1
Enabled: 0
Exec. actions at initialize: 0



VENUS Commands

(\Panel1\manual control\VENUS Commands)

Objects in panel "VENUS Commands":



VENUS Command



VENUS Commands
Display



VenusDelay



VenusCmd



Clear display



Send VENUS
Command



VENUS Command

(\Panel1\manual control\VENUS Commands\VENUS Command)

Output the text the user has typed.

Action list for Data-Entry object "VENUS Command":

- 1) Output to RS232 1 with VENUS Command, term.=CR, wait for completion?=1
- 2) Append to VENUS Commands Displa new line(s)=VENUS Command

Settings for Data-Entry object "VENUS Command":

Visible: 1
Enabled: 0
Exec. actions at initialize: 0
Initial Value:
Numeric: 0
Min. value:
Max. value:
Multi-line: 0



VENUS Commands Display

(\Panel1\manual control\VENUS Commands\VENUS Command)

Settings for Data-Entry object "VENUS Commands Display":

Visible: 1
Enabled: 1
Exec. actions at initialize: 0
Initial Value:
Numeric: 0
Min. value:
Max. value:
Multi-line: 1



Clear display

(\Panel1\manual control\VENUS Commands\Clear display)

Action list for Pushbutton object "Clear display":

- 1) Set VENUS Commands Displa to ____

Settings for Pushbutton object "Clear display":

Visible: 1
Enabled: 1
Exec. actions at initialize: 0



VenusDelay

(\Panel1\manual control\VENUS Commands\VenusDelay)

Settings for Time object "VenusDelay":

Time format: HH:MM:SS



Send VENUS Command

(\Panel1\manual control\VENUS Commands\Send VENUS Command)

Action list for Action object "Send VENUS Command":

- 1) Set VENUS Command to VenusCmd
- 2) Delay VenusDelay for 0.1 seconds
- 3) Set VENUS Command to ____

Settings for Action object "Send VENUS Command":

Action parameter phrase:
Action Name: Execute

Object Cross Reference

Object \Panel1\Initialisation\INI OK
 \Panel1\Initialisation\Check INI:line 14
 \Panel1\Initialisation\Check INI:line 20
 \Panel1\Initialisation\Check INI:line 21
 \Panel1\Initialisation\Check INI:line 25
 \Panel1\Initialisation\Check INI:line 26
 \Panel1\Initialisation\Check INI:line 27
 \Panel1\Initialisation\Check INI:line 29
 \Panel1\Initialisation\Check INI:line 30

Object \Panel1\Initialisation\Check INI
 \Panel1\Initialisation\Initialise Table\Initialise Table:line 16
 \Panel1\Initialisation\Initialise Table\Reset Table:line 13
 \Panel1\Initialisation\Initialise Camera\Initialise Camera:line 5
 \Panel1\Initialisation\Initialise Camera\Close Camera:line 5
 \Panel1\Main Loop\Abort Loop\STOP Run Loop:line 4
 \Panel1\Main Loop\Abort Loop\Enable Buttons RUN:line 1

Object \Panel1\Initialisation\BUTTONS ON/OFF
 \Panel1\Initialisation\Initialise Table\Initialise Table:line 15
 \Panel1\Initialisation\Initialise Camera\Initialise Camera:line 4
 \Panel1\Initialisation\Check INI:line 1
 \Panel1\Initialisation\Check INI:line 13

Object \Panel1\Initialisation\Initialise Table\RS232 1
 \Panel1\Initialisation\Initialise Table\RS232 1:line 1
 \Panel1\Initialisation\Initialise Table\RS232 1:line 2
 \Panel1\Initialisation\Initialise Table\Initialise Table:line 1
 \Panel1\manual control\VENUS Commands\VENUS Command:line 1

Object \Panel1\Initialisation\Initialise Table\Table Initialisation File
 \Panel1\Initialisation\Initialise Table\Initialise Table:line 2
 \Panel1\Initialisation\Initialise Table\Initialise Table:line 6
 \Panel1\Initialisation\Initialise Table\Initialise Table:line 8
 \Panel1\Initialisation\Initialise Table\Initialise Table:line 13
 \Panel1\Initialisation\Initialise Table\Load File Line & Send:line 1
 \Panel1\Initialisation\Initialise Table\Load File Line & Send:line 2

Object \Panel1\Initialisation\Initialise Table\Initialise Table
 \Panel1\Initialisation\Check INI:line 5
 \Panel1\Main Loop\Abort Loop\Disable Buttons RUN:line 3

Object \Panel1\Initialisation\Initialise Table\IniLoop
 \Panel1\Initialisation\Initialise Table\Initialise Table:line 4
 \Panel1\Initialisation\Initialise Table\Initialise Table:line 11

Object \Panel1\Initialisation\Initialise Table\Load File Line & Send
 \Panel1\Initialisation\Initialise Table\Initialise Table:line 5

Object \Panel1\Initialisation\Initialise Table\Condition1
 \Panel1\Initialisation\Initialise Table\Initialise Table:line 8
 \Panel1\Initialisation\Initialise Table\Initialise Table:line 10

Object \Panel1\Initialisation\Initialise Table\BOOL
 \Panel1\Initialisation\Initialise Table\Initialise Table:line 3
 \Panel1\Initialisation\Initialise Table\Initialise Table:line 4
 \Panel1\Initialisation\Initialise Table\Initialise Table:line 9

Object \Panel1\Initialisation\Initialise Table\Ini Cmd Delay
 \Panel1\Initialisation\Initialise Table\Initialise Table:line 7
 \Panel1\Initialisation\Initialise Table\Initialise Table:line 12

Object \Panel1\Initialisation\Initialise Table\Table Ready
 \Panel1\Initialisation\Initialise Table\Initialise Table:line 14
 \Panel1\Initialisation\Initialise Table\Reset Table:line 1
 \Panel1\Initialisation\Initialise Table\Reset Table:line 12

```
\Panel1\Initialisation\Check INI:line 14
\Panel1\Initialisation\Check INI:line 26
Object \Panel1\Initialisation\Initialise Table\Comm Errors
\Panel1\Initialisation\Initialise Table\Comm Errors:line 1
\Panel1\Initialisation\Initialise Table\Comm Errors:line 2
Object \Panel1\Initialisation\Initialise Table\Err msg display
\Panel1\Initialisation\Initialise Table\Comm Errors:line 1
\Panel1\Initialisation\Initialise Table\Err msg delay:line 1
Object \Panel1\Initialisation\Initialise Table\Err msg delay
\Panel1\Initialisation\Initialise Table\Comm Errors:line 3
\Panel1\Initialisation\Initialise Table\Err msg delay:line 2
Object \Panel1\Initialisation\Initialise Table\Reset Table
\Panel1\Initialisation\Check INI:line 7
\Panel1\Initialisation\Check INI:line 15
\Panel1\Main Loop\Abort Loop\Disable Buttons RUN:line 4
Object \Panel1\Initialisation\Initialise Camera\ShadoCamDDE
\Panel1\Initialisation\Initialise Camera\Open ShadoCam:line 3
\Panel1\Initialisation\Initialise Camera\Open ShadoCam:line 5
\Panel1\Initialisation\Initialise Camera\Take Frame & Store:line 3
\Panel1\Initialisation\Initialise Camera\Take Frame & Store:line 5
\Panel1\Initialisation\Initialise Camera\Take Frame & Store:line 7
\Panel1\Initialisation\Initialise Camera\Take Frame & Store:line 9
\Panel1\Initialisation\Initialise Camera\Close Camera:line 2
\Panel1\manual control\Take Frame and Store:line 3
\Panel1\manual control\Take Frame and Store:line 5
\Panel1\manual control\Take Frame and Store:line 7
\Panel1\manual control\Take Frame and Store:line 9
Object \Panel1\Initialisation\Initialise Camera\ShadocamExec
\Panel1\Initialisation\Initialise Camera\Open ShadoCam:line 1
Object \Panel1\Initialisation\Initialise Camera\GetActiveWindow
\Panel1\Initialisation\Initialise Camera\Get TP Window:line 1
\Panel1\Initialisation\Initialise Camera\Get TP Window:line 2
\Panel1\Initialisation\Initialise Camera\Open ShadoCam:line 7
\Panel1\Initialisation\Initialise Camera\Open ShadoCam:line 8
Object \Panel1\Initialisation\Initialise Camera\SetActiveWindow
\Panel1\Initialisation\Initialise Camera\Open ShadoCam:line 10
\Panel1\Initialisation\Initialise Camera\Go to ShadoCam Window:line 1
\Panel1\Initialisation\Initialise Camera\Go to TP Window:line 1
Object \Panel1\Initialisation\Initialise Camera\ShadoCamWindow
\Panel1\Initialisation\Initialise Camera\Open ShadoCam:line 8
\Panel1\Initialisation\Initialise Camera\Go to ShadoCam Window:line 1
Object \Panel1\Initialisation\Initialise Camera\TPWindow
\Panel1\Initialisation\Initialise Camera\Get TP Window:line 2
\Panel1\Initialisation\Initialise Camera\Open ShadoCam:line 10
\Panel1\Initialisation\Initialise Camera\Go to TP Window:line 1
Object \Panel1\Initialisation\Initialise Camera\Initialise Camera
\Panel1\Initialisation\Check INI:line 4
\Panel1\Initialisation\Check INI:line 22
\Panel1\Main Loop\Abort Loop\Disable Buttons RUN:line 9
Object \Panel1\Initialisation\Initialise Camera\Get TP Window
\Panel1\Initialisation\Initialise Camera\Initialise Camera:line 1
Object \Panel1\Initialisation\Initialise Camera\Open ShadoCam
\Panel1\Initialisation\Initialise Camera\Initialise Camera:line 2
Object \Panel1\Initialisation\Initialise Camera\Go to ShadoCam Window
\Panel1\Initialisation\Initialise Camera\Take Frame & Store:line 1
\Panel1\Initialisation\Initialise Camera\Close Camera:line 1
\Panel1\manual control\Take Frame and Store:line 1
```

Object \Panel1\Initialisation\Initialise Camera\Go to TP Window
 \Panel1\Initialisation\Initialise Camera\Take Frame & Store:line 10
 \Panel1\Initialisation\Initialise Camera\Close Camera:line 3
 \Panel1>manual control\Take Frame and Store:line 10
Object \Panel1\Initialisation\Initialise Camera\WindowDelay
 \Panel1\Initialisation\Initialise Camera\Open ShadoCam:line 2
 \Panel1\Initialisation\Initialise Camera\Open ShadoCam:line 4
 \Panel1\Initialisation\Initialise Camera\Open ShadoCam:line 6
 \Panel1\Initialisation\Initialise Camera\Open ShadoCam:line 9
 \Panel1\Initialisation\Initialise Camera\Open ShadoCam:line 11
 \Panel1\Initialisation\Initialise Camera\Go to ShadoCam Window:line 2
 \Panel1\Initialisation\Initialise Camera\Go to TP Window:line 2
 \Panel1\Initialisation\Initialise Camera\Take Frame & Store:line 2
 \Panel1\Initialisation\Initialise Camera\Take Frame & Store:line 4
 \Panel1\Initialisation\Initialise Camera\Take Frame & Store:line 6
 \Panel1\Initialisation\Initialise Camera\Take Frame & Store:line 8
 \Panel1>manual control\Take Frame and Store:line 2
 \Panel1>manual control\Take Frame and Store:line 4
 \Panel1>manual control\Take Frame and Store:line 6
 \Panel1>manual control\Take Frame and Store:line 8
 \Panel1>manual control\Take Frame and Store:line 11
Object \Panel1\Initialisation\Initialise Camera\Camera Ready
 \Panel1\Initialisation\Initialise Camera\Initialise Camera:line 3
 \Panel1\Initialisation\Initialise Camera\Close Camera:line 4
 \Panel1\Initialisation\Check INI:line 21
 \Panel1\Initialisation\Check INI:line 27
Object \Panel1\Initialisation\Initialise Camera\Take Frame & Store
 \Panel1>Main Loop\Run Loop:line 21
 \Panel1>Main Loop\Run Loop:line 44
Object \Panel1\Initialisation\Initialise Camera\Close Camera
 \Panel1\Initialisation\Check INI:line 6
 \Panel1\Initialisation\Check INI:line 23
 \Panel1>Main Loop\Abort Loop\Disable Buttons RUN:line 10
Object \Panel1>Main Loop\Run Loop
 \Panel1\Initialisation\Check INI:line 2
 \Panel1\Initialisation\Check INI:line 28
 \Panel1>Main Loop\Abort Loop\Disable Buttons RUN:line 1
Object \Panel1>Main Loop\Loop Initialisation
 \Panel1>Main Loop\Run Loop:line 4
Object \Panel1>Main Loop\FrameLoop
 \Panel1>Main Loop\Run Loop:line 17
 \Panel1>Main Loop\Run Loop:line 26
 \Panel1>Main Loop\Run Loop:line 40
 \Panel1>Main Loop\Run Loop:line 49
Object \Panel1>Main Loop\StopsLoop
 \Panel1>Main Loop\Run Loop:line 28
 \Panel1>Main Loop\Run Loop:line 52
Object \Panel1>Main Loop>MainLoop
 \Panel1>Main Loop\Run Loop:line 5
 \Panel1>Main Loop\Run Loop:line 60
Object \Panel1>Main Loop\----- calibrate at 0 deg.
 \Panel1>Main Loop\Run Loop:line 10
Object \Panel1>Main Loop\-----move table
 \Panel1>Main Loop\Run Loop:line 32
Object \Panel1>Main Loop\-----make pictures
 \Panel1>Main Loop\Run Loop:line 16
 \Panel1>Main Loop\Run Loop:line 39

Object \Panel1\Main Loop\-----
 \Panel1\Main Loop\Run Loop:line 27
 \Panel1\Main Loop\Run Loop:line 50
 \Panel1\Main Loop\Loop Initialisation:line 1
 \Panel1\Main Loop\Loop Initialisation:line 9
Object \Panel1\Main Loop\TimeDelay
 \Panel1\Main Loop\Run Loop:line 13
 \Panel1\Main Loop\Run Loop:line 24
 \Panel1\Main Loop\Run Loop:line 38
 \Panel1\Main Loop\Run Loop:line 47
 \Panel1\Main Loop\Run Loop:line 57
 \Panel1\Main Loop\Abort Loop\STOP Run Loop:line 2
Object \Panel1\Main Loop\Monitoring\Pictures taken
 \Panel1\Main Loop\Run Loop:line 23
 \Panel1\Main Loop\Run Loop:line 46
Object \Panel1\Main Loop\Monitoring\Turns made
 \Panel1\Main Loop\Run Loop:line 56
Object \Panel1\Main Loop\Monitoring\Finish Lamp
 \Panel1\Main Loop\Run Loop:line 2
 \Panel1\Main Loop\Run Loop:line 61
Object \Panel1\Main Loop\Abort Loop\STOP Run Loop
 \Panel1\Initialisation\Check INI:line 3
 \Panel1\Main Loop\Abort Loop\Disable Buttons RUN:line 2
Object \Panel1\Main Loop\Abort Loop\abort
 \Panel1\Main Loop\Run Loop:line 3
 \Panel1\Main Loop\Run Loop:line 6
 \Panel1\Main Loop\Run Loop:line 18
 \Panel1\Main Loop\Run Loop:line 29
 \Panel1\Main Loop\Run Loop:line 41
 \Panel1\Main Loop\Run Loop:line 53
 \Panel1\Main Loop\Abort Loop\STOP Run Loop:line 1
Object \Panel1\Main Loop\Abort Loop\BOOLisONE
 \Panel1\Main Loop\Run Loop:line 6
 \Panel1\Main Loop\Run Loop:line 8
 \Panel1\Main Loop\Run Loop:line 18
 \Panel1\Main Loop\Run Loop:line 20
 \Panel1\Main Loop\Run Loop:line 25
 \Panel1\Main Loop\Run Loop:line 29
 \Panel1\Main Loop\Run Loop:line 31
 \Panel1\Main Loop\Run Loop:line 41
 \Panel1\Main Loop\Run Loop:line 43
 \Panel1\Main Loop\Run Loop:line 48
 \Panel1\Main Loop\Run Loop:line 51
 \Panel1\Main Loop\Run Loop:line 53
 \Panel1\Main Loop\Run Loop:line 55
 \Panel1\Main Loop\Run Loop:line 58
 \Panel1\Main Loop\Run Loop:line 59
Object \Panel1\Main Loop\Abort Loop\ABORT
 \Panel1\Main Loop\Run Loop:line 7
 \Panel1\Main Loop\Run Loop:line 19
 \Panel1\Main Loop\Run Loop:line 30
 \Panel1\Main Loop\Run Loop:line 42
 \Panel1\Main Loop\Run Loop:line 54
Object \Panel1\Main Loop\Abort Loop\Disable Buttons RUN
 \Panel1\Main Loop\Run Loop:line 1

Object \Panel1\Main Loop\Abort Loop\Enable Buttons RUN
 \Panel1\Main Loop\Run Loop:line 62
 \Panel1\Main Loop\Abort Loop\STOP Run Loop:line 3

Object \Panel1\Main Loop\Variables\StopCounter
 \Panel1\Main Loop\Run Loop:line 15
 \Panel1\Main Loop\Run Loop:line 33
 \Panel1\Main Loop\Run Loop:line 34

Object \Panel1\Main Loop\Variables\TurnCounter
 \Panel1\Main Loop\Run Loop:line 9
 \Panel1\Main Loop\Run Loop:line 56
 \Panel1\Main Loop\Loop Initialisation:line 7

Object \Panel1\Main Loop\Variables\PicCounter
 \Panel1\Main Loop\Run Loop:line 22
 \Panel1\Main Loop\Run Loop:line 23
 \Panel1\Main Loop\Run Loop:line 45
 \Panel1\Main Loop\Run Loop:line 46
 \Panel1\Main Loop\Loop Initialisation:line 6

Object \Panel1\Main Loop\Variables\Position
 \Panel1\Main Loop\Run Loop:line 14
 \Panel1\Main Loop\Run Loop:line 34
 \Panel1\Main Loop\Run Loop:line 35
 \Panel1\Main Loop\Loop Initialisation:line 8

Object \Panel1\Main Loop\Variables\Angle
 \Panel1\Main Loop\Run Loop:line 34
 \Panel1\Main Loop\Loop Initialisation:line 5

Object \Panel1\Main Loop\Variables\Command
 \Panel1\Main Loop\Run Loop:line 35
 \Panel1\Main Loop\Run Loop:line 36

Object \Panel1\Main Loop\Variables\Number of Frames per Stop
 \Panel1\Main Loop\Loop Initialisation:line 10

Object \Panel1\Main Loop\Variables\Number of Stops per 360°
 \Panel1\Main Loop\Loop Initialisation:line 2

Object \Panel1\Main Loop\Variables\Number of full 360° Turns
 \Panel1\Main Loop\Loop Initialisation:line 3

Object \Panel1\Main Loop\Variables\Delay between frames (sec.)
 \Panel1\Main Loop\Run Loop:line 24
 \Panel1\Main Loop\Run Loop:line 47

Object \Panel1\Main Loop\Variables\Delay between full turns (sec.)
 \Panel1\Main Loop\Loop Initialisation:line 4

Object \Panel1\Main Loop\Variables\NoFrames
 \Panel1\Main Loop\Run Loop:line 17
 \Panel1\Main Loop\Run Loop:line 40
 \Panel1\Main Loop\Loop Initialisation:line 10

Object \Panel1\Main Loop\Variables\NoStops
 \Panel1\Main Loop\Run Loop:line 28
 \Panel1\Main Loop\Loop Initialisation:line 2
 \Panel1\Main Loop\Loop Initialisation:line 5

Object \Panel1\Main Loop\Variables\NoTurns
 \Panel1\Main Loop\Run Loop:line 5
 \Panel1\Main Loop\Loop Initialisation:line 3

Object \Panel1\Main Loop\Variables\Delay360
 \Panel1\Main Loop\Run Loop:line 57
 \Panel1\Main Loop\Loop Initialisation:line 4

Object \Panel1\manual control\nreset
 \Panel1\Initialisation\Check INI:line 10
 \Panel1\Initialisation\Check INI:line 17
 \Panel1\Main Loop\Abort Loop\Disable Buttons RUN:line 6

Object \Panel1\manual control\ncal
 \Panel1\Initialisation\Check INI:line 11
 \Panel1\Initialisation\Check INI:line 18
 \Panel1\Main Loop\Abort Loop\Disable Buttons RUN:line 7

Object \Panel1\manual control\limit switches OFF
 \Panel1\Initialisation\Check INI:line 12
 \Panel1\Initialisation\Check INI:line 19
 \Panel1\Main Loop\Abort Loop\Disable Buttons RUN:line 8

Object \Panel1\manual control\Send VENUS Command
 \Panel1\manual control\nreset:line 2
 \Panel1\manual control\ncal:line 2
 \Panel1\manual control\limit switches OFF:line 2
 \Panel1\manual control\limit switches OFF:line 4

Object \Panel1\manual control\Take Frame and Store
 \Panel1\Initialisation\Check INI:line 9
 \Panel1\Initialisation\Check INI:line 24
 \Panel1\Main Loop\Abort Loop\Disable Buttons RUN:line 11

Object \Panel1\manual control\VENUS Commands\VENUS Command
 \Panel1\Initialisation\Check INI:line 8
 \Panel1\Initialisation\Check INI:line 16
 \Panel1\Main Loop\Abort Loop\Disable Buttons RUN:line 5
 \Panel1\manual control\VENUS Commands\VENUS Command:line 1
 \Panel1\manual control\VENUS Commands\VENUS Command:line 2
 \Panel1\manual control\VENUS Commands\Send VENUS Command:line 1
 \Panel1\manual control\VENUS Commands\Send VENUS Command:line 3
 \Panel1\manual control\Send VENUS Command:line 1
 \Panel1\manual control\Send VENUS Command:line 3

Object \Panel1\manual control\VENUS Commands\Venuscmd
 \Panel1\Initialisation\Initialise Table\Load File Line & Send:line 2
 \Panel1\Initialisation\Initialise Table\Reset Table:line 2
 \Panel1\Initialisation\Initialise Table\Reset Table:line 4
 \Panel1\Initialisation\Initialise Table\Reset Table:line 7
 \Panel1\Initialisation\Initialise Table\Reset Table:line 9
 \Panel1\Main Loop\Run Loop:line 11
 \Panel1\Main Loop\Run Loop:line 36
 \Panel1\manual control\VENUS Commands\Send VENUS Command:line 1
 \Panel1\manual control\nreset:line 1
 \Panel1\manual control\ncal:line 1
 \Panel1\manual control\limit switches OFF:line 1
 \Panel1\manual control\limit switches OFF:line 3
 \Panel1\manual control\Send VENUS Command:line 1

Object \Panel1\manual control\VENUS Commands\VENUS Commands Display
 \Panel1\Initialisation\Initialise Table\RS232 1:line 2
 \Panel1\manual control\VENUS Commands\VENUS Command:line 2
 \Panel1\manual control\VENUS Commands\Clear display:line 1

Object \Panel1\manual control\VENUS Commands\VenuseDelay
 \Panel1\Initialisation\Initialise Table\Reset Table:line 6
 \Panel1\Initialisation\Initialise Table\Reset Table:line 11
 \Panel1\manual control\VENUS Commands\Send VENUS Command:line 2
 \Panel1\manual control\Send VENUS Command:line 2

Object \Panel1\manual control\VENUS Commands\Send VENUS Command
 \Panel1\Initialisation\Initialise Table\Load File Line & Send:line 3
 \Panel1\Initialisation\Initialise Table\Reset Table:line 3
 \Panel1\Initialisation\Initialise Table\Reset Table:line 5
 \Panel1\Initialisation\Initialise Table\Reset Table:line 8
 \Panel1\Initialisation\Initialise Table\Reset Table:line 10
 \Panel1\Main Loop\Run Loop:line 12
 \Panel1\Main Loop\Run Loop:line 37